Laponite hydrogel scaffolds containing graphene and phosphonate moieties for bone tissue engineering

A thesis submitted to the University of Manchester for the degree of Doctor of Philosophy in the Faculty of Science and Engineering

2021

Thunyaporn Srisubin

School of Natural Sciences

Department of Materials

TABLE OF CONTENTS

Word count: 56,560

LIST OF FIGURES

Chapter 1

Chapter 2

Chapter 3

Chapter 4

Chapter 5

Chapter 6

Appendix

LIST OF TABLES

Chapter 1

Chapter 2

Chapter 3

Chapter 4

LIST OF ABBREVIATIONS

Abbreviations	Meaning
2D	Two dimensional
3D	Three dimensional
AFM	Atomic force microscopy
ALP	Alkaline phosphatase
BMP	Bone morphogenetic proteins
BPs	Bisphosphonates
BSA	Bovine serum albumin
BTE	Bone tissue engineering
CVD	Chemical vapor deposition
DLS	Dynamic light scattering
DMEM	Dulbecco's Modified Eagle's Medium
dsDNA	Double-stranded DNA
ECM	Extracellular matrix
EDL	Electric double layer
FAK	focal adhesion kinase
FAs	Focal adhesions
FBS	Fetal bovine serum
Fn	Fibronectin
FTIR	Fourier-transform infrared
FWHM	Full width at half maximum
GFNs	Graphene-family nanomaterials
G–$PO(OH)_2$	Graphene phosphonate produced by the edge-specific functionalisation
G–PVPA	Graphene phosphonate produced by the edge-specific functionalisation
G–SO_3	Graphene sulfonate
G-SH	Graphene thiol
GNPs	Graphene nanoplatelets
GO	Graphene oxide
GO–$PO(OH)_2$	Graphene oxide phosphonate produced by the edge-specific functionalisation
GO–PVPA	Graphene oxide phosphonate produced by the radical polymerisation of PVPA-*co*-AA in the presence of GFNs
GO–SO_3	Graphene oxide sulfonate
GO-SH	Graphene oxide thiol
Lap	Laponite
Lap-GO	Laponite gel incorporated with GO

Abbreviations	Meaning
Lap-PVPA	Laponite gel incorporated with PVPA-*co*-AA
Lap-PVPA-GO	Laponite gel incorporated with PVPA-*co*-AA and GO
LbL	Layer-by-layer
LVE	Linear viscoelastic
HA	Hyaluronic acid
HOBs	Primary human osteoblasts
hASCs	Human adipose-derived stem cells
hBMSCs	Human bone marrow-derived mesenchymal stem cells
hMSCs	Human mesenchymal stem cells
HUVECs	Human umbilical vein endothelial cells
H&E	Haematoxylin and Eosin
MC3T3-E1	Mouse calvarial bone-derived nontransformed cell line
MMPs	Matrix metalloproteinases
PAA	Poly(acrylic acid)
PBS	Phosphate-buffered saline
PCL	Polycaprolactone
PDGF	Platelet-derived growth factor
PDGF-BB	Platelet derived growth factor β
PEG	Poly(ethylene glycol)
PEI	Polyethyleneimine
PEO	Poly(ethylene oxide)
PGA	Poly(L-glutamic acid)
PLA	Poly(lactic acid)
PLGA	Poly(lactic-co-glycolic acid)
PLL	Poly(L-lysine)
PMMA	Poly(methyl methacrylate)
PNIPAM	Poly(N-isopropylacrylamide)
pNP	p-nitrophenol
pNPP	p-nitrophenyl phosphate
PSS	Poly(sodium-4-styrene-sulfonate)
PVA	Polyvinyl alcohol
PVPA	Poly(vinylphosphonic acid)
PVPA-*co*-AA	Poly(vinylphosphonic acid-*co*-acrylic acid)
PUR	Polyurethane
QCM	Quartz crystal microbalance
RGD	L-arginyl-glycyl-L-aspartyl
rGO	Reduced graphene oxide
ROBs	Primary rat osteoblasts

Abbreviations	Meaning
ROS	Reactive oxygen species
Saos-2	Human osteosarcoma cell line
SAXS	Small-angle X-ray scattering
SEM	Scanning electron microscopy
TCP	Tissue culture plastic
TEM	Transmission electron microscopy
TERM	Tissue regeneration and regenerative medicine
TGA	Thermogravimetric analysis
TGF-β	Transforming growth factor-β
UV	Ultraviolet
UV-Vis	Ultraviolet-visible
VEGF	Vascular endothelial growth factor
XPS	X-ray photoelectron spectroscopy

ABSTRACT

The demand for materials for bone tissue engineering (BTE) to treat bone disorders has an upward trend, especially in ageing populations. The main aim of the work reported in this thesis was to develop injectable hydrogels comprising the nanoclay Laponite, graphene and phosphonate moieties that would provide biocompatible scaffolds with osteoconductive properties and mechanical properties tailored for use in BTE. The subordinate aim was to produce modified graphene-family nanomaterials (GFNs) that would provide functional groups by which to improve aqueous dispersibility of graphene, tether biomolecules, and accelerate osteogenic mineralisation.

Edge-specific functionalisation based upon electrophilic aromatic substitution and radical polymerisation in the presence of graphene were selected to produce functionalised graphene materials without introducing new defects into the graphene. Functionalisation was confirmed using FTIR, Raman, and XPS, which indicated a presence of functional groups and a low degree of defect in graphene structures, as well as demonstrating the change in aqueous dispersibility of graphene sheets. Phosphonate-modified graphene analogues were incorporated into two-dimensional polymer layer-by-layer (LbL) constructs for use in BTE. The biocompatibility and ability to support bone formation of GFN-containing LbL constructs were tested on human osteosarcoma Saos-2 cell line and primary human osteoblasts (HOBs). All GFN-containing LbL constructs supported cell adhesion, proliferation, and osteogenic mineralisation of Saos-2. On the other hand, cell attachment and cell activities of HOBs were highly dependent on protein adsorption, surface chemistry, and topography of constructs. Only HOBs seeded on GO LbL substrate exhibited cell adhesion, proliferation, and mineralisation. Consequently, GO was selected to incorporate into Laponite-based gels.

Injectable Laponite gels containing GO and poly(vinylphosphonic acid-*co*-acrylic acid) (PVPA-*co*-AA) were fabricated. The addition of PVPA-*co*-AA increased mechanical properties of Laponite gels whilst GO did not, likely due to a low concentration. Osteogenic mineralisation of Saos-2 within Laponite-based gels were determined to investigate a potential of Laponite-based scaffolds for use in BTE. Positive staining of alizarin red S staining was detected at 3 weeks post-seeding in all samples cultured in non-induction growth medium, suggesting the osteoinductive property of Laponite nanoclay. The addition of GO and PVPA-*co*-AA did not enhance or accelerate mineralisation of Saos-2 within nanoclay gel scaffolds. All Laponite-based gels maintained structural integrity up to 10 days. In summary, Laponite-based gels offer a potential scaffold to serve as osteogenic microenvironments with cytocompatibility and biodegradability. However, Laponite gels lacked the effective porosity to allow cell migration.

DECLARATION

The author of this thesis declares that no portion of the work referred to in the thesis has been submitted in support of an application for another degree or qualification of this or any other university or other institute of learning.

COPYRIGHT STATEMENT

ACKNOWLEDGEMENTS

I would never have been able to finish my thesis without the guidance of my supervisors, help from friends, and support from Royal Thai Government and my family. I also would like to thank the Department of Materials, University of Manchester for giving me the opportunity to undertake this PhD and granting me the programme extension due to the impact caused by COVID-19 pandemic.

I would like to thank my supervisors, Dr Christopher Blanford and Prof Julie Gough, for the patient, kind and professional guidance as well as the encouragement, and the advice they have provided throughout my time as their group's member. I have been extremely lucky to have both supervisors who very cared about my work, and responded to my questions and queries so promptly.

I would like to thank Louise Carney, Marie O'brien, and Nathan Murray for their training, helps, and supports either inside or outside laboratories. I would also like to thank Zara Smith, Chinnawich, Kasama, Thammarit, Cosimo Ligorio, Negin Kamyar, Fan Fei, Kanokporn, Piya, Blanford's group members, and Gough's group members for their useful advice, support, training, and entertainment which made my PhD enjoyable and not too stressful.

Furthermore, I would like to thank Dr Jonathan Dawson from the University of Southampton for his very helpful advice, guidance, and training about cell encapsulation within nanoclay gels. He also provided me Laponite powder and primary stem cells for a trial.

I would really like to thank my beloved spouse, Pongsiri Khamtui, for always being beside me through the good and bad times. My PhD journey would be much more difficult if I do not have him by my side. Moreover, I would like to thank my wonderful parents and family for their loves, encouragement and supports.

Special thank is given to BLACKPINK and BTS (South Korean girl group and boy band) for being one of my happiness during my PhD study. Their performances and songs could help me relaxed and relieved from stress.

Finally and most importantly, I would like to thank myself for being patient and never giving up even though there were many obstacles that made me frustrated and burnout. I would like to say to myself that "I am really proud of you☺"

COVID-19 IMPACT STATEMENT

The COVID-19 pandemic led to laboratory closure for 4.5 months (mid-March to the end of July 2020). Once laboratories and buildings re-opened, access was limited. Working and transporting samples between buildings was restricted, as was out-of-hours access. The COVID-19 pandemic also delayed the move of my primary research laboratory by approximately 3.5 months (mid-September 2020 to early January 2021). Although I could access to laboratories and facilities only 3.5 months even though I was granted a PhD programme extension for 8 months from July 2020 to February 2021. Accordingly, the COVID-19 pandemic and associated delays have had a significant effect on my ability to perform, and most importantly, repeat experiments.

The CQ1 imaging system was required for live-cell imaging in the study of cell migration (chapter 5 in this thesis), so that I could observe the movement of cells over time more accurately by using the same sample with fixed position throughout the test period. The CQ1 imaging system was also required to keep my images consistent. The system was packed for moving at the end of September 2020 but was not available until 4th March 2021, after the end date of my PhD programme extension. I used the SP8 confocal microscope instead of the CQ1 imaging system. However, the SP8 confocal microscope limits the image acquisition of samples in well plate, resulting in a non-sterile conditions during image acquisition. Hence, the different samples were used at different time point of analysis – for this reason, I could not accurately interpret the finding. Moreover, I did not have enough time to repeat this experiment.

I was also unable to quantify the calcium deposited in matrix mineralisation by a colorimetric assay this analysis because there were other three prioritised experiments to complete for this thesis in the last 1.5 months of my PhD programme extension. Therefore, only qualitative histological staining was performed on cross-sections of samples to indicate the mineralisation of SaOS-2 within Laponite-based gels (chapter 4 in this thesis).

Chapter 1

Introduction

1.1 Overview

1.1.1 High-level summary

Bone is a dynamic tissue that possesses an intrinsic ability to renew and repair through remodelling process in response to injury.[1, 2] However, spontaneous bone regeneration may be unable to develop in patients with bone injuries beyond the extent of self-healing, such as non-union fractures and bone-related diseases, which can lead to long-term bone defects and substantial pain for the patients.[2, 3] In the past few years, fragility fractures, bone loss due to tumour removal and infection that leads to the need for bone void fillers have become a crisis across the European countries. According to the International Osteoporosis Foundation (IOF), there are approximately 2.7 million cases of bone fractures every year and around 20 million people are diagnosed with osteoporosis in the EU.[4] In 2017, the associated costs on healthcare systems were about £4.52 billion and it could rise to £5.89 billion by 2030, in the UK alone.[5] Apparently, fragility fractures potentially incur further burden on patients and healthcare systems and remain a growing public health concern requiring urgent action.

Bone tissue engineering (BTE) is a field that aims to replace or repair bone and overcome the disadvantages of current treatments (e.g., donor site morbidity, immune response, limited availability and pathogen transfer).[6] The development of BTE requires biomaterial scaffolds that have ability to facilitate the delivery of cells and/or biological molecules to the site of defects or tissue damage, maintain cell viability, mimic the microenvironment of native extracellular matrix (ECM), and subsequently provide a template for bone tissue formation. Moreover, BTE scaffolds should provide sufficient transportation of nutrients and removal of waste during tissue regeneration process. To this function, parameters such as biomimetic 3D structure, osteoconductivity, bulk mechanical properties, degradation profiles, and delivery

system are essential. The optimisation of these parameters is one of remained unmet challenges in BTE.[2, 7, 8]

Hydrogels are a promising alternative scaffold to current bone graft materials, with advantages with lower cost, easier process, and reduced operating time. Furthermore, hydrogels possess ability to mimic the native ECM and facilitate transport of oxygen, nutrients, and waste, as well as soluble growth factors. Hydrogels have a unique advantage in which damage sites can be easily fulfilled with minimally invasive surgery and regardless of defect shape by using injection technique.[9-11]

Clay nanoparticles are a phyllosilicate mineral that is composed of layered structure of tetrahedral/octahedral sheets.[12, 13] Many research works that studied on clay nanoparticles ("nanoclay") for regenerative medicine have suggested the capability of nanoclay to become a new strategy of biomaterial scaffold design for tissue engineering and regenerative medicine (TERM).[12, 14] Laponite, a synthetic nanosilicate clay with a nominal formula of $Na^{+0.7}[(Si_8Mg_{5.5}Li_{0.3})O_{20}(OH)_4]^{-0.7}$, is a two-dimensional (2D) material that consists of disc-shaped crystals.[15, 16] Single Laponite crystal possesses a dual charge distribution, a permanent negative charge on the surface and a positive charge at the edges, which can interact with several types of chemical entities such as small molecules or ions, polymers and inorganic nanoparticles.[12, 15] Laponite is a potential candidate in biomedical applications because it degrades into nontoxic and bioactive products such as magnesium ions, sodium ions and orthosilicic acid which can be easily absorbed by human body.[15, 17] Laponite has been used in drug delivery,[18, 19] bioimaging[20, 21] and tissue engineering.[15, 22, 23] Laponite clay is discussed in detail in 1.8.1.

In 2018, the study of Dawson's group has shown that Laponite is an osteoinductive clay that can form an injectable hydrogel and serve as a host microenvironment for the osteogenic differentiation of human mesenchymal stem cells (hMSCs).[7] Furthermore, composite hydrogel scaffolds made of Laponite incorporated with other materials such as poly(ethylene oxide),[24] gelatin methacrylate[17, 25] and poly(*N*-acryloyl glycinamide)[26] have shown to promote cell adhesion, proliferation and osteogenic differentiation of hMSCs and osteoblast-like cells. These studies have highlighted the potential of Laponite to serve as BTE scaffolds. However, self-assembled nanoclay gels are classified as physical crosslinking hydrogels, which generally

exhibit lower mechanical properties and stability in a comparison to hydrogels obtained from chemical crosslinking. The poor stability and mechanical strength may restrict their use in biomedical applications. Consequently, composite hydrogels comprising of, for example, polymers,[26, 27] nanoclay,[26-28] and carbon-based nanomaterials,[27, 28] have been developed to achieved the greater mechanical and rheological properties with enhanced stability.

Graphene is a planar single layer of sp^2 hybridised carbon atoms arranged into a two-dimensional honeycomb lattice.[29] Graphene-family nanomaterials (GFNs) can also be classified based on chemical modification such as graphene oxide (GO). GO possesses oxygen-containing functional groups (carboxyl, hydroxyl and epoxide groups) at the edges and basal surfaces, allowing its dispersion in water and polar solvents.[30] Graphene is a stiff and readily modifiable form of carbon that can both tune the mechanical properties of composites and serve as a delivery platform for therapeutic agents.[31, 32] Graphene-based materials have been applied to BTE because GFNs not only support cell adhesion and proliferation, but also enhance osteogenic differentiation of stem cells.[33-36] Many studies demonstrated that GFNs can induce the differentiation of stem cells into osteogenic lineages[33-36] and support the adhesion and proliferation of osteoblasts.[37, 38] Graphene is discussed in detail in 1.8.2.

Phosphonates or phosphonic acids ($C–PO(OH)_2$) are organophosphorous molecules containing stable carbon–phosphorous (C–P) bonds in place of the labile carbon-oxygen-phosphorus linkages.[39] In biology and medicine, phosphonate compounds including bisphosphonates and phosphonate nucleoside analogues are commonly used as drugs in treatments of osteoporosis and antiviral therapy, respectively.[40, 41] A phosphonate-containing polymer, poly(vinylphosphonic acid-co-acrylic acid) (PVPA-*co*-AA) has been considered as a promising material for bone tissue engineering because it has been hypothesised to mimic the function of bone-protecting bisphosphonate drugs.[42-44] Bassi *et al*. have fabricated polycaprolactone (PCL)/PVPA-*co*-AA scaffold and investigated the healing potential of critical size defect created on parietal bones which were obtained from 4-day-old neonatal CD1 mice.[42] In a comparison to PCL scaffold, the presence of PVPA-*co*-AA in scaffold increased bone filling percentage and hydroxyapatite formation with a greater amount of calcium and phosphorous, indicative of the improvement in mineralisation and osteoblast proliferation. Moreover, PCL/ PVPA-*co*-AA scaffold showed a better integration into defect sites.[42] Phosphonates are discussed in detail in Section 1.9.

1.1.2 Hypothesis and research objectives

This work aimed to develop Laponite hydrogel scaffolds containing both graphene and phosphonate for BTE. The hypothesis of this research was that this composite would promote accelerated bone repair and regeneration due to the synergistic effect of all three components. The research objectives of this thesis are outlined below:

- To develop phosphonate-modified graphene derivatives by edge-specific functionalisation and radical polymerisation.
- To assess toxicity and ability to support bone cell formation of phosphonate-modified graphene derivatives towards primary human osteoblasts (HOBs) using 2D culture on layer-by-layer (LbL) assemblies.
- To incorporate graphene and phosphonate into Laponite hydrogel and compare its properties to unmixed Laponite hydrogel.
- To evaluate possibility of Laponite-based hydrogels to serve as a scaffold for BTE using 3D encapsulation model.

1.1.3 Structure of this thesis

This thesis is presented in the "traditional" format (rather than based on published papers) and is divided into 6 chapters. Chapter 1 introduces the theories and a review on previous literature that are relevant to the research studies presented in this thesis: bone biology, current treatments of bone fractures, BTE concept, injectable hydrogels and rheology, Laponite, graphene, phosphonates, and cell migration. Chapter 2 consists of the details of reagents, chemicals, experimental methods, and characterisations conducted in this project.

Chapter 3 presents the functionalisation of GFNs through the edge-specific functionalisation and the radical addition, along with characterisation to confirm the functional groups attached on GFNs. The biocompatibility and ability of phosphonate-modified GFNs to support osteogenic mineralisation of osteoblasts are also presented in this chapter. Chapter 4 presents the fabrication of injectable Laponite hydrogels containing GO and phosphonate moieties for use in BTE. Chapter 5 presents a study of osteoblasts migration in Laponite gels by seeding fluorescent dye-labelled Saos-2 on gel surface and acquiring stacked images using a confocal microscopy. The results were reported as 3D images to indicate the change in

distance between cells and a reference level over the test period. The cell responses towards surface of Laponite-based gels were also investigated and described in this chapter.

Chapter 6 summarises the overall key research findings and suggestions for additional experiments and future scope of the research studies presented in this thesis.

1.2 Bone biology

1.2.1 Bone structure, composition, and cells

Bone is a connective tissue that serves as the skeleton with the function of providing a structural support. On the microscopic level, the skeleton comprises of two major types of bone which are cortical bone (80%) and cancellous bone (20%).[1, 45-47] The proportion of each bone type varies at different sites in the skeleton.[47] Cortical bone is hard and dense, with a low surface area and 10% porous, which is mainly found in outer region of long bones (femur, tibia, ulna and radius) and flat bones (skull, sternum and scapula).[1, 45] Cortical bone is composed of blood vessels in middle surrounded by a bundle of coaxial lamellae layers which is called Haversian systems.[1] Cancellous bone (also known as trabecular bone) is a sponge-like morphology, with a honeycomb structure of trabeculae, which locates in the middle of long bones, flat bones, and vertebrae.[1, 47] The structure of cortical bone with cancellous bone located in the centre is illustrated in Figure 1-1. Cancellous bone has porosity between 50–90% whereas cortical bone is a compact structure, making the elastic modulus and compressive strength of cortical bone approximately 10 times higher than that of cancellous bone.[47] The mechanical properties of bone are described in Table 1-1.[48-50]

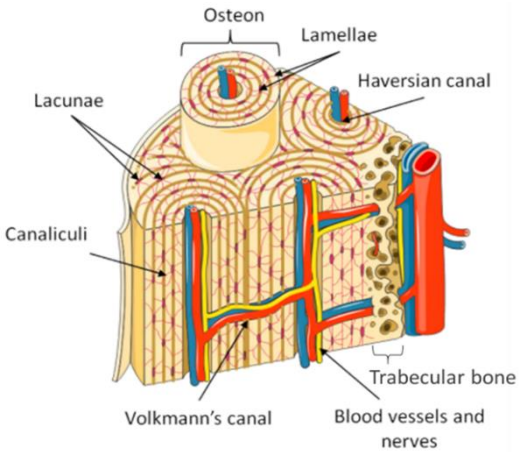

Figure 1-1. Cross-section of cortical bone with trabecular bone encased in the centre. Adapted from Chabanon, Morgan.[51]

Table 1-1. Mechanical properties of bone. Values taken from references 48–50.

Property	Cortical bone	Cancellous bone
Tensile strength (MPa)	50–190	10–100
Compressive strength (MPa)	90–230	2–45
Young's modulus (GPa)	7–30	0.02–0.5
Strain to failure (%)	1–3	5–7
Shear strength (MPa)	53–70	
Shear modulus (GPa)	3	

The typical compositions of bone are bone matrix (~90–95%), water (~5–10%) and cells.[45, 46] Bone matrix consists of organic matrix (40% dry weight) and inorganic matrix (60% dry weight). The main organic component is collagens, with type I collagen the predominant in bone matrix. Type I collagen is a triple-helix protein fibril assembled by two collagen alpha I (α_1) peptide chains and one collagen alpha II (α_2) peptide chain, which is mainly found in woven and lamellar bone.[1, 46] The organic matrix also contains non-collagenous proteins, enzymes, and growth factors. These include proteoglycans, glycoproteins, osteocalcin, fibronectin, alkaline phosphatase, and transforming growth factor-β (TGF-β).[1, 45, 46] The inorganic component of bone matrix is predominantly calcium hydroxyapatite ($Ca_{10}(PO_4)_6(OH)_2$), a crystal form of calcium and phosphate. Hydroxyapatite, integrated with tensile strength and elasticity derived from the organic matrix, is responsible for mechanical strength of bone. In addition to calcium and phosphorous, bone mineral also includes carbonate, magnesium, fluoride, and citrate in variable quantities.[1, 46] Important bone cells in bone biology include osteoblasts, osteocytes, and osteoclasts.[45, 46, 52]

1.2.2 Osteoblasts

Osteoblasts are cells that are located along bone surfaces and reponsible for the development of bone matrix formation. Osteoblasts originally differentiated from osteoprogenitor cells which are mesenchymal stem cells (MSCs).[45] Morphological characteristics of osteoblasts are cuboidal or columnar with a round nucleus and vary in size from hardly detectable under light microscope to maximum of 50 μm when activated.[45, 46, 52] The formation of bone matrix occurs by deposition of organic matrix where osteoblasts secrete collagen proteins, primarily type I collagen, proteoglycans, and non-collagenous proteins (osteocalcin, osteonectin, osteopontin, and bone sialoprotein). Subsequently, mineralisation of bone matrix takes place.[45, 52, 53] Furthermore, osteoblasts are invloved in bone remodelling process and

responsive to mechanical stimuli applied to bone tissue.[45, 53] Mature osteoblasts can show cytoplasmic processes towards the bone matrix and reach the osteocytes processes. At this stage, some of mature osteoblasts can possibly (1) undergo apoptosis or (2) further differentiate to osteocytes or bone-lining cells. [52-54] Bone-lining cells are inactive flat shaped osteoblasts. Their role is likely to prevent the direct interaction between osteoclasts and the bone matrix, where bone resorption should not occur.[52, 53]

The differentiation pathway of MSCs into osteoblastic cells is shown in Figure 1-2. The differentiation of stem cells is guided by multiple transcription factors and extracellular signalling molecules. In osteogenic differentiation, runt-related transcription factor 2 (Runx2) is identified as the master transciption factor regulating the expression of osteoblastogenic markers.[55-57] The expression of Runx2 in osteoblastogenesis is mediated and upregulated by bone morphogenetic proteins (BMPs) which are members of TGF-β superfamily of proteins.[56] Wnt signalling is required at the early stage to induce β-catenin translocation into the nucleus, after which osteoblastogenic target gene expression is enhanced.[56, 57] The development of precursor cells to functional osteoblasts requires the expression of Osterix (Osx), a crucial transcription of osteoblast commitment and differentiation. Osx can activate the expression of ALP, type I collagen, osteocalcin (OCN), osteopontin (OPN), and bone sialoprotein.[56] Activating transcription factor 4 (ATF4) is another essential transcription factor in osteoblastogenesis that generate the interaction with Runx2 directly to promote the secretion of OCN.[56, 57]

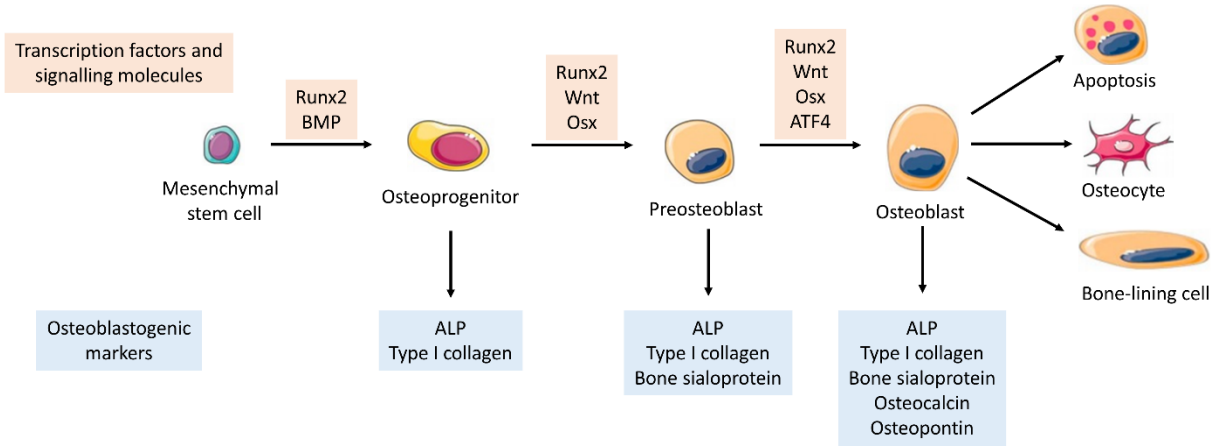

Figure 1-2. Schematic illustration of mesenchymal stem cell differentiation pathway into osteoblast lineage cells. Adapted from Arboleya *et al*.[55] and Amarasekara *et al*.[56]

1.2.3 Osteocytes

Osteocytes are the most abundant cells in bone, approximately 90–95% of the total bone cells, which are enclosed within gaps between lamellae (referred to lacunae) surrounded by mineralised bone matrix. Osteocytes have a dendritic morphology and they are derived from MSCs lineage through differentiation of mature osteoblasts.[52, 53] At the end of bone formation process, a subpopulation of osteoblasts become functional osteocytes. This process is accompanied by conspicuous morphological and ultrastructural changes, during which the rounded osteocytes become smaller and encased in mineralised bone matrix.[52] In bone formation, osteocytes are shown to promote transportation of small signalling molecules between cells and intercellular communication within the bone tissue by forming cellular network, through which osteocytes communicate among themselves and osteoblasts in order to maintain tissue viability. This cell–cell communication network is necessary in the response of bone to mechanical loads and biological signals.[45-47, 52, 53, 58] In addition to controlling bone formation, osteocytes also play a role in regulating bone resorption by producing factors that are important to osteoclastogenesis.[52, 58]

1.2.4 Osteoclasts

Osteoclasts are multinucleated cells (around 2–100 nuclei per cell) and primary responsible for bone resorption.[1, 45, 46, 52] Osteoclasts mostly locate in concavity called Howship's lacunae which are active sites for bone resorption.[45, 46] Osteoclasts originate from monocyte/macrophage of hematopoietic stem cells (HSCs) lineage which circulate in vascular system before reaching bone.[45, 46, 52] The differentiation of HSCs towards osteoclasts (Figure 1-3) is influenced by several factors secreted from MSCs, osteoblasts, osteocytes, and stromal cells. Osteoprogenitor MSCs and osteoblasts secrete the macrophage colony-stimulating factor (M-CSF) which binds to cFMS receptor presented in osteoclast precursors, subsequently stimulating osteoclast proliferation and preventing their apoptosis.[52, 59] The differentiation of osteoclasts also requires the activation of RANK receptor by its ligand RANKL. The RANKL factor is an essential factor for osteclastogenesis and mainly expressed by osteocytes but also by osteoblasts and stromal cells.[1, 52, 59] The interaction of RANKL/RANK also stimulate the expression of other osteoclastogenic factors that regulate osteoclast activity.[1, 52] Specific markers expressed by osteoclastic lineage include Tartrate-resistant acid phosphatase (TRAP), calcitonin receptor, cathepsin K, and integrin β3.[55, 59] Osteoclasts play a

role in bone remodelling process by secreting degradative enzymes to dissolve mineral components and digest bone matrix proteins.[1, 45, 52] During bone resorption, osteoclasts release coupling factors which are stored in bone matrix to stimulate osteoblastic activities, resulting in bone formation and subsequent completing bone remodelling cycle.[52, 60]

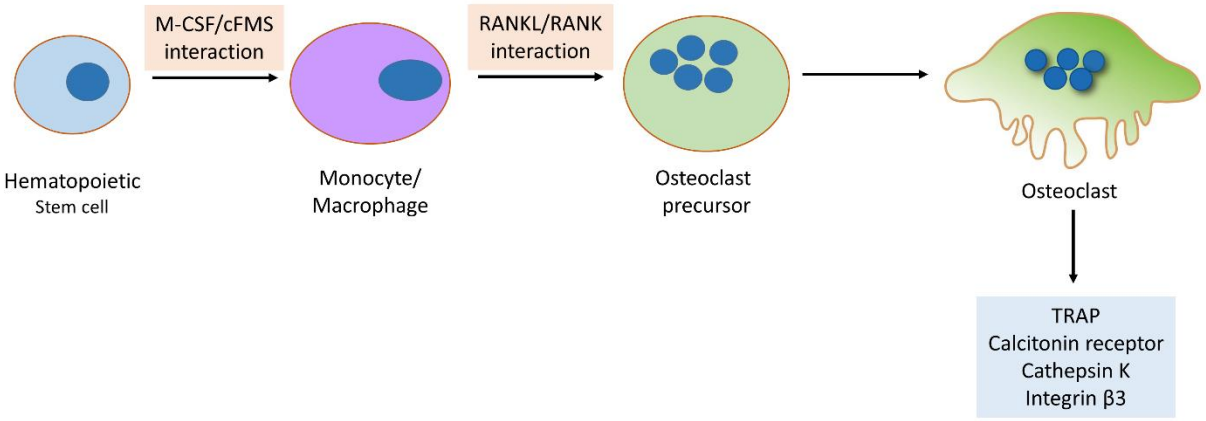

Figure 1-3. Schematic illustration of the osteoclast differentiation through hematopoietic stem cells. Adapted from Arboleya *et al*.[55] and Zhao *et al*.[59]

1.3 Bone formation and bone remodelling

Bone formation begins when collagenous proteins secreted from osteoprogenitor MSCs are replaced by bone tissue, resulting in the formation of woven bone.[47, 61] Woven bone is a primitive immature bone with randomly oriented collagen fibrils, numerous osteocyte, and incomplete vascularisation.[45, 47] Woven bone is subsequently calcified and further remodelled into mature bone called lamellar bone, which has more organised orientation of collagen fibres and greater mechanical properties.[45, 47, 61]

Bone formation occurs via two different processes: intramembranous ossification or endochondral ossification.[47, 61] At intramembranous ossification, bone is developed directly from the connective tissue membrane of undifferentiated MSCs. At the first stage, MSCs in the embryonic skeleton gather together, usually around blood vessels, and differentiate into osteoblasts, other osteogenic cells, and capillaries. Next, non-mineralised matrix (also known as osteoid) is secreted and mineralised by osteoblasts, after which osteoid continues to accumulate around blood vessels. Woven bone is then formed and remodelled into a vascularised mature lamellar bone.[47, 61] Intramembranous ossification is found the formation of flat bones, skull, and mandible.[45, 47, 61]

In contrast, long bones and short bones are produced by endochondral ossification.[47, 61] The process of endochondral ossification begins with the differentiation of MSCs into chondrocytes and subsequent formation of a cartilaginous matrix. Chondrocytes undergo hypertrophic changes and eventual death, after which the cartilage matrix is invaded by blood vessels and osteoblasts that are differentiated from osteoprogenitor cells in the perichondrium. The cartilage matrix is then calcified, following which bone matrix is deposited.[47, 61, 62]

Bone remodelling is essential process that required for not only the maintenance of its structural integrity and functions, but also the restoration of injured bone.[63, 64] Bone remodelling cycle initiates when hormonal (e.g., oestrogen or parathyroid hormone) or mechanical (e.g., bone damage or load changing) signals induce the expression of M-CSF and RANKL stimulating osteoclastic differentiation. Multinucleated osteoclasts subsequently attach to the bone surface and secrete hydrogen ions (H^+-adenosine triphosphatase) and enzymes, in particular cathepsin K, in order to resorb bone mineral and degrade the organic bone matrix, respectively. Osteoclasts eventually undergo apoptosis.[63, 64] Following bone resorption, there is a coupling mechanism that recruits the osteoprogenitor cells to promote bone formation. The coupling signals include TGF-β and insulin-like growth factor 1 (IGF1). At this stage, osteoclasts are replaced by osteoblast-lineage cells which initiate bone formation.[47, 63] Osteoblasts form bone matrix by producing several proteins including type I collagen, osteopontin, osteonectin, osteocalcin, and bone sialoprotein. As new bone is gradually mineralised, new bone is subsequently formed.[52, 53, 63] Osteoblasts also secrete alkaline phosphatase (ALP) which hydrolyses phosphate-containing compounds, releasing phosphate ions into matrix. Phosphate and calcium ions nucleate, forming hydroxyapatite crystals afterwards. As previously mentioned in Section 1.2.1, the mineral components of bone including hydroxyapatite, carbonate, magnesium, and acid phosphate provide mechanical rigidity and load-bearing strength whereas the organic matrix supplies elasticity and flexibility to bone.[52, 63] After mineralisation, bone returns to the quiescent stage, which is the original state of bone that is covered by the lining cells of inactive osteoblasts.[47, 63]

1.4 Fracture healing and current treatments for bone fracture

Bone possesses remarkable capability to repair itself to some extent following fracture or damage.[1, 2] Fracture healing is the process that involves bone development and bone remodelling, which can occur through either direct or indirect healing.[65-67] Direct (or primary) bone fracture healing does not generally occur because it requires a stability of correct anatomical reduction and rigid fixation. Direct fracture healing only relates to the remodelling of lamellar bone the Haversian canals, and blood vessels.[66, 67] In contrast, indirect or secondary fracture healing requires the callus formation prior to the formation of lamellar bone. Indirect healing is the most common mechanism of fracture healing which consists of three main stages: inflammation, callus formation, and remodelling.[65-67] Immediately following injury, inflammatory response is initiated. The inflammation induces the infiltration of inflammatory cells into a haematoma, the expression of cytokines and growth factors, and blood clot formation at the fracture sites to provide a template for MSCs migration and subsequent callus formation.[47, 65-67] After MSCs migrate to the fracture sites, cartilaginous matrix or *soft callus* is formed by chondrocytes differentiated from MSCs. This soft callus is then calcified and remodelled into *hard callus* (calcified cartilage) by osteoblasts, following which the hard callus is replaced with woven bone through both intramembranous and endochondral ossifications. At the remodelling stage, woven bone is gradually resorbed by osteoclasts and remodelled into a vascularised mature lamellar bone as commonly occurred in bone formation mechanism.[47, 65-67]

Current bone fracture treatments mostly require surgical interventions to facilitate bone healing with minimising complications as the natural process of bone regeneration may be impaired or insufficient due to mechanical and biological underlying factors.[67, 68] The process includes fracture fixation and immobilisation to stabilise the damaged site and minimising the fracture gap in order to promote bone healing enhancement.[67, 69] The ideal fixation system should be able to serve as a temporary platform which protects callus formation and accelerates the fracture healing process, allowing anatomy restoration and early mobilisation.[68] The bone fracture can be fixed and immobilised either externally or internally.[67, 70] External fixators provide fracture fixation on the basis of splinting and are the standard treatment for open fractures.[70] External fixators could be pins, screws, nails, and wires implantation with the fixator frame located externally and are mainly made of plaster

of Paris, synthetic casting materials, plastic or metal.[70] Due to the open wound, external fixation has high risk of infections which may require additional post-operative treatment including antibiotics and surgery.[70, 71] External fixation is also used in combination with internal fixators to provide further stability.[70] Internal fixation is the process in which the implants and fixators are located underneath skin, consequently the wound can be closed.

In addition to fixation and immobilisation procedures, bone healing can be modulated using bone grafting.[68] Bone grafting, the second most frequent tissue transplantation with over two million procedures annually worldwide, is one of the common techniques used in orthopaedic and trauma procedures to augment bone regeneration.[68, 72] Bone grafts can be harvested from either the same individuals or the genetically different donors of the same species, which are called "autografts" and "allografts" respectively.[72, 73] Among clinically available bone grafts, autografts are currently considered the gold standard for bone defect treatments due to its necessary properties which are osteoconduction, osteoinduction, and osteogenesis.[72, 73] Osteoconduction refers to the growth of bone on surface, therefore, osteoconductive biomaterials refer to the materials that support and allow tissue formation, osteoprogenitor cell growth, and bone development.[74, 75] Osteoinduction is defined as the stimulation of osteoprogenitor cells to differentiate into osteoblasts.[74, 75] Osteogenesis involves the differentiation of osteoprogenitor cells into osteoblasts and its subsequent mineralisation and formation of bone.[75]

Despite being the gold standard, autografting requires multiple surgeries and donor site complications are a concern, including the limitation of supply, dimension and shapes.[72] On the other hand, allografts are available in different shapes and dimension as cortical, cancellous, osteochondral and whole-bone segments.[68] Disadvantages of allografts are the risk of immunogenicity and immune reactions, possibility of infection transmission, cost, as well as the loss of osteogenic ability and mechanical properties during fabrication process.[3, 68, 72]

Due to these limitations, synthetic bone substitutes have been emerged as alternatives to natural bone grafts.[72] Calcium sulfate cements, calcium phosphate cements, bioactive glasses or the combinations of these materials are the common synthetic bone substitutes available currently.[68] Calcium sulfate cements possess osteoconductive properties, biodegradability,

easy preparation, and low cost.[72] According to a rapid resorption rate and low internal strength, calcium sulfate is mainly used to fill small bone defects with rigid internal fixation.[72, 76] The main disadvantage of calcium sulfate is faster degradation (1–3 weeks)[77, 78] independent from bone formation which can cause the loss of strength to support bone union, leading to unachievable optimal bone fusion rate and a risk of failure.[72, 79, 80] Calcium phosphate (CaP) cements are mainly used in trauma surgery and applied to fill bone voids.[80] CaP cements exhibit the longer resorption time with varying from 6 months to 10 years while calcium sulfate can be replaced by bone within 6–12 weeks.[80, 81] Phase separation of powder and liquid during injection is another important concern in clinical application, especially for minimally invasive surgical treatments.[72, 82] Bioactive glass is synthetic silicate-based ceramics that originally comprise of silicon dioxide (SiO_2), sodium oxide (Na_2O), calcium oxide (CaO), and phosphorus pentoxide (P_2O_5). Bioactive glass can achieve a strong physical bonding with host-bone and also generate dissolution products that stimulate osteogenic cells to produce bone matrix.[72, 83] However, bioactive glass is brittle, weak, and has a rapid degradation, leading to a higher pH and accumulated ions in the microenvironment which is not friendly to cells.[72, 83]

1.5 Bone tissue engineering: concept, biomaterials, and scaffolds for bone treatment

BTE has become an alternative approach for bone fracture treatments because of the limitations, complications and drawbacks of current treatments.[2, 84] BTE aims to overcome the problems of traditional grafts (i.e., donor site morbidity, immune response, limited availability of graft material, and pathogen transfer) to recover or repair bone.[6] BTE research began with bioactive glass research in 1960s, a material that has been used for clinical treatments since 1985.[85] The field expanded in the mid-1980s with Vacanti's "mouse with the human-ear" demonstration. In this work, a branching synthetic polymer was used as a scaffold for living chrondocytes.[86]

Tissue engineering requires three main components: cells, scaffolds, and regulatory signals. These combine to mimic the properties of natural autografts.[2, 87] In the context of BTE, regeneration of bone is driven by osteoprogenitor cells which are capable of differentiation into new osteoblasts and can be implanted in bone defects. Regarding the source of cells,

there are three classification which are autogeneic cells (patient's own cells), allogeneic cells (harvested from differrent people), and xenogenic cells (obtained from different species).[6, 87]

There are many potential cells commonly used in BTE including osteoblasts, preosteoblasts, and stem cells. MSCs have been extensively used to incorporate with BTE scaffolds as they can directly differentiate into osteoblasts under the osteogenic-induced culture condition.[88, 89] In addition to MSCs, isolated primary osteoblasts have been also used in research as they can potentially accerelate bone regeneration with the higher rate and extent.[89] The limitations of using primary cells are short lifespan during *in vitro* culture, substantial cost and risks of contamination, and variations of quality that are significantly dependent on the individual donor.[84, 89-91] For *in vitro* studies, the alternative to primary cells is immortalised cell lines which are usually derived from tumors. Immortalised cell lines have advantages over primary cells regarding unlimited expansion, no isolation required, ease of culture, and more stable characteristics. Potential osteoblastic cell lines widely used in bone biology including mouse calvarial bone-derived nontransformed cell line (MC3T3-E1) and human osteosarcoma-derived cell lines (Saos-2 and MG-63) demonstrated distinct similar activities with primary humen osteoblast (HOBs), such as proliferation, mineralisation, gene regulation, and ALP activity.[92, 93]

The ideal scenario for scaffold-based BTE is to create a living cells-bioengineered construct that can facilitate bone repair. A primary purpose of scaffolds is to provide temporary mechanical support with suitable microenvironment for tissue regeneration, in both cell-free and cell-containing systems.[2, 94] Ideally, scaffolds must be osteoinductive that can induce new bone formation through biomolecular signaling and recruiting progenitor cells. Scaffolds should also be able to act as a temporary extracellular matrixe and support cell attachment, proliferation and differentiation, including tissue regeneration without immune rejection or inflammation. Importantly, scaffolds need to possess mechanical properties which match the host bone tissue (Table 1-1). Furthermore, the degradation rate of scaffolds should be controllable and as close to the rate of bone tissue formation to preserve stable mechanical properties during regeneration.[2, 87, 94, 95] The degradation rate or resorption time of scaffolds may vary dependent on applications, for example, the spinal fusion requires scaffolds with the resorption time at least 9 months and scaffolds with the resorption time 3–6 months needed for the craniomaxillofacial applications.[48] Biomaterials for BTE can be classified

broadly into organic and inorganic materials, both naturally derived and synthetic components.[75, 94] Despite metallic implants being succesfully used in the clinical practice, the possibility of cytotoxic species (e.g., Ni, Co, Cr, V, Al ions) release through corrosion mechanisms is still concern because it can activate inflammation and allergic responses.[96] Corrosion may also lead to loosening and failure implantation.[96] Consequently, many classes of materials (e.g., ceramics, polymers, and composites) have been explored to integrate physical, chemical, and biological signals for being used as BTE scaffolds.[2, 94] An example of biological BTE scaffold is demineralised bone matrix (DBM) which is a form of highly processed allograft that possesses osteoinductive and osteoconductive properties.[72, 97] Ceramic-based scaffolds, such as hydroxyapatite, beta tricalcium phosphate, calcium sulfate, bioactive glassess, and calcium carbonate, have been currently used for BTE purposes due to comparable composition and mechanical properties to inorganic components of bone.[72, 75, 98] However, ceramic scaffolds have disadvantages with brittleness, excessive stiffness, and slow rate of degradation, possibly introducing a risk of complications such as unfully replacement by bone.[72, 83, 87, 99]

The alternative to inorganic materials is polymeric bone substitutes which can be both natural and synthetic polymers. The main advantage of polymers is tunable properties, making them more attractive materials for being used in BTE. Through the synthesis and processing, microscale and macroscale features of polymeric biomaterials, such as composition, binding groups, biodegradability, porosity, stiffness, and elasticity, can be tailored to specific requirements.[75, 100] Biomaterials made from natural polymers such as collagen,[101] cellulose,[102] alginate,[103] hyaluronic acid,[104] and chitosan,[102] can have biological recognition, enabling cell attachment and migration within structures.[100] However, natually derived polymers have complications in processing and purification as well as concerns regarding immunogenicity and batch-to-batch variations, leading to unpredictable outcomes in the clinics. On the other hand, synthetic polymers show more consistency in properties and versatile availability but lower bioactivity in respect to scaffold-host interactions.[75, 100] With respect to composition and biocompatibility, synthetic polymers commonly used in BTE include poly(lactic acid) (PLA),[105, 106] poly(acrylic acid) (PAA),[42, 107] polycaprolactone (PCL),[42, 105] poly(ethylene glycol) (PEG),[106, 108] polyurethane (PUR),[109, 110] and poly(methyl methacrylate) (PMMA).[72, 111, 112] In addition, organic and inorganic materials can be synergistically incorporated into composites

and hybrid biomaterials to improve characteristics and overcome the limitations of individual materials.[75] For example, hydroxyapatite nanoparticles have been incorporated with natural polymers to improve compressive strength and elastic modulus of scaffolds.[113, 114] Nanomaterials are currently studied for biomedical uses due to their intrinsic structural characteristics: increased surface area and roughness that are able to enhance mechanical properties, support cellular behaviours, and develop material-biomolecule interactions.[115, 116] Nanomaterials which are being intensive studied include graphene,[117] carbon nanotubes,[117] and clay nanoparticles.[118]

The implantation of scaffolds can be further complemented with signaling molecules to promote and enhance tissue regeneration both *in vitro* and *in vivo*. Signaling molecules, such as growth factors and cytokines, can be used to direct cell response and behaviour which are cell adhesion, proliferation, differentiation, migration, and viability. Examples of growth factors for BTE include BMPs, TGF-β, vascular endothelial growth factor (VEGF), platelet-derived growth factor (PDGF), and parathyroid hormone (PTH).[2, 72, 75, 87]

Research in scaffold-based BTE is ongoing to integrate mechanical strength, stiffness, biocompatibility, and bioactivity into scaffolds, in order to support vascularisation and bone tissue regenerative processes as well as minimisation of host rejection. Recently, 3D porous scaffolds, injectable system, nanomaterials, and nanotechnology have achieved significant progress in BTE research.[116, 119, 120] Porous scaffolds can provide a 3D network that mimics the architecture of ECM. Sufficient porosity with suitable pore size supplies an environment for cell growth, proliferation, infiltration, vascularisation, and differentiation.[119] Injectable hydrogels have demonstrated a great potential for use as 3D tissue scaffolds that allows filling bone defects with irregular shape.[120] The use of nanomaterials and nanotechnology can provide and control material properties at nanoscale to mimic surface properties and dimension of bone ECM.[116]

1.6 Cell migration within 3D matrix

Cell migration plays a crucial function in physiological processes including development of tissues and organs, immune defence, and wound healing.[121, 122] The ECM in cellular environment has essential roles in regulating cell behaviours such as directing cell migration by oriented fibres and governing cell morphology.[121] Cell migration requires the interactions

of cells with the ECM and highly coordinated changes in morphology. The morphological and physical behaviours of migrating cells are predominantly driven by the filamentous actin (F-actin) cytoskeleton that is mechanically coupled to the ECM through dynamic macromolecular protein complexes, known as focal adhesions (FAs).[122] In general, cell migration can be considered as a recurrent process with repetitive cycles of protrusion, adhesion and contraction (Figure 1-4). The initial response of cell to a migration-promoting agent is to polarise and extend protrusions, which can be lamellipodia and/or filopodia, in the direction of movement using actin polymerisation. Protrusions are stabilised by forming a new adhesion to the underlying substrate through integrins and transmembrane receptors that bind to the ECM or adjacent cells. These adhesions serve as traction sites for migration as the cell moves forward over them. The adhesion at the rear of the cell is weakened and detached as focal adhesions are turned over and actomyosin-mediated cell contraction takes place. The cycle then repeats with a new cell protrusion at the leading edge.[121, 123]

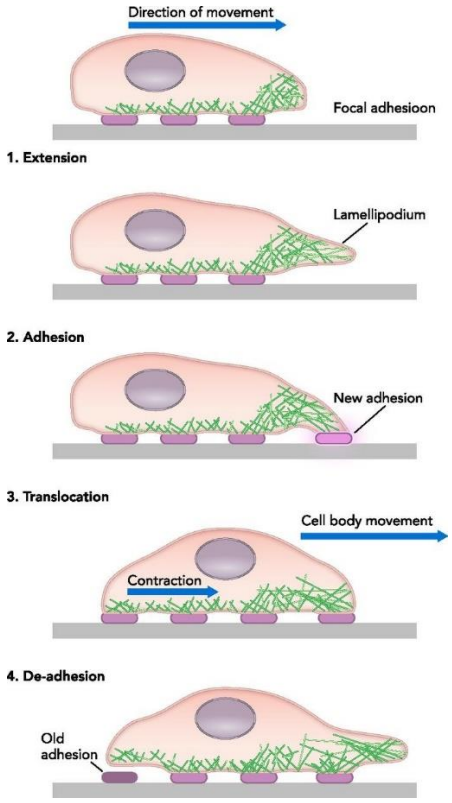

Figure 1-4. A cyclic process of cell migration on 2D substrate. (1) Cell protrudes lamellipodia and/or filopodia at their leading edge using actin polymerisation and extend protrusions into the direction of migration. (2) A new cell adhesion is formed with the underlying surface through integrins and transmembrane receptors. (3) Cell adhesion at the rear is diminished and cell actively retracts by actomyosin-mediated cell contraction. (4) The old cell adhesion at the rear is detached and cell slides forwardly. The cycle then repeats with a new cell protrusion at the leading edge.[121, 123]

In living tissues, most cells undergo 3D migration. Migration within 3D environments is challenging as it requests cell to compress through dense extracellular structures with specific requirement of cellular adaptations to mechanical features of the ECM. Moreover, cells generally interact with neighbouring cells and surroundings through physical and signalling interactions. Therefore, different from extensive studies of 2D migration on flat surfaces, the investigation of migration in 3D is much more complex and typically relevant to the design and utilisation of 3D scaffolds for cell movement.[121, 124]

Cell adhesion and extension can vary dependent on the substrate. Factors that influence cell adhesion including topography, surface charge, composition, protein adsorption, and mechanical stiffness of substrates.[125-127] In general, most of cell types preferentially attach and grow on stiffer substrates.[127-129] With respect to motility, some cells use the gradient sensing of stiffness as well as other physical properties of microenvironment as a guidance signal for directional movement.[121, 130, 131]

The migratory modes used by cells in 3D environments can be mainly classified into mesenchymal (proteolytic) and amoeboid (non-proteolytic).[121, 132] In the proteolytic migration, cells adhere to matrix and secrete matrix metalloproteinases (MMPs) which cleave or degrade the ECM protein networks and, hence, create macroscopic holes for allowing cell infiltration and movement within matrix.[132, 133] On the other hand, the amoeboid migratory mode is characterised by rounded morphology and low adhesive interactions to substrates. Cells, in this mode, migrate through filling existing holes or gaps within the matrix or deforming the ECM networks without matrix degradation.[121, 132]

To investigate cell migration in 3D environment, the use of biomimetic hydrogels is required to create physiological scaffolds. Collagen gels have been widely used as a matrix for 3D motilities study because collagen is the major component of the ECM and also cytocompatible with cells.[124, 132, 134] The measurement of 3D cell migration can be assessed via time-lapse imaging of cells using bright-field or fluorescent microscopy, electron microscopy, phase contrast, and differential interference contrast (DIC) microscopy.[124, 132, 134-136]

For example, Heat and Peachey examined fibroblast migration within collagen gels using intermediate voltage electron microscopy (IVEM).[134] The results showed that fibroblasts that moved through collagen matrix exhibited *in vivo*-like cylindrical cell morphology and major

pseudopodal processes. However, cells displayed small flat extensions at the leading edge of advancing pseudopodia similar to lamellipodium found in cells on 2D surfaces.[134] Also, the presence of cell–matrix adhesion complexes within the small lamellipodia-like protrusions of fibroblasts were observed within collagen gels using a high-resolution, spinning disc confocal imaging technique.[137]

Cell migration of hMSCs spheroids within alginate hydrogels was evaluated using a time-lapse fluorescent microscopy.[135] The alginate hydrogels modified with RGD at low level improved the migration of hMSCs spheroids. Additionally, Uchihashi *et al*. investigated the migration of osteoblasts in type I collagen gels. They found that osteoblasts migrated into the gel matrix, extended their dendritic processes to neighbouring cells, and synthesised collagen fibrils. The migrated cells also formed mineralisation around themselves, mimicking lacunae- and canaliculi-like structures.[138]

The influence of chemical gradients towards human osteoblast migration within 3D collagen gels was established by Movilla *et al*.[132] In order to create a chemical gradient, cell culture medium containing a platelet derived growth factor β (PDGF-BB) at concentrations of 5 ng mL^{-1} and 50 ng mL^{-1} was added to one channel while a growth factor-free culture medium was added to another channel. The chemical gradient was established by a diffusion across the hydrogel. The results showed that cell orientation in the direction of the gradient did not significantly altered, but at the lower concentration of growth factor, a migration stimulation effect on the cell velocities was changed by increasing the mean and effective speeds. Also, the cell migration of human osteoblasts in 3D is intrinsically highly anisotropic regardless of the cultured conditions.[132] Moreover, it was found that human osteoblasts individual migration within 3D matrix was regulated by the degradation of ECM or proteolysis.

Moreover, the effect of stiffness of hydrogels matrix on the migratory mode of cells was also studied. The migration of MC3T3-E1 preosteoblasts within PEG-based hydrogels with different stiffness was studied by Ehrbar *et al*.[139] Migration of preosteoblasts was strongly dependent on matrix stiffness and could be concluded that, at the relatively low matrix stiffness with larger pores, a non-proteolytic migratory mode was dominated whereas a proteolytic migration predominantly governed for preosteoblasts migration within hydrogels with higher stiffness.[139]

1.7 Injectable systems and hydrogels for tissue engineering and regenerative medicine

1.7.1 Clinical need for injectable scaffolds

From the clinical perspective, injectable scaffolds have been extensively researched and have become a promising approach for tissue engineering and drug delivery, predominantly due to minimisation of invasive surgical interventions, pain, scar formation, risk of infection at the operated sites, complications during implantations, and cost of treatment.[140, 141]

The use of prefabricated conventional scaffolds necessarily requires precise information of dimension and shape of defects for scaffold formation. Furthermore, defects with irregular shape can cause complications during fabrication process.[140, 142] Injectable systems not only overcome these limitations but also provide a greater homogeneous distribution of cells and bioactive molecules within matrixes *in vivo* because all the components are integrated before solidification. Injectable scaffolds can be implanted through injection of precursors that are able to form *in situ* crosslink or self-assemble under certain conditions, allowing scaffolds stay at injected sites or voids.[143, 144] Prior to injection, precursors can be a form of suspension, solution, paste, beads, micro or nanoparticles, and thread-like materials. After injection and solidification, an *in situ* forming scaffold provides a 3D matrix that self-assemble at injected sites and serve as a host for cells to adhere, proliferate, and differentiate, consequently leading to a regeneration of new functional tissues.[140, 142, 145]

1.7.2 Design parameters and requirements for hydrogels in tissue engineering

One challenge in tissue engineering is to design and create a potential platform that mimics ECM, supports vascularisation, and guides cells for functional tissue regeneration. Regarding the ECM analogy, engineered tissue scaffolds should, at least, provide 3D environment for cells. The 3D architecture better mimics natural tissue and allows for gene expression and morphology that cannot be achieved in 2D scaffolds.[146-148] For this respect, hydrogels have been one of the most promising scaffolds based on a three-dimensional network with a high-water content, desirable physical characteristics, and ability to facilitate transport of oxygen, nutrients, waste, and soluble growth factors.

Hydrogel-based scaffolds possess many advantages including low cost, flexible fabrication methods, and reduced operating time.[9-11, 146] Although hydrogels are suitable as engineered

tissue scaffolds, some certain parameters must be considered and required when designing a scaffold to meet the criteria for tissue regeneration. Most importantly, materials or components used for hydrogel preparation must be biocompatible and non-cytotoxic. These criteria also apply to leachable components or degradation products.

Biocompatibility is relevant to the ability of materials to exist and interact with host tissues in appropriate response and without damaging surrounded tissues and adjacent cells.[141, 146, 147, 149, 150] Chemicals that are used during synthesis and crosslinking processes can present a challenge for both *in vitro* and *in vivo* biocompatibility and may be introduce toxicity and inflammatory response to host cells.[146] For example, some photoinitiators used to synthesise hydrogels through free radical photopolymerisation showed cytotoxicity towards cells by decreasing cell viability at concentrations higher than 0.1%.[151, 152] Likewise, Shin *et al*. demonstrated that higher monomer concentration of oligo[poly(ethylene glycol) fumarate] (OPF) hydrogels, low molecular weight of crosslinking agents (PEG-diacrylate), and leachable products of OPF had adverse effects on viability of MSCs.[153] Hence, toxicity of components in all aspects must be comprehensively considered and evaluated both *in vitro* and *in vivo*.

By taking the vascularisation and diffusion into account, porosity and pore size within hydrogel structure are critical physical factors to enable nutrients and oxygen transport, elimination of waste, cell growth, and cell migration.[9, 146] The optimal pore size of scaffolds is, however, varied and highly dependent with cell types and activities. For example, pore sizes in the range of 100–400 μm are proposed for osteoblastic activities and mineralised bone formation, whereas smaller pores (<100 μm) are used for the growth of fibrous tissue or non-mineralised osteoid.[92, 154, 155] Also, pore sizes greater than 300 μm are recommended to support bone regeneration via vascularisation.[156] Migration of MSCs was observed to happen within hydrogels with pore sizes less than 30 μm,[157, 158] whereas the optimum pore size of scaffold for fibroblasts migration is about 100 μm.[159, 160]

Mechanical stiffness and strength are also important factors required for 3D scaffolds. Hydrogels should hold mechanical properties as the same level with strength and stiffness of native tissue. The stiffness of gels can influence cell adhesion and proliferation, differentiation, migration, and gene expression.[150, 158, 161, 162] Stiffness and strength of hydrogels can be altered by concentration of matrixed components, degree of crosslinking,

and fabrication methods.[150, 152, 162] For instance, Žigon-Branc *et al*. studied how the stiffness of methacrylate-modified gelatin (Gel-MOD) hydrogels affected the differentiation of human adipose-derived stem cells (hASCs).[162] The elastic modulus or stiffness and crosslink density of hydrogels increased with higher concentration of Gel-MOD. In contrast, measurement of osteogenic and chondrogenic differentiation as well as gene expression level were higher in 5% and 7.5% hydrogels, suggesting that softer Gel-MOD hydrogels better support differentiation of hASCs.[162] In addition to mechanical properties, stability of hydrogels is also required to retain the original structure and function until tissue restoration process is completed. Shrinkage is a characteristic that can reduce dimensional stability of hydrogels. Scaffolds with high degree of shrinkage can diminish the integration of implant with adjacent tissues.[9] Collagen hydrogels has poor stability, rapidly degrade hydrolytically and enzymatically, and vulnerable to dimensional shrinkage when immersed in liquids, limiting its applications in biomedical and tissue engineering.[163] To overcome this limitation, significant improvement in physicochemical and mechanical properties is necessary required and can be achieved by incorporating collagen with other materials, such as hydroxyapatite,[164] bioactive glass,[163] and polymers,[165] to introduce either chemical bonds or crosslinking structures.

The properties of BTE scaffolds required at each stage or timeline of tissue regeneration are described in Table 1-2.

Table 1-2. Mechanical properties of injectable BTE scaffolds required at each phase of bone tissue regeneration.

Time	Stage of tissue regeneration	Mechanical properties required for injectable BTE scaffolds
Upon injection		Low viscosity, shear-thinning, and self-recovering characteristics.[166-168]
0–8 weeks	Repair	Scaffolds should have sufficient mechanical properties (compressive strength, elastic modulus) to maintain structural integrity at the defect sites for allowing void filling, cell support, revascularisation, and tissue expansion.[169]
>8 weeks	Remodelling	Mechanical properties of scaffolds (compressive strength, tensile strength, elastic modulus) are required to match with host tissues to minimise stress-shielding.[169] Degradation rate of scaffolds should be controlled to correspond to rate of bone tissue formation to preserve stable mechanical properties during regeneration process.[2, 87, 94, 95]

Another crucial factor for designing hydrogel-based tissue scaffolds is degradation. The human body is normally in a constant rate of turnover. Homeostasis of bone tissue, for example, is maintained by balanced destructive and regenerative processes. Hence, as most living tissues, hydrogels should undergo the same profile of controlled breakdown and allow for new tissue replacement. Accomplished degradation would mitigate concerns about long-term implant integrity and stability.[9, 146] During regeneration process, degradation rate of hydrogels should be corresponding to rate of tissue development. Biodegradation mechanisms of hydrogel scaffolds include hydrolysis, dissolution, and enzymatic cleavage and can be modulated by controlling crosslink density, cell-mediated proteases, and incorporating materials with cleavable groups.[9, 140, 146] For example, Golafshan *et al*. developed composite hydrogels composing of Laponite:polyvinyl alcohol (PVA)-alginate (Lap:PVA-alginate).[170] Incorporation of 2% wt. of Laponite nanoclay decreased hydrolytic degradation rate of PVA-alginate due to the enhancement of physical crosslinking density between Laponite and alginate.[170]

Cell adhesion and interaction of hydrogel with bioactive molecules are also significant requirements. Cell adhesion has an effect on cell proliferation, differentiation, and its subsequent tissue formation.[9, 140, 147] Cells can communicate among themselves through adhesive interactions and assemble into 3D tissue structures.[9] In case of incorporation of growth factors and drugs, hydrogel scaffold is responsible for molecule release at the repair site, to create a conducive environment for tissue regeneration.[171] The binding ligands within ECM provide receptors for cell attachment and facilitate the connection between cytoskeletons of cells with surrounding environments. In order to enhance cell adhesion, it is necessary to incorporate proteins into hydrogel structure.[9, 172-174] The integrin binding arginine-glycine-aspartic acid (RGD) peptide sequence has been most often used to combine with hydrogels to promote cell adhesion.[174, 175] Furthermore, the increase in the extent of hydrophilicity is another approach to improve cell attachment.[172, 176]

In case of injectable hydrogels, the precursor solution must possess low viscosity to allow injectability passing through a syringe. After injection, the precursor should become a gel or solidify immediately to avoid flowing or spreading in surrounding tissues.[140, 172] Generally, injectability is related to rheological properties of materials which is shear-thinning characteristic. Shear-thinning or injectable hydrogels must behave as a fluid during injection

or when force is applied, at this stage, viscous modulus G'' is greater than elastic modulus G'. Once it is ejected, hydrogel behaves as a solid at rest (G'>G'').[11, 172, 177] This characteristic is further described in the Section 1.7.4.

All the features described above are mostly related, making it challenging to control and develop in an independent aspect. Composite systems can be applied to improve and tune properties of hydrogels to meet the requirements for use in tissue engineering and regenerative medicine.

1.7.3 Recent advances of injectable hydrogels for tissue engineering and minimally invasive treatment

The synthesis of hydrogels often involves with crosslinking systems to maintain a 3D network structure. To date, hydrogels are mainly prepared by two mechanisms which are chemical and physical crosslinking methods.[120, 178, 179] Chemical crosslinking can greatly improve stability of hydrogels with higher stiffness and strength due to strong covalent bonds.[9, 179] Chemically crosslinked hydrogels can be achieved by various methods including Michael addition reactions,[106] Schiff base crosslinking,[180] photo-crosslinking,[180] and enzymatic reactions.[120, 150, 178]

The Michael addition reaction, a promising strategy for fabricating biomimetic hydrogels, is relevant to the conjugate addition (1,4-addition) of unsaturated carbonyl compounds with nucleophiles such as amines, thiols, and phosphines.[181] This reaction is thermodynamically controlled and can be carried out under physiological conditions with aqueous media.[120, 179] In Schiff base crosslinking, the reaction between amine and aldehyde groups. This method has been utilised to form injectable hydrogels under physiological conditions without external stimulation.[120, 150] Photo-crosslinking method relates to radical polymerisation using UV or visible light source to interact with photoinitiators. Free radicals are subsequently initiated and interact with photo-curable polymers, such as gelatin methacrylate (GelMA),[182] pluronic,[183] poly(ethylene glycol diacrylate) (PEGDA),[184] and methacrylated hyaluronic acid (MeHA),[185] to trigger crosslinking reaction, leading to formation of hydrogels.[150, 178] Enzyme-mediated crosslinking has gained attention for preparation of injectable hydrogels due to ability to conduct under physiological conditions, low cytotoxicity with high biocompatibility, fast gelation, and high selectivity. Various enzymes extracted from both animals and plants

have been employed to catalyse the formation of chemical crosslinked hydrogels, for example, horseradish peroxidase (HRP), glucose oxidase (GOx), transglutaminase, tyrosinase, and laccase.[120, 178, 186]

On the other hand, physical hydrogels are a result from secondary forces or non-covalent interactions such as ionic/electrostatic interactions, hydrogen bonding, π-π stacking interaction, and hydrophobic interactions.[9, 178] As compared to chemical crosslinking networks, hydrogels with physically crosslinked structures possess relative lower stiffness and strength, and may prematurely disintegrate in the body. Physical injectable hydrogels do not require chemical crosslink agents and can be self-assembled under specific conditions, avoiding potential cytotoxicity from residual crosslinkers and making them more widely used in biomedical applications.[179, 187] More importantly, physical crosslinking can provide stimuli-responsible injectable hydrogels with self-healing characteristics under room temperature.[178, 187] An example of physical injectable hydrogel is self-assembling peptide-based hydrogels fabricated by Ligorio et al.[188] Peptide powder were simply dissolved in water and the pH was then adjusted to 4 using NaOH to obtain peptide-based hydrogels. Hybrid peptide/GO hydrogels was prepared by adding GO suspension after adjusting the pH. Peptide/GO hydrogels were formed by molecular self-assembly of peptide into β-sheet fibres conformation and generating electrostatic interaction (at pH 4) or hydrophobic interaction (at pH 7) to GO, resulting in peptide coating and forming short fibres on surface of GO.[188] To prepare injectable hydrogels by ionic crosslinking, ionisable polymeric solutions are mixed with ionic solutions of counter ions, such as calcium chloride ($CaCl_2$). Calcium ions (Ca^{2+}) generates ionic interactions with anionic polymer chains, leading to gel formation.[150, 178] Physical hydrogels can also be prepared from pH-sensitive and temperature-responsive polymers such as poly(lactic-co-glycolic acid)-PEG (PLGA-PEG),[189] poly(N-isopropylacrylamide) (PNIPAM),[190, 191] and chitosan.[192]

The majority of materials used to fabricate hydrogels are polymers, which can be broadly divided into naturally derived and synthetic components.[9, 172, 193]

Naturally derived polymers are frequently biocompatible and biodegradable and have been widely investigated and received an interest for use in injectable hydrogel-based scaffolds. The most common injectable hydrogels based on natural polymers include peptide,[188, 194, 195]

collagen,[163, 196, 197] gelatin,[182, 198, 199] hyaluronic acid,[180, 198, 200] alginate,[201-203] and chitosan.[180, 203, 204] Despite their favourable characteristics, natural polymers show some drawbacks that limit their use in broad applications such as insufficient physical strength and mechanical properties, poor cell adhesion, and rapid degradation.[163, 180, 193]

Synthetic polymers with reproducibility and controllable properties have been exploited for development of injectable hydrogels. These polymers include PEG,[205, 206] PAA,[207, 208] polyvinyl alcohol (PVA), [170, 209] poly(L-glutamic acid) (PGA),[200, 210] PCL,[167, 211] and PLGA.[189, 212] However, synthetic polymers are less biocompatible than natural polymers. Hydrogels produced from some synthetic polymers such as PVA, PEG, or its derivatives do not possess inherent bioactive properties.[213]

To address the limitations of both naturally derived and synthetic polymeric materials, composite or hybrid hydrogels have been developed. For example, Han *et al*. developed a novel dual-crosslinked injectable hydrogel from chitosan methacrylate (CHMA) and aldehyde-functionalised hyaluronate (oxidised HA, OHA).[180] The hydrogels were rapidly formed after injection due to electrostatic interactions between cationic primary ammonium groups of CHMA and anionic carboxyl of OHA, and Schiff base crosslinking between the amines and aldehydes, as shown in Figure 1-5. The secondary covalent crosslinking took place *in situ* via photopolymerisation of methacrylates, greatly improving stability of the hydrogel network. The injectable CHMA-OHA hydrogel possessed a rapid self-healing characteristic, high elastic modulus, and retention of rat bone marrow stromal stem cells (rBMSCs) viability.[180]

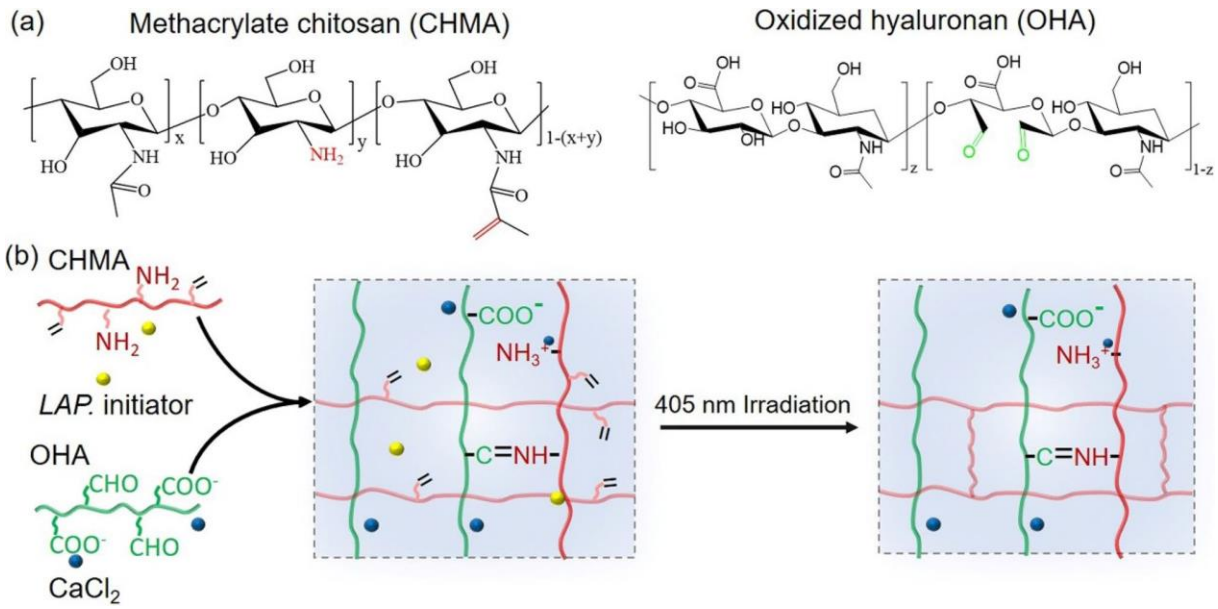

Figure 1-5. (a) Chemical structures of methacrylate chitosan (CHMA) and oxidised hyaluronate (OHA). (b) Schematic illustration of hydrogel formation due to electrostatic interactions and Schiff base crosslinking, followed by the secondary covalent crosslinking by photopolymerisation. Reproduced from Han *et al*.[180]

Similarly, Kim and collaborators successfully fabricated an injectable dual-network hydrogel, composed of the thermally responsive gelator PNIPAM and a chondroitin sulfate. They used the product as a platform for poly(L-lysine) (PLL) deliver and co-culturing encapsulation of MSCs and articular chondrocytes (ACs).[191] The hydrogel was responsible for the retention of PLL to promoting chrondogenesis of stem cells by generating covalent bonding between PLL and amine groups along with electrostatic force of PLL and anionic moieties present within hydrogel. Recently, a hyaluronic acid-based injectable hydrogel modified with BMP-2 mimetic peptide was prepared by chemically click-crosslinking via Diels–Alder cycloaddition.[214] The crosslinked HA-BMP2 peptide had excellent injectability and greater elastic modulus than HA gels. After subcutaneous injection into nude mice, the composite crosslinked HA-BMP2 peptide quickly formed hydrogel scaffold and better induced osteogenic differentiation of human dental pulp stem cells (hDPSCs) *in vivo*.

The integration of nanomaterials has emerged as a strategy for generating nanocomposite injectable hydrogels with enhanced mechanical reinforcement, improved biological behaviour, and controlled drug delivery. For instance, Zhang *et al*. utilised the charged nano-structure of Laponite (Lap) nanoclay towards mechanical properties and ability to uptake and sustained release of growth factors of RGD-alginate injectable hydrogels.[201] Compared to

alginate hydrogel, the hybrid RGD-alginate/Lap hydrogel had greater elastic modulus, *in vitro* faster degradation, *in vitro* controlled growth factor VEGF release, and upregulated odontogenic differentiation of hDPSCs with promoted pulp-like tissue regeneration *in vivo*. Another interesting nanomaterial used to create hybrid hydrogels is nanohydroxyapatite (nHAp). Kumar and collaborators developed a tri-component injectable microgel composed of chitin, PCL, and nanohydroxyapatite (chitin/PCL/nHAp).[211] Chitin provides cell adhesion and biomimetic properties whereas PCL implements favourable viscoelastic and mechanical properties. The incorporation of nHAp not only increased elastic modulus and thermal stability but also significant accelerated osteogenic differentiation and upregulated specific proteins expression of stem cells, as results shown in Figure 1-6.

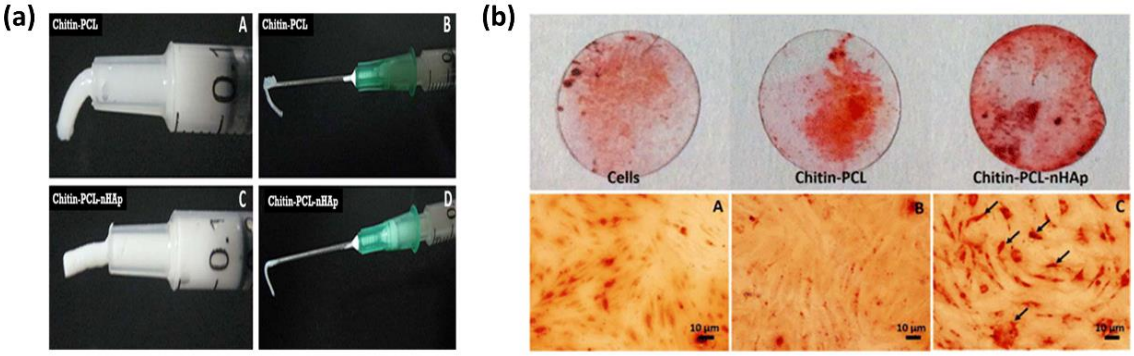

Figure 1-6. (a) Injectability of chitin-PCL hydrogels through a syringe nozzle and a 21G needle. Chitin-PCL hydrogels exhibited a shear-thinning property, the important requirement for injectable materials. Nanohydroxyapatite contributed to a smooth and continuous injectability of chitin-PCL composite hydrogel. (b) Alizarin red staining of rabbit adipose derived mesenchymal stem cells (rASCs) cultured on coverslips and incubated with osteogenic supplement medium containing chitin-PCL and chitin-PCL-nHAp microgels after 14 days post-culturing. Reproduced from Kumar *et al*.[211]

Besides nanoclay and inorganic nanoparticles, carbon-based nanomaterials including graphene (Section 1.8.2),[215] graphene oxide (Section 1.8.2),[182, 215] carbon nanotubes,[216] and carbon nanofibers[217] have been widely employed to provide electrical conductivity and enhance mechanical properties of composite hydrogels. For example, the incorporation of GO into GelMA using UV crosslinking process significantly enhanced electrical properties and mechanical strength as well as supported cell spreading and alignment with improved proliferation and viability within a 3D microenvironment.[182] Also, graphene and GO were mixed separately with the waterborne biodegradable polyurethane (PU) to make composite hydrogels as potential bioinks for 3D bioprinting constructs for neural tissue engineering.[218]

The addition of graphene nanomaterials disrupted the gelation of PU and lowered elastic modulus, but still sufficient to maintain the structure of scaffolds. With respect to neural differentiation, graphene nanomaterials enhanced cellular oxygen metabolic activity, subsequently inducing proliferation and differentiation of stem cells.

1.7.4 Rheology and rheological characterisations of injectable hydrogels

1.7.4.1 Basics of rheology

Rheology is the study of flow behaviour and deformation of materials. Rheometry, the measuring methodology used to characterise rheological properties, can be performed with continuous rotation (one direction of motion) and oscillation.[219, 220] A simple model to describe rheological measurement is the two-plate model, by which shear is applied to sample placed between a movable plate and a stationary plate. As illustrated in Figure 1-7, the bottom plate is fixed and remained at place while the top plate with shear area A (m^2) is moved parallel to the bottom plate by shear force F (N) at a velocity υ (m s^{-1}).The gap or distance between two plates, where sample is filled, is described by h (m).[219, 220] For the two-plate model, only a laminar flow is created and a turbulent flow regime with vortex must not occur as it would increase a flow resistance.[220]

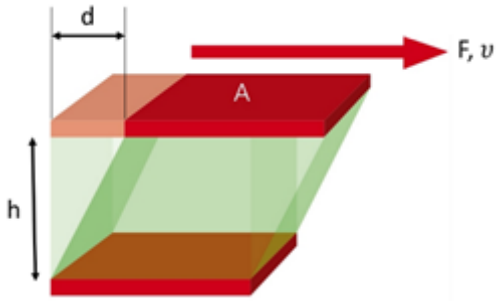

Figure 1-7. The two-plate model for rheological measurement. Adapted from "Basics of rheology" by Anton Paar GmbH.[220]

Shear stress (τ), shear strain (γ), and shear rate ($\dot{\gamma}$) are rheological parameters that characterise the behaviour within the two-plate model.[220] Shear stress (Pa) is a measurement of shear force per unit area that is applied to make the top plate moves in a distance d:

$$\tau = \frac{F}{A} \tag{1-1}$$

And shear strain is given by the ratio of deformation:

$$\gamma = \frac{d}{h} \tag{1-2}$$

Shear rate (s^{-1}) defines the rate at which a sample is sheared, determining from the velocity of the moving plate divided by the distance between two plates:

$$\dot{\gamma} = \frac{d}{h} \tag{1-3}$$

Viscosity or shear viscosity (η) is a measurement of material resistance to deformation in response to shear stress at a given shear rate, therefore, viscosity (Pa s) is defined as shear stress divided by shear rate:

$$\eta = \frac{\tau}{\dot{\gamma}} \tag{1-4}$$

Viscosity can be influenced by many conditions. Newtonian flow behaviour describes a fluid with a constant viscosity at all shear rates, in other words, viscosity is independent of shear rate.[220] Materials that show a variation in shear viscosity with respect to shear rate are known as non-Newtonian fluids. Such materials include fluids showing shear-thinning (or pseudoplastic) behaviour and shear-thickening (or dilatant) behaviour. Shear-thinning behaviour refers to a reduction of viscosity with increasing shear rates in a steady flow while shear-thickening characteristic means to an increment of viscosity with increasing shear rates.[219, 220]

A vast majority of materials exhibit rheological properties that is in a region somewhere between that of solids and liquids, which is called viscoelastic behaviour.[219, 220] Viscoelastic is a time-dependent behaviour which can be measured using oscillatory shear test. The two-plate model can also be used to explain oscillation, by which the upper plate moves back and forth parallel to the lower plate at a constant oscillating frequency.[220, 221] In the experiment, the oscillating torque is applied to the top, movable plate and the angular displacement is measured as strain or deformation (γ). The strain is plotted against time, resulting in a sine curve with the strain amplitude (γ_A). In addition, the force required to keep the lower plate remained in position is evaluated as shear stress and plotted in a sinusoidal curve of shear stress amplitude (τ_A).[220] An example of the two-plate model for oscillation with sinusoidal curves of stress and strain versus time is shown in Figure 1-8.

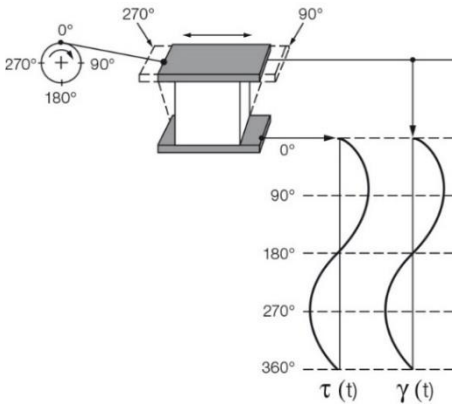

Figure 1-8. The two-plate model for describing oscillatory test. This example is for ideally elastic behaviour, by which stress and strain are in phase. Adapted from "Basics of rheology" by Anton Paar GmbH.[220]

For an ideally elastic deformation behaviour, the maximum stress occurs at the maximum strain (stress is proportional to stain), and both stress and strain are in phase. For a purely viscous deformation behaviour, the maximum stress appears at the maximum shear rate, and stress and strain are out of phase by 90° or $\frac{\pi}{2}$ radians. The phase shift (δ) of stress and strain for viscoelastic behaviour is between 0° and 90°.[220, 221]

In oscillatory shear test, the applied shear stress amplitude to the measured strain amplitude gives the complex shear modulus (G*) which determines material stiffness or material resistance to deformation.[220] Complex shear modulus (Pa) is defined as:

$$G^* = \frac{\tau_A}{\gamma_A} \tag{1-5}$$

Viscoelastic materials exhibit characteristics of both solid-like and liquid-like behaviours. The elastic and viscous contribution to G* can be determined using a trigonometry of the vector diagram as shown in Figure 1-9. Storage (G') and loss (G'') moduli represent the elastic and viscous portions of the viscoelastic behaviour, respectively, in response to oscillatory shear.[220, 221]

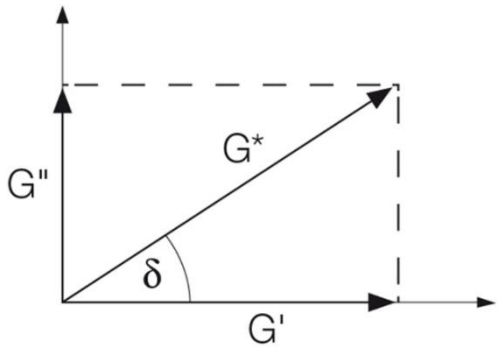

Figure 1-9. Vector diagram presenting the relationship between complex shear modulus (G*), storage modulus (G'), and loss modulus (G'') at the phase shift δ. Adapted from "Basic of rheology" by Anton Paar GmbH.[220]

Storage modulus measures the ability of materials to store or absorb energy in the deformed materials while loss modulus characterises the deformation energy lost or dissipation through internal friction when flowing.[220] Storage modulus and loss modulus are determined as:

$$G' = G^* \cos \delta \tag{1-6a}$$

$$G'' = G^* \sin \delta \tag{1-6b}$$

Loss factor or damping factor (tan δ) gives the ratio of elastic and viscous portions in viscoelastic behaviour. In diagrams of samples having phase transition such as gels, tanδ is generally presented in addition to the plots of G' and G''.[220]

$$\tan \delta = \frac{G''}{G'} \tag{1-7}$$

Thixotropic is also a time-dependent behaviour in which a reduction in magnitude of rheological properties (such as viscosity, storage modulus and shear stress) with time occurs when flow is applied to material at rest state and its subsequent recovery in magnitude happens after the cessation of flow and return to a rest state. In other words, thixotropy refers to a phenomenon of structural deformation under high shear and its subsequent recovery of the initial state takes place upon the cessation of flow.[220, 222, 223]

1.7.4.2 Rheological measurement of injectable hydrogels

Rheometry is used for determining rheological parameters such as shear stress, shear strain, shear modulus, viscosity, shear-thinning, and thixotropic properties which are important

characteristics to determine the self-healing, mechanical properties and stability of hydrogels for use in tissue engineering and biomedical applications.[177, 224]

The rheological technique to characterise hydrogels is small-amplitude oscillatory shear (SAOS). In SAOS, a sample is placed between a flat, stationary plate and a mobile component. The mobile component may be flat or cone-shaped, or it may operate in a 'couette' geometry, in which a film of liquid surrounds a mobile cylinder inside a larger cylinder. Then, a small-amplitude torsional oscillation generates shear flow in the sample.[219, 220, 224] The measurements are typically conducted at 37°C because, in tissue engineering applications, gels will form *in vivo* at or near the body temperature. An example of rheological assessment for injectable hydrogels is shown in Figure 1-10, which was performed by Chen *et al*.[177]

The limit of the linear viscoelastic (LVE) region is essentially determined to indicate the range in which the analysis can be performed without destroying the structure of a sample. In this regime, modulus is independent on amplitude strain. The LVE region of materials can be determined in amplitude strain sweep test at a constant frequency. The values of G' and G'' in the LVE regime are normally evaluated, providing the viscoelastic behaviours of samples. In most cases of gels, G' is dominant over G'' at low strain, exhibiting a gel-like or solid structure. Gel structure can be destroyed at higher strain amplitudes and displays a fluid structure, in this region, G'' exceeds G'. For oscillatory tests, the measurements are necessarily carried out at stress or strain within the LVE region. This means that the amplitude strain sweep test must firstly be determined to obtain the LVE region (Figure 1-10b).[177, 224, 225] Frequency sweeps measurement generally describes a time-dependent behaviour of samples in a non-destructive deformation regime and provide information about both structure and dynamics. Frequency sweeps allow a determination of G' and G'' as a function of frequency under a constant strain, as an example shown in Figure 1-10a. Relaxation times of material structures reduce with increasing frequencies, leading to dominant elastic properties (G') over viscous behaviours (G'') because materials do not have enough time to flow or dissipate energy during testing.[177, 225]

With the respect of injectable hydrogels, viscosity is relevant to the ability of hydrogels responding to variation of shear stress during injection. An important characteristic for injectable hydrogels is shear-thinning behaviour. Shear-thinning behaviour is characterised

by a decrease in viscosity under shear force using a continuous rotational flow test (Figure 1-10c).[177, 219, 220] Self-healing properties of hydrogels relate to thixotropic behaviour. The structural deformation and regeneration (thixotropy) can be characterised by a time-dependent behaviour in which materials are subjected to alternating step tests of low shear and high shear. The first interval of low shear is to simulate behaviour at nearly rest state. Subsequently, a high shear is applied to materials to simulate structural breakdown during application. Following a high shear rate, materials are subjected to a low shear rate to stimulate a structural recovery after application.[220, 222, 226, 227] For example, in Figure 1-10d, HA-based hydrogels displayed a deformation at high strain and an instant structural recovery at low strain after a cessation of shear, demonstrating the rapid self-healing properties of hydrogels.[177] Time-dependent behaviour can be performed through continuous rotational test and oscillatory test. The rheological behaviour obtained from the continuous rotation is related to only viscous behaviour (shear viscosity and shear stress) while the oscillation characterises both viscous (G'') and elastic (G') portions of materials, describing the complete viscoelastic behaviour.[226]

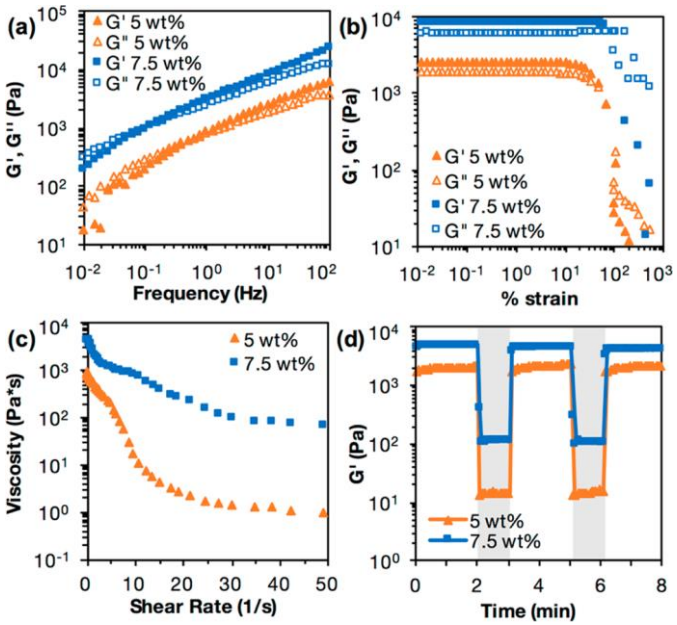

Figure 1-10. Rheological measurements of HA-based hydrogels. (a) G' ad G'' of hydrogels as a function of frequency sweeps at 0.2% strain. (b) The LVE region of HA-based hydrogels obtained from strain sweeps at a constant frequency 10 Hz. (c) The decrease in viscosity of hydrogels with increasing shear rates, indicating a shear-thinning characteristic of HA-based hydrogels. (d) The time-dependent cyclic strain sweeps to study the structural deformation and recover of hydrogels. Hydrogels were subjected to high strain 500% (shaded regions) and low strain 0.2% (unshaded regions). Reproduced from Chen *et al.*[177]

1.8 "Two-dimensional" nanomaterials in regenerative medicine

Two-dimensional nanomaterials are defined as materials with surface, internal structure, or other constituent components at least one dimension measuring in a range of 1–100 nm. Nanomaterials have been used as promising candidates for improving engineered tissue constructs and drug delivery systems since nanomaterials can mimic surface characteristics of natural tissues in nanoscale, uptake and deliver drugs at the target sites.[116, 228] Nanomaterials currently used in biomedical applications include porous nanomaterials,[229] nanoparticles (gold, silver, polymer),[230] nanoceramics,[231] nanofibers,[232] and two-dimensional nanomaterials.[233]

2D nanomaterials refer to a class of materials with sheet-like structures characterised by a reduction in the material size to the limit of atomic layer thickness in one dimension while the material size is relatively large in the other two dimensions. Due to their particular shape, 2D nanomaterials possess large specific surface areas, inherent optical properties, and anisotropic physical/chemical properties, making them favourable for applications requiring high levels of surface interactions with other molecules on a small scale.[14, 233, 234] Over the past few decades, a large number of 2D nanomaterials have been discovered for use in biomedical applications, ranging from drug delivery, cancer treatment, bioimaging, tissue engineering and regenerative medicine. These materials, for example, include graphene-family nanomaterials,[31, 235] black phosphorus,[235, 236] layered double hydroxides (LDHs),[237] hexagonal boron nitride (h-BN),[238] and silicate clays.[118, 239]

1.8.1 Laponite clay nanoparticles

1.8.1.1 Clay structure and compositions

Clays are composed of layers of tetrahedral/octahedral silicate sheets, typically derived from natural sources and feature one or more phyllosilicate mineral. Clays can be classified into different families depending on composition, dimensions, and layered structural arrangement such as serpentine-kaolinite, smectites (or bentonite), and sepiolite-palygorskite.[12, 13] Clay minerals generally possess high sorption capacity, water solubility and swelling, large surface area, reactivity toward acids. Due to favourable physicochemical properties along with low cost and extensive availability, clay minerals have been often utilised in pharmaceutical and cosmetic products, in particular, the smectite group of

phyllosilicate clay minerals.[15, 240] According to naturally derived sources, composition and properties of clays may vary considerably depending on the geological origin. More recently, synthetic mineral clays has gained interest for being used in biomedical applications to provide materials with reproducible and highly controlled composition, impurities, properties, and dimensions as well as to eliminate the inhomogeneity that made them inadequate and risky for parenteral administration or implantation.[13, 15] With this respect, a commercial synthetic smectite clay under a trademark product of BYK Additives and Instruments, known as Laponite, have shown to be a suitable clay for use in medical purposes.[16]

1.8.1.2 Structure, composition, and microscopic interactions of Laponite nanoclay

Laponite is a synthetic smectite clay and analogous to the natural clay mineral hectorites, which are a part of sheet silicates (phyllosilicates) group including kaolinite, montmorillonite, and vermiculite. The structure of Laponite composes of an octahedral sheet of magnesium oxide sandwiched between tetrahedral sheets of silica with lower heavy-metal content, as compared to the natural clays (Figure 1-11). Laponite nanoclay has an empirical formula of $Na^{+}_{0.7}[(Si_8Mg_{5.5}Li_{0.3})O_{20}(OH)_4]^{-0.7}$ where lithium cations randomly substitute those of magnesium ions presented within the octahedral sheet in the middle).[12, 13, 15] Laponite crystals possess a disc shape with approximate 25−30 nm diameter and 1 nm thickness, allowing a high specific surface. Cation substitution of Li^{+} for Mg^{2+} within the tetrahedral and/or octahedral layers provides a negative charge on the surface of Laponite disc-shaped crystal which is balanced by the positive charge of Na^{+}/Ca^{2+} located the interlayer between crystals as well as the surrounding water molecules. In contrast, the edge of Laponite crystal exhibits a weak, localised positive charge due to broken Si−O, Al−OH, and Mg−OH bonds, generating cleaved Mg^{2+} or Li^{+} exposure to an aqueous environment.[12, 13, 16] The charge of Laponite edge is, however, dependent on the pH which controls the ionisation and protonation of hydroxyl groups located at the particle edges, where the positive charge at edges decreases with increasing pH at a constant temperature.[12, 241]

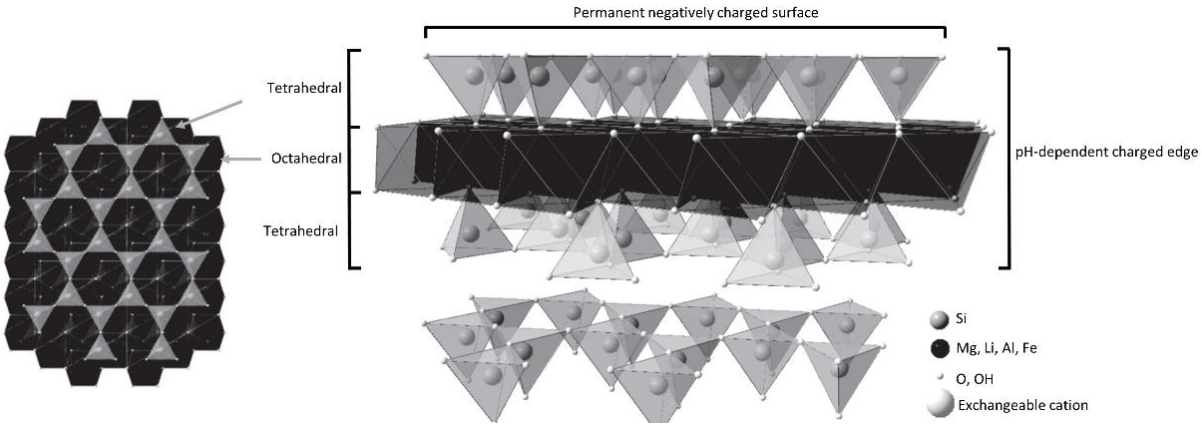

Figure 1-11. The structure of smectite clay that are formed of layered tetrahedral and octahedral sheets. The octahedral sheet of metal oxides (generally Mg^{2+} or Al^{3+}) is sandwiched between two tetrahedral sheets of silica. Laponite crystal exhibits anisotropic and heterogeneous charge with a permanent negatively charged surface generated by cation substitution within the layered structure and a pH-dependent positively charged edge due to broken Si−O, Al−OH, and Mg−OH bonds. Adapted from Mousa *et al*.[12]

In dry environments, the anisotropy of charge distribution attributes to electrostatic interactions of intercalated sodium cations with nanoclay sheets, resulting in the formation of crystal stacks or "tactoids". In aqueous media, the crystal stacks of Laponite clay undergo a complete delamination or exfoliation by osmotic swelling, leading to the separation of individual crystals that may interact with each other to form stable self-assembled gels.[13, 15] The aqueous exfoliation of tactoids typically occur in two steps. Firstly, water molecules penetrate into the interlayer of tetrahedral/octahedral sheets, which results in an expansion of the basal spacing, allowing more water molecules to enter. Sodium ions presented on the surface of Laponite, then, dissociate and diffuse into the bulk due to an osmotic gradient, rendering negatively charged surfaces. This negative charge generates repulsive forces between Laponite platelets. In the second step, electric double layer (EDL) repulsion pushes particles further apart, leading to a delamination of Laponite discs.[242]

After exfoliation in aqueous solutions, nanoclay orders into complex internal arrangements. The heterogeneity of charges introduces a microscopic competition between attractive and repulsive interactions.[243] The phase diagram and microscopic interactions of Laponite dispersions have been largely investigated using a wide range of characterisation techniques.[242-248] It has been proposed that the dissimilar charges of clay may lead to electrostatic attraction (face-to-edge association) and electrostatic repulsion (face-to-face

and edge-to-edge associations). The plate-like particles may experience van der Waals interactions which also drive face-to-face and edge-to-edge associations.[242, 245] The microscopic interactions of Laponite dispersions have been reported that the system spontaneously evolves toward different arrested states depending on clay concentration and ionic strength.[243] The microstructure and its evolution as a function of time are dependent to the temperature and pH of the medium as well as the presence of external additives such as different kinds of salts and polymers.[242, 244-246]

The arrangement of Laponite particles, particularly above 2 wt%, has been debated and controversial in the literature with two different mechanisms that have been mainly suggested. The first proposed microstructure is that Laponite particles remain in a self-suspended state stabilised by repulsive interactions without forming connected network, leading to a repulsive glass microstructure which is known as a Wigner glass.[242, 243, 245, 246] Laponite suspensions (concentration ≥ 2.5% w/w) in water without additional additives have been studied using small-angle X-ray scattering (SAXS). SAXS scattering curves of Laponite dispersed in water suggested repulsive forces between particles and the measured static structure factor $S^M(Q)$ corresponded to the evolution of a homogeneous state which is a characteristic of colloidal glass, indicating that Laponite tends to form a Wigner glass in salt-free suspensions.[243, 245, 246]

Another purposed microstructure is referred to as a house-of-cards structure which is governed by edge-to-face attractive interactions resulting in a gel-like structure.[244-246] Cryo-TEM image of a 2.8% Laponite dispersion at pH 10 suggested the presence of a gel-like microstructure formed by attractive interactions, wherein edge-to-face bonds at different angles and overlapping coin configuration can be observed (Figure 1-12).[244] At the presence of salts or polyelectrolytes (or at high ionic strength), Laponite particles tend to form edge-to-face attractive interactions, resulting in a house-of-cards structure.[245, 246] The addition of salts or polyelectrolytes such as NaCl,[244, 247] sodium polystyrene sulfonic acid,[246] and sodium polyacrylate[245, 248] reduce ageing time by inducing the transition of glass state to gel state, leading to an increment of viscosity. This is potentially due to a decrease of Debye radius and its subsequent partial screening of a strong electrostatic repulsion between Laponite particles.[246, 247]

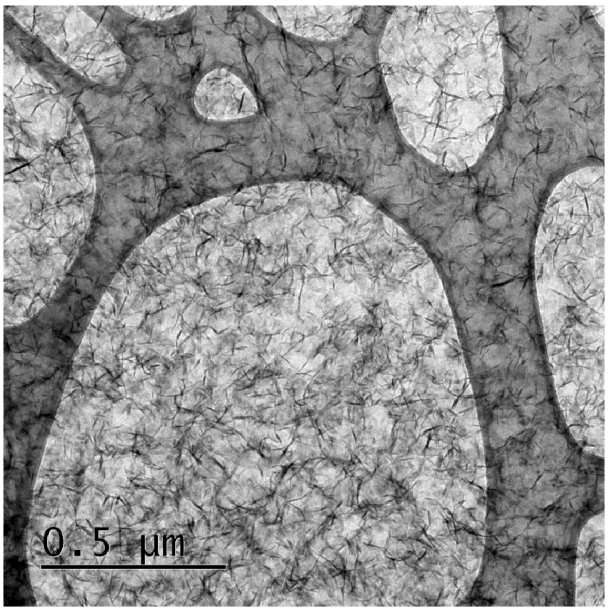

Figure 1-12. Cryo-TEM image representing overlapping coin structure formed in 2.8% Laponite dispersion at pH 10 and 110 hours after gelation. Reproduced from Suman *et al*.[244]

1.8.1.3 Stability and dissociation of nanoclay in physiological conditions

Physiological solutions, such as cell culture medium and phosphate-buffered saline (PBS), contain salts and serum proteins that can interact with Laponite particles and subsequently influence microstructure and stability.[7, 13] The ionic constituents of physiological media include NaCl, $CaCl_2$, KCl, $NaHCO_3$, Na_2HPO_4, and $MgSO_4$.[249]

Laponite dispersed in water create an environment with pH ≈ 10 in which the exfoliated particles form a Wigner glass structure. When transferred to physiological media, Laponite dispersions undergo flocculation driven by a reduction of an electric double layer and electrostatic repulsion between nanoclay particles due to the diffusion of ions/proteins. Moreover, at pH 7.4 in PBS and serum containing culture medium, the protonation of hydroxyl groups (–OH) at the edges of Laponite is enhanced, consequently the positive rim charge increases. In case of saline or PBS solution, the diffusion of monovalent ions results in a compressive electric double layer and a reduced face-to-face repulsion while the lower pH, as compared to native pH 10 of Laponite dispersion, leads to a formation of edge-to-face attractive forces due to enhanced positive rim charges. Therefore, aggregations of Laponite suspension is expected by a combination of a compressed EDL and a promoted rim charge.[7] In case of serum protein, divalent ions are expected to further reduce a range of EDL and a

corresponding tendency toward van der Waals mediated face-to-face attraction, causing overlapping coin arrangement.[7, 250] Additionally, Laponite platelets can interact with proteins in serum through adsorption mechanism, generating clay-protein bridges and account for an increase of network stiffness.[7] Suggested interactions of Laonite in water, PBS, and serum, provided by Dawson's group are presented in Figure 1-13.

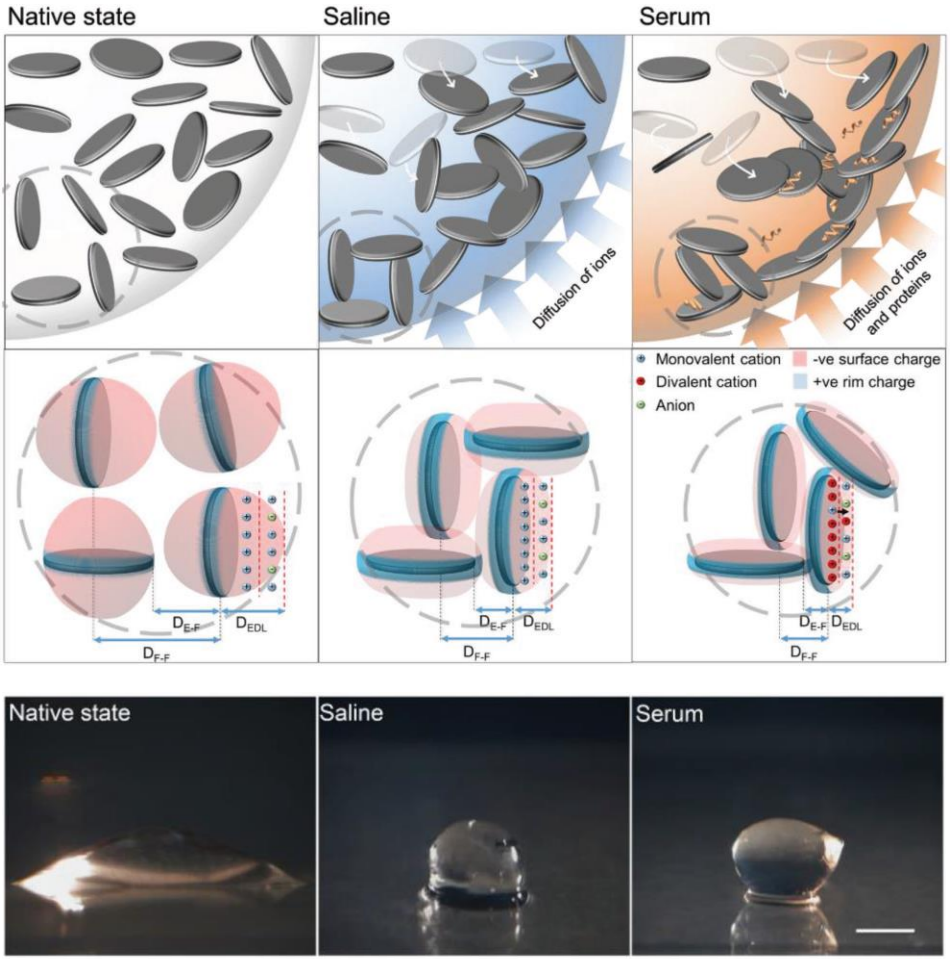

Figure 1-13. Suggested interactions of exfoliated Laonite in water and physiological solutions, provided by Dawson's group.[7] In water (pH ≈ 10), exfoliated nanoclay forms a Wigner glass phase due to the predominant negative charges generating repulsive interactions between particles. In PBS solution, the diffusion of monovalent ions decreases a range of EDL and reduce face-to-face (F-F) repulsion along with the lower pH 7.4 of saline as compared to the native state increases the positive rim charge, driving the formation of edge-to-face (E-F) attractive interactions. In protein-containing serum, additional divalent ions may further reduce the EDL and enhance van der Waals F-F attraction, causing overlapping coin configuration. Proteins in serum can also be adsorbed to clay particles, creating clay-protein interactions which introduce a network stiffness to Laponite suspensions, becoming a stable gel. Reproduced from Shi *et al*.[7]

The isoelectric point of nanoclay is pH≈10, at higher pH, nanoclay tends to form a stable structure, while at lower pH chemical dissociation of individual particles is observed.[251, 252] Thompson and Butterworth first established the investigation of the stability of a Laponite dispersion at low concentration (0.1–1 wt%).[251] Dissolution of Laponite was found to occur at pH<9, at which the concentration of magnesium solution and dissolved silica (in aqueous NaCl) increased exponentially with decreasing pH. The degradation of Laponite particles leads to the leaching of Mg^{2+}, Li^{+}, $Si(OH)_4$, and Na^{+} according to the reaction:

$$Na_{0.7}[(Si_8Mg_{5.5}Li_{0.3}O_{20}(OH)_4] + 12\ H^{+} + 8\ H_2O \rightarrow 0.7Na^{+} + 8Si(OH)_4 + 5.5Mg^{2+} + 0.3Li^{+} \quad (1)$$

Chemical stability of Laponite dispersion was further investigated with respect to the influence of storage environment.[253] Samples preserved under ambient atmosphere showed traces of Mg^{2+} leaching whereas samples stored under N_2 atmosphere did not, suggesting that CO_2 from atmosphere promoted acidic environment by producing carbonic acid and consequently resulted in a progressive dissociation of Laponite and a gradual increase of ionic strength.[253] The dissolution of atmospheric CO_2 in water to form carbonate species occurs via the following reaction:

$$CO_2 + H_2O \rightleftarrows H_2CO_3 \rightleftarrows H^{+} + HCO_3^{-} \quad (2)$$

Interestingly, Joshi and collaborators studied the chemical stability of Laponite dispersions at various concentration (1, 1.7, and 2.8 wt %) and pH (from pH 3 to 10), with and without salts.[252, 254] It was found that the degradation of Laponite in aqueous medium was observed at not only pH<9, but also at pH≥10. However, at the range of pH 3 to 10, no dissolution was observed from samples with high concentration of Laponite (2.8 wt%) over the tested duration of 30 days.[252] The stability in Laponite suspension at high concentration against the attack of H^{+} ions is attributed to the greater concentration of Na^{+} ions, which could be a result of dissociated Na^{+} counterions or from externally added salts. These findings suggested that the higher concentration of Laponite and salts, the greater chemical stability of Laponite suspensions.[252, 254]

1.8.1.4 Cytocompatibility and interaction of Laponite with cells

Cytocompatibility and toxicity of Laponite has been examined using a wide range of biochemical assessments, such as monitoring cell viability, cytoskeletal organisation,

metabolic activity, and cell cycle.[13] Direct exposure of cells to Laponite suspension with varying concentration was used to determine the half maximal inhibitory concentration (IC_{50}). The toxicity of Laponite solution at different concentration was evaluated by examining cell metabolic activity and the levels of reactive oxygen species (ROS) and pro-inflammatory cytokines. At low concentrations (<100 μg mL^{-1}), Laponite did not cause toxicity or alter cell metabolic activity, with enhancing mineralised matrix formation, and IC_{50} was observed at 4–5 mg mL^{-1} for hMSCs and preosteoblasts.[25, 255] Recently, Carrow *et al.* investigated the effect of Laponite nanosilicates towards hMSCs by monitoring cell cycle, metabolic activity, and cytoskeletal organisation.[256] Cell viability and metabolic activity were assessed using AlamarBlue and MTT assays, confirming cytocompatibility of nanosilicates until the concentration of Laponite reached 100 μg mL^{-1}. Cell cycle analysis supported that most cells were in cell growth phase when treated with <100 μg mL^{-1} nanosilicates. Also, the nanoclay treatment did not show a significant influence on cytoskeletal organisation of cells, as compared to untreated cells.[255, 256]

However, a dose-dependent cytotoxicity of Laponite towards cells was induced at higher concentrations (≥100 μg mL^{-1}).[25, 255, 257] Cell viability and metabolic activity significantly decreased when cells were exposed to Laponite solution with higher concentration. The cell activity changing arises from an up-regulation of ROS, leading to the development of apoptosis or inflammation.[25, 257] Consequently, it can be considered that, at low concentrations, Laponite suspension possess an *in vitro* cytocompatbility towards mammalian cells and do not adversely alter cell functions during direct exposure.

Specific interactions between cells and substrates are important to regulate cell functions, tissue homeostasis, and matrix remodelling.[258, 259] Interactions of nanoclay with cells highly depend on shape, size, and charge of clay particles.[259] Owing to the high surface area of disc-shaped crystals and dual charged surface, these characteristics facilitate interactions of nanoclay with a wide range of proteins. It was evident that proteins presented in serum-containing cell culture medium were physically adsorbed on nanoclay surface through electrostatic interactions.[256] The adsorption of proteins on surface governs cellular interactions with nanoparticles and the formation of protein corona is expected to facilitate cell surface receptor-mediated endocytosis, which initiates internalisation of nanoclay.[13, 256] Recent study demonstrated that nanosilicates attached to cell membrane and subsequently

showed a rapid cellular internalisation within 5 minutes, as visualised by hyperspectral imaging, confocal microscopy, and flow cytometry.[256] The cellular uptake of nanosilicates activated stress-responsive pathways such as mitogen-activated protein kinase (MAPK), subsequently guiding hMSCs differentiation into osteogenic and chondrogenic lineages.[256]

Cell adhesion and proliferation on biomaterials are crucial aspects that are involved in tissue regeneration and biomedical applications such as wound healing. Cell attachment is the basis of cell viability, division, differentiation, and motility.[258] The early study in the past decade demonstrated that the incorporation of Laponite nanosilicates enhanced cell adhesion and proliferation of fibroblasts on PEO films (Figure 1-14).[260] Cells readily attached, spread, and proliferated on the composite films containing Laponite nanoclay more than 40 wt% of the total solid contents. Cell viability on surfaces of all composite films remained above 95% for over 14-day culture period, meaning that the addition of Laponite was not cytotoxic to cells even at the highest composition (70 wt%). The degree of cell spreading and proliferation increased with higher Laponite contents (60 and 70 wt%) whereas adherent cells on composite films with Laponite 40 and 50 wt% exhibited rounded morphology (Figure 1-14C). Furthermore, fibroblasts showed an adhesion on surface of composite films in serum free culture medium, although cells seeded under this condition exhibited a spherical shape without spreading and showed no signs of functional adhesion. The difference in cell morphology and activities, under culture conditions with and without serum, suggests that cell adhesion is supported by adsorption of proteins to the nanoclay surfaces.[260] Other studies also reported that the incorporation of Laponite into polymer matrix enhanced cell adhesion of hMSCs,[24] MC3T3-E1 mouse preosteoblasts,[261] HepG2 human hepatoma,[262] human dermal fibroblasts,[262] and human umbilical vein endothelial cells (HUVECs).[262]

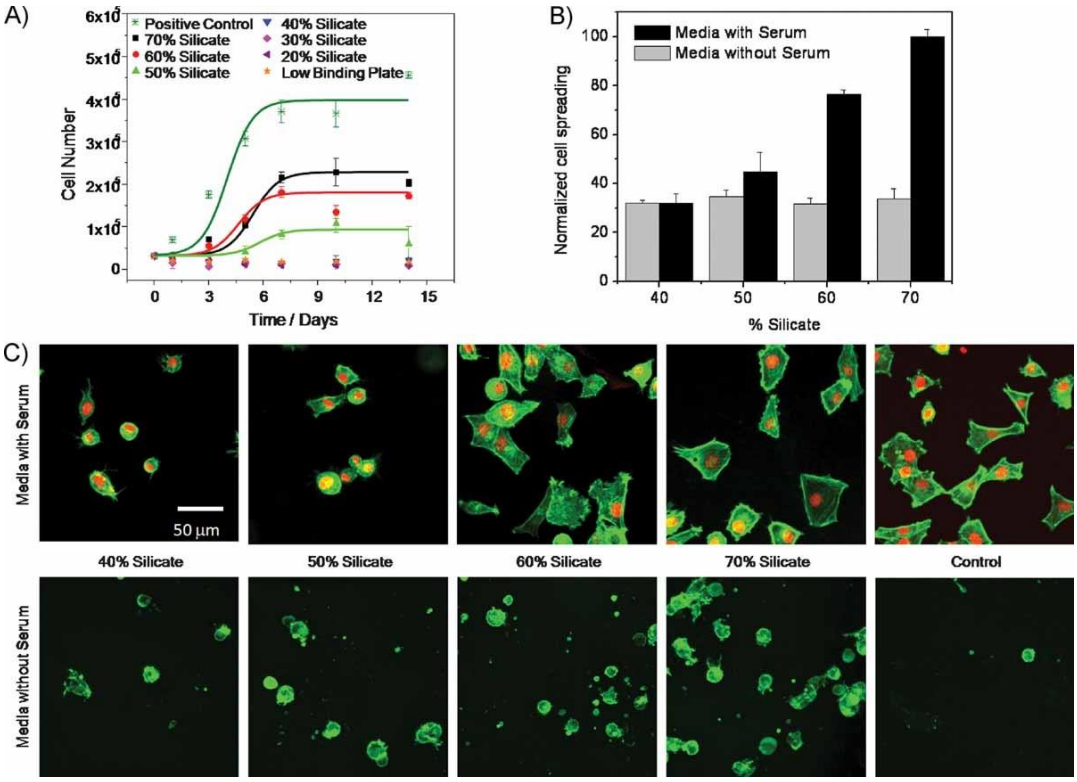

Figure 1-14. Cell proliferation, adhesion, and spreading on composite films with various Laponite concentrations. A) Cell number estimated from cell proliferation assay (Promega). Fibroblasts proliferated to the greater extent on composite films with higher Laponite nanosilicate concentrations. In contrast, the lower contents of PEO, the higher cell proliferation on composite films. B) Degree of cell spreading quantified by the area cells encompass and normalised by both spreading area and cell number to the 70 wt% nanosilicate group. Under culture condition with serum containing medium, degree of cell spreading significantly increased with increasing Laponite nanoclay concentrations ($n = 4$, $p < 0.05$). Composite films containing 40 and 50 wt% nanosilicate did not show a significant difference in cell spreading. Fibroblasts seeded on all composite films and cultured in serum free medium did not show cell spreading. C) Representative images of cytoskeletal organisation labelled with Alexa Flour 488 phalloidin (green) and nucleus counterstained with 7-aminoactinomycin D (Invitrogen). Fibroblasts exhibited obvious actin stress fibres when seeded on films containing 60 and 70 wt% Laponite whereas cells displayed a rounded morphology when seeded on composite films with Laponite 40 and 50%, and cultured in serum free medium. Reproduced from Schexnailder *et al*.[260]

1.8.1.5 Laponite nanoclay for tissue engineering and regenerative medicine

The degradation products of nanosilicates are potentially useful for TERM and biomedical applications.[17] The presence of Mg^{2+}, Li^{+}, and $Si(OH)_4$ may control a variety of cell processes. It has been suggested that Mg^{2+} ions contribute to promoted cell adhesion through enhancing interactions with integrin receptors that compliments the formation of protein corona on

biomaterials, subsequently improving interactions of matrix with cells.[13, 263] Additionally, it was demonstrated that divalent ions such as Mg^{2+} significantly enhanced stem cells differentiation towards osteogenic lineage.[264] Divalent ions are required for the degradation of mitochondrial metabolic proteins.[265] It has been hypothesised that Mg^{2+} may stabilise mRNA and alter the rate of protein degradation, leading to increase of collagenous and non-collagenous proteins. As a result, the cellular differentiation is promoted by enhancing or advancing protein expression.[264] Furthermore, orthosilicic acid stimulates a synthesis of collagen type I and osteoblast differentiation via the Wnt/β-catenin signaling pathway while Li^{+} activates Wnt-responsive genes by elevating cytoplasmic β-catenin.[17, 266, 267] Orthosilicic acid is also essential for metabolic activity and angiogenesis during bone regeneration and calcification of bone tissue.[268, 269] The inherent bioactivity of these soluble degradative products encourages Laponite for a potential use in tissue engineering and regenerative medicine applications.

The high adsorption, specific surface area, and charge heterogeneity of nanoclay allow for interactions with various molecules including polymers, proteins, biomolecules, and drugs. The incorporation of nanoclay into synthetic and natural polymers to modify rheological properties has been widely explored. The addition of nanoclay to polymer matrix offers a formation of shear-thinning hydrogels which are extensively applied in therapeutic delivery, tissue adhesives, wound healing, and tissue regeneration.[205, 270-272] Several studies demonstrated that Laponite-containing scaffolds have shown to promote cell adhesion, proliferation, osteogenic differentiation of stem cells.[17, 22, 24-26, 273-275] For example, gelatin-based hydrogels reinforced with Laponite showed the accelerated osteogenesis of pre-osteoblast MC3T3 cells,[17] and hMSCs[25] in the absence of osteoinductive factors, with the increased ALP activity, and mineralised matrix formation *in vitro*.

3D-printed Laponite-containing nanocomposite hydrogels were made and encapsulated with primary rat osteoblasts (ROBs) by Zhai *et al*.[26] The 3D-bioprinted nanocomposite hydrogels exhibited biocompatibility, with >95% cell viability, and enhanced osteogenic differentiation of ROBs by producing suitable microenvironment, both *in vitro* and *in vivo*. Recently, Dawson's group demonstrated a direct contact of cells with Laponite coated substrates and cell-encapsulated within self-assembled hydrogels for osteogenic microenvironment with results shown in Figure 1-15.[7]

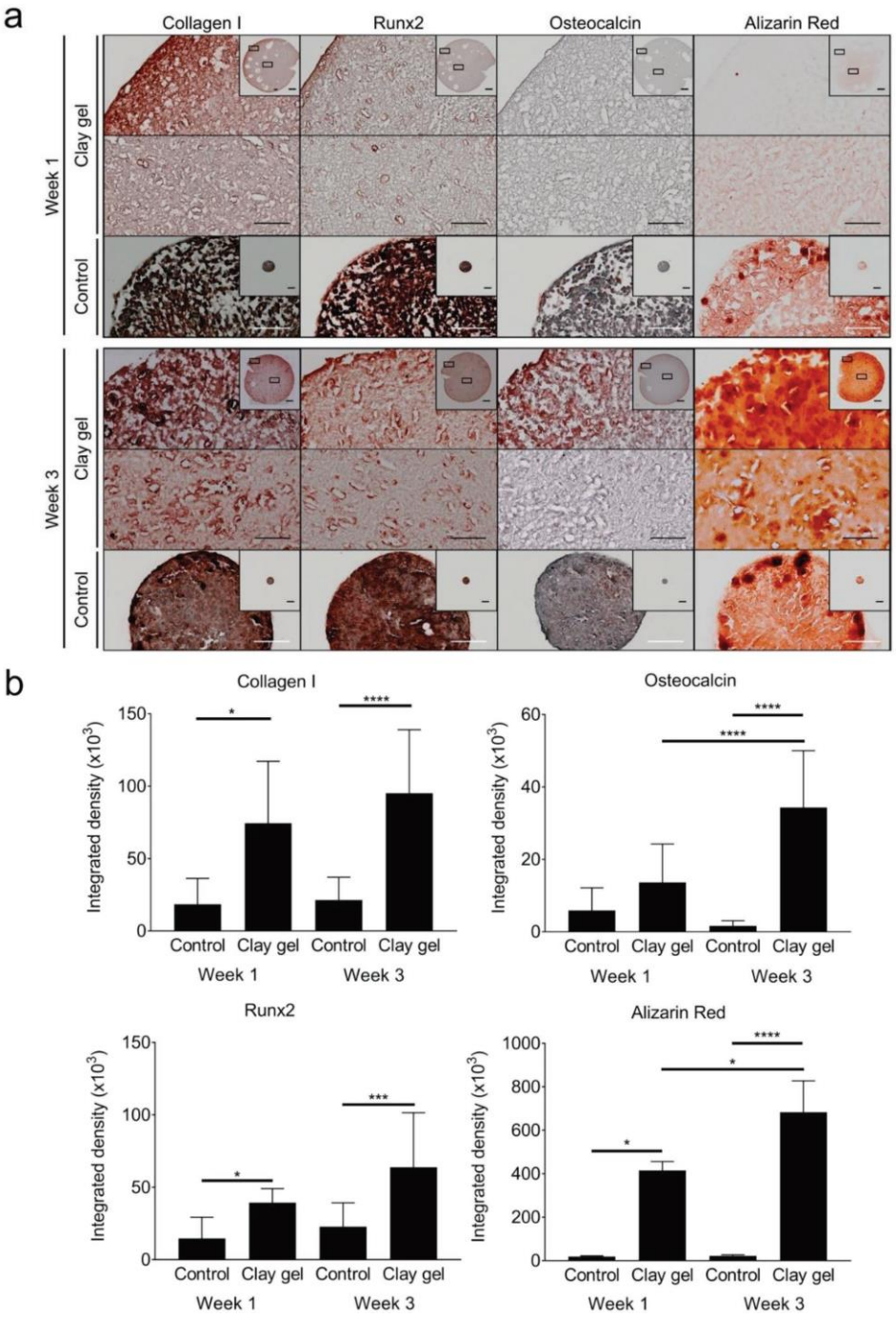

Figure 1-15. The investigation of hMSCs osteogenic differentiation in 3D Laponite diffusion gels. hBMSCs were suspended in 28 mg mL^{-1} Laponite dispersions and added drop-wise into culture medium to induce the formation of gels prior subjecting to osteogenic conditions. After 1 week and 3 weeks post-culturing, samples were histological stained across markers to assess osteogenic differentiation and mineralisation. Scaffold-free cell pellets were used as controls. (a) Representative images showing parallel sections from surface and middle areas of samples stained with each marker. Insets display the entire constructs. (b) Statistical analysis of quantified staining areas across multiple sections (n = 4). Error bars = SD, *, ***, and **** indicate $P < 0.05$, $P < 0.001$, and $P < 0.0001$, respectively, by one way ANOVA with Tukey's multiple comparisons test.[7]

Laponite dried films supported cell adhesion, proliferation and differentiation of human bone marrow-derived mesenchymal stem cells (hBMSCs) towards osteogenic cells in 2D. Cytoskeletal organisation and cell spreading on Laponite films showed no apparent difference from cells seeded on glass. In addition, self-assembled hydrogels were obtained from aqueous exfoliation of nanoclay suspension and used to encapsulate with hBMSCs. Laponite gel encapsulation significantly increased osteogenic protein expression, such as collagen I, RUNX2, and osteocalcin, as compared with 3D pellet culture controls (Figure 1-15b).[7]

Laponite nanoclay has shown potential use in cartilage tissue engineering because of its ability to support chondrogenic differentiation of stem cells and secretion of glycosaminoglycan (GAGs) and aggrecan.[256, 276] Laponite nanosilicate was incorporated into the silylated hydroxypropylmethyl cellulose (Si-HPMC) hydrogel to improve mechanical properties.[276] The addition of Laponite increased mechanical strength of Si-HPMC hydrogel by the development of a hybrid interpenetrating network. The Laponite-containing composite hydrogels were encapsulated with chondrocytes and subcutaneous implanted in nude mice to investigate *in vivo* chondrogenesis induced by composite hydrogels. This study revealed that the Laponite-containing hydrogels were able to support the production of cartilaginous ECM of chondrocytes.[276]

In 2019, Laponite gels were utilised in VEGF-loaded scaffold for vascularisation.[277, 278] VEGF has significant potential in stimulating the growth and regeneration of blood vessels, but it is intrinsically unstable. Injectable Laponite gels showed the ability to generate interactions with VEGF and retained at the injection site for a prolonged period, resulting in an enhancement of blood vessel formation *in vivo*.[277] Similarly, under *ex vivo* implantation, VEGF-loaded Laponite-GelMA scaffolds demonstrated the excellent integration with a chick chorioallantoic membrane model and significantly promoted vessel penetration.[278] Accordingly, Laponite nanoclay would be a promising material for use in skin wound healing applications.

Nanoclay also serves as a platform for fabricating polymer–nanoclay nanocomposites for the treatment of haemorrhage owing to the dual charged nature that can attract blood components and plasma proteins, activating the clotting factors.[272, 279] The incorporation of Laponite into gelatin resulting in the assembly of shear-thinning injectable hydrogels with enhanced haemostatic activity, as a result from promoted coagulation *in vitro* and *in vivo*.[272]

The charged surface of nanosilicates were able to interact with plasma proteins and blood cells, inducing the colocalisation of silicates and blood components and its subsequent platelet aggregation near nanocomposite surface.[272] Likewise, Lokhande *et al*. reported that the addition of Laponite nanosilicates to κ-carrageenan attributed to the greater amount of protein adsorbed on nanocomposite hydrogels, resulting in improved cell adhesion and spreading, increased platelet binding, and reduced blood clotting time.[279]

1.8.2 Graphene

1.8.2.1 Introduction to graphene-family nanomaterials

Graphene, a '2D' material, is a single carbon monolayer which made of sp^2 hybridised atoms arranged into a hexagonal lattice.[29] Graphene possess the superlative materials properties such as excellent mechanical properties (60–130 GPa and 1 TPa for elastic modulus and intrinsic strength, respectively),[280] high surface area ($\sim$2600m^2 g^{-1})[30] and high electron mobility ($\sim 2 \times 10^5$ cm^2 V^{-1} s^{-1} at room temperature).[281] GFNs can also be classified based on chemical modification such as GO and reduced graphene oxide (rGO). rGO is another derivative of graphene which is prepared via a reduction of GO to produce graphene-like sheets by removing the oxygen-containing groups with the restoration of a conjugated structure.[30, 280]

Pristine graphene is limited in its use in biological aspects, mostly due to its poor aqueous dispersibility and lack of functional groups for binding with biologically relevant molecules. Other GFNs, such as GO, an oxidised form of graphene with sp^3 carbons and oxygen-containing defects on the basal plane, have been widely utilised as they can provide a greater ability to disperse in aqueous solution and possesses functional groups by which to attach biological molecules.[282] Nevertheless, the defects present on GO sheets diminish some of the desirable properties of graphene, such as mechanical strength and conductivity.[283, 284] The modification of GFNs is employed to enhance a favourable properties such as solubility,[285] sensing ability,[286] dispersibility,[286] and biocompatibility[287, 288] of GFNs. Functionalisation could be achieved through both covalent bonds and non-covalent interactions.

1.8.2.2 Modification of graphene-family nanomaterials

1.8.2.2.1 Covalent functionalisation of graphene-family nanomaterials

Covalent functionalisation of GFNs can be achieved by, for example, nucleophilic substitution,[289] electrophilic substitution,[290] amidation,[291] esterification[292] and radical addition.[293, 294] By taking advantage of the abundant oxygen-containing functional groups, GO is often selected as a starting material for covalent modification. As an example to illustrate the functionalisation of GO through covalent functionalisation, Avinash *et al.* produced the ferrocene-functionalised GO by Friedel-Crafts acylation, a kind of electrophilic aromatic substitution.[290] Shan *et al*. also prepared a soluble graphene by amidation reaction of amino groups of PLL onto GO surface via epoxide groups.[291] This PLL-functionalised graphene possessed a good solubility in water and abundance of active amino groups which offer biocompatible part for immobilisation of biomolecules. Furthermore, amine-terminated PEG was covalently bonded to carboxylic groups of GO to form amide linkages.[295] The PEGylated GO exhibited excellent stable dispersion in aqueous solutions including buffer, cell medium and serum.

Additionally, the synthesis of polymer-grafted GO by radical polymerisation has been demonstrated. GO was used as a backbone for tethering with various vinyl monomers, including acrylates, methacrylates, styrenics, acrylamides, and 4-vinylpyridine, through free-radical polymerisation. The resulting polymer-grafted GO formed a stable dispersion in various solvents.[293]

Apart from polymers, biomolecules can be also functionalised onto GO surface. de Sousa *et al*. demonstrated the covalent functionalisation of GO with *D*-mannose, a monosaccharide that is important in human metabolism, using mannosylated ethylenediamine (Figure 1-16) The functionalisation of GO with mannosylated ethylenediamine reduced toxicity to human red blood cells compared to unmodified GO which is promising for biomedical applications such as cell-targeting for gene therapy.

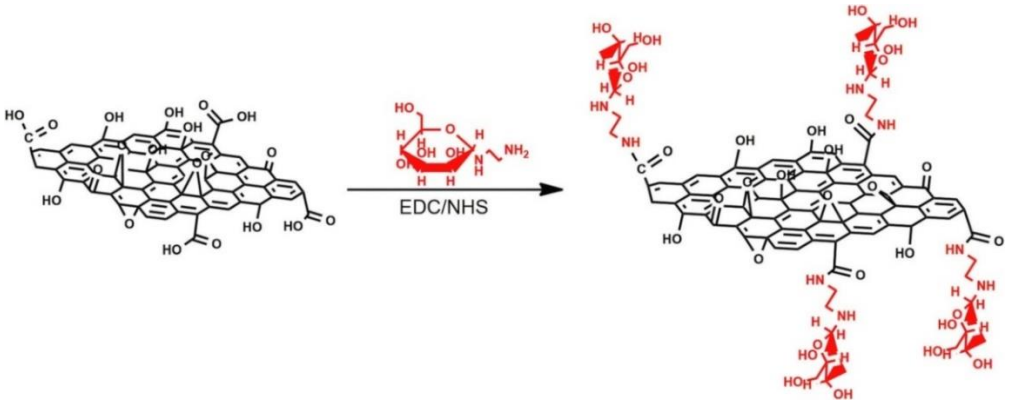

Figure 1-16. Covalent functionalisation of GO with mannosylated ethylenediamine (red) using EDC and NHS crosslinking reagents. Reproduced from de Sousa *et al*.[296]

Covalent functionalisation of graphene (rather than GO) is the process related to grafting molecules onto the basal plane or edges of graphene.[282] Pristine graphene has been covalently functionalised using radicals or dienophiles.[282] However, this method can cause the deterioration of electron or phonon transport as a result of the conversion of sp^2 carbon (C=C) into sp^3 carbon (C–C).[294] The common reactions of covalent attachment to pristine graphene are based on diazonium chemistry, which diazonium salt can generate active radicals under heat or electrochemical reduction and attack the graphene's basal plane.[282] Sinitskii *et al*. functionalised graphene from the oxidative unzipping of carbon nanotube with 4-nitrobenzene diazonium tetrafluoroborate.[297] Furthermore, Englert *et al*. reported a reduction of graphite with a sodium/potassium alloy to produce exfoliated graphene sheets which were further used to functionalise with diazonium salts.[298] Other groups which can be possible tethered by this reaction include azobenzenes[299] and polymers.[300, 301]

Another most common reaction of pristine graphene functionalisation is 1,3-dipolar-cycloaddition.[302, 303] Georgakilas *et al*. used azomethine ylide to functionalise graphene sheets by 1,3-dipolar-cycloaddition where the modified graphene are easily dispersed in polar solvents and water (Figure 1-17).[302]

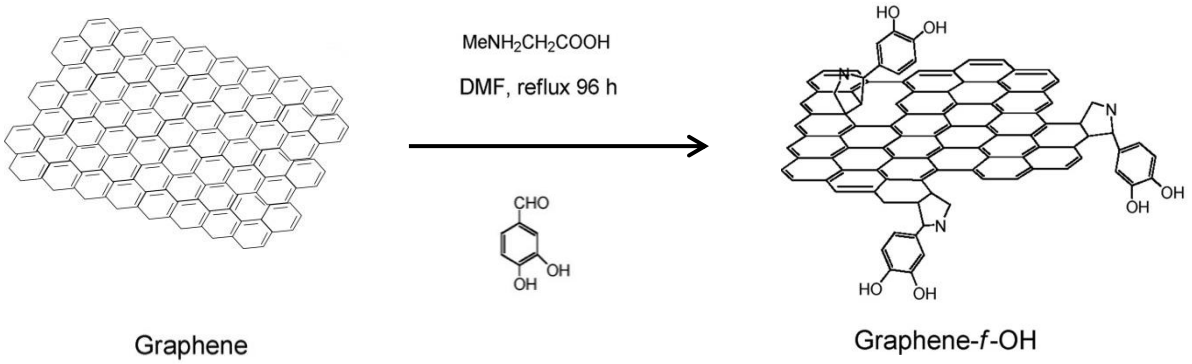

Figure 1-17. Schematic representation of the 1,3 dipolar cycloaddition of azomethine ylide on graphene. Reproduced from Georgakilas *et al*.[302]

1.8.2.2.2 Non-covalent functionalisation of graphene-family nanomaterials

Non-covalent functionalisation is the process that allows molecules to attach with graphene surface through π–π interactions, polymer wrapping, hydrogen bonding, electron donor—acceptor complexes and van der Waals forces.[286] The relative strength of π–π or CH–π interactions is normally 7–16 times lower than covalent bonds, by which the dissipation energies of carbon-carbon single, double, and triple bonds are approximately 350 kJ mol^{-1}, 611 kJ mol^{-1}, and 835 kJ mol^{-1}, respectively, whereas the dissipation energy is less than 50 kJ mol^{-1} for π–π or CH–π interactions.[304] This method is often preferable as it causes little interruption to the structure of graphene, while covalent modification introduces sp^3 defects.[286] Due to a rich extended aromatic system and a limited binding site, common strategies of non-covalent modification of pristine graphene will occur on π–π and methyl–π interactions. A fabrication of non-covalent functionalisation of graphene with 1-pyrenebutanoic acid succinimidyl ester (PYR-NHS) was established by Zhou *et al*.[305] PYR-NHS has a non-polar, aromatic pyrene group that is an identical structure to the conjugated aromatic system of graphene, allowing a strong π–π stacking interactions. Graphene can be also formed π–π interactions with other aromatic molecules, including 1-pyrenecarboxylic acid,[306] quinolone,[307] and triphenylene[308] to increase hydrophilicity and improve aqueous dispersibility.

On the other hand, graphene oxide has a limited aromatic region due to a disruption from oxidation process, meaning that π-π interactions of GO with aromatic molecules are limited. However, there are some existing examples of non-covalent modification of GO with aromatic molecules such as phthalocyanine[309] and naphthalene,[310] where interactions arise from

different polarity. Additionally, GO can serve as a support for immobilisation of drugs,[311-313] DNA[314, 315] and protein[314] through π–π stacking.

Also, GO possesses oxygen-containing functional groups such as carboxylates and hydroxyl groups which can perform ionic interactions or hydrogen bonds with molecules.[286] For examples, many polymers such as poly(vinyl alcohol),[316] epoxy,[317] poly(methyl methacrylate),[318] polyacrylonitrile,[318] and polyaniline,[318] and drugs[313] have been used to functionalise with GO via hydrogen-bonding interactions.

1.8.2.2.3 Edge-specific functionalisation of graphene-family nanomaterials

Edge-specific functionalisation is an alternative approach to the large-scale production of graphene sheets without the disruption of graphitic structure or basal plane.[319] One method for achieving edge-specific functionalisation of graphene is the ball milling graphite in the presence of gases or gas mixtures which can produce reactive species (e.g., radicals, cations and anions) at the edges of graphene sheets (Figure 1-18).[319, 320] Several functional groups have been attached onto graphene edges via ball mill process including hydrogen,[319] carboxylic acid,[319] sulfonic acid[319] and phosphonic acid.[321] However, there is a safety concern of this technique which is a violent sparking generated from the reaction between remaining active carbon species and metallic debris and moister in the air.[322] Also, there are metallic residues left from the steel balls, which require acidic work up to remove.[322]

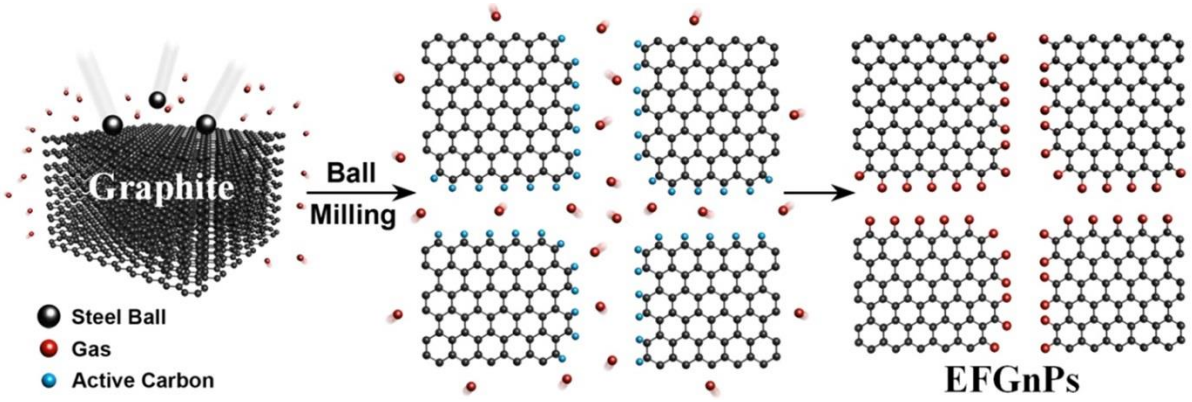

Figure 1-18. Schematic representation of the edge-specific functionalisation of graphene by ball milling in the presence of corresponding gases. The red balls represent the reactant gases such as hydrogen, carbon dioxide, sulfur trioxide, and air moisture (oxygen and moisture). Reproduced from Jeon *et al*.[319]

Another strategy for edge-specific functionalisation is Friedel-Crafts acylation in the polyphosphoric acid (PPA)/phosphorous pentoxide (P_2O_5) medium,[323] which was first developed to functionalised pristine graphite at edge-defected sites (mostly sp^2 C–H) by Baek's group.[324] PPA can protonate the surface of graphite and delaminate by its strong ionic interaction with the ionised graphite surface. PPA's viscosity increases the shear force to graphite layers during mechanical stirring, allowing the edges of graphite to be opened up. Then, the PPA can penetrate the gap and obstruct restacking of graphene sheets, then subsequently attack sp^2 C–H by acylium ions ($–C^+=O$) generated from small organic molecules. The molecules attached to graphene structure by this method include either small molecules (e.g., benzoic acid derivatives,[324, 325] *L*-phenylalanine[326] and niacin[327]) or macromolecules (e.g., poly(ether-ketone)[328, 329] and poly(p-phenylene benzobisoxazole)[330]).

Besides Friedel-Crafts acylation, edge-specific functionalisation of graphene with oxygenated groups (–COOH, $–CH_2OH$) by the Reimer–Tiemann reaction has been described.[331] In this approach, polyhydroxylated graphene (G-OH) is prepared by ball milling process of graphite in the presence of KOH and the product is reacted with $CHCl_3$/KOH/H_2O to produce carboxylates and alcohol at the edges of graphene layers.

Additionally, edge-specific sulfonated graphene synthesised via a facile chemical proceeding has been reported by Abdolmaleki *et al*.[332] In this method, graphite is reacted with chlorosulfonic acid and delaminated to obtain the few-layer sulfonated graphene. The proposed chemical mechanism for this procedure is shown in Figure 1-19.

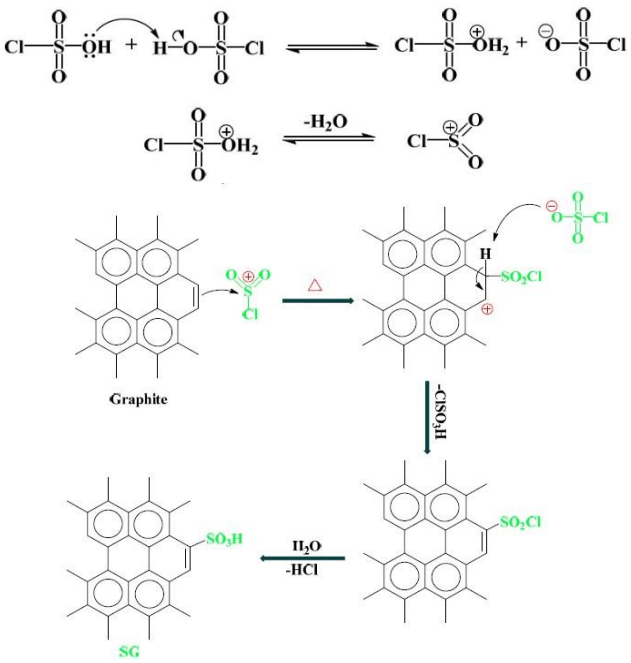

Figure 1-19. Schematic diagram of the proposed mechanism for the edge-specific sulfonated graphite with chlorosulfonic acid. Reproduced from Abdolmaleki *et al*.[332]

Furthermore, the edge-specific sulfonation and thiol functionalisation of pristine graphene based upon electrophilic aromatic substitution have been demonstrated by our previous work. The functionalised-graphene derivatives in this study possessed a low level of defects with target functional groups. The functionalisation also was shown to be edge-specific by attaching a fluorescent protein to thiol functional groups on the edges.[333]

1.8.2.3 Toxicity and biological effects of graphene-family nanomaterials

1.8.2.3.1 Materials properties related to toxicity and biological effects

The biocompatibility and biological effects of GFNs depends on many factors, including surface area, number of layers, lateral dimension, surface chemistry and purity.[334] Surface area is an important feature affecting the interactions of nanomaterials with biological systems such as cell membrane and protein, and also relevant to pulmonary inflammation.[335] The number of layers is related to determining specific surface area, stiffness and biological adsorptive capability.[334] Chatterjee *et al*.[336] and Peruzynska *et al*.[337] demonstrated that single-layered GO is more toxic than multi-layered GO. This effect might be due to the higher ability to adsorb protein from cultured media, leading to the formation of protein corona that may prevent direct interaction with cell plasma membrane and induce indirect toxicity.[338, 339]

The lateral dimensions of nanomaterials have an effect on cell interactions, internalisation, accumulation, and excrete *in vivo*.[334, 340, 341] The role of lateral dimension of GO in cellular response was evaluated by Yue *et al*.[342] The 350 nm GO and 2 μm GO were used to compare the cell uptake in macrophage. The results showed size-independent uptake, however, the GO in micro-size could affect the intracellular event and cytokine profiles, leading to a stronger inflammation.[342] Likewise, Ma *et al*. reported that smaller GO was more easily taken up by macrophages while GO with larger size produced a stronger adsorption to plasma membrane with less phagocytosis, resulting in a greater inflammation cytokines production and promoting recruitment of immune cells.[343] Another study found that, after injection of GO suspension in mice, larger GO mainly accumulated in lung whereas smaller GO mostly found in liver with little amount in lung and spleen. Regardless of lateral dimension, GO was quickly cleared from blood.[344]

Surface chemistry is another crucial factor that can also affect the cell response towards GFNs.[334] Chatterjee *et al*. described that graphene nanoplatelets (GNPs) exhibited higher cytotoxicity to human bronchial epithelial cells (Beas2B cells) than GO, but functionalised GNPs with carboxylate (G-COOH) and amide (G-NH_2) showed less toxicity than pristine GNPs.[336] Also, graphene and GO were used to assess cytotoxicity in skin fibroblasts.[345] The results revealed that graphene sheets caused more damaging to fibroblasts than GO due to its strong hydrophobic interactions with cell membranes. In contrast, some studies reported that GO was found to be more toxic *in vivo* than rGO or GNPs by production of pulmonary thromboembolism.[346-348] Also, Pelin *et al*. reported the higher cytotoxicity of GO on skin keratinocytes compared to pristine graphene and the greater toxicity was observed in GO with the more degree of oxidation.[349] Interestingly, functionalisation can reduce toxicity of graphene[336, 350, 351] and GO[345, 346, 352] *in vitro* and *in vivo*.

Additionally, impurities may have an influence on biocompatibility of GFNs with cells. In a typical synthesis of GO, various chemicals are used such as permanganate, nitrate and sulfate. These reagents may leave residues if the properly washing process is not applied.[334] Also, GO may also contain low molecular weight oxidative debris which is attached on graphene surface.[334] Although the effect of impurities on biological effects is little known, the example still exists. Ali-Boucetta *et al*. illustrated that cytotoxicity of GO *in vitro* and inflammation *in vivo* were reduced by further purification.[353]

1.8.2.3.2 Toxicity of graphene-family nanomaterials *in vitro*

Graphene-family nanomaterials have been cultured with various cell lines to evaluate their toxicity and to obtain reliable information for further study with animals. Graphene and GO have been reported to induce dose- and exposure time-dependent cytotoxicity.[354-357] Primary human corneal epithelium cells (hCorECs) and human conjunctiva epithelium cells (hConECs) were exposed to cell media-containing GO in a range of concentration 12.5–100 μg mL^{-1}.[354] The results showed that the exposure of cells to GO for 2 hours did not induce significant cytotoxic at every concentration but, after 24 hours post-seeding, cell viability decreased with an increasing concentration of GO. Furthermore, a study of flow cytometry of hCorECs exposed to GO (50 μg mL^{-1}) exhibited a significant increase in cell apoptosis after 24 hours, by 3 times higher than control, while no apoptotic cells were observed at 2 hours exposure.[354] Similarly, the toxicity of graphene platelets (GPs) on human glioblastoma U87 and U118 cell lines was studied.[358] The increased concentration of GPs resulted in decreasing of cell viability and greater disruption of cell membranes. However, GPs only induced apoptosis without activating necrosis in the U118 cell line which is promising to use GPs in cancer therapy.[358] Graphene platelets and GO sheets were also found to induce dose-dependent toxicity *in vitro* to other target cells, including human lung epithelial cells (Beas2B[356] and A549[357]), human neuronal cells (PC12),[359] human skin fibroblasts (CRL-2522),[345] human hepatocellular carcinoma cell (Hep G2),[360] and mouse macrophage cell line RAW264.7.[361]

Graphene-family nanomaterials are also found to generate ROS and oxidative stress, leading to mechanism proposed for toxicity.[334, 357, 362, 363] Change *et al*. performed a study on toxicity of GO towards A549 cells where GO could induce ROS level in A549 cells even at low concentration (10 μg mL^{-1}) and GO also exhibited dose-dependent ROS.[357] Additionally, pristine graphene showed the production of intracellular ROS in murine RAW 264.7 macrophages, resulting in the subsequent apoptosis by activation of the mitochondrial pathway.[363]

In contrast to those studies, many studies showed that GFNs did not induce toxicity towards cells. Kucki *et al*. studied the interaction of GO and GNPs with and without acid treatment on Caco-2 cells derived from human colorectal adenocarcinoma.[355] Although GFNs could interact with cell membranes and induce ROS formation, no significant change in cell viability after

exposure to GFNs even at high concentration (80 μg mL^{-1}).[355] GO was also used to incorporate with poly-D,L-lactic acid/polyethylene glycol (PDLLA) hydrogel at concentration up to 100 μg mL^{-1}.[364] The results of 3D cell culture with hBMSCs exhibited the uniform distribution of cells with viability higher than 90% in all hydrogels. Cellular metabolism of hBMSCs in all hydrogels also increased as a function of time after culturing for over 2 weeks.[364] Graphene monolayer prepared by chemical vapor deposition (CVD) was found to be biocompatible with L929 fibroblasts and also supported cell adhesion and proliferation within 24 hours post-culturing.[365]

As previously outlined, functionalisation of GFNs can reduce the toxicity. Chatterjee *et al*. demonstrates that amine- and carboxylate-functionalised graphene nanoplatelets (G-NH_2 and G-COOH, respectively) exhibited lower toxicity on Beas2B cells than pristine graphene because of improved hydrophilicity and clearance.[336] Coating chitosan on GO surface could improve hemocompatibility by eliminating hemolytic activity in red blood cells.[345] Pinto *et al*. modified graphene nanoplatelets with several polymers but only modified graphene with PVA and hydroxyethyl cellulose (HEC) showed the biocompatibility to red blood cells.[351] Functionalised graphene with PVA also improved ROS level and reduced toxicity in human foreskin fibroblasts (HFF-1) compared to unmodified graphene.

However, in some cases of functionalisation, toxicity of materials is not reduced. For example, GO functionalised with polyvinylpyrrolidone (PVP) exhibited a significant decrease in mussel cell viability at a low concentration (10 μg mL^{-1}) while non-functionalised GO did not show a cell number loss at a concentration up to 25 μg mL^{-1} or 50 μg mL^{-1} depends on its original source.[311, 366] Matesanz *et al*. decorated GO with poly(ethylene glycol-amine) and studied the biocompatibility with Saos-2 osteoblasts, MC3T3-E1 preosteoblasts and RAW-264.7 macrophages.[367] The results suggested that the uptake amount of GO depends on cell types and the internalised GO was localised on F-actin filaments, leading to cell alterations, apoptosis and oxidative stress formation.[367]

Graphene-family nanomaterials have been reported to cause toxicity to bacteria, gaining much of interest in antibacterial applications.[368] The mechanisms of antibacterial activities of graphene and GO have been proposed, including membrane stress,[368-370] oxidative stress,[368, 371, 372] electron or charge transfer.[368, 373] A physical damage of bacteria membranes caused by

sharp edges of GFNs sheets can lead to the loss of viability and inactivation of bacteria. The membrane degradation of *Escherichia coli* (*E. coli*) incubated in 100 μg mL^{-1} of GO was confirmed by TEM images, showing a damage of cell membrane with lower surface phospholipid density and its subsequent loss of cellular integrity.[369] The computational simulation performed by Tu *et al*. suggested two types of interaction mechanisms for graphene-induced membrane stress which are the insertion/penetration and the destructive lipid extraction, causing toxicity to *E. coli*. The larger lateral sizes and higher concentration of GO also led to an increase in antibacterial activity.[369] Similarly, Akhavan and Ghaderi studied toxicity of GO and rGO towards *E. coli* and *Staphylococcus aureus* (*S. aureus*), finding that both GO and rGO exhibited antibacterial activity. However, rGO showed more toxicity to bacteria than GO due to its sharpened edges which caused a greater disruption to bacterial membranes.[370]

Similar to those cells described previously, ROS and oxidative stress produced by GFNs can be harmful and toxic to bacteria. Excessive ROS can damage cell membranes by oxidising fatty acids, disrupting cell permeability and cell functions.[374] Liu *et al*. observed the antibacterial activity of GFNs on *E. coli* and suggested that the toxicity towards bacteria results from membrane stress, induced by direct contact of cells with sharp edges of GFNs sheets, producing oxidative stress to bacteria.[371] Hu *et al*. also studied antibacterial propeties and cytotoxicity of GO and rGO nanosheets. Tem images confirmed the loss of cellular integrity and leakage of cytoplasm of *E. coli* due to cell membranes damaging, which could arise from oxidative stress and physical disruption.[372]

Toxicity of GFNs towards bacteria may also arise from electrons or charge transfer between the bacterial membrane to the graphene sheet.[368] Li *et al*. demonstrated antibacterial properties of graphene films on Cu (conductive), Ge (semi-conductive), and SiO_2 (insulating) towards *E. coli* and *S. aureus*.[373] Graphene films on Cu and Ge inhibited the growth of bacteria while no evidence of cell membrane disruption was observed in the direct contact of both bacteria with graphene films on SiO_2.

1.8.2.3.3 Inconsistencies in reports on graphene toxicology

Owing to the growing usage of GFNs in biomedical applications, the evaluation of toxicity and impact on biological systems is required. In the past decades, several studies on

biocompatibility have been undertaken, but it is still a controversy over current findings related to this topic, leading to difficulty in drawing conclusions regarding the potential toxicity of GFNs *in vitro* and *in vivo*. This is probably due to the inconsistent experimental setups, the diversity of material forms used in studies, the different cell types and experimental setup.[375, 376]

Several reviews have attempted to determine patterns regarding toxicity of GFNs and understand biological responses towards them, by mining literatures and separating studies according to the physicochemical features of GFNs such as number of layers, lateral dimension, surface chemistry (including oxidative defects or C/O ratio) and material purity.[334, 377-379] Several parameters were analysed, including the routes of administration, the administered doses, the duration of exposure, the organs in which the accumulation of GFNs observed, adverse effects, and toxicity mechanisms.[378, 379]

According to the variation in toxicity and biological responses dependent on physicochemical properties of GFNs, it is strongly recommended that studies need to provide data on characterisations of materials used in research. This is very important for evaluation of literatures to conduct meaningful future studies and to prepare GFNs for safe *in vitro* and *in vivo* uses. In 2013, Bussy *et al*. provided a review of graphene and carbon nanotubes (CNTs) toxicity studies and produced a set of criteria for safety considerations and guidelines in the development of GFNs, which likely to minimise the risks of graphene for use in biomedical applications.[380] The use of small dimensioned, single graphene sheets for efficient internalisation by macrophages and remove was highlighted, as well as the preparation of stable dispersions of GFNs to avoid accumulation and aggregation *in vivo*.[380]

1.8.2.4 Graphene-family nanomaterials in tissue engineering and regenerative medicine

Graphene-based materials have been applied in BTE applications because GFNs not only support cell adhesion and proliferation, but also enhance osteogenic differentiation of stem cells.[30] Many studies demonstrated that GFNs can induce the differentiation of stem cells into osteogenic lineages[33-36] and support the adhesion and proliferation of osteoblast-like cells.[37, 38] Graphene-coated substrates produced by CVD and GO films formed by using a Langmuir–Blodgett (LB) trough accelerated the osteogenic differentiation of hMSCs in the present of osteogenic inducers (dexamethasone, ascorbic acid, and β-glycerophosphate), compared to

unmodified substrates (Si/SiO_2, glass, PET and PDMS).[34, 36] Furthermore, self-supporting graphene hydrogel prepared form rGO enhanced osteogenic differentiation of rBMSCs without chemical inducers, whereas, in the presence of osteogenic induction, the differentiation could be promoted at earlier time and much stronger.[33]

GFNs can be also incorporated with other materials to use as a platform for BTE. Duan *et al*. demonstrated that, in a comparison with carbon nanotube, the acid oxidised graphene-containing poly(L-lactide) (PLLA) scaffolds exhibited good biocompatibility and strongly induced osteogenesis of BMSCs both *in vitro* and *in vivo*.[381] Moreover, Türk and Deliormanli studied the effect of graphene-containing polycaprolactone (PCL) coated borate glass scaffolds on osteoblastic differentiation.[382] The results showed that graphene nanoparticles promoted an early stage of pre-osteoblast MC3T3-E1 differentiation with the higher ALP activity compared to the bare PCL-coated borate scaffolds. However, the graphene-containing PCL scaffolds exhibited the cytotoxicity after 7 days of incubation and cell viability in the sample with graphene strating from 3 wt% had decreased after 14 days.

Apart from graphene nanoparticles, GO shows a potential candidate in osteogenic differentiation and has been widely used to create scaffolds for BTE as well.[383-386] For example, in the work of Hwang's group, GO was used to embedded in PEG-based cryogel and cultured with human tonsil-derived mesenchymal stem cells (hTMSCs).[383] The PEG-GO cryogels could support cell adhesion, proliferation and viability of hTMSCs, with improving focal adhesion kinase (FAK) signalling activation and stimulating osteogenic differentiation. Chen *et al*. described an approach to synthesis hydroxyapatite (HAp) nanowhiskers at GO surfaces (HAp-GO) and used it to incorporate with PLA.[384] The PLA/HAp-GO showed cytocompatibility to osteoblast-like MG-63 cells, with improving strength and toughness compared to the neat PLA scaffold.

Additionally, GFNs have also been shown to enhance the adipogenic differentiation of stem cells. For example, a composite thermogel composed of GO and polypeptide (GO/P), formed by temperature-sensitive sol-to-gel transition of a GO-suspended PEG-poly(*L*-alanine) aqueous solution significantly enhanced the expression of adipogenic biomarkers. The enhanced adipogenesis was attributed to the ability of insulin to strongly bind to GO.[387] In addition, Kim *et al*. demonstrated the efficiency of GO films to support cell adhesion, revealed

by a large number of focal adhesion, and generate a strong affinity with hASCs with enhanced adipogenesis and epithelial genesis. GO films also showed the high correlation between the organisation of actin filaments and vinculin bands as compared to glass substrate.[388]

Taking advantage of electrical properties, GFNs have been shown a potential platform for promoting neuronal differentiation. A monolayer highly uniform graphene produced by CVD process provided an environment for the formation of hMSCs spheroids and regulated the interactions of cell-substrate and cell-cell interfaces Consequently, the neuronal differentiation of hMSCs was promoted, indicating by the upregulation of early neurogenesis-related genes.[389] Serrano *et al*. fabricated GO-based 3D scaffolds and used to culture with embryonic neural progenitor cells (ENPC). On GO-based 3D scaffolds, the presence of highly viable and interconnected neural networks were observed, consisting of both neurons and glial cells with plenty of dendrites, axons and synaptic connections.[390]

1.9 Poly(vinylphosphonic acid) – a promoter of bone regeneration

Bisphosphonates (BPs) are a class of drugs that have been most widely used as the effective treatment of bone diseases, especially for osteoporosis, by inhibiting osteoclast-mediated bone resorption.[40, 391] BPs are classified as a synthetic derivatives of pyrophosphates by which the P–O–P group in pyrophosphate is replaced with the P–C–P bond (Figure 1-20), giving rise in the stability against a hydrolysis. The P–C–P backbone in BPs enable the biding efficiency to divalent ions such as Ca^{2+}. Consequently, BPs are capable to tether bone mineral surfaces *in vivo*. This occurs via a bidentate manner through the chelation of divalent ions with one of oxygen atom from the phosphonate groups or a formation of tridentate conformation involving the R_2 side chain.[391, 392]

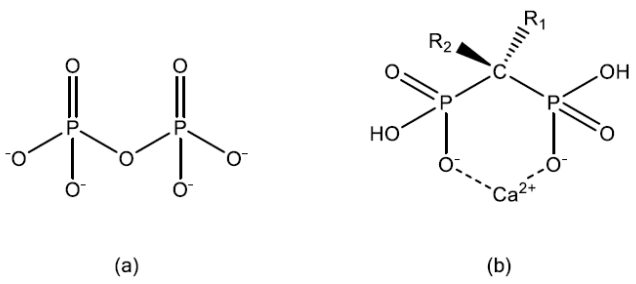

Figure 1-20. Chemical structures of (a) pyrophosphate and (b) bisphosphonates with showing the coordination of Ca^{2}+ with oxygen atoms from the phosphonate groups.[391, 392]

BPs have been acknowledged as one of the most effective bone resorption inhibitors. BPs can bind to hydroxyapatite and inhibit the process of hydroxyapatite dissolution into amorphous calcium phosphate, afterward, bone resorption is suppressed.[393] At the cellular level, bisphosphonate endocytosis into osteoclast happens directly from the bone surface, leading to preventing osteoclast maturation and inhibiting the functions of osteoclasts. Subsequently, bone resorption is reduced.[391, 393] Moreover, BPs have shown to directly regulate the osteoblast maturation and bone-forming activities by increasing ALP activity as well as enhancing gene expression of BMP-2, type I collagen, and osteocalcin.[394, 395] However, some undesirable medical occurrences associated with BPs therapy have been reported, including osteonecrosis of the jaw, gastrointestinal intolerance, and nephrotoxic at a rapid administration of high dose.[40]

Polymers, both natural and synthetic, are attractive candidates for use as a matrix in tissue engineering due to its tuneable and reproducible mechanical and chemical properties.[396] Phosphonate-containing polymers have been considered as a promising material for use in BTE. It is hypothesised that P–C bonds in phosphonate-containing polymers can mimic P–C–P backbone found in bisphosphonates.[397] Moreover, it is known that several proteins interact with polymers through acid moieties and phosphate-rich proteins can initiate bone growth, therefore, phosphonate-containing polymers should provide interactions with proteins, together with enhancing mineralised matrix.[398]

In the past decade, poly(vinylphosphonic acid) (PVPA) has been integrated with various polymers and biomaterials to use as a platform for BTE.[42, 43, 398, 399] Gemeinhart *et al*. produced a graft-copolymer of PVPA with acrylamide and investigated MC3T3-E1 cells response towards this material.[398] It was shown that copolymer with 30% of PVPA in feed could increase cell adhesion, proliferation and induced mineralised matrix production of MC3T3-E1. Moreover, HAp was modified with PVPA and chitosan for improving the integration and stability of scaffold to bone tissue.[399] The PVPA-chitosan- modified scaffolds were not only nontoxic to rBMSCs but also improved cell adhesion, proliferation and spreading *in vitro*, and stimulated early interfacial implant-bone tissue integration with enhancing new bone formation *in vivo*.

Additionally, a biomimetic mineralisation strategy has been developed by binding PVPA and PAA to collagen fibrils for guiding the scale and distribution of apatites.[400] PAA is utilised for creating metastable amorphous calcium phosphate nanoprecursors in the presence of calcium and phosphate ions while PVPA mimics the negative charges of phosphoproteins, for example, phosphophoryn and bone sialoprotein. Under the treatment of a phosphate-containing simulated body fluid with the presence of PAA and PVPA, the mineralisation of collagen fibrils was observed and closely identical to those of natural bone.[400]

In addition, a copolymer of poly(vinylphosphonic acid-*co*-acrylic acid) (PVPA-*co*-AA) was synthesised and incorporated with PCL scaffold for studying on the healing potential of critical size defect created on parietal bones which were obtained from 4-day-old neonatal CD1 mice.[42] The results showed that the presence of PVPA-*co*-AA in the scaffold increased bone filling percentage and hydroxyapatite formation, subsequently improving mineralisation and osteoblast proliferation as well as significantly decreasing osteoclast viability compared to PCL scaffold. Furthermore, Dey *et al*. demonstrated that, with increasing vinylphosphonic acid (VPA) content in copolymer, there was an increase in calcium chelation, reaching a maximum at *ca*. 30 mol % VPA and PVPA-*co*-AA had no adverse effect on metabolic activity of Saos-2 cells, regardless of copolymer composition.[43] The effect of PVPA-*co*-AA copolymer towards osteogenesis was investigated by culturing osteoblastic Saos-2 and hMSCs with culture medium containing phosphonate-based copolymers.[401] The PVPA-*co*-AA copolymers not only enhanced the mineralisation of Saos-2, but also promoted hMSCs differentiation towards osteogenic lineage.

1.10 Layer-by-layer assemblies

The layer-by-layer (LbL) technique, first established by Decher and Hong in 1991, is a method to fabricate multilayered structure.[402] The LbL technique was developed due to the limitations in Langmuir-Blodgett technique, which was required special equipment, limited to amphiphilic molecules and substrate size, and had to be formed on the surface of water before being transferred to other solid supports.[403] The LbL technique is based on mainly electrostatic attraction between positive charge and negative charge by immersing charged surfaces in a solution containing oppositely charged ions. Once the charged species deposits as a first layer on top of the surface, this surface is washed off and exposed to a solution

containing oppositely charged ion to the first layer. The immersion of surfaces in alternating positively and negatively charged polyelectrolytes several cycles generates the multilayered structure. A schematic of the LbL assembly of a polyelectrolyte multilayer is shown in Figure 1-21. LbL assemblies can be created on various materials by exploiting driving forces such as electrostatic interaction, hydrogen bonding, covalent bonding, and donor/acceptor interactions.[404]

The LbL process is a low-cost method of fabrication and environmental friendly because the deposition step can be performed in mild condition (usually in water at room temperature). Additionally, this technique does not require a special equipment and the thickness of layers can be controlled by adjusting the solutions in which surface is submerged.[403] Instead of a traditional dip-coating technique, LbL assemblies can be also achieved by a spray-coating method, providing a thinner with reduced interfacial roughness of multilayered structures.[405] Despite the LbL assemblies generally involve the use of polyelectrolytes,[406-408] other species which have been integrated into LbL constructs include dyes,[409] proteins,[410] DNA,[411] and graphene-family materials.[408, 412, 413]

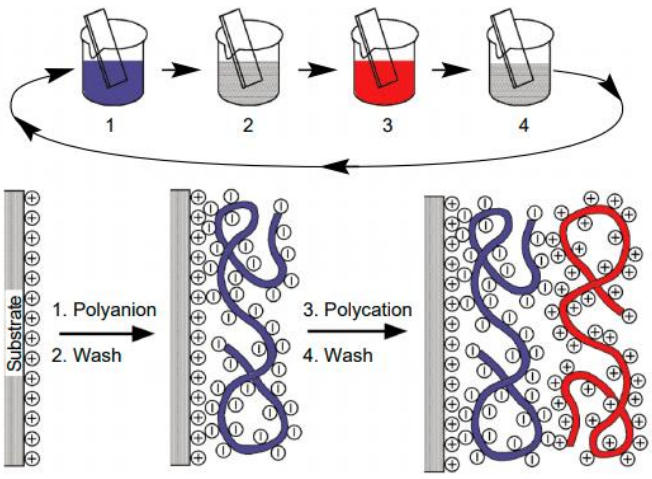

Figure 1-21. Layer-by-layer (LbL) procedure, showing deposition of first two layers of a film on a positively charged substrate. The charged substrate is first immersed in a polyanion solution, washed, and then immersed in a polycation solution. Reproduced from Decher *et al*.[403, 414]

The build-up of LbL multilayered films can be monitored using UV-visible spectroscopy.[413, 415] Figure 1-22 shows how the growth of sulfonated graphene oxide (SRGO) with polystyrene-based diazonium salts (PSDAS) LbL films was followed.[413] The increase of UV-Visible spectra

indicates the formation of LbL assemblies. The absorbance at 270 nm and 650 nm, which were attributed to the adsorption of both SRGO and PSDAS, were plotted against the number of bilayers. A linear relationship of absorbance and number of bilayers can be referred to a high-ordered film.[416]

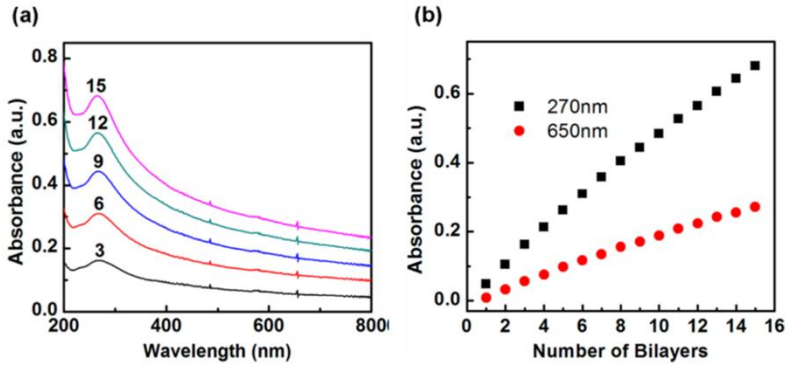

Figure 1-22. (a) UV-visible absorption spectra of SRGO/PSDAS multilayered film on a quartz slide and (b) the plot of absorbance at 270 nm and 650 nm with the number of bilayers. Reproduced from Xiong *et al*.[413]

In addition to a linear growth, sub-linear and super-linear trends can be observed in some cases of LbL multilayered formation. A super-linear (or exponential) growth relates to either an increase of surface coverage functional groups of polyelectrolytes, or the molecules diffusion from the internal to the outermost layer during deposition process. A sub-linear growth could arise from a stagnation of layer growth due to a decrease of surface coverage functional groups.[404] The formation of LbL multilayered films can also be monitored by quartz crystal microbalance (QCM) which is used to measure a frequency change during the adsorption of LbL assemblies. The frequency change is converted to a mass change using the Sauerbrey equation.[412]

LbL assemblies have emerged in a variety of tissue engineering and biomedical applications. Polymers have been widely incorporated into substrates using the LbL technique for surface modification, subsequently promoting cell attachment, cell proliferation and osteogenic differentiation.[417, 418] Synthetic polymers that are commonly used in LbL assemblies for cellular and tissue engineering applications include PLL,[419] PAA,[420, 421] poly(sodium-4-styrene-sulfonate) (PSS),[422] poly(ethyleneimine) (PEI),[423] PGA, [419, 420] and poly(allylamine hydrochloride) (PAH).[421, 422] In addition to synthetic polyelectrolytes, natural polymers such as collagen,[424] fibronectin,[425] heparin,[423, 424] and chondroitin sulfate (CS)[424] which are

components of extracellular matrix (ECM) proteins have been also used in LbL constructs to improve cell adhesion and spreading.

GFNs have been incorporated into LbL assemblies for in tissue engineering, with GO commonly used as polyanions in the LbL process.[415, 426-428] For example, Qi *et al*. assembled GO/PLL films for use as a scaffold for MSCs by dip-coating alternating layers of GO and PLL on glass coverslips.[426] The GO/PLL films had ability to support stem cells adhesion with high proliferation rate and accelerated osteogenic differentiation, resulting in strong ALP and gene expression.[426] Qi *et al*. also studied fibroblast proliferation on PAH/GO LbL constructs, indicating greater proliferation and cell spreading on the PAH/GO LbL film than on PAH/PSS control substrates.[415] Likewise, Shin *et al*. demonstrated the formation of 3D cardiac tissue constructs using LbL assembly of cardiomyocytes and epithelial cells with PLL-GO thin film as an interlayer, improving cardiac cell organization, maturation, and cell-cell electrical coupling.[427] Recently, Kashte and co-workers modified PCL scaffold with GO and *Cissus quadrangularis* (CQ) plant callus extract using the LbL technique.[428] The PCL/GO/CQ scaffold enhanced differentiation of MSCs into osteogenic lineage without the presence of chemical inducers.[428] Reduced graphene oxide was also used to fabricate 3D composite scaffold with polypyrrole and hydroxyapatite through the LbL process for use in bone tissue engineering.[429] On the other hand, pristine graphene is not generally used in LbL assemblies because it is uncharged, otherwise it is modified to introduce the necessary charge for LbL formation. For example, Sham *et al*. produced surfactant-modified graphene to incorporate charge on edge defects of pristine graphene platelets and used it to form LbL multilayered films with PEI.[412]

1.11 Research outline

Due to the limitations and complications of current treatments, BTE has become an alternative approach for treatments of bone fractures and diseases. Injectable hydrogels has shown to become a promising strategy for use in BTE, largely due to minimisation of invasive surgical operations, scar formation, and risk of infection at the operated sites. To overcome limitations of *in situ* crosslinking hydrogel systems such as required external stimuli to induce gelation process, self-assembled hydrogels provide an alternative strategy for fabricating injectable hydrogels. Self-assembly is a main route to fabricate shear-thinning hydrogels and can be achieved via physical crosslinking, for example, electrostatic interactions, ionic

interactions, and hydrogen bonding.[150, 430] To design injectable scaffolds, enhancing mechanical properties with maintaining injectability would be challenging. Consequently, the aim of this research was to develop injectable hydrogels comprising of Laponite nanoclay, GFNs, and phosphonate-containing polymers for BTE scaffolds.

Laponite is a synthetic silicate nanoclay composed of dual charged crystals that is able to form shear-thinning hydrogels through electrostatic forces. Laponite can also degrade into nontoxic products that stimulate cell adhesion and osteogenic differentiation of stem cells. From literatures, a study of using Laponite as a main phase for fabrication of engineered tissue scaffolds is still limited. Dawson's group demonstrated Laponite self-assembled diffusion gels for bioactive osteogenic microenvironments by fabricating Laponite gel encapsulation with hMSCs and culturing in osteogenic conditions.[7] Nanoclay diffusion gels exhibited matrix mineralisation and osteogenic protein expression after three weeks post-culturing in osteogenic-induced conditions. This study demonstrated a potentiality of Laponite as a scaffold for use in BTE. With respect to unique characteristics, Laponite was chosen as a main material for creating injectable hydrogels in this project. The research hypothesis was that GFNs would improve the mechanical properties of Laponite-based hydrogels and served as a delivery platform for therapeutic agents while the incorporation of phosphonates aimed to mimic the function of bone-protecting bisphosphonate drugs.

In this thesis, pristine graphene and GO were firstly modified with vinylphosphonic acid via edge-specific modification and radical polymerisation to purposely achieved favourable properties such as dispersibility in aqueous media. This thesis also aims to provide an alternative procedure to produce modified graphene that retains the structure of graphene sheets and can be extended to a variety of functional groups. Additionally, it was hypothesised that phosphonate groups (–$PO(OH_2)$) attached to graphene sheets or edges would enhance ability of GFNs to support bone cell formation and matrix mineralisation. The 2D culture of osteoblasts using LbL assemblies were carried out to present the response of cells towards the modified GFNs. Cell adhesion, proliferation, and mineralisation of osteoblasts were examined. According to the results, the most acceptable modified GFNs analogues was selected for the further study.

Laponite-based composite hydrogels containing PVPA-*co*-AA and GFNs were then created and encapsulated with osteoblasts to study cell mineralisation in 3D microenvironment. The technique of hydrogel preparation in this research was simple, fast and under mild conditions by which Laponite powder was dispersed in DI water at room temperature, followed by vigorously stirred using magnetic stirrer, and self-assembled hydrogels were subsequently formed. Rheological and mechanical properties of Laponite-based hydrogels were assessed using a rheometer. The ability of Laponite-based hydrogels to serve as an osteogenic microenvironment was investigated by encapsulating osteoblast-like cells in 3D gels and culturing in normal condition and osteogenic-induced condition. The cytoskeletal organisation and cell response of osteoblasts were determined using phalloidin staining and histological assessment, respectively.

Finally, cell migration of osteoblasts within 3D scaffolds and the effect of chemical gradient on cell migration were investigated using the confocal microscopy to acquire stacked images of fluorescent dye-labelled cells. The effect of chemical gradient was also studied using culture medium containing PDGF-BB as followed the protocol described by Movilla *et al*.[132] The migration of osteoblasts was reported by the difference in distance between cell layers and a fixed reference level. Cell response towards Laponite-based hydrogel in 2D culture were studied. The cytoskeletal organisation and cell response of osteoblasts on 2D culture were determined using the same assessments as 3D encapsulation.

1.12 References

1. Ralston, S. H., Bone structure and metabolism. *Medicine* **2017,** *45* (9), 560-564.
2. Shi, R.; Huang, Y.; Ma, C.; Wu, C.; Tian, W., Current advances for bone regeneration based on tissue engineering strategies. *Frontiers of medicine* **2019,** *13* (2), 160-188.
3. Dimitriou, R.; Jones, E.; McGonagle, D.; Giannoudis, P. V., Bone regeneration: current concepts and future directions. *BMC medicine* **2011,** *9* (1), 66.
4. Kanis, J.; McCloskey, E.; Harvey, N.; Javaid, K.; Borgström, F., Broken bones, Broken lives: A roadmap to solve the fragility fracture crisis in Europe. *International Osteoporosis Foundation* **2018**, 1-32.
5. Kanis, J.; McCloskey, E.; Harvey, N.; Javaid, K.; Borgström, F., Broken bones, Broken lives: A roadmap to solve the fragility fracture crisis in the United Kingdom. *International Osteoporosis Foundation* **2018**, 1-19.
6. Amini, A. R.; Laurencin, C. T.; Nukavarapu, S. P., Bone tissue engineering: recent advances and challenges. *Critical Review in Biomedical Engineering* **2012,** *40* (5), 363–408.
7. Shi, P.; Kim, Y. H.; Mousa, M.; Sanchez, R. R.; Oreffo, R. O.; Dawson, J. I., Self-Assembling Nanoclay Diffusion Gels for Bioactive Osteogenic Microenvironments. *Advanced healthcare materials* **2018,** *7* (15), 1800331.

8. Place, E. S.; Evans, N. D.; Stevens, M. M., Complexity in biomaterials for tissue engineering. *Nature materials* **2009,** *8* (6), 457-470.
9. Guan, X.; Avci-Adali, M.; Alarçin, E.; Cheng, H.; Kashaf, S. S.; Li, Y.; Chawla, A.; Jang, H. L.; Khademhosseini, A., Development of hydrogels for regenerative engineering. *Biotechnology Journal* **2017,** *12* (5), 1600394.
10. Kondiah, P. J.; Choonara, Y. E.; Kondiah, P. P. D.; Marimuthu, T.; Kumar, P.; du Toit, L. C.; Pillay, V., A Review of Injectable Polymeric Hydrogel Systems for Application in Bone Tissue Engineering. *Molecules* **2016,** *21* (11), 1580.
11. Lü, S.; Bai, X.; Liu, H.; Ning, P.; Wang, Z.; Gao, C.; Ni, B.; Liu, M., An injectable and self-healing hydrogel with covalent cross-linking in vivo for cranial bone repair. *Journal of Materials Chemistry B* **2017,** *5* (20), 3739-3748.
12. Mousa, M.; Evans, N. D.; Oreffo, R. O.; Dawson, J. I., Clay nanoparticles for regenerative medicine and biomaterial design: A review of clay bioactivity. *Biomaterials* **2018,** *159*, 204-214.
13. Gaharwar, A. K.; Cross, L. M.; Peak, C. W.; Gold, K.; Carrow, J. K.; Brokesh, A.; Singh, K. A., 2D nanoclay for biomedical applications: Regenerative medicine, therapeutic delivery, and additive manufacturing. *Advanced Materials* **2019,** *31* (23), 1900332.
14. Chimene, D.; Alge, D. L.; Gaharwar, A. K., Two-dimensional nanomaterials for biomedical applications: Emerging trends and future prospects. *Advanced Materials* **2015,** *27* (45), 7261-7284.
15. Tomás, H.; Alves, C. S.; Rodrigues, J., Laponite®: A key nanoplatform for biomedical applications? *Nanomedicine: Nanotechnology, Biology and Medicine* **2017**.
16. Additives & Instruments, B., Laponite: Performance Additive. *Technical Information B-RI 21* **2014**.
17. Xavier, J. R.; Thakur, T.; Desai, P.; Jaiswal, M. K.; Sears, N.; Cosgriff-Hernandez, E.; Kaunas, R.; Gaharwar, A. K., Bioactive nanoengineered hydrogels for bone tissue engineering: a growth-factor-free approach. *ACS Nano* **2015,** *9* (3), 3109-3118.
18. Park, J. K.; Choy, Y. B.; Oh, J.-M.; Kim, J. Y.; Hwang, S.-J.; Choy, J.-H., Controlled release of donepezil intercalated in smectite clays. *International Journal of Pharmaceutics* **2008,** *359* (1-2), 198-204.
19. Jung, H.; Kim, H.-M.; Choy, Y. B.; Hwang, S.-J.; Choy, J.-H., Itraconazole–Laponite: Kinetics and mechanism of drug release. *Applied Clay Science* **2008,** *40* (1-4), 99-107.
20. Grabolle, M.; Starke, M.; Resch-Genger, U., Highly Fluorescent dye–nanoclay Hybrid Materials Made from Different Dye Classes. *Langmuir* **2016,** *32* (14), 3506-3513.
21. Zhou, B.; Xiong, Z.; Zhu, J.; Shen, M.; Tang, G.; Peng, C.; Shi, X., PEGylated polyethylenimine-entrapped gold nanoparticles loaded with gadolinium for dual-mode CT/MR imaging applications. *Nanomedicine* **2016,** *11* (13), 1639-1652.
22. Mihaila, S. M.; Gaharwar, A. K.; Reis, R. L.; Khademhosseini, A.; Marques, A. P.; Gomes, M. E., The osteogenic differentiation of SSEA-4 sub-population of human adipose derived stem cells using silicate nanoplatelets. *Biomaterials* **2014,** *35* (33), 9087-9099.
23. Wang, C.; Wang, S.; Li, K.; Ju, Y.; Li, J.; Zhang, Y.; Li, J.; Liu, X.; Shi, X.; Zhao, Q., Preparation of laponite bioceramics for potential bone tissue engineering applications. *PloS one* **2014,** *9* (6), e99585.
24. Gaharwar, A. K.; Kishore, V.; Rivera, C.; Bullock, W.; Wu, C. J.; Akkus, O.; Schmidt, G., Physically Crosslinked Nanocomposites from Silicate-Crosslinked PEO: Mechanical Properties and Osteogenic Differentiation of Human Mesenchymal Stem Cells. *Macromolecular Bioscience* **2012,** *12* (6), 779-793.
25. Paul, A.; Manoharan, V.; Krafft, D.; Assmann, A.; Uquillas, J. A.; Shin, S. R.; Hasan, A.; Hussain, M. A.; Memic, A.; Gaharwar, A. K., Nanoengineered biomimetic hydrogels for guiding human stem cell osteogenesis in three dimensional microenvironments. *Journal of Materials Chemistry B* **2016,** *4* (20), 3544-3554.

26. Zhai, X.; Ma, Y.; Hou, C.; Gao, F.; Zhang, Y.; Ruan, C.; Pan, H.; Lu, W. W.; Liu, W., 3D-printed high strength bioactive supramolecular polymer/clay nanocomposite hydrogel scaffold for bone regeneration. *ACS Biomaterials Science & Engineering* **2017,** *3* (6), 1109-1118.
27. Zhang, E.; Wang, T.; Lian, C.; Sun, W.; Liu, X.; Tong, Z., Robust and thermo-response graphene–PNIPAm hybrid hydrogels reinforced by hectorite clay. *Carbon* **2013,** *62*, 117-126.
28. Kumar, A.; Zo, S. M.; Kim, J. H.; Kim, S.-C.; Han, S. S., Enhanced physical, mechanical, and cytocompatibility behavior of polyelectrolyte complex hydrogels by reinforcing halloysite nanotubes and graphene oxide. *Composites Science and Technology* **2019,** *175*, 35-45.
29. Geim, A. K., Graphene: status and prospects. *Science* **2009,** *324* (5934), 1530-1534.
30. Dubey, N.; Bentini, R.; Islam, I.; Cao, T.; Castro Neto, A. H.; Rosa, V., Graphene: A Versatile Carbon-Based Material for Bone Tissue Engineering. *Stem Cells International* **2015**, 1-12.
31. Goenka, S.; Sant, V.; Sant, S., Graphene-based nanomaterials for drug delivery and tissue engineering. *J. Control. Release* **2014,** *173*, 75-88.
32. Banerjee, A. N., Graphene and its derivatives as biomedical materials: future prospects and challenges. *Interface Focus* **2018,** *8* (3), 20170056.
33. Lu, J.; He, Y. S.; Cheng, C.; Wang, Y.; Qiu, L.; Li, D.; Zou, D., Self-supporting graphene hydrogel film as an experimental platform to evaluate the potential of graphene for bone regeneration. *Advanced Functional Materials* **2013,** *23* (28), 3494-3502.
34. Lee, W. C.; Lim, C. H. Y.; Shi, H.; Tang, L. A.; Wang, Y.; Lim, C. T.; Loh, K. P., Origin of enhanced stem cell growth and differentiation on graphene and graphene oxide. *ACS Nano* **2011,** *5* (9), 7334-7341.
35. Akhavan, O.; Ghaderi, E.; Shahsavar, M., Graphene nanogrids for selective and fast osteogenic differentiation of human mesenchymal stem cells. *Carbon* **2013,** *59*, 200-211.
36. Nayak, T. R.; Andersen, H.; Makam, V. S.; Khaw, C.; Bae, S.; Xu, X.; Ee, P.-L. R.; Ahn, J.-H.; Hong, B. H.; Pastorin, G., Graphene for controlled and accelerated osteogenic differentiation of human mesenchymal stem cells. *ACS Nano* **2011,** *5* (6), 4670-4678.
37. Kalbacova, M.; Broz, A.; Kong, J.; Kalbac, M., Graphene substrates promote adherence of human osteoblasts and mesenchymal stromal cells. *Carbon* **2010,** *48* (15), 4323-4329.
38. Borghi, F. F.; Bean, P. A.; Evans, M. D. M.; van der Laan, T.; Kumar, S.; Ostrikov, K., Nanostructured Graphene Surfaces Promote Different Stages of Bone Cell Differentiation. *Nano-Micro Lett.* **2018,** *10* (3), 12.
39. Yu, X.; Doroghazi, J. R.; Janga, S. C.; Zhang, J. K.; Circello, B.; Griffin, B. M.; Labeda, D. P.; Metcalf, W. W., Diversity and abundance of phosphonate biosynthetic genes in nature. *Proceedings of the National Academy of Sciences* **2013,** *110* (51), 20759-20764.
40. McClung, M.; Harris, S. T.; Miller, P. D.; Bauer, D. C.; Davison, K. S.; Dian, L.; Hanley, D. A.; Kendler, D. L.; Yuen, C. K.; Lewiecki, E. M., Bisphosphonate therapy for osteoporosis: benefits, risks, and drug holiday. *The American journal of medicine* **2013,** *126* (1), 13-20.
41. Pertusat, F.; Serpi, M.; McGuigan, C., Medicinal chemistry of nucleoside phosphonate prodrugs for antiviral therapy. *Antiviral Chemistry and Chemotherapy* **2012,** *22* (5), 181-203.
42. Bassi, A.; Gough, J.; Downes, S., A novel phosphonate for the repair of critical size bone defects. *Journal of Tissue Engineering and Regenerative Medicine* **2012,** *6* (10), 833-840.
43. Dey, R. E.; Zhong, X.; Youle, P. J.; Wang, Q. G.; Wimpenny, I.; Downes, S.; Hoyland, J. A.; Watts, D. C.; Gough, J. E.; Budd, P. M., Synthesis and Characterization of Poly (vinylphosphonic acid-*co*-acrylic acid) Copolymers for Application in Bone Tissue Scaffolds. *Macromolecules* **2016,** *49* (7), 2656-2662.
44. Dey, R. E.; Wimpenny, I.; Gough, J. E.; Watts, D. C.; Budd, P. M., Poly(vinylphosphonic acid-co-acrylic acid) hydrogels: The effect of copolymer composition on osteoblast adhesion and proliferation. *J Biomed Mater Res A* **2018,** *106* (1), 255-264.
45. Khurana, J. S.; Safadi, F. F., Bone structure, development and bone biology. In *Essentials in Bone and Soft-Tissue Pathology*, Springer: 2010; pp 1-15.

46. Markel, M. D., Bone structure and the response of bone to stress. *Equine fracture repair* **2019**, 1-11.
47. Sikavitsas, V. I.; Temenoff, J. S.; Mikos, A. G., Biomaterials and bone mechanotransduction. *Biomaterials* **2001,** *22* (19), 2581-2593.
48. Velasco, M. A.; Narváez-Tovar, C. A.; Garzón-Alvarado, D. A., Design, materials, and mechanobiology of biodegradable scaffolds for bone tissue engineering. *BioMed research international* **2015,** *2015*.
49. Bandyopadhyay-Ghosh, S., Bone as a collagen-hydroxyapatite composite and its repair. *Trends Biomater Artif Organs* **2008,** *22* (2), 116-124.
50. Hannink, G.; Arts, J. C., Bioresorbability, porosity and mechanical strength of bone substitutes: what is optimal for bone regeneration? *Injury* **2011,** *42*, S22-S25.
51. Chabanon, M. Multiscale study of a perfusion bioreactor for bone tissue engineering. Ecole Centrale Paris, 2015.
52. Florencio-Silva, R.; Sasso, G. R. d. S.; Sasso-Cerri, E.; Simões, M. J.; Cerri, P. S., Biology of bone tissue: structure, function, and factors that influence bone cells. *BioMed research international* **2015,** *2015*.
53. Capulli, M.; Paone, R.; Rucci, N., Osteoblast and osteocyte: games without frontiers. *Archives of biochemistry and biophysics* **2014,** *561*, 3-12.
54. Ott, S. M., Bone Remodeling. In *Encyclopedia of Endocrine Diseases (Second Edition)*, Huhtaniemi, I.; Martini, L., Eds. Academic Press: Oxford, 2018; pp 10-18.
55. Arboleya, L.; Castañeda, S., Osteoimmunology: the study of the relationship between the immune system and bone tissue. *Reumatología Clínica (English Edition)* **2013,** *9* (5), 303-315.
56. Amarasekara, D. S.; Kim, S.; Rho, J., Regulation of Osteoblast Differentiation by Cytokine Networks. *International Journal of Molecular Sciences* **2021,** *22* (6), 2851.
57. Chen, D.; Gong, Y.; Xu, L.; Zhou, M.; Li, J.; Song, J., Bidirectional regulation of osteogenic differentiation by the FOXO subfamily of Forkhead transcription factors in mammalian MSCs. *Cell Proliferation* **2019,** *52* (2), e12540.
58. Prideaux, M.; Findlay, D. M.; Atkins, G. J., Osteocytes: the master cells in bone remodelling. *Current opinion in pharmacology* **2016,** *28*, 24-30.
59. Zhao, Q.; Shao, J.; Chen, W.; Li, Y.-P., Osteoclast differentiation and gene regulation. *Frontiers in bioscience : a journal and virtual library* **2007,** *12*, 2519-29.
60. Howard, G. A.; Bottemiller, B. L.; Turner, R. T.; Rader, J. I.; Baylink, D. J., Parathyroid hormone stimulates bone formation and resorption in organ culture: evidence for a coupling mechanism. *Proceedings of the National Academy of Sciences* **1981,** *78* (5), 3204-3208.
61. Setiawati, R.; Rahardjo, P., Bone Development and Growth. In *Osteogenesis and bone regeneration*, IntechOpen: 2018.
62. Mackie, E. J.; Ahmed, Y. A.; Tatarczuch, L.; Chen, K. S.; Mirams, M., Endochondral ossification: How cartilage is converted into bone in the developing skeleton. *The International Journal of Biochemistry & Cell Biology* **2008,** *40* (1), 46-62.
63. Katsimbri, P., The biology of normal bone remodelling. *European journal of cancer care* **2017,** *26* (6), e12740.
64. Kohli, N.; Ho, S.; Brown, S. J.; Sawadkar, P.; Sharma, V.; Snow, M.; García-Gareta, E., Bone remodelling in vitro: Where are we headed?:-A review on the current understanding of physiological bone remodelling and inflammation and the strategies for testing biomaterials in vitro. *Bone* **2018,** *110*, 38-46.
65. Schindeler, A.; McDonald, M. M.; Bokko, P.; Little, D. G. In *Bone remodeling during fracture repair: The cellular picture*, Seminars in cell & developmental biology, Elsevier: 2008; pp 459-466.
66. Marsell, R.; Einhorn, T. A., The biology of fracture healing. *Injury* **2011,** *42* (6), 551-555.
67. Jahagirdar, R.; Scammell, B. E., Principles of fracture healing and disorders of bone union. *Surgery (Oxford)* **2009,** *27* (2), 63-69.

68. Marongiu, G.; Dolci, A.; Verona, M.; Capone, A., The biology and treatment of acute long-bones diaphyseal fractures: Overview of the current options for bone healing enhancement. *Bone reports* **2020,** *12*, 100249.
69. Einhorn, T. A.; Gerstenfeld, L. C., Fracture healing: mechanisms and interventions. *Nature Reviews Rheumatology* **2015,** *11* (1), 45.
70. Taljanovic, M. S.; Jones, M. D.; Ruth, J. T.; Benjamin, J. B.; Sheppard, J. E.; Hunter, T. B., Fracture fixation. *Radiographics* **2003,** *23* (6), 1569-1590.
71. Kazmers, N. H.; Fragomen, A. T.; Rozbruch, S. R., Prevention of pin site infection in external fixation: a review of the literature. *Strategies in Trauma and Limb Reconstruction* **2016,** *11* (2), 75-85.
72. Wang, W.; Yeung, K. W., Bone grafts and biomaterials substitutes for bone defect repair: A review. *Bioactive materials* **2017,** *2* (4), 224-247.
73. Roberts, T. T.; Rosenbaum, A. J., Bone grafts, bone substitutes and orthobiologics: the bridge between basic science and clinical advancements in fracture healing. *Organogenesis* **2012,** *8* (4), 114-124.
74. Albrektsson, T.; Johansson, C., Osteoinduction, osteoconduction and osseointegration. *European spine journal* **2001,** *10* (2), S96-S101.
75. Shrivats, A. R.; McDermott, M. C.; Hollinger, J. O., Bone tissue engineering: state of the union. *Drug discovery today* **2014,** *19* (6), 781-786.
76. Carson, J. S.; Bostrom, M. P. G., Synthetic bone scaffolds and fracture repair. *Injury* **2007,** *38* (1, Supplement), S33-S37.
77. Huan, Z.; Chang, J., Self-setting properties and in vitro bioactivity of calcium sulfate hemihydrate–tricalcium silicate composite bone cements. *Acta Biomaterialia* **2007,** *3* (6), 952-960.
78. Hing, K. A.; Wilson, L. F.; Buckland, T., Comparative performance of three ceramic bone graft substitutes. *The Spine Journal* **2007,** *7* (4), 475-490.
79. Niu, C.-C.; Tsai, T.-T.; Fu, T.-S.; Lai, P.-L.; Chen, L.-H.; Chen, W.-J., A comparison of posterolateral lumbar fusion comparing autograft, autogenous laminectomy bone with bone marrow aspirate, and calcium sulfate with bone marrow aspirate: a prospective randomized study. *Spine* **2009,** *34* (25), 2715-2719.
80. Marongiu, G.; Verona, M.; Cardoni, G.; Capone, A., Synthetic Bone Substitutes and Mechanical Devices for the Augmentation of Osteoporotic Proximal Humeral Fractures: A Systematic Review of Clinical Studies. *Journal of Functional Biomaterials* **2020,** *11* (2), 29.
81. Ferguson, J.; Diefenbeck, M.; McNally, M., Ceramic biocomposites as biodegradable antibiotic carriers in the treatment of bone infections. *Journal of bone and joint infection* **2017,** *2* (1), 38.
82. Sugawara, A.; Asaoka, K.; Ding, S.-J., Calcium phosphate-based cements: clinical needs and recent progress. *Journal of Materials Chemistry B* **2013,** *1* (8), 1081-1089.
83. Jones, J. R., Review of bioactive glass: From Hench to hybrids. *Acta Biomaterialia* **2013,** *9* (1), 4457-4486.
84. Dimitriou, R.; Jones, E.; McGonagle, D.; Giannoudis, P. V., Bone regeneration: current concepts and future directions. *BMC medicine* **2011,** *9* (1), 1-10.
85. Hench, L. L., The story of Bioglass®. *Journal of Materials Science: Materials in Medicine* **2006,** *17* (11), 967-978.
86. Vacanti, C. A., History of tissue engineering and a glimpse into its future. *Tissue engineering* **2006,** *12* (5), 1137-1142.
87. Murphy, C. M.; O'Brien, F. J.; Little, D. G.; Schindeler, A., Cell-scaffold interactions in the bone tissue engineering triad. **2013**.
88. Seong, J. M.; Kim, B.-C.; Park, J.-H.; Kwon, I. K.; Mantalaris, A.; Hwang, Y.-S., Stem cells in bone tissue engineering. *Biomedical materials* **2010,** *5* (6), 062001.
89. Jayakumar, P.; Di Silvio, L., Osteoblasts in bone tissue engineering. *Proceedings of the Institution of Mechanical Engineers, Part H: Journal of Engineering in Medicine* **2010,** *224* (12), 1415-1440.

90. D'ippolito, G.; Schiller, P. C.; Ricordi, C.; Roos, B. A.; Howard, G. A., Age-related osteogenic potential of mesenchymal stromal stem cells from human vertebral bone marrow. *Journal of bone and mineral research* **1999,** *14* (7), 1115-1122.
91. Zaim, M.; Karaman, S.; Cetin, G.; Isik, S., Donor age and long-term culture affect differentiation and proliferation of human bone marrow mesenchymal stem cells. *Annals of hematology* **2012,** *91* (8), 1175-1186.
92. Kartsogiannis, V.; Ng, K. W., Cell lines and primary cell cultures in the study of bone cell biology. *Molecular and cellular endocrinology* **2004,** *228* (1-2), 79-102.
93. Czekanska, E. M.; Stoddart, M. J.; Ralphs, J. R.; Richards, R.; Hayes, J., A phenotypic comparison of osteoblast cell lines versus human primary osteoblasts for biomaterials testing. *Journal of biomedical materials research Part A* **2014,** *102* (8), 2636-2643.
94. Alonzo, M.; Primo, F. A.; Kumar, S. A.; Mudloff, J. A.; Dominguez, E.; Fregoso, G.; Ortiz, N.; Weiss, W. M.; Joddar, B., Bone tissue engineering techniques, advances and scaffolds for treatment of bone defects. *Current Opinion in Biomedical Engineering* **2020**, 100248.
95. Bose, S.; Roy, M.; Bandyopadhyay, A., Recent advances in bone tissue engineering scaffolds. *Trends in biotechnology* **2012,** *30* (10), 546-554.
96. Eliaz, N., Corrosion of metallic biomaterials: A review. *Materials* **2019,** *12* (3), 407.
97. Drosos, G. I.; Kazakos, K. I.; Kouzoumpasis, P.; Verettas, D.-A., Safety and efficacy of commercially available demineralised bone matrix preparations: A critical review of clinical studies. *Injury* **2007,** *38*, S13-S21.
98. Zhang, L.-Y.; Bi, Q.; Zhao, C.; Chen, J.-Y.; Cai, M.-H.; Chen, X.-Y., Recent Advances in Biomaterials for the Treatment of Bone Defects. *Organogenesis* **2020**, 1-13.
99. Afifi, A. M.; Gordon, C. R.; Pryor, L. S.; Sweeney, W.; Papay, F. A.; Zins, J. E., Calcium phosphate cements in skull reconstruction: a meta-analysis. *Plastic and reconstructive surgery* **2010,** *126* (4), 1300-1309.
100. Liu, X.; Ma, P. X., Polymeric scaffolds for bone tissue engineering. *Annals of biomedical engineering* **2004,** *32* (3), 477-486.
101. Li, Z.; Du, T.; Ruan, C.; Niu, X., Bioinspired mineralized collagen scaffolds for bone tissue engineering. *Bioactive Materials* **2020,** *6* (5), 1491-1511.
102. Wang, Y.; Qian, J.; Zhao, N.; Liu, T.; Xu, W.; Suo, A., Novel hydroxyethyl chitosan/cellulose scaffolds with bubble-like porous structure for bone tissue engineering. *Carbohydrate polymers* **2017,** *167*, 44-51.
103. Venkatesan, J.; Bhatnagar, I.; Manivasagan, P.; Kang, K.-H.; Kim, S.-K., Alginate composites for bone tissue engineering: a review. *International journal of biological macromolecules* **2015,** *72*, 269-281.
104. Patterson, J.; Siew, R.; Herring, S. W.; Lin, A. S. P.; Guldberg, R.; Stayton, P. S., Hyaluronic acid hydrogels with controlled degradation properties for oriented bone regeneration. *Biomaterials* **2010,** *31* (26), 6772-6781.
105. Yao, Q. Q.; Cosme, J. G. L.; Xu, T.; Miszuk, J. M.; Picciani, P. H. S.; Fong, H.; Sun, H. L., Three dimensional electrospun PCL/PLA blend nanofibrous scaffolds with significantly improved stem cells osteogenic differentiation and cranial bone formation. *Biomaterials* **2017,** *115*, 115-127.
106. Yoneda, M.; Terai, H.; Imai, Y.; Okada, T.; Nozaki, K.; Inoue, H.; Miyamoto, S.; Takaoka, K., Repair of an intercalated long bone defect with a synthetic biodegradable bone-inducing implant. *Biomaterials* **2005,** *26* (25), 5145-5152.
107. Lin, Y.-J.; Hsu, F.-C.; Chou, C.-W.; Wu, T.-H.; Lin, H.-R., Poly (acrylic acid)–chitosan–silica hydrogels carrying platelet gels for bone defect repair. *Journal of Materials Chemistry B* **2014,** *2* (47), 8329-8337.
108. Skaalure, S. C.; Chu, S.; Bryant, S. J., An Enzyme-Sensitive PEG Hydrogel Based on Aggrecan Catabolism for Cartilage Tissue Engineering. *Advanced Healthcare Materials* **2015,** *4* (3), 12.
109. Marzec, M.; Kucińska-Lipka, J.; Kalaszczyńska, I.; Janik, H., Development of polyurethanes for bone repair. *Materials Science and Engineering: C* **2017,** *80*, 736-747.

110. Fassina, L.; Visai, L.; Benazzo, F.; Benedetti, L.; Calligaro, A.; De Angelis, M. G. C.; Farina, A.; Maliardi, V.; Magenes, G., Effects of electromagnetic stimulation on calcified matrix production by SAOS-2 cells over a polyurethane porous scaffold. *Tissue Engineering* **2006,** *12* (7), 1985-1999.
111. Cortizo, M. S.; Belluzo, M. S., Biodegradable polymers for bone tissue engineering. In *Industrial Applications of Renewable Biomass Products*, Springer: 2017; pp 47-74.
112. Webb, J.; Spencer, R., The role of polymethylmethacrylate bone cement in modern orthopaedic surgery. *The Journal of bone and joint surgery. British volume* **2007,** *89* (7), 851-857.
113. Yu, P.; Bao, R.-Y.; Shi, X.-J.; Yang, W.; Yang, M.-B., Self-assembled high-strength hydroxyapatite/graphene oxide/chitosan composite hydrogel for bone tissue engineering. *Carbohydrate Polymers* **2017,** *155*, 507-515.
114. Kim, H. L.; Jung, G. Y.; Yoon, J. H.; Han, J. S.; Park, Y. J.; Kim, D. G.; Zhang, M. Q.; Kim, D. J., Preparation and characterization of nano-sized hydroxyapatite/alginate/chitosan composite scaffolds for bone tissue engineering. *Mater. Sci. Eng. C-Mater. Biol. Appl.* **2015,** *54*, 20-25.
115. Li, B.; Webster, T., *Orthopedic Biomaterials: Progress in Biology, Manufacturing, and Industry Perspectives*. Springer: 2018.
116. Zhang, L.; Webster, T. J., Nanotechnology and nanomaterials: Promises for improved tissue regeneration. *Nano Today* **2009,** *4* (1), 66-80.
117. Venkatesan, J.; Pallela, R.; Kim, S.-K., Applications of carbon nanomaterials in bone tissue engineering. *Journal of biomedical nanotechnology* **2014,** *10* (10), 3105-3123.
118. Dawson, J. I.; Oreffo, R. O., Clay: new opportunities for tissue regeneration and biomaterial design. *Advanced Materials* **2013,** *25* (30), 4069-4086.
119. Abbasi, N.; Hamlet, S.; Love, R. M.; Nguyen, N.-T., Porous scaffolds for bone regeneration. *Journal of Science: Advanced Materials and Devices* **2020,** *5* (1), 1-9.
120. Liu, M.; Zeng, X.; Ma, C.; Yi, H.; Ali, Z.; Mou, X. B.; Li, S.; Deng, Y.; He, N. Y., Injectable hydrogels for cartilage and bone tissue engineering. *Bone Res.* **2017,** *5*, 20.
121. Yamada, K. M.; Sixt, M., Mechanisms of 3D cell migration. *Nature Reviews Molecular Cell Biology* **2019,** *20* (12), 738-752.
122. Gardel, M. L.; Schneider, I. C.; Aratyn-Schaus, Y.; Waterman, C. M., Mechanical integration of actin and adhesion dynamics in cell migration. *Annual review of cell and developmental biology* **2010,** *26*, 315-333.
123. Tschumperlin, D. J., Fibroblasts and the ground they walk on. *Physiology* **2013,** *28* (6), 380-390.
124. Wu, P.-H.; Gilkes, D. M.; Wirtz, D., The biophysics of 3D cell migration. *Annual Review of Biophysics* **2018,** *47*, 549-567.
125. Wilson, C. J.; Clegg, R. E.; Leavesley, D. I.; Pearcy, M. J., Mediation of biomaterial–cell interactions by adsorbed proteins: a review. *Tissue Engineering* **2005,** *11* (1-2), 1-18.
126. Phillips, J. E.; Petrie, T. A.; Creighton, F. P.; García, A. J., Human mesenchymal stem cell differentiation on self-assembled monolayers presenting different surface chemistries. *Acta Biomaterialia* **2010,** *6* (1), 12-20.
127. Best, J. P.; Javed, S.; Richardson, J. J.; Cho, K. L.; Kamphuis, M. M.; Caruso, F., Stiffness-mediated adhesion of cervical cancer cells to soft hydrogel films. *Soft Matter* **2013,** *9* (18), 4580-4584.
128. M. Jonker, A.; A. Bode, S.; H. Kusters, A.; van Hest, J. C. M.; Löwik, D. W. P. M., Soft PEG-Hydrogels with Independently Tunable Stiffness and RGDS-Content for Cell Adhesion Studies. *Macromolecular Bioscience* **2015,** *15* (10), 1338-1347.
129. Missirlis, D.; Spatz, J. P., Combined Effects of PEG Hydrogel Elasticity and Cell-Adhesive Coating on Fibroblast Adhesion and Persistent Migration. *Biomacromolecules* **2014,** *15* (1), 195-205.
130. Kuo, C. H. R.; Xian, J.; Brenton, J. D.; Franze, K.; Sivaniah, E., Complex stiffness gradient substrates for studying mechanotactic cell migration. *Advanced materials* **2012,** *24* (45), 6059-6064.
131. Cheng, S.-Y.; Heilman, S.; Wasserman, M.; Archer, S.; Shuler, M. L.; Wu, M., A hydrogel-based microfluidic device for the studies of directed cell migration. *Lab on a Chip* **2007,** *7* (6), 763-769.

132. Movilla, N.; Borau, C.; Valero, C.; García-Aznar, J., Degradation of extracellular matrix regulates osteoblast migration: a microfluidic-based study. *Bone* **2018,** *107*, 10-17.
133. Vu, L. T.; Jain, G.; Veres, B. D.; Rajagopalan, P., Cell migration on planar and three-dimensional matrices: a hydrogel-based perspective. *Tissue Engineering Part B: Reviews* **2015,** *21* (1), 67-74.
134. Heath, J. P.; Peachey, L. D., Morphology of fibroblasts in collagen gels: a study using 400 keV electron microscopy and computer graphics. *Cell motility and the cytoskeleton* **1989,** *14* (3), 382-392.
135. Ho, S. S.; Keown, A. T.; Addison, B.; Leach, J. K., Cell migration and bone formation from mesenchymal stem cell spheroids in alginate hydrogels are regulated by adhesive ligand density. *Biomacromolecules* **2017,** *18* (12), 4331-4340.
136. Gadea, G.; de Toledo, M.; Anguille, C.; Roux, P., Loss of p53 promotes RhoA–ROCK-dependent cell migration and invasion in 3D matrices. *The Journal of cell biology* **2007,** *178* (1), 23-30.
137. Doyle, A. D.; Carvajal, N.; Jin, A.; Matsumoto, K.; Yamada, K. M., Local 3D matrix microenvironment regulates cell migration through spatiotemporal dynamics of contractility-dependent adhesions. *Nature Communications* **2015,** *6* (1), 8720.
138. Uchihashi, K.; Aoki, S.; Matsunobu, A.; Toda, S., Osteoblast migration into type I collagen gel and differentiation to osteocyte-like cells within a self-produced mineralized matrix: A novel system for analyzing differentiation from osteoblast to osteocyte. *Bone* **2013,** *52* (1), 102-110.
139. Ehrbar, M.; Sala, A.; Lienemann, P.; Ranga, A.; Mosiewicz, K.; Bittermann, A.; Rizzi, S.; Weber, F. E.; Lutolf, M., Elucidating the role of matrix stiffness in 3D cell migration and remodeling. *Biophysical journal* **2011,** *100* (2), 284-293.
140. Hou, Q.; Paul, A.; Shakesheff, K. M., Injectable scaffolds for tissue regeneration. *Journal of Materials Chemistry* **2004,** *14* (13), 1915-1923.
141. Kretlow, J. D.; Klouda, L.; Mikos, A. G., Injectable matrices and scaffolds for drug delivery in tissue engineering. *Advanced drug delivery reviews* **2007,** *59* (4-5), 263-273.
142. Salem, A. K.; Rose, F. R.; Oreffo, R. O.; Yang, X.; Davies, M. C.; Mitchell, J. R.; Roberts, C. J.; Stolnik-Trenkic, S.; Tendler, S. J.; Williams, P. M., Porous polymer and cell composites that self-assemble in situ. *Advanced Materials* **2003,** *15* (3), 210-213.
143. Wu, J.; Chen, Q.; Deng, C.; Xu, B.; Zhang, Z.; Yang, Y.; Lu, T., Exquisite design of injectable Hydrogels in Cartilage Repair. *Theranostics* **2020,** *10* (21), 9843-9864.
144. Zhu, W.; Liu, Y.-W.; Zhou, L.-Z.; Weng, X.-S., Strategy of injectable hydrogel and its application in tissue engineering. *Chinese Medical Journal* **2021,** *134* (3), 275-277.
145. Wintermantel, E.; Mayer, J.; Blum, J.; Eckert, K.-L.; Lüscher, P.; Mathey, M., Tissue engineering scaffolds using superstructures. *Biomaterials* **1996,** *17* (2), 83-91.
146. Slaughter, B. V.; Khurshid, S. S.; Fisher, O. Z.; Khademhosseini, A.; Peppas, N. A., Hydrogels in regenerative medicine. *Advanced materials* **2009,** *21* (32-33), 3307-3329.
147. Lee, K. Y.; Mooney, D. J., Hydrogels for tissue engineering. *Chemical reviews* **2001,** *101* (7), 1869-1880.
148. Novosel, E. C.; Kleinhans, C.; Kluger, P. J., Vascularization is the key challenge in tissue engineering. *Advanced Drug Delivery Reviews* **2011,** *63* (4), 300-311.
149. Williams, D. F., *The Williams dictionary of biomaterials*. Liverpool University Press: 1999.
150. Sivashanmugam, A.; Kumar, R. A.; Priya, M. V.; Nair, S. V.; Jayakumar, R., An overview of injectable polymeric hydrogels for tissue engineering. *European Polymer Journal* **2015,** *72*, 543-565.
151. Bryant, S. J.; Nuttelman, C. R.; Anseth, K. S., Cytocompatibility of UV and visible light photoinitiating systems on cultured NIH/3T3 fibroblasts in vitro. *Journal of Biomaterials Science, Polymer Edition* **2000,** *11* (5), 439-457.
152. Mironi-Harpaz, I.; Wang, D. Y.; Venkatraman, S.; Seliktar, D., Photopolymerization of cell-encapsulating hydrogels: Crosslinking efficiency versus cytotoxicity. *Acta Biomaterialia* **2012,** *8* (5), 1838-1848.
153. Shin, H.; Temenoff, J. S.; Mikos, A. G., In vitro cytotoxicity of unsaturated oligo [poly (ethylene glycol) fumarate] macromers and their cross-linked hydrogels. *Biomacromolecules* **2003,** *4* (3), 552-560.

154. Hulbert, S.; Young, F.; Mathews, R.; Klawitter, J.; Talbert, C.; Stelling, F., Potential of ceramic materials as permanently implantable skeletal prostheses. *Journal of biomedical materials research* **1970,** *4* (3), 433-456.
155. Cheng, M.-q.; Wahafu, T.; Jiang, G.-f.; Liu, W.; Qiao, Y.-q.; Peng, X.-c.; Cheng, T.; Zhang, X.-l.; He, G.; Liu, X.-y., A novel open-porous magnesium scaffold with controllable microstructures and properties for bone regeneration. *Scientific reports* **2016,** *6* (1), 1-14.
156. Karageorgiou, V.; Kaplan, D., Porosity of 3D biomaterial scaffolds and osteogenesis. *Biomaterials* **2005,** *26* (27), 5474-5491.
157. He, D.; Zhao, A. S.; Su, H.; Zhang, Y.; Wang, Y. N.; Luo, D.; Gao, Y.; Li, J. A.; Yang, P., An injectable scaffold based on temperature-responsive hydrogel and factor-loaded nanoparticles for application in vascularization in tissue engineering. *Journal of Biomedical Materials Research Part A* **2019,** *107* (10), 2123-2134.
158. Peyton, S. R.; Kalcioglu, Z. I.; Cohen, J. C.; Runkle, A. P.; Van Vliet, K. J.; Lauffenburger, D. A.; Griffith, L. G., Marrow-Derived stem cell motility in 3D synthetic scaffold is governed by geometry along with adhesivity and stiffness. *Biotechnology and bioengineering* **2011,** *108* (5), 1181-1193.
159. Ashworth, J. C.; Mehr, M.; Buxton, P. G.; Best, S. M.; Cameron, R. E., Optimising collagen scaffold architecture for enhanced periodontal ligament fibroblast migration. *Journal of Materials Science: Materials in Medicine* **2018,** *29* (11), 166.
160. Harley, B. A. C.; Kim, H.-D.; Zaman, M. H.; Yannas, I. V.; Lauffenburger, D. A.; Gibson, L. J., Microarchitecture of Three-Dimensional Scaffolds Influences Cell Migration Behavior via Junction Interactions. *Biophysical Journal* **2008,** *95* (8), 4013-4024.
161. Huang, S.; Ingber, D. E., The structural and mechanical complexity of cell-growth control. *Nature cell biology* **1999,** *1* (5), E131-E138.
162. Žigon-Branc, S.; Markovic, M.; Van Hoorick, J.; Van Vlierberghe, S.; Dubruel, P.; Zerobin, E.; Baudis, S.; Ovsianikov, A., Impact of hydrogel stiffness on differentiation of human adipose-derived stem cell microspheroids. *Tissue Engineering Part A* **2019,** *25* (19-20), 1369-1380.
163. El-Fiqi, A.; Lee, J. H.; Lee, E.-J.; Kim, H.-W., Collagen hydrogels incorporated with surface-aminated mesoporous nanobioactive glass: Improvement of physicochemical stability and mechanical properties is effective for hard tissue engineering. *Acta Biomaterialia* **2013,** *9* (12), 9508-9521.
164. Kikuchi, M.; Itoh, S.; Ichinose, S.; Shinomiya, K.; Tanaka, J., Self-organization mechanism in a bone-like hydroxyapatite/collagen nanocomposite synthesized in vitro and its biological reaction in vivo. *Biomaterials* **2001,** *22* (13), 1705-1711.
165. Lotz, C.; Schmid, F. F.; Oechsle, E.; Monaghan, M. G.; Walles, H.; Groeber-Becker, F., Cross-linked Collagen Hydrogel Matrix Resisting Contraction To Facilitate Full-Thickness Skin Equivalents. *ACS Applied Materials & Interfaces* **2017,** *9* (24), 20417-20425.
166. Yesilyurt, V.; Webber, M. J.; Appel, E. A.; Godwin, C.; Langer, R.; Anderson, D. G., Injectable self-healing glucose-responsive hydrogels with pH-regulated mechanical properties. *Advanced materials* **2016,** *28* (1), 86-91.
167. Alarçin, E.; Lee, T. Y.; Karuthedom, S.; Mohammadi, M.; Brennan, M. A.; Lee, D. H.; Marrella, A.; Zhang, J.; Syla, D.; Zhang, Y. S., Injectable shear-thinning hydrogels for delivering osteogenic and angiogenic cells and growth factors. *Biomaterials science* **2018,** *6* (6), 1604-1615.
168. Zheng, Y.; Liang, Y.; Zhang, D.; Sun, X.; Liang, L.; Li, J.; Liu, Y.-N., Gelatin-based hydrogels blended with gellan as an injectable wound dressing. *ACS omega* **2018,** *3* (5), 4766-4775.
169. Kanczler, J. M.; Wells, J. A.; Gibbs, D. M. R.; Marshall, K. M.; Tang, D. K. O.; Oreffo, R. O. C., Chapter 50 - Bone tissue engineering and bone regeneration. In *Principles of Tissue Engineering (Fifth Edition)*, Lanza, R.; Langer, R.; Vacanti, J. P.; Atala, A., Eds. Academic Press: 2020; pp 917-935.
170. Golafshan, N.; Rezahasani, R.; Esfahani, M. T.; Kharaziha, M.; Khorasani, S., Nanohybrid hydrogels of laponite: PVA-Alginate as a potential wound healing material. *Carbohydrate polymers* **2017,** *176*, 392-401.
171. Whitaker, M.; Quirk, R.; Howdle, S.; Shakesheff, K., Growth factor release from tissue engineering scaffolds. *Journal of Pharmacy and Pharmacology* **2001,** *53* (11), 1427-1437.

172. Piantanida, E.; Alonci, G.; Bertucci, A.; De Cola, L., Design of nanocomposite injectable hydrogels for minimally invasive surgery. *Accounts of chemical research* **2019,** *52* (8), 2101-2112.
173. Ajiro, H.; Watanabe, J.; Akashi, M., Cell adhesion and proliferation on poly (N-vinylacetamide) hydrogels and double network approaches for changing cellular affinities. *Biomacromolecules* **2008,** *9* (2), 426-430.
174. Xu, Q.; Zhang, Z.; Xiao, C.; He, C.; Chen, X., Injectable Polypeptide Hydrogel as Biomimetic Scaffolds with Tunable Bioactivity and Controllable Cell Adhesion. *Biomacromolecules* **2017,** *18* (4), 1411-1418.
175. Wohlrab, S.; Müller, S.; Schmidt, A.; Neubauer, S.; Kessler, H.; Leal-Egaña, A.; Scheibel, T., Cell adhesion and proliferation on RGD-modified recombinant spider silk proteins. *Biomaterials* **2012,** *33* (28), 6650-6659.
176. Hu, X.; Wang, Y.; Zhang, L.; Xu, M.; Dong, W.; Zhang, J., Fabrication of Salecan/poly(AMPS-co-HMAA) semi-IPN hydrogels for cell adhesion. *Carbohydrate Polymers* **2017,** *174*, 171-181.
177. Chen, M. H.; Wang, L. L.; Chung, J. J.; Kim, Y.-H.; Atluri, P.; Burdick, J. A., Methods to assess shear-thinning hydrogels for application as injectable biomaterials. *ACS biomaterials science & engineering* **2017,** *3* (12), 3146-3160.
178. Sun, Y.; Nan, D.; Jin, H.; Qu, X., Recent advances of injectable hydrogels for drug delivery and tissue engineering applications. *Polymer Testing* **2020,** *81*, 106283.
179. Yue, S.; He, H.; Li, B.; Hou, T., Hydrogel as a Biomaterial for Bone Tissue Engineering: A Review. *Nanomaterials* **2020,** *10* (8), 1511.
180. Han, C.; Zhang, H.; Wu, Y.; He, X.; Chen, X., Dual-crosslinked hyaluronan hydrogels with rapid gelation and high injectability for stem cell protection. *Scientific reports* **2020,** *10* (1), 1-7.
181. Mather, B. D.; Viswanathan, K.; Miller, K. M.; Long, T. E., Michael addition reactions in macromolecular design for emerging technologies. *Progress in Polymer Science* **2006,** *31* (5), 487-531.
182. Shin, S. R.; Aghaei-Ghareh-Bolagh, B.; Dang, T. T.; Topkaya, S. N.; Gao, X. G.; Yang, S. Y.; Jung, S. M.; Oh, J. H.; Dokmeci, M. R.; Tang, X. W.; Khademhosseini, A., Cell-laden Microengineered and Mechanically Tunable Hybrid Hydrogels of Gelatin and Graphene Oxide. *Advanced Materials* **2013,** *25* (44), 6385-6391.
183. Lee, S.-Y.; Tae, G., Formulation and in vitro characterization of an in situ gelable, photo-polymerizable Pluronic hydrogel suitable for injection. *J. Control. Release* **2007,** *119* (3), 313-319.
184. Clark, E. A.; Alexander, M. R.; Irvine, D. J.; Roberts, C. J.; Wallace, M. J.; Sharpe, S.; Yoo, J.; Hague, R. J. M.; Tuck, C. J.; Wildman, R. D., 3D printing of tablets using inkjet with UV photoinitiation. *International Journal of Pharmaceutics* **2017,** *529* (1), 523-530.
185. Poldervaart, M. T.; Goversen, B.; De Ruijter, M.; Abbadessa, A.; Melchels, F. P.; Öner, F. C.; Dhert, W. J.; Vermonden, T.; Alblas, J., 3D bioprinting of methacrylated hyaluronic acid (MeHA) hydrogel with intrinsic osteogenicity. *PLoS One* **2017,** *12* (6), e0177628.
186. Kurisawa, M.; Lee, F.; Wang, L.-S.; Chung, J. E., Injectable enzymatically crosslinked hydrogel system with independent tuning of mechanical strength and gelation rate for drug delivery and tissue engineering. *Journal of Materials Chemistry* **2010,** *20* (26), 5371-5375.
187. Hu, W.; Wang, Z.; Xiao, Y.; Zhang, S.; Wang, J., Advances in crosslinking strategies of biomedical hydrogels. *Biomaterials science* **2019,** *7* (3), 843-855.
188. Ligorio, C.; Zhou, M.; Wychowaniec, J. K.; Zhu, X.; Bartlam, C.; Miller, A. F.; Vijayaraghavan, A.; Hoyland, J. A.; Saiani, A., Graphene oxide containing self-assembling peptide hybrid hydrogels as a potential 3D injectable cell delivery platform for intervertebral disc repair applications. *Acta Biomaterialia* **2019,** *92*, 92-103.
189. Maeda, T., Structures and Applications of Thermoresponsive Hydrogels and Nanocomposite-Hydrogels Based on Copolymers with Poly (Ethylene Glycol) and Poly (Lactide-Co-Glycolide) Blocks. *Bioengineering* **2019,** *6* (4), 107.
190. Ashraf, S.; Park, H.-K.; Park, H.; Lee, S.-H., Snapshot of phase transition in thermoresponsive hydrogel PNIPAM: Role in drug delivery and tissue engineering. *Macromolecular Research* **2016,** *24* (4), 297-304.

191. Kim, Y. S.; Chien, A. J.; Guo, J. L.; Smith, B. T.; Watson, E.; Pearce, H. A.; Koons, G. L.; Navara, A. M.; Lam, J.; Scott, D. W.; Grande-Allen, K. J.; Mikos, A. G., Chondrogenesis of cocultures of mesenchymal stem cells and articular chondrocytes in poly(L-lysine)-loaded hydrogels. *J. Control. Release* **2020,** *328*, 710-721.
192. Chiu, Y.-L.; Chen, S.-C.; Su, C.-J.; Hsiao, C.-W.; Chen, Y.-M.; Chen, H.-L.; Sung, H.-W., pH-triggered injectable hydrogels prepared from aqueous N-palmitoyl chitosan: in vitro characteristics and in vivo biocompatibility. *Biomaterials* **2009,** *30* (28), 4877-4888.
193. Liang, K.; Bae, K. H.; Kurisawa, M., Recent advances in the design of injectable hydrogels for stem cell-based therapy. *Journal of Materials Chemistry B* **2019,** *7* (24), 3775-3791.
194. Wan, S.; Borland, S.; Richardson, S. M.; Merry, C. L. R.; Saiani, A.; Gough, J. E., Self-assembling peptide hydrogel for intervertebral disc tissue engineering. *Acta Biomaterialia* **2016,** *46*, 29-40.
195. Haines-Butterick, L.; Rajagopal, K.; Branco, M.; Salick, D.; Rughani, R.; Pilarz, M.; Lamm, M. S.; Pochan, D. J.; Schneider, J. P., Controlling hydrogelation kinetics by peptide design for three-dimensional encapsulation and injectable delivery of cells. *Proceedings of the National Academy of Sciences* **2007,** *104* (19), 7791-7796.
196. Xing, R.; Liu, K.; Jiao, T.; Zhang, N.; Ma, K.; Zhang, R.; Zou, Q.; Ma, G.; Yan, X., An injectable self-assembling collagen–gold hybrid hydrogel for combinatorial antitumor photothermal/photodynamic therapy. *Advanced materials* **2016,** *28* (19), 3669-3676.
197. Pupkaite, J.; Rosenquist, J.; Hilborn, J. n.; Samanta, A., Injectable Shape-Holding Collagen Hydrogel for Cell Encapsulation and Delivery Cross-linked Using Thiol-Michael Addition Click Reaction. *Biomacromolecules* **2019,** *20* (9), 3475-3484.
198. Hozumi, T.; Kageyama, T.; Ohta, S.; Fukuda, J.; Ito, T., Injectable hydrogel with slow degradability composed of gelatin and hyaluronic acid cross-linked by Schiff's base formation. *Biomacromolecules* **2018,** *19* (2), 288-297.
199. Feng, Q.; Wei, K.; Lin, S.; Xu, Z.; Sun, Y.; Shi, P.; Li, G.; Bian, L., Mechanically resilient, injectable, and bioadhesive supramolecular gelatin hydrogels crosslinked by weak host-guest interactions assist cell infiltration and in situ tissue regeneration. *Biomaterials* **2016,** *101*, 217-228.
200. Ma, X.; Xu, T.; Chen, W.; Qin, H.; Chi, B.; Ye, Z., Injectable hydrogels based on the hyaluronic acid and poly (γ-glutamic acid) for controlled protein delivery. *Carbohydrate polymers* **2018,** *179*, 100-109.
201. Zhang, R.; Xie, L.; Wu, H.; Yang, T.; Zhang, Q.; Tian, Y.; Liu, Y.; Han, X.; Guo, W.; He, M., Alginate/laponite hydrogel microspheres co-encapsulating dental pulp stem cells and VEGF for endodontic regeneration. *Acta biomaterialia* **2020,** *113*, 305-316.
202. Yan, J.; Miao, Y.; Tan, H.; Zhou, T.; Ling, Z.; Chen, Y.; Xing, X.; Hu, X., Injectable alginate/hydroxyapatite gel scaffold combined with gelatin microspheres for drug delivery and bone tissue engineering. *Materials Science and Engineering: C* **2016,** *63*, 274-284.
203. Wei, Z.; Zhao, J. Y.; Chen, Y. M.; Zhang, P. B.; Zhang, Q. Q., Self-healing polysaccharide-based hydrogels as injectable carriers for neural stem cells. *Scientific Reports* **2016,** *6*, 12.
204. Qu, J.; Zhao, X.; Liang, Y.; Zhang, T.; Ma, P. X.; Guo, B., Antibacterial adhesive injectable hydrogels with rapid self-healing, extensibility and compressibility as wound dressing for joints skin wound healing. *Biomaterials* **2018,** *183*, 185-199.
205. Nojoomi, A.; Tamjid, E.; Simchi, A.; Bonakdar, S.; Stroeve, P., Injectable polyethylene glycol-laponite composite hydrogels as articular cartilage scaffolds with superior mechanical and rheological properties. *International Journal of Polymeric Materials and Polymeric Biomaterials* **2017,** *66* (3), 105-114.
206. Wang, X.; Partlow, B.; Liu, J.; Zheng, Z.; Su, B.; Wang, Y.; Kaplan, D. L., Injectable silk-polyethylene glycol hydrogels. *Acta Biomaterialia* **2015,** *12*, 51-61.
207. Boonlai, W.; Tantishaiyakul, V.; Hirun, N.; Sangfai, T.; Suknuntha, K., Thermosensitive Poloxamer 407/poly (acrylic acid) hydrogels with potential application as injectable drug delivery system. *AAPS PharmSciTech* **2018,** *19* (5), 2103-2117.

208. Niu, Y.; Guo, T.; Yuan, X.; Zhao, Y.; Ren, L., An injectable supramolecular hydrogel hybridized with silver nanoparticles for antibacterial application. *Soft Matter* **2018,** *14* (7), 1227-1234.
209. Zhao, Y.; Li, M.; Liu, B.; Xiang, J.; Cui, Z.; Qu, X.; Qiu, D.; Tian, Y.; Yang, Z., Ultra-tough injectable cytocompatible hydrogel for 3D cell culture and cartilage repair. *Journal of Materials Chemistry B* **2018,** *6* (9), 1351-1358.
210. Cho, S.-H.; Noh, J.-R.; Cho, M. Y.; Go, M.-J.; Kim, Y.-H.; Kang, E. S.; Kim, Y. H.; Lee, C.-H.; Lim, Y. T., An injectable collagen/poly (γ-glutamic acid) hydrogel as a scaffold of stem cells and α-lipoic acid for enhanced protection against renal dysfunction. *Biomaterials science* **2017,** *5* (2), 285-294.
211. Arun Kumar, R.; Sivashanmugam, A.; Deepthi, S.; Iseki, S.; Chennazhi, K. P.; Nair, S. V.; Jayakumar, R., Injectable Chitin-Poly(ε-caprolactone)/Nanohydroxyapatite Composite Microgels Prepared by Simple Regeneration Technique for Bone Tissue Engineering. *ACS Applied Materials & Interfaces* **2015,** *7* (18), 9399-9409.
212. Zhao, J.; Guo, B.; Ma, P. X., Injectable alginate microsphere/PLGA–PEG–PLGA composite hydrogels for sustained drug release. *RSC Advances* **2014,** *4* (34), 17736-17742.
213. Bhatia, S., Natural polymers vs synthetic polymer. In *Natural Polymer Drug Delivery Systems*, Springer: 2016; pp 95-118.
214. Park, S. H.; Park, J. Y.; Ji, Y. B.; Ju, H. J.; Min, B. H.; Kim, M. S., An injectable click-crosslinked hyaluronic acid hydrogel modified with a BMP-2 mimetic peptide as a bone tissue engineering scaffold. *Acta Biomaterialia* **2020,** *117*, 108-120.
215. Huang, C.-T.; Shrestha, L. K.; Ariga, K.; Hsu, S.-h., A graphene–polyurethane composite hydrogel as a potential bioink for 3D bioprinting and differentiation of neural stem cells. *Journal of Materials Chemistry B* **2017,** *5* (44), 8854-8864.
216. Roshanbinfar, K.; Mohammadi, Z.; Mesgar, A. S.-M.; Dehghan, M. M.; Oommen, O. P.; Hilborn, J.; Engel, F. B., Carbon nanotube doped pericardial matrix derived electroconductive biohybrid hydrogel for cardiac tissue engineering. *Biomaterials science* **2019,** *7* (9), 3906-3917.
217. Meng, X. L.; Stout, D. A.; Sun, L. L.; Beingessner, R. L.; Fenniri, H.; Webster, T. J., Novel injectable biomimetic hydrogels with carbon nanofibers and self assembled rosette nanotubes for myocardial applications. *Journal of Biomedical Materials Research Part A* **2013,** *101* (4), 1095-1102.
218. Huang, C.-T.; Kumar Shrestha, L.; Ariga, K.; Hsu, S.-h., A graphene–polyurethane composite hydrogel as a potential bioink for 3D bioprinting and differentiation of neural stem cells. *Journal of Materials Chemistry B* **2017,** *5* (44), 8854-8864.
219. Barnes, H. A.; Hutton, J. F.; Walters, K., *An introduction to rheology*. Elsevier: 1989; Vol. 3.
220. Basics of rheology by Anton Paar. https://wiki.anton-paar.com/uk-en/basics-of-rheology/ (accessed 10th May 2021).
221. A Basic Introduction to Rheology by Malvern Instrument White Paper. https://cdn.technologynetworks.com/TN/Resources/PDF/WP160620BasicIntroRheology.pdf (accessed 11th May 2021).
222. Barnes, H. A., Thixotropy—a review. *Journal of Non-Newtonian fluid mechanics* **1997,** *70* (1-2), 1-33.
223. Mewis, J.; Wagner, N. J., Thixotropy. *Advances in Colloid and Interface Science* **2009,** *147*, 214-227.
224. Zuidema, J. M.; Rivet, C. J.; Gilbert, R. J.; Morrison, F. A., A protocol for rheological characterization of hydrogels for tissue engineering strategies. *Journal of Biomedical Materials Research Part B: Applied Biomaterials* **2014,** *102* (5), 1063-1073.
225. Janmey, P. A.; Georges, P. C.; Hvidt, S., Basic rheology for biologists. *Methods in cell biology* **2007,** *83*, 1-27.
226. Mezger, T. G., *The rheology handbook: for users of rotational and oscillatory rheometers*. Vincentz Network GmbH & Co KG: 2006.
227. Samimi Gharaie, S.; Dabiri, S. M. H.; Akbari, M., Smart shear-thinning hydrogels as injectable drug delivery systems. *Polymers* **2018,** *10* (12), 1317.

228. Teleanu, D. M.; Negut, I.; Grumezescu, V.; Grumezescu, A. M.; Teleanu, R. I., Nanomaterials for Drug Delivery to the Central Nervous System. *Nanomaterials* **2019,** *9* (3), 371.
229. Zhang, D.-X.; Esser, L.; Vasani, R. B.; Thissen, H.; Voelcker, N. H., Porous silicon nanomaterials: recent advances in surface engineering for controlled drug-delivery applications. *Nanomedicine* **2019,** *14* (24), 3213-3230.
230. Fathi-Achachelouei, M.; Knopf-Marques, H.; Ribeiro da Silva, C. E.; Barthès, J.; Bat, E.; Tezcaner, A.; Vrana, N. E., Use of nanoparticles in tissue engineering and regenerative medicine. *Frontiers in bioengineering and biotechnology* **2019,** *7*, 113.
231. Sethu, S. N.; Namashivayam, S.; Devendran, S.; Nagarajan, S.; Tsai, W.-B.; Narashiman, S.; Ramachandran, M.; Ambigapathi, M., Nanoceramics on osteoblast proliferation and differentiation in bone tissue engineering. *International Journal of Biological Macromolecules* **2017,** *98*, 67-74.
232. Nemati, S.; Kim, S.-j.; Shin, Y. M.; Shin, H., Current progress in application of polymeric nanofibers to tissue engineering. *Nano convergence* **2019,** *6* (1), 1-16.
233. Zhang, J.; Chen, H.; Zhao, M.; Liu, G.; Wu, J., 2D nanomaterials for tissue engineering application. *Nano Research* **2020,** *13* (8), 2019-2034.
234. Hu, T.; Mei, X.; Wang, Y.; Weng, X.; Liang, R.; Wei, M., Two-dimensional nanomaterials: fascinating materials in biomedical field. *Science Bulletin* **2019,** *64* (22), 1707-1727.
235. Liu, X.; Miller, A. L.; Park, S.; George, M. N.; Waletzki, B. E.; Xu, H.; Terzic, A.; Lu, L., Two-dimensional black phosphorus and graphene oxide nanosheets synergistically enhance cell proliferation and osteogenesis on 3D printed scaffolds. *ACS applied materials & interfaces* **2019,** *11* (26), 23558-23572.
236. Raucci, M. G.; Fasolino, I.; Caporali, M.; Serrano-Ruiz, M.; Soriente, A.; Peruzzini, M.; Ambrosio, L., Exfoliated black phosphorus promotes in vitro bone regeneration and suppresses osteosarcoma progression through cancer-related inflammation inhibition. *ACS applied materials & interfaces* **2019,** *11* (9), 9333-9342.
237. Chen, Y.-X.; Zhu, R.; Ke, Q.-F.; Gao, Y.-S.; Zhang, C.-Q.; Guo, Y.-P., MgAl layered double hydroxide/chitosan porous scaffolds loaded with PFTα to promote bone regeneration. *Nanoscale* **2017,** *9* (20), 6765-6776.
238. Weng, Q.; Wang, B.; Wang, X.; Hanagata, N.; Li, X.; Liu, D.; Wang, X.; Jiang, X.; Bando, Y.; Golberg, D., Highly water-soluble, porous, and biocompatible boron nitrides for anticancer drug delivery. *ACS nano* **2014,** *8* (6), 6123-6130.
239. Khatoon, N.; Chu, M. Q.; Zhou, C. H., Nanoclay-based drug delivery systems and their therapeutic potentials. *Journal of Materials Chemistry B* **2020,** *8* (33), 7335-7351.
240. Carretero, M. I.; Pozo, M., Clay and non-clay minerals in the pharmaceutical and cosmetic industries Part II. Active ingredients. *Applied Clay Science* **2010,** *47* (3-4), 171-181.
241. Tawari, S. L.; Koch, D. L.; Cohen, C., Electrical double-layer effects on the Brownian diffusivity and aggregation rate of Laponite clay particles. *Journal of Colloid and Interface Science* **2001,** *240* (1), 54-66.
242. Suman, K.; Joshi, Y. M., Microstructure and soft glassy dynamics of an aqueous laponite dispersion. *Langmuir* **2018,** *34* (44), 13079-13103.
243. Marques, F. A. d. M.; Angelini, R.; Ruocco, G.; Ruzicka, B., Isotopic effect on the gel and glass formation of a charged colloidal clay: Laponite. *The Journal of Physical Chemistry B* **2017,** *121* (17), 4576-4582.
244. Suman, K.; Mittal, M.; Joshi, Y. M., Effect of sodium pyrophosphate and understanding microstructure of aqueous LAPONITE® dispersion using dissolution study. *Journal of Physics: Condensed Matter* **2020,** *32* (22), 224002.
245. Becher, T. B.; Braga, C. B.; Bertuzzi, D. L.; Ramos, M. D.; Hassan, A.; Crespilho, F. N.; Ornelas, C., The structure–property relationship in LAPONITE® materials: from Wigner glasses to strong self-healing hydrogels formed by non-covalent interactions. *Soft matter* **2019,** *15* (6), 1278-1289.
246. Savenko, V.; Bulavin, L.; Rawiso, M.; Lebovka, N., Aging of aqueous Laponite dispersions in the presence of sodium polystyrene sulfonate. *arXiv preprint arXiv:1406.2992* **2014**.

247. Mohanty, R. P.; Suman, K.; Joshi, Y. M., In situ ion induced gelation of colloidal dispersion of Laponite: Relating microscopic interactions to macroscopic behavior. *Applied Clay Science* **2017,** *138*, 17-24.
248. Takeno, H.; Nakamura, A., Effects of molecular mass of polymer on mechanical properties of clay/poly (ethylene oxide) blend hydrogels, and comparison between them and clay/sodium polyacrylate blend hydrogels. *Colloid and Polymer Science* **2019,** *297* (4), 641-649.
249. Sheikhi, A.; Afewerki, S.; Oklu, R.; Gaharwar, A. K.; Khademhosseini, A., Effect of ionic strength on shear-thinning nanoclay–polymer composite hydrogels. *Biomaterials science* **2018,** *6* (8), 2073-2083.
250. Swartzen-Allen, S. L.; Matijevic, E., Surface and colloid chemistry of clays. *Chemical Reviews* **1974,** *74* (3), 385-400.
251. Thompson, D. W.; Butterworth, J. T., The nature of laponite and its aqueous dispersions. *Journal of Colloid and Interface Science* **1992,** *151* (1), 236-243.
252. Jatav, S.; Joshi, Y. M., Chemical stability of Laponite in aqueous media. *Applied clay science* **2014,** *97*, 72-77.
253. Mourchid, A.; Levitz, P., Long-term gelation of laponite aqueous dispersions. *Physical Review E* **1998,** *57* (5), R4887.
254. Mohanty, R. P.; Joshi, Y. M., Chemical stability phase diagram of aqueous Laponite dispersions. *Applied Clay Science* **2016,** *119*, 243-248.
255. Gaharwar, A. K.; Mihaila, S. M.; Swami, A.; Patel, A.; Sant, S.; Reis, R. L.; Marques, A. P.; Gomes, M. E.; Khademhosseini, A., Bioactive silicate nanoplatelets for osteogenic differentiation of human mesenchymal stem cells. *Advanced Materials* **2013,** *25* (24), 3329-3336.
256. Carrow, J. K.; Cross, L. M.; Reese, R. W.; Jaiswal, M. K.; Gregory, C. A.; Kaunas, R.; Singh, I.; Gaharwar, A. K., Widespread changes in transcriptome profile of human mesenchymal stem cells induced by two-dimensional nanosilicates. *Proceedings of the National Academy of Sciences* **2018,** *115* (17), E3905-E3913.
257. Li, T.; Liu, Z. L.; Xiao, M.; Yang, Z. Z.; Peng, M. Z.; Di Li, C.; Zhou, X. J.; Wang, J. W., Impact of bone marrow mesenchymal stem cell immunomodulation on the osteogenic effects of laponite. *Stem Cell Research & Therapy* **2018,** *9* (1), 100.
258. Chang, H.-Y.; Huang, C.-C.; Lin, K.-Y.; Kao, W.-L.; Liao, H.-Y.; You, Y.-W.; Lin, J.-H.; Kuo, Y.-T.; Kuo, D.-Y.; Shyue, J.-J., Effect of Surface Potential on NIH3T3 Cell Adhesion and Proliferation. *The Journal of Physical Chemistry C* **2014,** *118* (26), 14464-14470.
259. Sandri, G.; Bonferoni, M.; Rossi, S.; Ferrari, F.; Aguzzi, C.; Viseras, C.; Caramella, C., Clay minerals for tissue regeneration, repair, and engineering. In *Wound Healing Biomaterials*, Elsevier: 2016; pp 385-402.
260. Schexnailder, P. J.; Gaharwar, A. K.; Bartlett II, R. L.; Seal, B. L.; Schmidt, G., Tuning cell adhesion by incorporation of charged silicate nanoparticles as cross-linkers to polyethylene oxide. *Macromolecular bioscience* **2010,** *10* (12), 1416-1423.
261. Gaharwar, A. K.; Schexnailder, P. J.; Kline, B. P.; Schmidt, G., Assessment of using Laponite® cross-linked poly (ethylene oxide) for controlled cell adhesion and mineralization. *Acta biomaterialia* **2011,** *7* (2), 568-577.
262. Haraguchi, K.; Takehisa, T.; Ebato, M., Control of cell cultivation and cell sheet detachment on the surface of polymer/clay nanocomposite hydrogels. *Biomacromolecules* **2006,** *7* (11), 3267-3275.
263. Zreiqat, H.; Howlett, C.; Zannettino, A.; Evans, P.; Schulze-Tanzil, G.; Knabe, C.; Shakibaei, M., Mechanisms of magnesium-stimulated adhesion of osteoblastic cells to commonly used orthopaedic implants. *Journal of Biomedical Materials Research: An Official Journal of The Society for Biomaterials, The Japanese Society for Biomaterials, and The Australian Society for Biomaterials and the Korean Society for Biomaterials* **2002,** *62* (2), 175-184.
264. Zreiqat, H.; Evans, P.; Howlett, C. R., Effect of surface chemical modification of bioceramic on phenotype of human bone-derived cells. *Journal of Biomedical Materials Research: An Official Journal*

of The Society for Biomaterials, The Japanese Society for Biomaterials, and The Australian Society for Biomaterials **1999,** *44* (4), 389-396.
265. Nakai, T.; Mera, Y.; Yasuhara, T.; Ohashi, A., Divalent metal ion-dependent mitochondrial degradation of unassembled subunits 2 and 3 of cytochrome c oxidase. *The Journal of Biochemistry* **1994,** *116* (4), 752-758.
266. Clément-Lacroix, P.; Ai, M.; Morvan, F.; Roman-Roman, S.; Vayssière, B.; Belleville, C.; Estrera, K.; Warman, M. L.; Baron, R.; Rawadi, G., Lrp5-independent activation of Wnt signaling by lithium chloride increases bone formation and bone mass in mice. *Proceedings of the National Academy of Sciences* **2005,** *102* (48), 17406-17411.
267. Clevers, H., Wnt/β-catenin signaling in development and disease. *Cell* **2006,** *127* (3), 469-480.
268. Zhai, W.; Lu, H.; Chen, L.; Lin, X.; Huang, Y.; Dai, K.; Naoki, K.; Chen, G.; Chang, J., Silicate bioceramics induce angiogenesis during bone regeneration. *Acta Biomaterialia* **2012,** *8* (1), 341-349.
269. Reffitt, D.; Ogston, N.; Jugdaohsingh, R.; Cheung, H.; Evans, B. A. J.; Thompson, R.; Powell, J.; Hampson, G., Orthosilicic acid stimulates collagen type 1 synthesis and osteoblastic differentiation in human osteoblast-like cells in vitro. *Bone* **2003,** *32* (2), 127-135.
270. Shen, M.; Li, L.; Sun, Y.; Xu, J.; Guo, X.; Prud'homme, R. K., Rheology and adhesion of poly (acrylic acid)/laponite nanocomposite hydrogels as biocompatible adhesives. *Langmuir* **2014,** *30* (6), 1636-1642.
271. Zhang, Y.; Chen, M.; Dai, Z.; Cao, H.; Li, J.; Zhang, W., Sustained protein therapeutics enabled by self-healing nanocomposite hydrogels for non-invasive bone regeneration. *Biomaterials science* **2020,** *8* (2), 682-693.
272. Gaharwar, A. K.; Avery, R. K.; Assmann, A.; Paul, A.; McKinley, G. H.; Khademhosseini, A.; Olsen, B. D., Shear-thinning nanocomposite hydrogels for the treatment of hemorrhage. *ACS nano* **2014,** *8* (10), 9833-9842.
273. Zou, Y.; Qazvini, N. T.; Zane, K.; Sadati, M.; Wei, Q.; Liao, J.; Fan, J.; Song, D.; Liu, J.; Ma, C., Gelatin-Derived Graphene–Silicate Hybrid Materials Are Biocompatible and Synergistically Promote BMP9-Induced Osteogenic Differentiation of Mesenchymal Stem Cells. *ACS Applied Materials & Interfaces* **2017,** *9* (19), 15922-15932.
274. Arab-Ahmadi, S.; Irani, S.; Bakhshi, H.; Atyabi, F.; Ghalandari, B., Immobilization of carboxymethyl chitosan/laponite on polycaprolactone nanofibers as osteoinductive bone scaffolds. *Polymers for Advanced Technologies* **2021,** *32* (2), 755-765.
275. Atrian, M.; Kharaziha, M.; Emadi, R.; Alihosseini, F., Silk-Laponite® fibrous membranes for bone tissue engineering. *Applied Clay Science* **2019,** *174*, 90-99.
276. Boyer, C.; Figueiredo, L.; Pace, R.; Lesoeur, J.; Rouillon, T.; Le Visage, C.; Tassin, J. F.; Weiss, P.; Guicheux, J.; Rethore, G., Laponite nanoparticle-associated silated hydroxypropylmethyl cellulose as an injectable reinforced interpenetrating network hydrogel for cartilage tissue engineering. *Acta Biomaterialia* **2018,** *65*, 112-122.
277. Page, D. J.; Clarkin, C. E.; Mani, R.; Khan, N. A.; Dawson, J. I.; Evans, N. D., Injectable nanoclay gels for angiogenesis. *Acta biomaterialia* **2019,** *100*, 378-387.
278. Cidonio, G.; Alcala-Orozco, C. R.; Lim, K. S.; Glinka, M.; Mutreja, I.; Kim, Y.-H.; Dawson, J. I.; Woodfield, T. B.; Oreffo, R. O., Osteogenic and angiogenic tissue formation in high fidelity nanocomposite Laponite-gelatin bioinks. *Biofabrication* **2019,** *11* (3), 035027.
279. Lokhande, G.; Carrow, J. K.; Thakur, T.; Xavier, J. R.; Parani, M.; Bayless, K. J.; Gaharwar, A. K., Nanoengineered injectable hydrogels for wound healing application. *Acta Biomaterialia* **2018,** *70*, 35-47.
280. Basirun, W. J.; Nasiri-Tabrizi, B.; Baradaran, S., Overview of hydroxyapatite–graphene nanoplatelets composite as bone graft substitute: mechanical behavior and in-vitro biofunctionality. *Critical Reviews in Solid State and Materials Sciences* **2018,** *43* (3), 177-212.
281. Singh, V.; Joung, D.; Zhai, L.; Das, S.; Khondaker, S. I.; Seal, S., Graphene based materials: past, present and future. *Progress in Materials Science* **2011,** *56* (8), 1178-1271.

282. Georgakilas, V.; Otyepka, M.; Bourlinos, A. B.; Chandra, V.; Kim, N.; Kemp, K. C.; Hobza, P.; Zboril, R.; Kim, K. S., Functionalization of graphene: covalent and non-covalent approaches, derivatives and applications. *Chemical Reviews* **2012,** *112* (11), 6156-6214.
283. Liu, L.; Zhang, J.; Zhao, J.; Liu, F., Mechanical properties of graphene oxides. *Nanoscale* **2012,** *4* (19), 5910-5916.
284. Suk, J. W.; Piner, R. D.; An, J.; Ruoff, R. S., Mechanical properties of monolayer graphene oxide. *ACS Nano* **2010,** *4* (11), 6557-6564.
285. Si, Y.; Samulski, E. T., Synthesis of water soluble graphene. *Nano Letters* **2008,** *8* (6), 1679-1682.
286. Georgakilas, V.; Tiwari, J. N.; Kemp, K. C.; Perman, J. A.; Bourlinos, A. B.; Kim, K. S.; Zboril, R., Noncovalent functionalization of graphene and graphene oxide for energy materials, biosensing, catalytic, and biomedical applications. *Chemicals Review* **2016,** *116* (9), 5464-5519.
287. Wang, Y.; Li, Z.; Wang, J.; Li, J.; Lin, Y., Graphene and graphene oxide: biofunctionalization and applications in biotechnology. *Trends in Biotechnology* **2011,** *29* (5), 205-212.
288. Lee, D. Y.; Khatun, Z.; Lee, J.-H.; Lee, Y.-k.; In, I., Blood compatible graphene/heparin conjugate through noncovalent chemistry. *Biomacromolecules* **2011,** *12* (2), 336-341.
289. Park, S.; Dikin, D. A.; Nguyen, S. T.; Ruoff, R. S., Graphene oxide sheets chemically cross-linked by polyallylamine. *The Journal of Physical Chemistry C* **2009,** *113* (36), 15801-15804.
290. Avinash, M.; Subrahmanyam, K.; Sundarayya, Y.; Govindaraju, T., Covalent modification and exfoliation of graphene oxide using ferrocene. *Nanoscale* **2010,** *2* (9), 1762-1766.
291. Shan, C.; Yang, H.; Han, D.; Zhang, Q.; Ivaska, A.; Niu, L., Water-soluble graphene covalently functionalized by biocompatible poly-L-lysine. *Langmuir* **2009,** *25* (20), 12030-12033.
292. Xu, C.; Wang, X.; Wang, J.; Hu, H.; Wan, L., Synthesis and photoelectrical properties of β-Cyclodextrin functionalized graphene materials with high bio-recognition capability. *Chemical Physics Letters* **2010,** *498* (1-3), 162-167.
293. Kan, L.; Xu, Z.; Gao, C., General avenue to individually dispersed graphene oxide-based two-dimensional molecular brushes by free radical polymerization. *Macromolecules* **2010,** *44* (3), 444-452.
294. Layek, R. K.; Nandi, A. K., A review on synthesis and properties of polymer functionalized graphene. *Polymer* **2013,** *54* (19), 5087-5103.
295. Liu, Z.; Robinson, J. T.; Sun, X.; Dai, H., PEGylated nanographene oxide for delivery of water-insoluble cancer drugs. *Journal of the American Chemical Society* **2008,** *130* (33), 10876-10877.
296. de Sousa, M.; Martins, C. H.; Franqui, L. S.; Fonseca, L. C.; Delite, F. S.; Lanzoni, E. M.; Martinez, D. S. T.; Alves, O. L., Covalent functionalization of graphene oxide with D-mannose: evaluating the hemolytic effect and protein corona formation. *Journal of Materials Chemistry B* **2018,** *6* (18), 2803-2812.
297. Sinitskii, A.; Dimiev, A.; Corley, D. A.; Fursina, A. A.; Kosynkin, D. V.; Tour, J. M., Kinetics of diazonium functionalization of chemically converted graphene nanoribbons. *ACS Nano* **2010,** *4* (4), 1949-1954.
298. Englert, J. M.; Dotzer, C.; Yang, G.; Schmid, M.; Papp, C.; Gottfried, J. M.; Steinrück, H.-P.; Spiecker, E.; Hauke, F.; Hirsch, A., Covalent bulk functionalization of graphene. *Nature Chemistry* **2011,** *3* (4), 279.
299. Saini, D., Covalent functionalisation of graphene: novel approach to change electronic structure of graphene. *Materials Research Innovations* **2015,** *19* (4), 287-294.
300. Fang, M.; Wang, K.; Lu, H.; Yang, Y.; Nutt, S., Covalent polymer functionalization of graphene nanosheets and mechanical properties of composites. *Journal of Materials Chemistry* **2009,** *19* (38), 7098-7105.
301. Fang, M.; Wang, K.; Lu, H.; Yang, Y.; Nutt, S., Single-layer graphene nanosheets with controlled grafting of polymer chains. *Journal of Materials Chemistry* **2010,** *20* (10), 1982-1992.
302. Georgakilas, V.; Bourlinos, A. B.; Zboril, R.; Steriotis, T. A.; Dallas, P.; Stubos, A. K.; Trapalis, C., Organic functionalisation of graphenes. *Chemical Communications* **2010,** *46* (10), 1766-1768.

303. Quintana, M.; Spyrou, K.; Grzelczak, M.; Browne, W. R.; Rudolf, P.; Prato, M., Functionalization of graphene via 1, 3-dipolar cycloaddition. *ACS Nano* **2010,** *4* (6), 3527-3533.
304. Georgakilas, V.; Tiwari, J. N.; Kemp, K. C.; Perman, J. A.; Bourlinos, A. B.; Kim, K. S.; Zboril, R., Noncovalent Functionalization of Graphene and Graphene Oxide for Energy Materials, Biosensing, Catalytic, and Biomedical Applications. *Chemical Reviews* **2016,** *116* (9), 5464-5519.
305. Zhou, L.; Mao, H.; Wu, C.; Tang, L.; Wu, Z.; Sun, H.; Zhang, H.; Zhou, H.; Jia, C.; Jin, Q.; Chen, X.; Zhao, J., Label-free graphene biosensor targeting cancer molecules based on non-covalent modification. *Biosensors and Bioelectronics* **2017,** *87*, 701-707.
306. An, X.; Simmons, T.; Shah, R.; Wolfe, C.; Lewis, K. M.; Washington, M.; Nayak, S. K.; Talapatra, S.; Kar, S., Stable aqueous dispersions of noncovalently functionalized graphene from graphite and their multifunctional high-performance applications. *Nano letters* **2010,** *10* (11), 4295-4301.
307. Kim, J.; Song, S. H.; Im, H. G.; Yoon, G.; Lee, D.; Choi, C.; Kim, J.; Bae, B. S.; Kang, K.; Jeon, S., Moisture barrier composites made of non-oxidized graphene flakes. *Small* **2015,** *11* (26), 3124-3129.
308. Das, S.; Irin, F.; Ahmed, H. T.; Cortinas, A. B.; Wajid, A. S.; Parviz, D.; Jankowski, A. F.; Kato, M.; Green, M. J., Non-covalent functionalization of pristine few-layer graphene using triphenylene derivatives for conductive poly (vinyl alcohol) composites. *Polymer* **2012,** *53* (12), 2485-2494.
309. Zhang, X.-F.; Shao, X., π–π binding ability of different carbon nano-materials with aromatic phthalocyanine molecules: Comparison between graphene, graphene oxide and carbon nanotubes. *Journal of Photochemistry and Photobiology A: Chemistry* **2014,** *278*, 69-74.
310. Yang, X.; Li, J.; Wen, T.; Ren, X.; Huang, Y.; Wang, X., Adsorption of naphthalene and its derivatives on magnetic graphene composites and the mechanism investigation. *Colloids and Surfaces A: Physicochemical and Engineering Aspects* **2013,** *422*, 118-125.
311. Koninti, R. K.; Sengupta, A.; Gavvala, K.; Ballav, N.; Hazra, P., Loading of an anti-cancer drug onto graphene oxide and subsequent release to DNA/RNA: a direct optical detection. *Nanoscale* **2014,** *6* (5), 2937-2944.
312. Balcioglu, M.; Rana, M.; Yigit, M. V., Doxorubicin loading on graphene oxide, iron oxide and gold nanoparticle hybrid. *Journal of Materials Chemistry B* **2013,** *1* (45), 6187-6193.
313. Zhou, L.; Jiang, H.; Wei, S.; Ge, X.; Zhou, J.; Shen, J., High-efficiency loading of hypocrellin B on graphene oxide for photodynamic therapy. *Carbon* **2012,** *50* (15), 5594-5604.
314. Lu, C. H.; Yang, H. H.; Zhu, C. L.; Chen, X.; Chen, G. N., A graphene platform for sensing biomolecules. *Angewandte Chemie* **2009,** *121* (26), 4879-4881.
315. Bonanni, A.; Chua, C. K.; Zhao, G.; Sofer, Z. k.; Pumera, M., Inherently electroactive graphene oxide nanoplatelets as labels for single nucleotide polymorphism detection. *ACS Nano* **2012,** *6* (10), 8546-8551.
316. Liang, J.; Huang, Y.; Zhang, L.; Wang, Y.; Ma, Y.; Guo, T.; Chen, Y., Molecular-level dispersion of graphene into poly (vinyl alcohol) and effective reinforcement of their nanocomposites. *Advanced Functional Materials* **2009,** *19* (14), 2297-2302.
317. Rafiee, M. A.; Rafiee, J.; Wang, Z.; Song, H.; Yu, Z.-Z.; Koratkar, N., Enhanced mechanical properties of nanocomposites at low graphene content. *ACS Nano* **2009,** *3* (12), 3884-3890.
318. Ramanathan, T.; Abdala, A.; Stankovich, S.; Dikin, D.; Herrera-Alonso, M.; Piner, R.; Adamson, D.; Schniepp, H.; Chen, X.; Ruoff, R., Functionalized graphene sheets for polymer nanocomposites. *Nature Nanotechnology* **2008,** *3* (6), 327.
319. Jeon, I.-Y.; Choi, H.-J.; Jung, S.-M.; Seo, J.-M.; Kim, M.-J.; Dai, L.; Baek, J.-B., Large-Scale Production of Edge-Selectively Functionalized Graphene Nanoplatelets via Ball Milling and Their Use as Metal-Free Electrocatalysts for Oxygen Reduction Reaction. *Journal of the American Chemical Society* **2013,** *135* (4), 1386-1393.
320. Cho, D. W.; Parthasarathi, R.; Pimentel, A. S.; Maestas, G. D.; Park, H. J.; Yoon, U. C.; Dunaway-Mariano, D.; Gnanakaran, S.; Langan, P.; Mariano, P. S., Nature and Kinetic Analysis of

Carbon− Carbon Bond Fragmentation Reactions of Cation Radicals Derived from SET-Oxidation of Lignin Model Compounds. *The Journal of Organic Chemistry* **2010,** *75* (19), 6549-6562.
321. Kim, M.-J.; Jeon, I.-Y.; Seo, J.-M.; Dai, L.; Baek, J.-B., Graphene phosphonic acid as an efficient flame retardant. *ACS Nano* **2014,** *8* (3), 2820-2825.
322. Jeon, I. Y.; Bae, S. Y.; Seo, J. M.; Baek, J. B., Scalable Production of Edge-Functionalized Graphene Nanoplatelets via Mechanochemical Ball-Milling. *Adv. Funct. Mater.* **2015,** *25* (45), 6961-6975.
323. Seo, J. M.; Tan, L. S.; Baek, J. B., Defect/Edge-Selective Functionalization of Carbon Materials by "Direct" Friedel–Crafts Acylation Reaction. *Advanced Materials* **2017,** *29* (19), 1606317.
324. Choi, E.-K.; Jeon, I.-Y.; Bae, S.-Y.; Lee, H.-J.; Shin, H. S.; Dai, L.; Baek, J.-B., High-yield exfoliation of three-dimensional graphite into two-dimensional graphene-like sheets. *Chemical Communications* **2010,** *46* (34), 6320-6322.
325. Bae, S.-Y.; Jeon, I.-Y.; Yang, J.; Park, N.; Shin, H. S.; Park, S.; Ruoff, R. S.; Dai, L.; Baek, J.-B., Large-area graphene films by simple solution casting of edge-selectively functionalized graphite. *ACS Nano* **2011,** *5* (6), 4974-4980.
326. Abdolmaleki, A.; Mallakpour, S.; Borandeh, S., Structure, morphology and electronic properties of L-phenylalanine edge-functionalized graphite platelets through Friedel–Crafts acylation reaction. *RSC Advances* **2014,** *4* (104), 60052-60057.
327. Chen, H.-C.; Yang, H.-W.; Yang, K.-H.; Chen, C.-H.; Hou, C.-C.; Tu, Y.-M., Facile preparation of electroactive graphene derivative and its potential application in electrochemical detection. *Sensors and Actuators B: Chemical* **2017,** *240*, 1153-1159.
328. Choi, E.-K.; Jeon, I.-Y.; Oh, S.-J.; Baek, J.-B., "Direct" grafting of linear macromolecular "wedges" to the edge of pristine graphite to prepare edge-functionalized graphene-based polymer composites. *Journal of Materials Chemistry* **2010,** *20* (48), 10936-10942.
329. Choi, E.-K.; Jeon, I.-Y.; Shin, Y.-R.; Baek, J.-B., Strain-induced delamination of edge-grafted graphite. *Chemical Communications* **2012,** *48* (90), 11109-11111.
330. Hu, Z.; Li, N.; Li, J.; Zhang, C.; Song, Y.; Li, X.; Wu, G.; Xie, F.; Huang, Y., Facile preparation of poly (p-phenylene benzobisoxazole)/graphene composite films via one-pot in situ polymerization. *Polymer* **2015,** *71*, 8-14.
331. Barbera, V.; Brambilla, L.; Porta, A.; Bongiovanni, R.; Vitale, A.; Torrisi, G.; Galimberti, M., Selective edge functionalization of graphene layers with oxygenated groups by means of Reimer–Tiemann and domino Reimer–Tiemann/Cannizzaro reactions. *Journal of Materials Chemistry A* **2018,** *6* (17), 7749-7761.
332. Abdolmaleki, A.; Mallakpour, S.; Mahmoudian, M., Preparation and Evaluation of Edge Selective Sulfonated Graphene by Chlorosulfuric Acid as an Active Metal-Free Electrocatalyst for Oxygen Reduction Reaction in Alkaline Media. *ChemistrySelect* **2017,** *2* (34), 11211-11217.
333. Shellard, P. M.; Srisubin, T.; Hartmann, M.; Butcher, J.; Fei, F.; Cox, H.; McNamara, T. P.; McArdle, T.; Shepherd, A. M.; Jacobs, R. M., A versatile route to edge-specific modifications to pristine graphene by electrophilic aromatic substitution. *Journal of Materials Science* **2020,** *55*, 10284-10302.
334. Sanchez, V. C.; Jachak, A.; Hurt, R. H.; Kane, A. B., Biological interactions of graphene-family nanomaterials: an interdisciplinary review. *Chemical Research in Toxicology* **2011,** *25* (1), 15-34.
335. Nel, A. E.; Mädler, L.; Velegol, D.; Xia, T.; Hoek, E. M.; Somasundaran, P.; Klaessig, F.; Castranova, V.; Thompson, M., Understanding biophysicochemical interactions at the nano–bio interface. *Nature Materials* **2009,** *8* (7), 543.
336. Chatterjee, N.; Yang, J. S.; Park, K.; Oh, S. M.; Park, J.; Choi, J., Screening of toxic potential of graphene family nanomaterials using in vitro and alternative in vivo toxicity testing systems. *Environmental Health and Toxicology* **2015,** *30*.
337. Peruzynska, M.; Cendrowski, K.; Barylak, M.; Tkacz, M.; Piotrowska, K.; Kurzawski, M.; Mijowska, E.; Drozdzik, M., Comparative in vitro study of single and four layer graphene oxide nanoflakes—Cytotoxicity and cellular uptake. *Toxicology In Vitro* **2017,** *41*, 205-213.

338. Hu, W.; Peng, C.; Lv, M.; Li, X.; Zhang, Y.; Chen, N.; Fan, C.; Huang, Q., Protein corona-mediated mitigation of cytotoxicity of graphene oxide. *ACS Nano* **2011,** *5* (5), 3693-3700.
339. Guo, L.; Von Dem Bussche, A.; Buechner, M.; Yan, A.; Kane, A. B.; Hurt, R. H., Adsorption of essential micronutrients by carbon nanotubes and the implications for nanotoxicity testing. *Small* **2008,** *4* (6), 721-727.
340. Liu, S.; Hu, M.; Zeng, T. H.; Wu, R.; Jiang, R.; Wei, J.; Wang, L.; Kong, J.; Chen, Y., Lateral dimension-dependent antibacterial activity of graphene oxide sheets. *Langmuir* **2012,** *28* (33), 12364-12372.
341. Aillon, K. L.; Xie, Y.; El-Gendy, N.; Berkland, C. J.; Forrest, M. L., Effects of nanomaterial physicochemical properties on in vivo toxicity. *Advanced Drug Delivery Reviews* **2009,** *61* (6), 457-466.
342. Yue, H.; Wei, W.; Yue, Z.; Wang, B.; Luo, N.; Gao, Y.; Ma, D.; Ma, G.; Su, Z., The role of the lateral dimension of graphene oxide in the regulation of cellular responses. *Biomaterials* **2012,** *33* (16), 4013-4021.
343. Ma, J.; Liu, R.; Wang, X.; Liu, Q.; Chen, Y.; Valle, R. P.; Zuo, Y. Y.; Xia, T.; Liu, S., Crucial role of lateral size for graphene oxide in activating macrophages and stimulating pro-inflammatory responses in cells and animals. *ACS Nano* **2015,** *9* (10), 10498-10515.
344. Liu, J.-H.; Yang, S.-T.; Wang, H.; Chang, Y.; Cao, A.; Liu, Y., Effect of size and dose on the biodistribution of graphene oxide in mice. *Nanomedicine* **2012,** *7* (12), 1801-1812.
345. Liao, K.-H.; Lin, Y.-S.; Macosko, C. W.; Haynes, C. L., Cytotoxicity of graphene oxide and graphene in human erythrocytes and skin fibroblasts. *ACS Applied Materials & Interfaces* **2011,** *3* (7), 2607-2615.
346. Singh, S. K.; Singh, M. K.; Kulkarni, P. P.; Sonkar, V. K.; Grácio, J. J.; Dash, D., Amine-modified graphene: thrombo-protective safer alternative to graphene oxide for biomedical applications. *ACS Nano* **2012,** *6* (3), 2731-2740.
347. Singh, S. K.; Singh, M. K.; Nayak, M. K.; Kumari, S.; Shrivastava, S.; Grácio, J. J.; Dash, D., Thrombus inducing property of atomically thin graphene oxide sheets. *Acs Nano* **2011,** *5* (6), 4987-4996.
348. Wang, X.; Duch, M. C.; Mansukhani, N.; Ji, Z.; Liao, Y.-P.; Wang, M.; Zhang, H.; Sun, B.; Chang, C. H.; Li, R., Use of a pro-fibrogenic mechanism-based predictive toxicological approach for tiered testing and decision analysis of carbonaceous nanomaterials. *ACS Nano* **2015,** *9* (3), 3032-3043.
349. Pelin, M.; Fusco, L.; León, V.; Martín, C.; Criado, A.; Sosa, S.; Vázquez, E.; Tubaro, A.; Prato, M., Differential cytotoxic effects of graphene and graphene oxide on skin keratinocytes. *Scientific Reports* **2017,** *7*, 40572.
350. Sasidharan, A.; Panchakarla, L.; Chandran, P.; Menon, D.; Nair, S.; Rao, C.; Koyakutty, M., Differential nano-bio interactions and toxicity effects of pristine versus functionalized graphene. *Nanoscale* **2011,** *3* (6), 2461-2464.
351. Pinto, A. M.; Magalhães, F. D.; Gonçalves, I. C., Polymer surface adsorption as a strategy to improve the biocompatibility of graphene nanoplatelets. *Colloids and Surfaces B: Biointerfaces* **2016,** *146*, 818-824.
352. Karahan, H. E.; Wei, L.; Goh, K.; Wiraja, C.; Liu, Z.; Xu, C.; Jiang, R.; Wei, J.; Chen, Y., Synergism of water shock and a biocompatible block copolymer potentiates the antibacterial activity of graphene oxide. *Small* **2016,** *12* (7), 951-962.
353. Ali-Boucetta, H.; Bitounis, D.; Raveendran-Nair, R.; Servant, A.; Van den Bossche, J.; Kostarelos, K., Purified graphene oxide dispersions lack in vitro cytotoxicity and in vivo pathogenicity. *Advanced Healthcare Materials* **2013,** *2* (3), 433-441.
354. Wu, W.; Yan, L.; Wu, Q.; Li, Y.; Li, Q.; Chen, S.; Yang, Y.; Gu, Z.; Xu, H.; Yin, Z. Q., Evaluation of the toxicity of graphene oxide exposure to the eye. *Nanotoxicology* **2016,** *10* (9), 1329-1340.
355. Kucki, M.; Rupper, P.; Sarrieu, C.; Melucci, M.; Treossi, E.; Schwarz, A.; León, V.; Kraegeloh, A.; Flahaut, E.; Vázquez, E., Interaction of graphene-related materials with human intestinal cells: an in vitro approach. *Nanoscale* **2016,** *8* (16), 8749-8760.

356. Vallabani, N.; Mittal, S.; Shukla, R. K.; Pandey, A. K.; Dhakate, S. R.; Pasricha, R.; Dhawan, A., Toxicity of graphene in normal human lung cells (BEAS-2B). *Journal of Biomedical Nanotechnology* **2011,** *7* (1), 106-107.
357. Chang, Y.; Yang, S.-T.; Liu, J.-H.; Dong, E.; Wang, Y.; Cao, A.; Liu, Y.; Wang, H., In vitro toxicity evaluation of graphene oxide on A549 cells. *Toxicology letters* **2011,** *200* (3), 201-210.
358. Jaworski, S.; Sawosz, E.; Grodzik, M.; Winnicka, A.; Prasek, M.; Wierzbicki, M.; Chwalibog, A., In vitro evaluation of the effects of graphene platelets on glioblastoma multiforme cells. *International Journal of Nanomedicine* **2013,** *8*, 413.
359. Zhang, Y.; Ali, S. F.; Dervishi, E.; Xu, Y.; Li, Z.; Casciano, D.; Biris, A. S., Cytotoxicity effects of graphene and single-wall carbon nanotubes in neural phaeochromocytoma-derived PC12 cells. *ACS Nano* **2010,** *4* (6), 3181-3186.
360. Lammel, T.; Boisseaux, P.; Fernández-Cruz, M.-L.; Navas, J. M., Internalization and cytotoxicity of graphene oxide and carboxyl graphene nanoplatelets in the human hepatocellular carcinoma cell line Hep G2. *Particle and Fibre Toxicology* **2013,** *10* (1), 27.
361. Chen, G.-Y.; Yang, H.-J.; Lu, C.-H.; Chao, Y.-C.; Hwang, S.-M.; Chen, C.-L.; Lo, K.-W.; Sung, L.-Y.; Luo, W.-Y.; Tuan, H.-Y., Simultaneous induction of autophagy and toll-like receptor signaling pathways by graphene oxide. *Biomaterials* **2012,** *33* (27), 6559-6569.
362. Duch, M. C.; Budinger, G. S.; Liang, Y. T.; Soberanes, S.; Urich, D.; Chiarella, S. E.; Campochiaro, L. A.; Gonzalez, A.; Chandel, N. S.; Hersam, M. C., Minimizing oxidation and stable nanoscale dispersion improves the biocompatibility of graphene in the lung. *Nano Letters* **2011,** *11* (12), 5201-5207.
363. Li, Y.; Liu, Y.; Fu, Y.; Wei, T.; Le Guyader, L.; Gao, G.; Liu, R.-S.; Chang, Y.-Z.; Chen, C., The triggering of apoptosis in macrophages by pristine graphene through the MAPK and TGF-beta signaling pathways. *Biomaterials* **2012,** *33* (2), 402-411.
364. Shen, H.; Lin, H.; Sun, A. X.; Song, S.; Zhang, Z.; Dai, J.; Tuan, R. S., Chondroinductive factor-free chondrogenic differentiation of human mesenchymal stem cells in graphene oxide-incorporated hydrogels. *Journal of Materials Chemistry B* **2018,** *6* (6), 908-917.
365. Lasocka, I.; Szulc-Dąbrowska, L.; Skibniewski, M.; Skibniewska, E.; Strupinski, W.; Pasternak, I.; Kmieć, H.; Kowalczyk, P., Biocompatibility of pristine graphene monolayer: Scaffold for fibroblasts. *Toxicology in Vitro* **2018,** *48*, 276-285.
366. Katsumiti, A.; Tomovska, R.; Cajaraville, M. P., Intracellular localization and toxicity of graphene oxide and reduced graphene oxide nanoplatelets to mussel hemocytes in vitro. *Aquatic Toxicology* **2017,** *188*, 138-147.
367. Matesanz, M.-C.; Vila, M.; Feito, M.-J.; Linares, J.; Gonçalves, G.; Vallet-Regi, M.; Marques, P.-A. A.; Portolés, M.-T., The effects of graphene oxide nanosheets localized on F-actin filaments on cell-cycle alterations. *Biomaterials* **2013,** *34* (5), 1562-1569.
368. Shi, L.; Chen, J.; Teng, L.; Wang, L.; Zhu, G.; Liu, S.; Luo, Z.; Shi, X.; Wang, Y.; Ren, L., The antibacterial applications of graphene and its derivatives. *Small* **2016,** *12* (31), 4165-4184.
369. Tu, Y.; Lv, M.; Xiu, P.; Huynh, T.; Zhang, M.; Castelli, M.; Liu, Z.; Huang, Q.; Fan, C.; Fang, H., Destructive extraction of phospholipids from Escherichia coli membranes by graphene nanosheets. *Nature nanotechnology* **2013,** *8* (8), 594.
370. Akhavan, O.; Ghaderi, E., Toxicity of graphene and graphene oxide nanowalls against bacteria. *ACS nano* **2010,** *4* (10), 5731-5736.
371. Liu, S.; Zeng, T. H.; Hofmann, M.; Burcombe, E.; Wei, J.; Jiang, R.; Kong, J.; Chen, Y., Antibacterial activity of graphite, graphite oxide, graphene oxide, and reduced graphene oxide: membrane and oxidative stress. *ACS nano* **2011,** *5* (9), 6971-6980.
372. Hu, W.; Peng, C.; Luo, W.; Lv, M.; Li, X.; Li, D.; Huang, Q.; Fan, C., Graphene-based antibacterial paper. *ACS nano* **2010,** *4* (7), 4317-4323.
373. Li, J.; Wang, G.; Zhu, H.; Zhang, M.; Zheng, X.; Di, Z.; Liu, X.; Wang, X., Antibacterial activity of large-area monolayer graphene film manipulated by charge transfer. *Scientific reports* **2014,** *4* (1), 1-8.

374. Smith, S. C.; Rodrigues, D. F., Carbon-based nanomaterials for removal of chemical and biological contaminants from water: A review of mechanisms and applications. *Carbon* **2015,** *91*, 122-143.
375. Volkov, Y.; McIntyre, J.; Prina-Mello, A., Graphene toxicity as a double-edged sword of risks and exploitable opportunities: a critical analysis of the most recent trends and developments. *2D Materials* **2017,** *4* (2), 022001.
376. Yang, K.; Li, Y.; Tan, X.; Peng, R.; Liu, Z., Behavior and toxicity of graphene and its functionalized derivatives in biological systems. *Small* **2013,** *9* (9-10), 1492-1503.
377. Wick, P.; Louw-Gaume, A. E.; Kucki, M.; Krug, H. F.; Kostarelos, K.; Fadeel, B.; Dawson, K. A.; Salvati, A.; Vázquez, E.; Ballerini, L., Classification framework for graphene-based materials. *Angewandte Chemie International Edition* **2014,** *53* (30), 7714-7718.
378. Ema, M.; Gamo, M.; Honda, K., A review of toxicity studies on graphene-based nanomaterials in laboratory animals. *Regulatory Toxicology and Pharmacology* **2017,** *85*, 7-24.
379. Bussy, C.; Jasim, D.; Lozano, N.; Terry, D.; Kostarelos, K., The current graphene safety landscape–a literature mining exercise. *Nanoscale* **2015,** *7* (15), 6432-6435.
380. Bussy, C.; Ali-Boucetta, H.; Kostarelos, K., Safety considerations for graphene: lessons learnt from carbon nanotubes. *Accounts of chemical research* **2013,** *46* (3), 692-701.
381. Duan, S.; Yang, X.; Mei, F.; Tang, Y.; Li, X.; Shi, Y.; Mao, J.; Zhang, H.; Cai, Q., Enhanced osteogenic differentiation of mesenchymal stem cells on poly (L-lactide) nanofibrous scaffolds containing carbon nanomaterials. *Journal of Biomedical Materials Research Part A* **2015,** *103* (4), 1424-1435.
382. Türk, M.; Deliormanlı, A. M., Graphene-containing PCL-coated Porous 13-93B3 Bioactive Glass Scaffolds for Bone Regeneration. *Materials Research Express* **2018,** *5* (4), 045406.
383. Kim, H. D.; Kim, J.; Koh, R. H.; Shim, J.; Lee, J.-C.; Kim, T.-I.; Hwang, N. S., Enhanced Osteogenic commitment of human Mesenchymal stem cells on polyethylene glycol-based Cryogel with Graphene oxide substrate. *Acs Biomaterials Science & Engineering* **2017,** *3* (10), 2470-2479.
384. Chen, C.; Sun, X.; Pan, W.; Hou, Y.; Liu, R.; Jiang, X.; Zhang, L., Graphene Oxide-Templated Synthesis of Hydroxyapatite Nanowhiskers To Improve the Mechanical and Osteoblastic Performance of Poly (lactic acid) for Bone Tissue Regeneration. *ACS Sustainable Chemistry & Engineering* **2018,** *6* (3), 3862-3869.
385. Han, L.; Sun, H.; Tang, P.; Li, P.; Xie, C.; Wang, M.; Wang, K.; Weng, J.; Tan, H.; Ren, F., Mussel-inspired graphene oxide nanosheet-enwrapped Ti scaffolds with drug-encapsulated gelatin microspheres for bone regeneration. *Biomaterials Science* **2018,** *6* (3), 538-549.
386. Yu, Z.; Xiao, C.; Huang, Y.; Chen, M.; Wei, W.; Yang, X.; Zhou, H.; Bi, X.; Lu, L.; Ruan, J., Enhanced bioactivity and osteoinductivity of carboxymethyl chitosan/nanohydroxyapatite/graphene oxide nanocomposites. *RSC Advances* **2018,** *8* (32), 17860-17877.
387. Patel, M.; Moon, H. J.; Ko, D. Y.; Jeong, B., Composite System of Graphene Oxide and Polypeptide Thermogel As an Injectable 3D Scaffold for Adipogenic Differentiation of Tonsil-Derived Mesenchymal Stem Cells. *ACS Applied Materials & Interfaces* **2016,** *8* (8), 5160-5169.
388. Kim, J.; Choi, K. S.; Kim, Y.; Lim, K. T.; Seonwoo, H.; Park, Y.; Kim, D. H.; Choung, P. H.; Cho, C. S.; Kim, S. Y., Bioactive effects of graphene oxide cell culture substratum on structure and function of human adipose-derived stem cells. *Journal of Biomedical Materials Research Part A: An Official Journal of The Society for Biomaterials, The Japanese Society for Biomaterials, and The Australian Society for Biomaterials and the Korean Society for Biomaterials* **2013,** *101* (12), 3520-3530.
389. Kim, J.; Park, S.; Kim, Y. J.; Jeon, C. S.; Lim, K. T.; Seonwoo, H.; Cho, S.-P.; Chung, T. D.; Choung, P.-H.; Choung, Y.-H., Monolayer graphene-directed growth and neuronal differentiation of mesenchymal stem cells. *Journal of biomedical nanotechnology* **2015,** *11* (11), 2024-2033.
390. Serrano, M. C.; Patiño, J.; García-Rama, C.; Ferrer, M. L.; Fierro, J. L. G.; Tamayo, A.; Collazos-Castro, J. E.; del Monte, F.; Gutiérrez, M. C., 3D free-standing porous scaffolds made of graphene oxide as substrates for neural cell growth. *Journal of Materials Chemistry B* **2014,** *2* (34), 5698-5706.

391. Heymann, D.; Ory, B.; Gouin, F.; Green, J. R.; Rédini, F., Bisphosphonates: new therapeutic agents for the treatment of bone tumors. *Trends in Molecular Medicine* **2004,** *10* (7), 337-343.
392. Coxon, F. P.; Thompson, K.; Rogers, M. J., Recent advances in understanding the mechanism of action of bisphosphonates. *Current Opinion in Pharmacology* **2006,** *6* (3), 307-312.
393. Drake, M. T.; Clarke, B. L.; Khosla, S., Bisphosphonates: mechanism of action and role in clinical practice. *Mayo Clin Proc* **2008,** *83* (9), 1032-1045.
394. Im, G.-I.; Qureshi, S. A.; Kenney, J.; Rubash, H. E.; Shanbhag, A. S., Osteoblast proliferation and maturation by bisphosphonates. *Biomaterials* **2004,** *25* (18), 4105-4115.
395. Reinholz, G. G.; Getz, B.; Pederson, L.; Sanders, E. S.; Subramaniam, M.; Ingle, J. N.; Spelsberg, T. C., Bisphosphonates directly regulate cell proliferation, differentiation, and gene expression in human osteoblasts. *Cancer research* **2000,** *60* (21), 6001-6007.
396. Beldjilali-Labro, M.; Garcia Garcia, A.; Farhat, F.; Bedoui, F.; Grosset, J.-F.; Dufresne, M.; Legallais, C., Biomaterials in Tendon and Skeletal Muscle Tissue Engineering: Current Trends and Challenges. *Materials* **2018,** *11* (7), 1116.
397. Russell, R.; Watts, N.; Ebetino, F.; Rogers, M., Mechanisms of action of bisphosphonates: similarities and differences and their potential influence on clinical efficacy. *Osteoporosis International* **2008,** *19* (6), 733-759.
398. Gemeinhart, R. A.; Bare, C. M.; Haasch, R. T.; Gemeinhart, E. J., Osteoblast-like cell attachment to and calcification of novel phosphonate-containing polymeric substrates. *Journal of Biomedical Materials Research Part A: An Official Journal of The Society for Biomaterials, The Japanese Society for Biomaterials, and The Australian Society for Biomaterials and the Korean Society for Biomaterials* **2006,** *78* (3), 433-440.
399. Abueva, C. D.; Jang, D.-W.; Padalhin, A.; Lee, B.-T., Phosphonate-chitosan functionalization of a multi-channel hydroxyapatite scaffold for interfacial implant-bone tissue integration. *Journal of Materials Chemistry B* **2017,** *5* (6), 1293-1301.
400. Kim, Y. K.; Gu, L.-s.; Bryan, T. E.; Kim, J. R.; Chen, L.; Liu, Y.; Yoon, J. C.; Breschi, L.; Pashley, D. H.; Tay, F. R., Mineralisation of reconstituted collagen using polyvinylphosphonic acid/polyacrylic acid templating matrix protein analogues in the presence of calcium, phosphate and hydroxyl ions. *Biomaterials* **2010,** *31* (25), 6618-6627.
401. Wang, Q. G.; Wimpenny, I.; Dey, R. E.; Zhong, X.; Youle, P. J.; Downes, S.; Watts, D. C.; Budd, P. M.; Hoyland, J. A.; Gough, J. E., The unique calcium chelation property of poly (vinyl phosphonic acid-co-acrylic acid) and effects on osteogenesis in vitro. *Journal of Biomedical Materials Research Part A* **2018,** *106* (1), 168-179.
402. Decher, G.; Hong, J. D. In *Buildup of ultrathin multilayer films by a self-assembly process, 1 consecutive adsorption of anionic and cationic bipolar amphiphiles on charged surfaces*, Makromolekulare Chemie. Macromolecular Symposia, Wiley Online Library: 1991; pp 321-327.
403. Decher, G., Fuzzy nanoassemblies: toward layered polymeric multicomposites. *science* **1997,** *277* (5330), 1232-1237.
404. Decher, G., Layer-by-layer assembly (putting molecules to work). *Multilayer thin films* **2012,** *1*, 1-21.
405. Félix, O.; Zheng, Z.; Cousin, F.; Decher, G., Are sprayed LbL-films stratified? A first assessment of the nanostructure of spray-assembled multilayers by neutron reflectometry. *Comptes Rendus Chimie* **2009,** *12* (1-2), 225-234.
406. Sukhorukov, G. B.; Donath, E.; Lichtenfeld, H.; Knippel, E.; Knippel, M.; Budde, A.; Möhwald, H., Layer-by-layer self assembly of polyelectrolytes on colloidal particles. *Colloids and Surfaces A: physicochemical and engineering aspects* **1998,** *137* (1-3), 253-266.
407. Kotov, N. A.; Dekany, I.; Fendler, J. H., Layer-by-layer self-assembly of polyelectrolyte-semiconductor nanoparticle composite films. *The Journal of Physical Chemistry* **1995,** *99* (35), 13065-13069.

408. Zhang, D.; Tong, J.; Xia, B.; Xue, Q., Ultrahigh performance humidity sensor based on layer-by-layer self-assembly of graphene oxide/polyelectrolyte nanocomposite film. *Sensors and Actuators B: Chemical* **2014,** *203*, 263-270.
409. Ariga, K.; Lvov, Y.; Kunitake, T., Assembling alternate dye− polyion molecular films by electrostatic layer-by-layer adsorption. *Journal of the American Chemical Society* **1997,** *119* (9), 2224-2231.
410. Lvov, Y.; Ariga, K.; Ichinose, I.; Kunitake, T., Assembly of multicomponent protein films by means of electrostatic layer-by-layer adsorption. *Journal of the American Chemical Society* **1995,** *117* (22), 6117-6123.
411. Pei, R.; Cui, X.; Yang, X.; Wang, E., Assembly of alternating polycation and DNA multilayer films by electrostatic layer-by-layer adsorption. *Biomacromolecules* **2001,** *2* (2), 463-468.
412. Sham, A. Y.; Notley, S. M., Layer-by-layer assembly of thin films containing exfoliated pristine graphene nanosheets and polyethyleneimine. *Langmuir* **2014,** *30* (9), 2410-2418.
413. Xiong, Z.; Gu, T.; Wang, X., Self-assembled multilayer films of sulfonated graphene and polystyrene-based diazonium salt as photo-cross-linkable supercapacitor electrodes. *Langmuir* **2014,** *30* (2), 522-532.
414. Decher, G.; Eckle, M.; Schmitt, J.; Struth, B., Layer-by-layer assembled multicomposite films. *Current opinion in colloid & interface science* **1998,** *3* (1), 32-39.
415. Qi, W.; Xue, Z.; Yuan, W.; Wang, H., Layer-by-layer assembled graphene oxide composite films for enhanced mechanical properties and fibroblast cell affinity. *Journal of Materials Chemistry B* **2014,** *2* (3), 325-331.
416. Yang, M.; Hou, Y.; Kotov, N. A., Graphene-based multilayers: Critical evaluation of materials assembly techniques. *Nano Today* **2012,** *7* (5), 430-447.
417. Ren, K.-f.; Hu, M.; Zhang, H.; Li, B.-c.; Lei, W.-x.; Chen, J.-y.; Chang, H.; Wang, L.-m.; Ji, J., Layer-by-layer assembly as a robust method to construct extracellular matrix mimic surfaces to modulate cell behavior. *Progress in Polymer Science* **2019,** *92*, 1-34.
418. Shukla, A.; Almeida, B., Advances in cellular and tissue engineering using layer-by-layer assembly. *Wiley Interdisciplinary Reviews: Nanomedicine and Nanobiotechnology* **2014,** *6* (5), 411-421.
419. Grohmann, S.; Rothe, H.; Liefeith, K., Investigations on the secondary structure of polypeptide chains in polyelectrolyte multilayers and their effect on the adhesion and spreading of osteoblasts. *Biointerphases* **2012,** *7* (1), 62.
420. Cao, B.; Yan, S.; Zhang, K.; Song, Z.; Cao, T.; Chen, X.; Cui, L.; Yin, J., A poly (acrylic acid)-block-poly (l-glutamic acid) diblock copolymer with improved cell adhesion for surface modification. *Macromolecular bioscience* **2011,** *11* (7), 970-977.
421. Pattabhi, S. R.; Lehaf, A. M.; Schlenoff, J. B.; Keller III, T. C., Human mesenchymal stem cell osteoblast differentiation, ECM deposition, and biomineralization on PAH/PAA polyelectrolyte multilayers. *Journal of Biomedical Materials Research Part A* **2015,** *103* (5), 1818-1827.
422. Cai, P.; Xue, Z.; Qi, W.; Wang, H., Adsorbed BMP-2 in polyelectrolyte multilayer films for enhanced early osteogenic differentiation of mesenchymal stem cells. *Colloids and Surfaces A: Physicochemical and Engineering Aspects* **2013,** *434*, 110-117.
423. Niepel, M. S.; Mano, J. o. F.; Groth, T., Effect of Polyelectrolyte Multilayers Assembled on Ordered Nanostructures on Adhesion of Human Fibroblasts. *ACS applied materials & interfaces* **2016,** *8* (38), 25142-25151.
424. Mhanna, R. F.; Vörös, J.; Zenobi-Wong, M., Layer-by-layer films made from extracellular matrix macromolecules on silicone substrates. *Biomacromolecules* **2011,** *12* (3), 609-616.
425. Wittmer, C. R.; Phelps, J. A.; Saltzman, W. M.; Van Tassel, P. R., Fibronectin terminated multilayer films: protein adsorption and cell attachment studies. *Biomaterials* **2007,** *28* (5), 851-860.
426. Qi, W.; Yuan, W.; Yan, J.; Wang, H., Growth and accelerated differentiation of mesenchymal stem cells on graphene oxide/poly-l-lysine composite films. *Journal of Materials Chemistry B* **2014,** *2* (33), 5461-5467.

427. Shin, S. R.; Aghaei-Ghareh-Bolagh, B.; Gao, X.; Nikkhah, M.; Jung, S. M.; Dolatshahi-Pirouz, A.; Kim, S. B.; Kim, S. M.; Dokmeci, M. R.; Tang, X., Layer-by-layer assembly of 3D tissue constructs with functionalized graphene. *Advanced functional materials* **2014,** *24* (39), 6136-6144.
428. Kashte, S.; Sharma, R.; Kadam, S., Layer-by-layer decorated herbal cell compatible scaffolds for bone tissue engineering: A synergistic effect of graphene oxide and Cissus quadrangularis. *Journal of Bioactive and Compatible Polymers* **2020,** *35* (1), 57-73.
429. Song, F.; Jie, W.; Zhang, T.; Li, W.; Jiang, Y.; Wan, L.; Liu, W.; Li, X.; Liu, B., Room-temperature fabrication of a three-dimensional reduced-graphene oxide/polypyrrole/hydroxyapatite composite scaffold for bone tissue engineering. *RSC advances* **2016,** *6* (95), 92804-92812.
430. Guvendiren, M.; Lu, H. D.; Burdick, J. A., Shear-thinning hydrogels for biomedical applications. *Soft matter* **2012,** *8* (2), 260-272.

Chapter 2

Materials and methods

2.1 Synthesis of modified graphene-family nanomaterials

The protocol of edge-specific functionalisation of sulfonated graphene and thiolated graphene in this thesis was followed the procedure from Shellard *et al*.[1]

2.1.1 Synthesis of graphene sulfonate

500 mg graphene nanoplatelets (Grade C750, surface area 750 m^2 g^{-1}, XG Sciences) were added into 10 mL chlorosulphonic acid (1.75 g cm^{-3}, ≥98%, Merck Chemicals). The mixture was heated to 100°C with stirring and connected to a condenser to recovery the acid. After 20 hours, the mixture was slowly dropped into ice water (heat and fume are generated during drop) and hydrolysed with concentrated sodium hydroxide (NaOH, ≥97 %, Fisher Scientific) solution where the pH is neutral. Finally, the mixture was purified by SnakeSkin dialysis tubing (10kDa MWCO, 35mm dry ID) for 24 hours. The water was changed 3 times at intervals of at least 8 hours, followed by filtration and freeze-drying to obtain graphene sulfonate (G–SO_3).

2.1.2 Synthesis of graphene thiol

50 mg graphene sulfonate (G–SO_3) were suspended in 30 mL toluene (AR grade, Fisher Scientific) and sonicated under N_2 atmosphere for 15 minutes. The reaction flask was then connected to a condenser with nitrogen flow. 2.5 g triphenylphosphine (99%, Sigma-Aldrich) and 200 mg iodine (≥99.8%, solid, Sigma-Aldrich) were added and the mixture was stirred under a N_2 atmosphere at 80°C for 21 hours. The product was filtered and washed with toluene, acetone, 0.1 M sodium thiosulphate (≥99.5%, Sigma-Aldrich) solution and Milli-Q water (purified to a resistivity of 18.2 MΩ cm at 25 °C), followed by freeze-drying to obtain graphene thiol (G–SH).

2.1.3 Synthesis of phosphonate-modified graphene

Graphene phosphonate was prepared by edge modification of graphene thiol and polymerisation of PVPA-*co*-AA in the presence of pristine graphene.

In a typical synthesis using edge-modified graphene, 50 mg thiolated graphene was added into 20 mL dimethylformamide (DMF, 99%, Fisher Scientific). Then, 2 mL vinylphosphonic acid monomer (VPA, 97%, Sigma-Aldrich) and 20 mg 2,2'-azobis(2-methylpropionitrile) (AIBN, 98%, Sigma-Aldrich) were added into the mixture. The reaction mixture was heated at 90°C for 24 hours with stirring under N_2. The product was purified using SnakeSkin dialysis tubing (10kDa MWCO, 35mm dry ID) for one day. The water was changed 3 times at intervals of at least 8 hours, followed by filtration, washing with Milli-Q water and freeze-drying to obtain graphene phosphonate (G–$PO(OH)_2$).

In a typical synthesis using polymerisation of PVPA-*co*-AA in the presence of pristine graphene (G–PVPA), the protocol of Dey *et al*.[2] was adapted. 100 mg pristine graphene (Grade C750, surface area 750m^2 g^{-1}, XG Sciences) and 2.78 g VPA (97%, Sigma-Aldrich) were add into 8 ml Milli-Q water, then, the reaction mixture was heated at 90°C for 30 minutes with stirring under N_2. 4.24 g Acrylic acid (AA, anhydrous, 99%, Sigma-Aldrich) and 0.024 g 2,2-azobis(2-methylpropionamidine) (AAPH, 97%, Sigma-Aldrich) were dissolved in Milli-Q water separately. Separate solutions of AA (0.62 mL) and AAPH (0.18 mL) solutions were added into the reaction flask batch-wise every 30 minutes, over the courses of 6 hours. After the last addition of AA and initiator, the reaction was further left for 18 hours and was then purified using SnakeSkin dialysis tubing (10kDa MWCO, 35mm dry ID) for one day. The water was changed 3 times at intervals of at least 8 hours. Finally, the mixture was filtered and washed with distilled water, followed by freeze-drying to obtain modified graphene.

2.1.4 Synthesis of graphene oxide sulfonate

100 mg graphene oxide powder (GO graphene, William Blythe) was added into 100 mL DMF (99%, Fisher Scientific). 5 mL chlorosulphonic acid (1.75 g cm^{-3}, ≥98%, Merck Chemicals) was added dropwise, with stirring. The mixture was then heated to 55°C with stirring overnight. After 20 hours, the mixture was slowly dropped into ice water and hydrolysed with concentrated NaOH (≥97 %, Fisher Scientific) solution where the pH is neutral. Finally, the

mixture was filtered, washed with Milli-Q water and freeze-dried to obtain graphene oxide sulfonate (GO–SO_3).

2.1.5 Synthesis of graphene oxide thiol

Graphene oxide thiol (GO–SH) was produced using the method outlined in 2.1.2 and the starting material was GO–SO_3 obtained from 2.1.4.

2.1.6 Synthesis of phosphonate-modified graphene oxide

Phosphonate-modified graphene oxide was prepared by edge modification (GO–$PO(OH)_2$) and radical polymerisation of PVPA-*co*-AA (GO–PVPA), which the procedure is described in 2.2.3. In this instance, the starting graphene materials were GO–SH obtained from 2.1.5 and GO powders (GO graphene, William Blythe) for edge modification and radical polymerisation, respectively.

2.2 Characterisation of graphene and modified-graphene

2.2.1 Fourier-transform infrared spectroscopy

Fourier-transform infrared (FTIR) spectra were acquired from 4000-400 cm^{-1} with 32 scans and 4 cm^{-1} in transmission mode using Nicolet 5700 FTIR spectrometer (Thermo Fisher). Spectra were analysed using OMNIC software. Samples were prepared by mixing 0.2 mg of graphene with 0.3 g of KBr (spectroscopic grade, 99%, Acros Organics) using mortar and pestle, then pressing them in a hydraulic press at 10 tons for 5 minutes to obtain a thin and transparent disc of sample.

2.2.2 Raman spectroscopy

Raman spectra were determined using Renishaw inVia, with a 633 nm He/Ne laser. The spectra were collected at Raman shifts from 100–3200 cm^{-1}, laser power was set at 10% (0.886 mW) with a Si reference for calibration (520 cm^{-1}), and exposure time was 10 seconds. Data were processed using WiRE 4.2 software to zero the baseline and remove cosmic rays. The ratio of D to G peak intensities (I_D/I_G) was calculated by averaging the measurements from three spots, and using the intensities calculated from Lorentzian fits to both peaks.

2.2.3 X-ray photoelectron spectroscopy

X-ray photoelectron spectroscopy (XPS) analysis was carried out on powdered samples. The X-ray source was an Al K_α source (1486.6 eV–, 15 kV, 10 mA). The pressure in the vacuum chamber was typically < $5x10^{-8}$ mbar throughout the measurements. CASA XPS software was used to fit the survey spectra. The binding energy was calibrated by charge correcting the binding energy (BE) of the sp^2 component of the C 1s peak to 284.8 eV. Then, the peaks for all elements were shifted automatically with the same amount based on the shift of C 1s peak. The C 1s peak was fit as five components summarised Table 2-1, which consistently fit the data adequately for all samples. Fits to $2p_{1/2}$ and $2p_{3/2}$ peaks were constrained to have identical FWHM values and an area ratio of 1:2.

Table 2-1. Fit parameters used for deconvoluting the XPS spectra for C 1s peaks.

Chemical identity (binding energy)[3]	Line shape[a]	Binding energy constraint	FWHM constraint
C 1s sp^2 (284.5 eV)	LA(1,1.6,50)	none	none
C 1s sp^3 (284.8 eV)	GL(30)	BE(sp^2) + 0.3 eV	none
C 1s C–O (285.5–286.5 eV)	GL(30)	BE(sp^2) + 2 eV	same as sp^3
C 1s C=O (287.5–288.9 eV)	GL(30)	BE(sp^2) + 4 eV	same as sp^3
C 1s π-π* (290–292 eV)	GL(30)	290–292 eV	none

[a] GL(30) is a symmetric lineshape that is 30% Lorentzian and 70% Gaussian. LA(1,1.6,50) is an asymmetric Lorentzian lineshape numerically convoluted with a Gaussian; at binding energies above the peak maximum, the Lorentzian function is taken to the 1.6 power.[4]

2.2.4 Thermogravimetric analysis

Thermogravimetric analysis (TGA) is a method to determine characteristic decomposition of different functional groups presented in materials. TGA was performed on a TA Instruments Q500 thermogravimetric analyser. 1–3 mg freeze-dried graphene was heated at 10°C min^{-1} from 30–800°C in an N_2 atmosphere.

2.2.5 Elemental analysis

Elemental analysis was used to determine an amount of carbon, hydrogen, nitrogen and sulphur (CHNS) in graphene and functionalised graphene. Elemental or CHNS analysis was performed using Thermo Scientific Flash 2000 Series.

2.2.6 Zeta potential measurement

Zeta potential was determined using a Malvern Zetasizer Nano series. Aqueous graphene suspensions (0.05 mg mL^{-1}) were prepared by dispersing graphene powder in deionised water, after which graphene suspensions were sonicated for 2–3 minutes and placed in disposable foldable capillary cells for testing. The measurement was repeated 6 times for each type of functionalised graphene.

2.2.7 Dispersibility assessment

Dispersibility was qualitatively assayed by dispersing pristine graphene (G), GO, and modified GFNs at a concentration of 0.1 mg mL^{-1} in Milli-Q water. Suspensions of pristine graphene and modified graphene (G–SO_3, G–SH, G–$PO(OH)_2$, G–PVPA) were sonicated for 5 minutes while 2-hour sonication was applied for suspensions of GO, GO–SO_3, GO–SH, GO–$PO(OH)_2$, and GO–PVPA to get homogeneous dispersions. Images of all suspensions were taken immediately after sonication and at 72 hours post-sonication.

2.2.8 Fabrication of modified graphene containing layer-by-layer constructs

Layer-by-layer (LbL) constructs of modified graphene and poly(ethyleneimine) solution (PEI, 50% w/v in H_2O, Fluka) were formed on glass slides and glass coverslips (13 mm diameter, No.1.5, Scientific Laboratory Supplies) by dip coating. These substrates were first cleaned by immersing in 5:1:1 (v:v) mixture of distilled water, H_2O_2 (30%, Fisher Scientific) and ammonia solution (35%, Fisher Scientific) at 75°C for 5 minutes, then, by UV/ozone treatment for 15 minutes, followed by surface modification with 3-(Trihydroxysilyl)propane-1-sulfonic acid (THSPS, 35% in H_2O, Fluorochem) solution by soaking overnight. THSPS-modified substrates were alternately dipped in 10 g L^{-1} of positively charged PEI solution 10 g L^{-1} and 0.1 g L^{-1} negatively charged functionalised graphene suspension. Each layer was left to form for 10 minutes. To eliminate excess polyelectrolytes and prevent cross-contamination of solutions, the substrates were rinsed with Milli-Q water after each deposition step and dried with nitrogen flow. LbL assemblies of modified graphene incorporated with PEI were composed of three bilayers (six layers).

2.3 Characterisation of layer-by-layer constructs

2.3.1 UV-Visible spectroscopy

UV-Visible spectra were obtained during LbL process by using Agilent Technologies Cary 60 over the wavelength range of 200–800 nm. UV-Visible spectra of GFN-containing LbL assemblies were measured every cycle of bilayers deposition to observe the change of absorbance during the LbL process.

2.3.2 Atomic force microscopy

Atomic force microscopy (AFM) was performed using an Asylum MFP-3D in tapping mode. The Gwyddion software was used to process images. Data was levelled by a mean plane subtraction, and horizontal scar correction was performed. LbL constructs were prepared on glass coverslips.

2.3.3 Contact angle measurement

Contact angle were measured on a Drop Shape Analyzer DSA100 (KRÜSS), by placing a 20 µL water droplet onto the LbL substrate and the angle recorded. Sessile analysis was performed.

2.4 Primary human osteoblasts response towards LbL constructs

2.4.1 Cell growth, expansion and seeding

Primary human osteoblasts (HOBs), which are isolated from cancellous bone of a 58-year-old male, were supplied from PromoCell GmbH (C-12750, Lot number 422Z051). HOBs were grown up in osteoblast growth medium (C27001, PromoCell GmbH), supplemented with 1% v/v antibiotic antimycotic solution (Penicillin-Streptomycin solution, Sigma-Aldrich), in CELLSTAR® T25 and/or T75 flasks (Greiner Bio-One). Once nearly 80-90% confluent of cell monolayer was reached, growth media was removed and washed with Dulbecco's phosphate buffered saline (DPBS, without calcium chloride and magnesium chloride, Sterile, Sigma-Aldrich) for approximately 10 seconds. 1-2 mL trypsin-EDTA solution (0.05% trypsin, 0.02% ethylenediaminetetraacetic acid, Sigma-Aldrich) was then added to the flasks to delaminate cell monolayer. The flasks were placed in an incubator (37 °C, 5% CO_2) for 5-7 minutes, after which a fresh warm medium, Dulbecco's Modified Eagle's Medium (DMEM, high glucose, Sigma-Aldrich) supplemented with 10% FBS and 1% v/v antibiotics antimycotic solution

(Sigma-Aldrich), was added. The collected cell suspension was centrifuged at 13,000 g for 5 minutes and re-suspended in a fresh warm DMEM.

Osteoblast-like cells, SaOS-2, were also used in this experiment. Saos-2 cells were supplied from the European Collection of Authenticated Cell Cultures (ECACC). SaOS-2 were grown up in McCoy's 5A medium (Modified, with sodium bicarbonate, without L-glutamine, Sigma-Aldrich) supplemented with 10% FBS, 1.5 mM L-glutamine solution (200 mM, BioXtra, Sigma-Aldrich), and 1% antibiotics antimycotic solution (Sigma-Aldrich). Cell expansion, and delamination were done as described above. McCoy's 5A medium was used in all procedures and experiments for SaOS-2.

To count cell number, 10 µL cell suspension was mixed with 10 µL trypan blue, after which 10 µL cell-containing mixture was placed into C-Chip haemocytometer (NanoEnTek) and viewed under light microscope using the 10x objective lens.

In the experiment, cells were seeded on LbL constructs at a density of 10,000 cells per cm^2 into 24-well plates (Greiner Bio-One) and incubated at 37°C, 5% CO_2. After 24 hours, post-seeding, culture medium was changed to remove un-attached cells. Culture medium was replenished every 2-3 days afterwards.

2.4.2 Osteogenic medium

Osteogenic medium for HOBs was prepared using DMEM (high glucose, Sigma-Aldrich) supplemented with 10% FBS, 1% antibiotics antimycotic solution (Sigma-Aldrich), 10 mM β-glycerophosphate (Sigma-Aldrich), 10 nM dexamethasone (Sigma-Aldrich), and 50 µg mL^{-1} ascorbic acid (<98 %, Sigma-Aldrich). Osteogenic medium for SaOS-2 was prepared using the same recipe but McCoy's 5A medium (Modified, with sodium bicarbonate, without L-glutamine, Sigma-Aldrich) was used instead of DMEM.

2.4.3 Osteogenesis induction procedure

To study the effect of materials on osteogenic mineralisation, HOBs seeded on LbL constructs were cultured in osteogenic medium to compare with those in basal growth medium. Cells were seeded at a density of 10,000 cells per cm^2 into 24-well plates (Greiner Bio-One) and incubated at 37°C, 5% CO_2. After 24 hours, post-seeding, basal growth medium was changed to osteogenic medium. Culture medium was then replenished every 2-3 days.

2.4.4 LIVE/DEAD assay for cell viability

Viability of osteoblasts on LbL constructs was evaluated by LIVE/DEAD Assay kit (Thermo Fisher Scientific) at 1, 4, and 7 days. The LIVE/DEAD stock solutions were thawed to room temperature. 20 µL of the 2 mM Ethidium Homodimer-1 (EthD-1) stock solution was added to 10 mL of DPBS. Then, 5 µL of the 4 mM calcein AM stock solution was added to the 10 mL EthD-1/PBS solution, giving the working solution.

At each time point, culture medium was removed from the samples and washed with DPBS. Approximately 150–200 µL LIVE/DEAD solution was added directly to cells, and incubated at 37% for 15–20 minutes in an incubator (37 °C, 5% CO_2). 10 µL fresh working solution was then added to a clean microscope slide. The wet coverslips were mounted onto the microscope slides. LIVE/DEAD stained cells were viewed using a Nikon Eclipse 50i fluorescence microscope with Plan Fluor 10X, 20X, and 40X objectives. Green fluorescence and red fluorescence filters were used to view live cells and dead cells, respectively.

2.4.5 Cell coverage measurement using ImageJ

After LIVE/DEAD images were obtained, cell coverage on surfaces were calculated using ImageJ software. Colour channels were split and images converted to greyscale, so that cells appeared as white areas. Threshold of images was manually adjusted to include all of the cell coverage area appeared in images. Cell coverage were calculated as the area fraction of white portion.

2.4.6 AlamarBlue assay

Cell metabolic activity was measured using AlamarBlue assay. The stock 'AlamarBlue' solution was prepared by dissolving 5 mg resazurin salt (Sigma-Aldrich) in 40 mL of sterile tissue culture grade DPBS. The working 'AlamarBlue' solution was prepared by diluting the stock solution in culture medium at 10% v/v concentration. Culture medium was removed from samples and samples were washed twice with warm, sterile DPBS. The light of the microbiological safety cabinet was turned off, after which 500 µL of the working solution was added to each well. The working solution was added into three additional wells, as controls. Samples were incubated at 37 °C, 5% CO_2 for 2 hours, following which 150 µL of solution was taken from each well and transferred to a 96-well plate. Three 150 µL samples were taken from each well

in order to take triplicate readings. Fluorescence was recorded using λ_{exc} = 530 nm, λ_{em} = 590 nm using a Plate reader (FLUOstar OPTIMA, BMG Labtech).

2.4.7 PicoGreen assay

A Quant-iT™ PicoGreen™ dsDNA Assay Kit (Invitrogen) was used to measure double-stranded DNA content. Working PicoGreen solution was prepared by diluting the stock 200x PicoGreen solution to 1x solution using 1x TE buffer. Deionised water was used as a lysis buffer. Culture media was removed from samples and samples were washed with DPBS twice. 600 µL of lysis buffer was added to each well, and the cell lysis in water was subjected to a freeze-thaw process three times to release DNA before proceeding with the assay. A 21G syringe needle was used to scrap and remove cells from substrates, after which cell-containing suspensions were transferred to eppendorfs, and centrifuged at 13,000 g for three minutes. 80 µL × 3 of supernatant was added to each well of a black-bottomed 96-well plate, along with 80 µL PicoGreen working solution. Solutions were incubated at room temperature for 5 minutes and protected from light. Fluorescence intensity was recorded with λ_{exc} = 480 nm, λ_{em} = 520 nm using a plate reader (FLUOstar OPTIMA, BMG Labtech). Fluorescence intensities were then converted to dsDNA concentration by reference to the DNA standard curve. DNA standards were made by diluting the DNA stock standard 50x in deionised water to obtain a working concentration of 1 µg mL^{-1}, from which a dilution series was prepared (in deionised water) in the range 0–1 µg mL^{-1}. The DNA standard curve is shown in Figure 2-1.

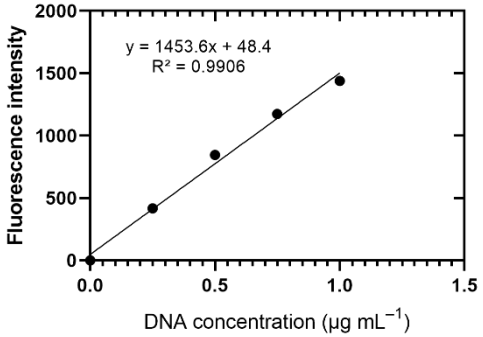

Figure 2-1. PicoGreen DNA standard curve.

2.4.8 Alkaline phosphatase activity assay

Alkaline phosphatase (ALP) activity of osteoblasts was measured at 7 days, 14 days, and 21 days post-seeding. The rest of cell lysis in water obtained from the samples for PicoGreen assay was used for ALP activity assay. 80 µL × 4 of cell lysate was added to each well of a 96-

well plate. 50 µL of Thermo Scientific Pierce 1-Step™ pNPP (p-nitrophenyl phosphate disodium salt) substrate solution was added into three wells. One well was used as a negative control, by which 20 µL of 2N NaOH (stop solution) was added before adding the pNPP substrate solution. The reaction was left at room temperature and protected from light for 60 minutes, after which stop solution was added to three wells of samples to terminate the reaction. A yellow hue in sample solution was developed due to the action of ALP on pNPP to yield p-nitrophenol (pNP) which can be measured at absorbance at 405 nm. In this study, a wavelength of 412 nm was used to detect the production of pNP due to instrument constraints. The standard curve was generated by reacting known amount of pNPP with ALP enzyme to calculate the amount of produced pNP as a function of absorbance. The pNP standard curve is shown in Figure 2-2. The ALP activity was calculated using the equation: A/V/T, where A is the amount of pNP generated (in µmol), V is the volume of cell lysate used in each well (in mL), and T is reaction time (in minutes).

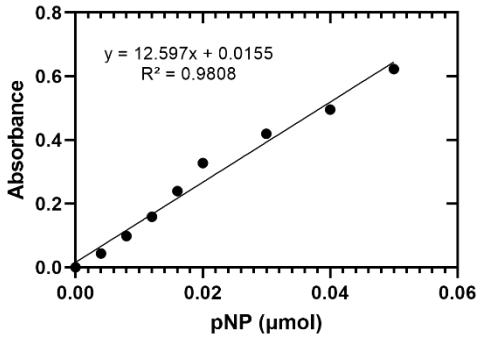

Figure 2-2. The pNP standard curve.

2.4.9 Alizarin red S staining

Culture medium was removed from samples, washed twice with DPBS, and once with de-ionised H_2O. Cells were fixed with 10% neutral buffered formalin solution (Sigma-Aldrich) for 15–20 minutes at room temperature. Alizarin red solution was prepared by dissolving 2 g Alizarin red S (Sigma-Aldrich) in 100 mL de-ionised H_2O and pH was adjusted to 4.2, after which the solution was filtered using 0.2-micron filter. 1 ml alizarin red solution (pH 4.2) was added into each well and left under darkness for 30 minutes. After this, samples were rinsed with de-ionised H_2O until the solution was clear. Then samples were viewed under 10x magnification on EVOSxl transmitted light microscope (AMG).

2.5 Laponite-based hydrogel scaffolds for bone tissue engineering

Gel forming grades of Laponite includes RD, XLG, and XL21.[5] Laponite RD is a general purpose grade which is used in universal applications such as surface coating, household products, and industrial fields. On the other hand, Laponite XLG and XL21 are personal care grades which possess high purity, certified low heavy metal, and low microbiological content.[5] Laponite XLG and XL21 are generally used for rheology control in personal care and cosmetic applications, but Laponite XL21 has been designed for use in products with formulations stabilised at pH 5.5 or lower.[5]

2.5.1 Preparation of Laponite suspensions

Laponite XLG (kindly gifted by BYK Additives, Widnes, UK and Dawson's lab from the University of Southampton) was used in this thesis. Laponite dispersions were prepared by adding Laponite powder in Milli-Q water (18.2 MΩ cm, pH 7) at the desired concentration, with stirring for 2 hours. In this experiment, GO suspension (0.1 g L^{-1}) and PVPA-*co*-AA solution (0.5 mg mL^{-1}) were used in preparation of composite hydrogels. For example, to prepare 3% Laponite composite hydrogels, 0.3 g Laponite powder was dispersed in 9 mL GO suspension, with stirring, after which 1 mL PVPA-*co*-AA solution was added into mixture. The mixture was left under stirring for 2 hours.

2.5.2 Rheological analysis

Rheological measurements were conducted on the new Discovery Series Hybrid Rheometer (DHR-2, TA Instruments) using a 20 mm parallel plate geometry. 1.8 mL Laponite suspensions prepared from 2.6.1 were loaded onto the rheometer plate with a 4.5 mm gap. Gels were soaked at 37 °C for 5 minutes prior testing for all rheological measurements.

2.5.2.1 Determination of viscoelasticity and the limit of LVE region

Storage (G') and loss (G'') modulus of Laponite-based hydrogels were recorded in an amplitude sweep covering the range 0.01–75% strain at a constant frequency of 1 Hz (or 6.28 rad S^{-1}) and temperature of 37 °C.

2.5.2.2 Investigation of shear-thinning behaviour and injectability

Variations of viscosity were recorded over the flow sweep of shear rate from 0.01 to 300 S^{-1} at 37 °C to investigate a shear-thinning behaviour of Laponite-based hydrogels.

Injectability of Laponite-based hydrogels was performed on flow peak hold procedure in which hydrogels were subjected to alternating cycles of low shear rate (2 S^{-1}, 5 minutes) and high shear rate (200 S^{-1}, 5 minutes). Injectability was also investigated by injecting Laponite suspensions through a 21G gauge needle.

2.5.3 Cell seeding for 2D culture

SaOS-2 cells were expanded, delaminated, and counted as described previously in 2.4.1. Laponite suspensions prepared from 2.5.1 were placed into ThinCert™ Cell Culture Inserts (Greiner Bio-One) in 24-well plates and left at room temperature until a gel state was reached, after which hydrogels were sterilised under UV for 2 hours. 200 µL McCoy's 5A medium (Modified, with sodium bicarbonate, without L-glutamine, Sigma-Aldrich) supplemented with 10% FBS, 1.5 mM L-glutamine solution (200 mM, BioXtra, Sigma-Aldrich), and 1% antibiotics antimycotic solution (Sigma-Aldrich) was added on top of gel in insert and another 1 mL culture medium was put in well around insert. Samples were incubated at 37 °C, 5% CO_2 overnight prior cell seeding. Cells were seeded on top of hydrogels at a density of 20,000 cells per insert and incubated at 37°C, 5% CO_2. Cell culture medium both in inserts and wells was changed on the following day after seeding to remove un-attached cells, and every 2-3 days afterwards.

2.5.4 Cell encapsulation within Laponite hydrogel scaffolds

Cell expansion, delamination, and counting were done as described in 2.4.1. A seeding density used in this experiment is 5×10^6 cells mL^{-1}. Cell encapsulation within hydrogel structure was attempted by two different procedures as described below;

2.5.4.1 Cell encapsulation within hydrogel discs

Laponite dispersions prepared from 2.5.1 were sterilised by autoclave and consequently became gels. 100 µL of cell-containing culture medium at a density of 5×10^6 cells was mixed with 900 µL Laponite hydrogels using positive displacement pipettes (Gilson). 100 µL of cell-containing Laponite hydrogels were placed into ThinCert™ Cell Culture Inserts (Greiner Bio-

One) in 24-well plates to make hydrogel discs which were approximately 2 mm thick. Culture medium was replenished every 2-3 days.

2.5.4.2 Cell encapsulation within hydrogel droplets

Laponite dispersions prepared from 2.5.1 were sterilised under UV for 2 hours and used to produce gels immediately after preparation. 100 µL of cell-containing culture medium at a density of 5×10^6 cells was homogenously dispersed in 900 µL Laponite suspensions. Cell-containing Laponite hydrogels were then added drop-wise as 10 µL volume into culture medium in 24-well plates. There was only 1 droplet per well. Culture medium was changed every 2-3 days.

2.5.5 Osteogenic medium

Osteogenic medium was prepared as described previously in 2.4.2.

2.5.6 Osteogenesis induction procedure

Cells were encapsulated within hydrogels as described in 2.5.4. After 24 hours, post-seeding, basal growth medium was changed to osteogenic medium. Culture medium was then replenished every 2-3 days.

2.5.7 LIVE/DEAD assay

LIVE/DEAD reagent was prepared as stated previously in section 2.5.2. LIVE/DEAD assay was performed on hydrogels seeded with HOBs on the top layer at 1 and 5 days after seeding. At each time point, culture medium was removed from the samples and washed with DPBS for 20 minutes to reduce the auto fluorescence of gels. 200 µL of LIVE/DEAD reagent was then added directly to gels in insert and incubated at 37% for 40 minutes. 10 µL fresh working solution was added to a clean microscope slide, after which the incubated gel was placed on this slide. Images were acquired using Leica TCS SP5 confocal microscope where live cells fluoresce in green (excitation: 490–495 nm, emission: 515 nm) and dead cells fluoresce in red (excitation: 535 nm, emission: 617 nm).

2.5.8 AlamarBlue assay

Metabolic activity was measured by AlamarBlue assay at 1, 4 and 7 days. The procedure of measurement are described previously in 2.4.6.

2.5.9 Phalloidin staining

Phalloidin is used to visualise cytoskeleton of cells because it selectively binds to actin filaments. Culture medium was aspirated from wells, after which samples were washed with DPBS twice for 5 minutes each. Samples were fixed with 10% neutral buffered formalin solution (Sigma-Aldrich) for 45–60 minutes and washed with DPBS three times for 5 minutes each. Samples were then extracted with 0.1% Triton X–100 (Sigma-Aldrich) in DPBS for 5 minutes and washed with DPBS three times for 5 minutes each. Working solution was made by mixing 1 µL of 1000X phalloidin stock solution (CytoPainter Phalloidin-iFluor 488 Reagent, Abcam) in 1 mL of 1% BSA in DPBS. 200 µL working solution was added to each insert and well. Samples were left to incubate with phalloidin solution overnight at 4 °C, after which samples were washed with DPBS twice for 5 minutes each to remove the left-over phalloidin. Fluoroshield mounting medium (Abcam) was added 2 drops on the resultant gels and samples were visualised using Leica SP8 MP confocal microscope.

2.5.10 Histological staining

After 1 week and 3 weeks, post-seeding, the 3D culture samples were fixed with 10% neutral buffered formalin solution (Sigma-Aldrich) and embedded in paraffin blocks. Sections were cut using Leica RM2145 rotary microtome and placed on glass slides. Prior to staining, sections were de-waxed in xylene (Fisher Scientific) for 5 minutes and rehydrated through descending grades of ethanol (Fisher Scientific), 100%, 95%, 80%, and 70%, to water.

2.5.10.1 Haematoxylin and Eosin

Haematoxylin solution was prepared by dissolving 1 g of haematoxylin (Fisher Scientific) in 1 L of distilled water using gentle heat. 50 g aluminium potassium sulfate (Alum, ≥98%, Sigma-Aldrich) was added and dissolved using gentle heat. Once the alum was dissolved and the solution was cooled down, 0.2 g sodium iodate (≥99%, Sigma-Aldrich) was added and agitated to dissolve. The solution was then filtered and 20 mL of glacial acetic acid (Fisher Scientific) was added. Eosin solution was prepared by mixing 50 mL of 1% eosin (Eosin Y solution, Sigma-Aldrich) with 390 mL of 95% ethanol, after which 2 mL of glacial acetic acid (Fisher Scientific) was added.

Deparaffinised and rehydrated sections were stained in haematoxylin solution for 5 minutes, following which sections were immersed in running water for 5 minutes. Sections were then stained with eosin solution for 2 minutes and dehydrated by transferring directly to 95% ethanol 3 times and absolute ethanol 3 times for 1 minute each. After that, sections were cleared in xylene and mounted with coverslip using DPX mounting media (Sigma-Aldrich). Stained sections were visualised under light transmission using Leica DM2700 M microscope.

2.5.10.2 Alizarin red S

Alizarin red solution was prepared as described in 2.5.6. Deparaffinised and rehydrated sections were stained with alizarin red solution for 5 minutes. Sections were gently rinsed with de-ionised water to remove any excess stain and blotted. Sections were then quickly rinsed in absolute ethanol twice, cleared in xylene and mounted with coverslip using DPX mounting media (Sigma-Aldrich). Stained sections were visualised under light transmission using Leica DM2700 M microscope.

2.5.10.3 Collagen type I and fibronectin

Primary antibodies for Collagen type I and fibronectin staining used in this experiment were Goat Anti-Type I Collagen (Cambridge Bioscience) and Anti-Fibronectin antibody produced in rabbit (Sigma-Aldrich), respectively. Working solution was prepared by diluting primary antibody in diluent at a 1:200 dilution. Lab Vision Autostainer 480 (Thermo Scientific) and UltraVision Quanto Detection System HRP DAB Kit (Thermo Scientific) were used in this procedure. The kit components include Hydrogen Peroxide Block, Ultra V Block, Primary Antibody Amplifier Quanto, HRP Polymer Quanto, DAB Quanto Substrate, and DAB Quanto Chromogen.

In this protocol, all steps were performed at room temperature and buffer wash was applied at the end of each step, except for Ultra V Block incubation. Deparaffinised and rehydrated sections were firstly washed with buffer. Section slides were incubated in Hydrogen Peroxide Block to minimise nonspecific background staining due to endogenous peroxidase, after which sections were incubated with Ultra V Block to impede nonspecific background staining. A 1:200 dilution primary antibody was applied to section slides and left on incubation. Sections were then incubated with Primary Antibody Amplifier Quanto, followed by HRP Polymer Quanto. One drop of DAB Quanto Chromogen was added to 1 mL DAB Quanto

Substrate, mixed by swirling, and applied to sections. All slides were counterstained with haematoxylin, rinsed with buffer and de-ionised water, and mounted with coverslips. Stained sections were visualised under light transmission using Leica DM2700 M microscope.

2.6 Cell migration

Laponite suspensions were prepared as described in 2.5.1 and placed into ThinCert™ Cell Culture Inserts (Greiner Bio-One) in 24-well plates, and left at room temperature until a gel state was reached, after which hydrogels were sterilised under UV for 2 hours. SaOS-2 cells were expanded, delaminated, and counted as described previously in 2.4.1. Cells were labelled with Cell Tracking Dye Kit-Red–Cytopainter (Abcam) and re-suspended in serum-free McCoy's 5A medium (Modified, with sodium bicarbonate, without L-glutamine, Sigma-Aldrich) supplemented with 1.5 mM L-glutamine solution (200 mM, BioXtra, Sigma-Aldrich) and 1% antibiotics antimycotic solution (Sigma-Aldrich). Cells in serum-free medium were seeded on surface of clay gels at a density of 20,000 cells per insert, and 150 µL fresh serum-free medium was added into insert. 1 mL of serum-containing McCoy's 5A medium (supplemented with 10% FBS, 1.5 mM L-glutamine solution, and 1% antibiotics antimycotic solution) was added into well to create protein gradient. After 4 hours, 1 day, and 2 days post-seeding, media was removed and fresh serum-free media was added into insert while serum-containing media was added into well. Insert was transferred into 12-well plate and placed on Thermanox^{TM} coverslip (a reference position) which generate autofluorescence in blue. Diagram of experimental set up for cell culture and for image acquisition is shown in Figure 2-3. Cells labelled with red fluorescent dye were visualised under the CQ1 imaging system (Yokogawa) to acquire stacked images from a reference level to a top layer of cells on gel surface using the 4x objective lens. Slice spacing was 5 µm. The recombinant human platelet derived growth factor β (PDGF-BB, Invitrogen) was also used in this experiment to create protein gradient and encourage cell migration of osteoblasts, by which PDGF-BB was added into serum-containing culture medium at concentration of 5 ng mL^{-1}. The growth factor-containing medium was added in well while serum-free medium was added in insert as previously did. Stacked images were acquired using the SP8 LIGHTNING confocal microscope (Leica) with the 4x objective lens and slice spacing was 5 µm.

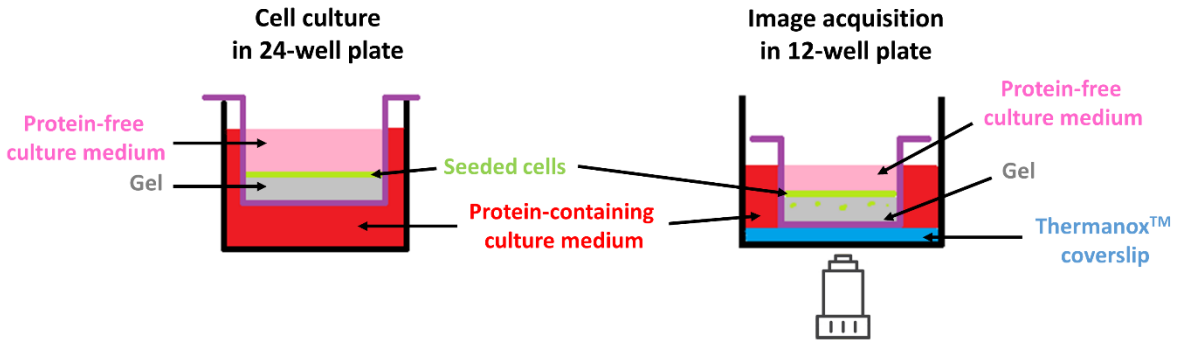

Figure 2-3. Diagram illustration of experimental set up for migration study.

2.7 Statistical analysis

Statistical analysis was performed on GraphPad Prism 7 software. One-way and Two-way ANOVA tests were performed along with Tukey's HSD (honestly significant difference) post hoc test to determine the origins of significance. Values reported were: no significant ($p > 0.05$), * ($p \leq 0.05$), ** ($p \leq 0.01$), *** ($p \leq 0.001$), **** ($p \leq 0.0001$).

2.8 References

1. Shellard, P. M.; Srisubin, T.; Hartmann, M.; Butcher, J.; Fei, F.; Cox, H.; McNamara, T. P.; McArdle, T.; Shepherd, A. M.; Jacobs, R. M., A versatile route to edge-specific modifications to pristine graphene by electrophilic aromatic substitution. *Journal of Materials Science* **2020,** *55*, 10284-10302.
2. Dey, R. E.; Zhong, X.; Youle, P. J.; Wang, Q. G.; Wimpenny, I.; Downes, S.; Hoyland, J. A.; Watts, D. C.; Gough, J. E.; Budd, P. M., Synthesis and Characterization of Poly (vinylphosphonic acid-*co*-acrylic acid) Copolymers for Application in Bone Tissue Scaffolds. *Macromolecules* **2016,** *49* (7), 2656-2662.
3. Ganguly, A.; Sharma, S.; Papakonstantinou, P.; Hamilton, J., Probing the Thermal Deoxygenation of Graphene Oxide Using High-Resolution In Situ X-ray-Based Spectroscopies. *J. Phys. Chem. C* **2011,** *115* (34), 17009-17019.
4. Fairley, N., *CasaXPS Manual 2.3.15 Spectroscopy*. Casa Software Ltd: 2009.
5. Additives & Instruments, B., Laponite: Performance Additive. *Technical Information B-RI 21* **2014**.

Chapter 3

Modified graphene-family nanomaterials for bone tissue engineering

3.1 Chapter abstract

Modified graphene-family nanomaterials (GFNs) containing phosphonate moieties for use in BTE were developed. The modified GFNs presented in this chapter were produced through edge-selective modification using electrophilic aromatic substitution, which causes minimal damage to the graphene sheet, thus preserving its physical properties, and via radical polymerisation of phosphonate-containing copolymer in the presence of GFNs. Pristine graphene and GO were used as starting materials for preparation of modified GFNs. In total, eight different graphene derivatives were prepared: G–SO_3, G–SH, G–$PO(OH)_2$, G–PVPA, GO–SO_3, GO–SH, GO–$PO(OH)_2$, and GO–PVPA. The presence of functional groups in as-prepared graphene analogous nanomaterials is confirmed by Fourier-transform infrared (FTIR) spectroscopy, Raman spectroscopy, elemental analysis, X-ray photoelectron spectroscopy (XPS), and thermogravimetric analysis (TGA). The functionalisation changed the aqueous dispersibility of pristine graphene, by reducing the aggregation. The phosphonate-modified GFNs produced via radical polymerisation possessed the higher composition of phosphorus in a comparison to modified graphene analogues prepared via edge-specific functionalisation.

Phosphonate-modified GFNs were incorporated into layer-by-layer (LbL) constructs with polyethyleneimine (PEI) and used to culture with osteoblastic cells. The ability of constructs to support cell adhesion, proliferation, alkaline phosphatase activity and osteogenic mineralisation of osteoblasts was assessed. The results show that only PEI/GO LbL construct could support cell attachment, proliferation, and osteogenic mineralisation of primary human osteoblasts (HOBs) whereas LbL constructs containing phosphonate-modified GFNs showed a variation in cell activities and functions. On the other hand, all GFN-containing LbL

constructs exhibited the ability to support cell adhesion, proliferation, and mineralisation of osteoblast-like cells (Saos-2).

The aims of research described and discussed in this chapter were to:

- Develop modified GFNs containing phosphonate moieties through edge-selective functionalisation and radical polymerisation of copolymer that can alter aqueous dispersibility of GFNs and provide functional groups that accelerate osteogenic mineralisation and tether biomolecules.
- Incorporate modified GFNs into LbL constructs that were uses as substrates for cell culturing.
- Assess and investigate the effect of modified graphene analogues on osteoblasts attachment, proliferation, and mineralisation.
- Highlight the most acceptable/suitable GFNs for further use in the fabrication of Laponite-based gels for BTE research.

3.2 Results

3.2.1 Characterisation of modified graphene-family nanomaterials

3.2.1.1 Fourier-transform infrared spectroscopy

FTIR was used to identify functional groups present in GFNs. FTIR spectra of graphene, graphene oxide, functionalised graphene derivatives and PVPA-*co*-AA are shown in Figure 3-1. Peaks at 1024 cm^{-1} and 1178 cm^{-1} are assigned to S=O stretching of sulfonic group ($–SO_3H$), and the peak at 1375 cm^{-1} is attributed to $–SO_3H$ stretching.[1] These peaks are found in the spectra of $G–SO_3$ and $GO–SO_3$ which indicate to the presence of sulfonic group, however, it is difficult to see in the spectra of G–SH and GO–SH because of a strong and broad peak at around 1120 cm^{-1} and the weakness of these bands in the IR. The peak of sulfonate group can be still observed in the spectra of $G–PO(OH)_2$ and $GO–PO(OH)_2$ which indicates to the incomplete thiol functionalisation of G–SH and GO–SH before polymerising with vinylphosphonic acid monomers. The S-H stretch of thiol group should be at around 2550-2600 cm^{-1}, but is not observed in G–SH. However, this stretch is known to be weak and can be obscured by any carboxyl absorptions in the same region.[2]

Peaks at 1165 cm^{-1} and 905–1000 cm^{-1}, display in the spectrum of PVPA-*co*-AA, can be assigned to P=O and P-O stretching, respectively, which are from poly(vinylphosphonic acid) whereas the peak at 1715 cm^{-1} is attributed to C=O stretching of carboxylic group from poly(acrylic acid).[3] The spectrum of GO–PVPA also exhibit characteristic peaks found in copolymer, confirming a successful functionalisation. In contrast, the spectra of G–PVPA, G–$PO(OH)_2$ and GO–$PO(OH)_2$ show an unclear peak of phosphonate group which might be due to a low degree of functionalisation. This is supported by the elemental composition obtained by CHNS analysis (Table 3-1), by which the amount of phosphorous was less than 1 wt% in G–$PO(OH)_2$ and GO–$PO(OH)_2$.

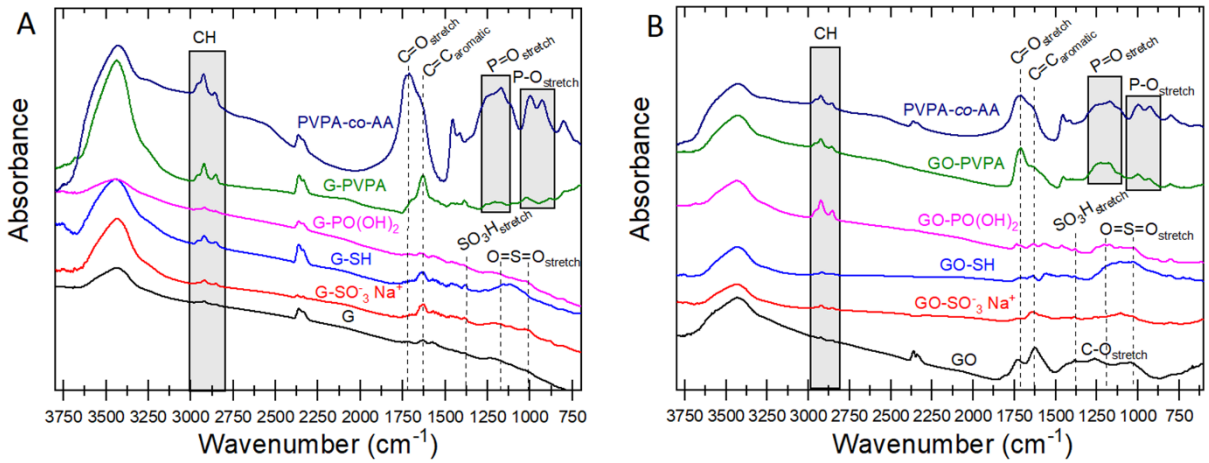

Figure 3-1. FTIR spectra of GFNs. A) Pristine graphene and modified graphene. B) GO and modified GO. Characterisation was performed in transmission mode with background correction. The vertical black lines and grey boxes represent peaks and regions of interest. The band of CO_2 at approximately 2350 cm^{-1} is due to a common background artefact in IR spectra.

Table 3-1. Elemental composition by CHNS analysis. All values in weight percent.

Material	C	H	N	S	P	Other (O, Na, etc.)
Graphene (G)	91.98 ± 2.57	0.62 ± 0.13	0.53 ± 0.11	-	-	6.87 ± 2.56
G–SO_3	81.04 ± 0.99	0.76 ± 0.07	0.49 ± 0.04	0.64 ± 0.20	-	17.07 ± 0.68
G–SH	82.61 ± 2.83	1.75 ± 0.30	0.73 ± 0.13	0.64 ± 0.04	-	14.27 ± 2.96
G–$PO(OH)_2$	81.57 ± 0.64	1.83 ± 0.31	0.91 ± 0.14	0.83 ± 0.11	0.62 ± 0.06	14.24 ± 0.52
G–PVPA	63.72 ± 10.17	3.33 ± 0.30	0.98 ± 0.79	-	2.58 ± 0.85	29.39 ± 8.23
GO	52.74 ± 2.16	2.49 ± 0.16	-	-	-	51.85 ± 1.99
GO–SO_3	49.84 ± 1.24	2.54 ± 0.25	0.35 ± 0.11	2.97 ± 0.21	-	44.30 ± 0.66
GO–SH	66.76 ± 0.66	2.10 ± 0.18	0.22 ± 0.08	0.26 ± 0.1	-	30.66 ± 0.49
GO–$PO(OH)_2$	66.97 ± 0.48	2.36 ± 1.07	0.99 ± 0.11	0.86 ± 0.08	0.42 ± 0.10	28.40 ± 1.43
GO–PVPA	44.36 ± 1.80	4.45 ± 0.30	0.20 ± 0.10	-	4.00 ± 0.38	46.99 ± 1.22

3.2.1.2 Raman spectroscopy

Raman spectra are displayed in Figure 3-2. All graphene derivatives showed three main characteristic peaks which are D, G and 2D peak for graphene-family nanomaterials (GFNs). The D band arises from the inherent defects and the edge effect of graphene crystallites while the G band appears due to in-plane bond stretching mode of sp^2 carbon and indicates to aromatic domain. A small D' peak, which is disorder-induced, can be observed at approximately 1600 cm^{-1} in pristine graphene and functionalised graphene. The 2D (also known as G') band originates from second-order Raman scattering process and relates to stacking order of nanoplatelets that can be used to identify the monolayer and multilayer graphene.[4, 5] The position of D, G and 2D peaks of each material are reported in Table 3-2 and are corresponding to the values in previous reports.[4, 5]

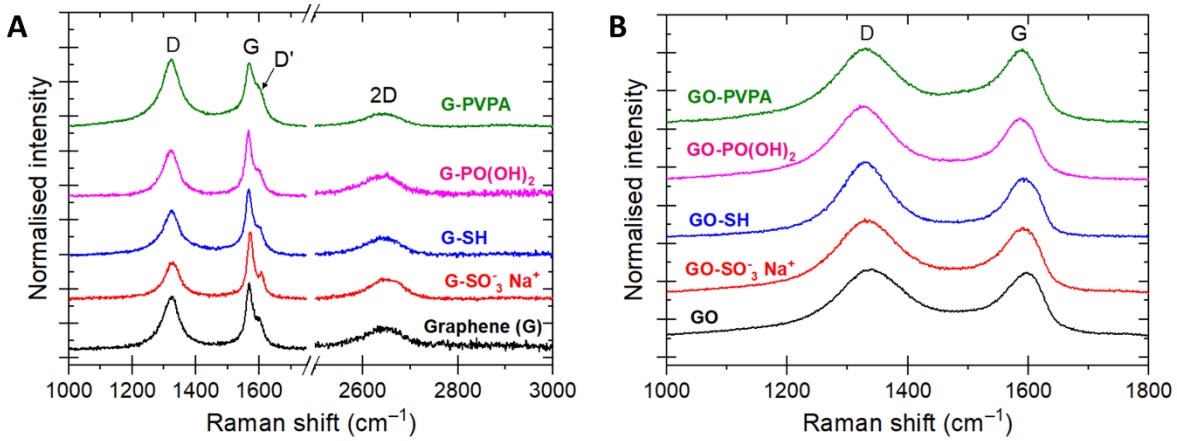

Figure 3-2. Baseline-corrected representative Raman spectra of functionalised graphene. A) Pristine graphene and modified graphene. B) GO and modified GO. Intensity is normalised to G peak intensity.

The D band in spectra of modified graphene, GO and functionalised GO displayed broad peaks with higher relative intensity due to the presence of more defects in structure when compared to pristine graphene. The defects or disorders were a result of exfoliation occurred by oxidation and ultrasonication that caused the breaking of π-π bonds at adjacent and planar carbon atoms, resulting in a conversion of sp^2 to sp^3 carbon and disrupting π conjugation.[6] This could be supported by the C 1s fitted peaks from XPS spectra of pristine graphene, GO, and modified GFNs in Figure 3-4. Defects or disorders also affected to the blue shift (upshift to higher frequency) of G band due to the lower area of in-plane sp^2 carbon and an alternating pattern of single-double carbon bonds.[5, 7, 8] The position of the 2D peak has been reported, both by Ferrari *et al.*[4] and Park *et al.*,[9] to increase with an increasing number of layers, as has

the full width at half maximum (FWHM) of the peak. The shape and position of 2D band for graphene and modified graphene were comparable to the previous report which indicated to graphene between 3–5 layers.[4, 10] There was no 2D peak in spectra of GO and functionalised GO due to the oxidation process which causes highly defective structure consisting of functional groups between graphitic layers, subsequently breakdown of stacking order.[11, 12]

Table 3-2. Data for Raman spectra of modified graphene-family nanomaterials. I_D/I_G was calculated form 3 measurements. Errors are from the repeated measurement.

Material	Position of D peak (cm^{-1})	Position of G peak (cm^{-1})	Position of 2D peak (cm^{-1})	FWHM of D peak (cm^{-1})	FWHM of G peak (cm^{-1})	FWHM of 2D peak (cm^{-1})	$(I_D/I_G)_{avg}$
Graphene (G)	1322	1572	2647	73	23	88	0.88 ± 0.02
G-SO_3	1327	1579	2649	73	38	93	0.90 ± 0.29
G-SH	1327	1579	2643	78	43	90	0.90± 0.17
G-$PO(OH)_2$	1322	1576	2642	68	46	95	0.90 ± 0.16
G-PVPA	1322	1576	2645	75	34	94	1.10 ± 0.04
GO	1343	1590	-	135	72	-	1.19 ± 0.05
GO-SO_3	1336	1585	-	142	84	-	1.22± 0.03
GO-SH	1330	1589	-	113	72	-	1.34± 0.06
GO-$PO(OH)_2$	1327	1582	-	117	49	-	1.29 ± 0.04
GO-PVPA	1334	1580	-	120	52	-	1.16 ± 0.05

The ratio of D to G peak intensities (I_D/I_G) is related to crystallite size and level of defects. A higher I_D/I_G (or higher intensity of D peak) indicates to smaller crystallite size (L_a), but a higher number of defects.[5, 13, 14] This relationship is called Tuinstra-Koenig (TK) relationship.[13, 14] However, this relationship can be applied to the L_a down to a limit of about 2 nm, after which the pattern reverses.[13, 15] Table 3-2 shows that functionalisation of graphene by free-radical polymerisation could introduce defects to graphene structure, giving rise to higher I_D/I_G compared to pristine graphene. In contrast, selective-edge modification seemed to cause minimal damage to the graphene sheet. This can be evident by comparable I_D/I_G of the selective-edge functionalised graphene analogues to I_D/I_G of pristine graphene (Table 3-2).

On the other hand, I_D/I_G of GO was lower than edge-functionalised GO but higher than GO–PVPA, implying that the edge-specific functionalisation likely introduces defects to the structure of GO which leads to the lower L_a and the higher D peak intensity which is following the TK relationship.[13, 14] With this interpretation, it is assuming that GO and functionalised GO in this thesis possessed crystallite size larger than 2 nm or were not fully amorphised carbons, therefore, the TK relationship is valid.[13, 15]

3.2.1.3 X-ray photoelectron spectroscopy

XPS was performed to study elemental compositions in modified GFNs. It can be seen from the XPS survey scan of GFNs (Figure 3-3) that all materials, including pristine graphene, had oxygen in their structure. The S 2p peaks presented in the XPS survey scan of GO–SO_3, but it is difficult to see in other edge-functionalised GFNs due to the lower degree of functionalisation. Moreover, the P 2p peaks were clearly observed in the survey scans of G–PVPA and GO–PVPA compared to G–$PO(OH)_2$ and GO–$PO(OH)_2$, implying to the higher amount of phosphorus which correlates to the CHNS analysis (Table 3-1) and elemental composition quantified from XPS survey scans (Table 3-3).

Compared to unfunctionalised graphene, the relative oxygen content (O/C ratio in Table 3-3) significantly increased in GO, edge-modified derivatives, G–PVPA and GO–PVPA due to the presence of oxygen-containing functional groups such as –COOH, –OH, –SO_3 and –$PO(OH)_2$, which agree with the evidence in the FTIR spectra in Figure 3-1.

Table 3-3. Parameters obtained from XPS survey scans and C 1s peaks of GFNs

Material	O/C ratio[a]	sp^3/sp^2 ratio[b]	Elemental composition (At%)[c]			
			C	O	S	P
Graphene (G)	0.01	No sp^3 detected	98.87	1.13	-	-
G-SO_3	0.10	2.76	90.06	9.42	0.52	-
G-SH	0.06	0.37	94.07	5.78	0.16	-
G-$PO(OH)_2$	0.11	1.14	89.56	10.15	0.12	0.17
G-PVPA	0.23	1.22	79.85	18.35	-	1.79
GO	0.32	2.72	75.58	24.42	-	-
GO-SO_3	0.50	8.60	63.39	31.72	4.89	-
GO-SH	0.10	0.27	90.47	9.27	0.25	-
GO-$PO(OH)_2$	0.17	1.28	85.02	14.54	0.17	0.27
GO-PVPA	0.37	2.90	70.60	26.10	-	3.30

[a,c] Taken from the quantification of survey scans shown in Figure 3-3 processed by CasaXPS.

[b] Taken from the deconvolution of C 1s scans shown in Figure 3-4 processed by CasaXPS.

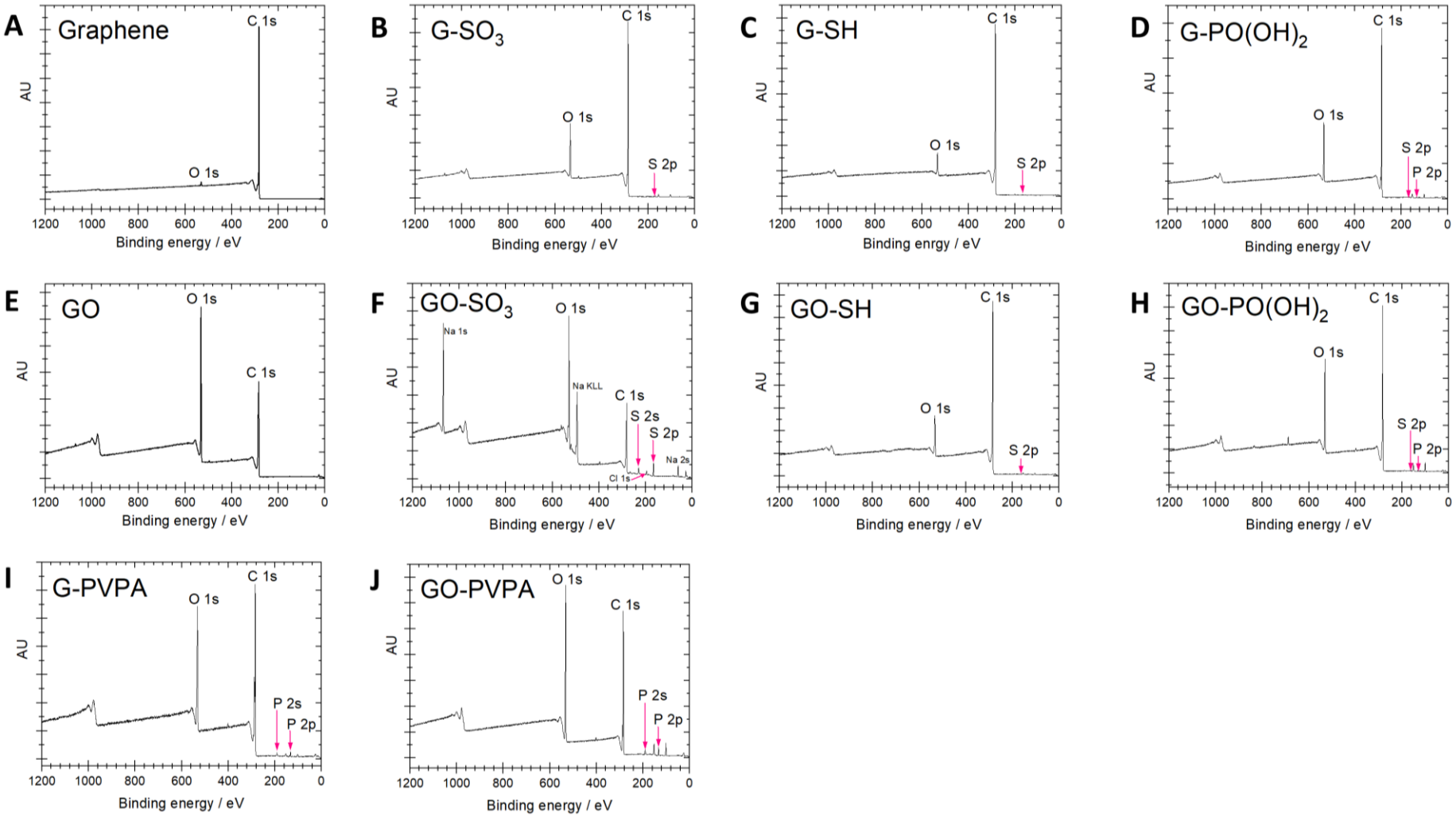

Figure 3-3. XPS survey scans of graphene-family nanomaterials.

C 1s peaks of GFNs with the peak fitting results are illustrated in Figure 3-4. Pristine graphene showed a characteristic peak of sp^2 carbon, which is asymmetry and the frequent presence of the π-π* shakeup, with a small degree of oxygen-containing functionality (C-O), corresponding to findings from Coleman *et al*.[16] The C 1s peak of G–PVPA was different to unfunctionalised graphene and other graphene derivatives because there was a peak appeared at around 288 eV which was assigned to C-O. This peak may arise from copolymer (PVPA-*co*-AA) which did not attach to graphene sheets or edges because I_D/I_G of G–PVPA from Raman (Table 3-2) was comparable to pristine graphene and slightly lower than edge-modified derivatives, suggesting to a low degree of functionalisation and oxidation.

Table 3-3 lists the sp^3/sp^2 ratios from the fits to C 1s. The fraction of sp^3 carbon (C-C) increased after sulfonation of graphene and GO which is due to a disruption of π-conjugated system. Interestingly, the sp^2 carbon fraction increased during thiol functionalisation. It is reasonable to consider that oxygen-containing functional groups such as –COOH, –OH and $–SO_3$ were reduced, upon transformation of $G–SO_3$ and $GO–SO_3$ to G–SH and GO–SH, respectively, which is similar to a reduction of GO to rGO.[17, 18] This is evident from decreasing in magnitude of the C-O peak fit of graphene thiol analogues (Figure 3-4C and Figure 3-4G).

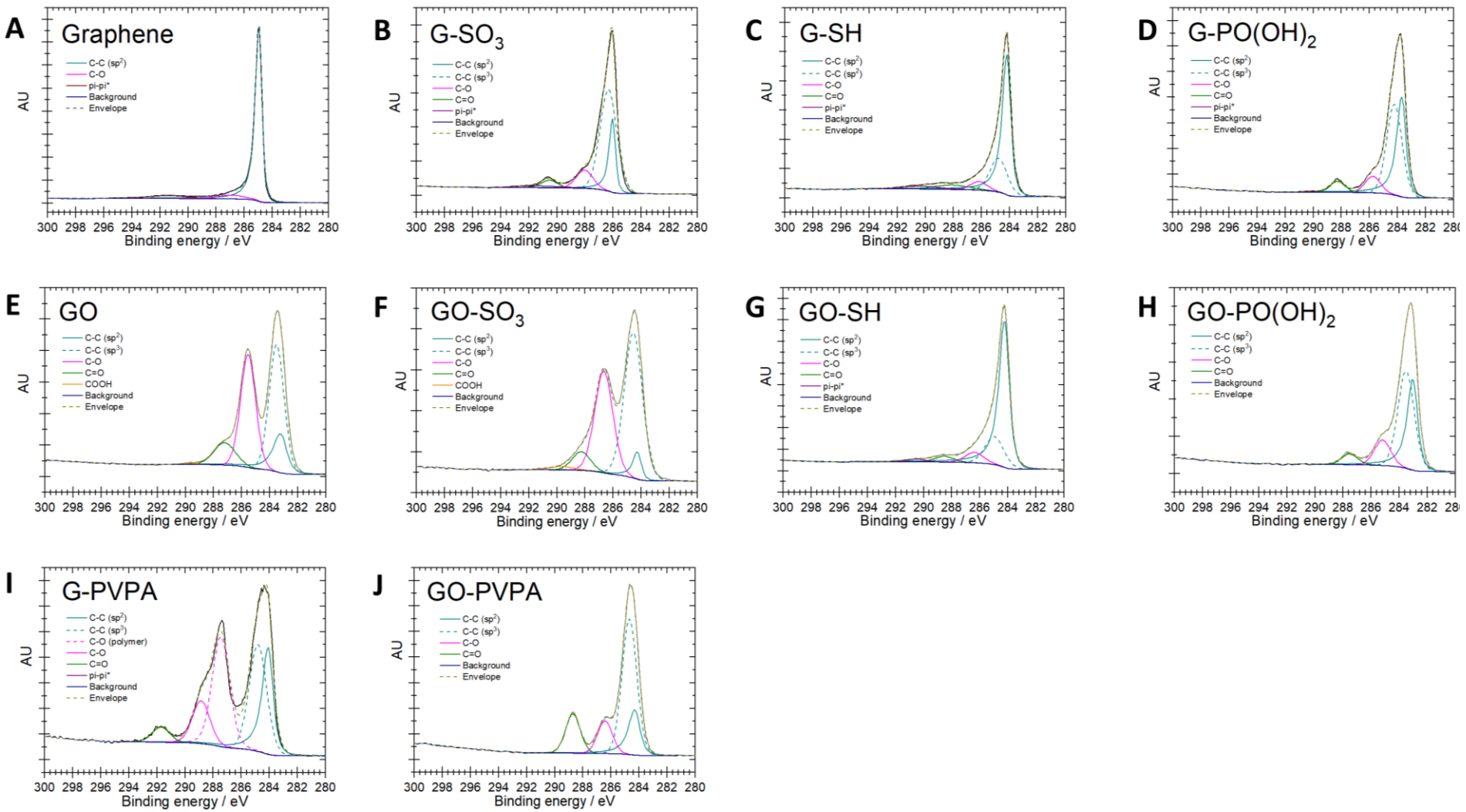

Figure 3-4. C 1s scans with the peak fitting results of unfunctionalised graphene and its derivatives.

The S 2p scans of edge-modified analogues are displayed in Figure 3-5. The presence of S 2p peaks could be observed in edge-functionalised derivatives. The S 2p peak fitting showed the existence of C-S bonds which are split into S $2p_{1/2}$ and S $2p_{3/2}$ as a result of spin-orbit coupling. These findings demonstrated to functionalisation of pristine graphene and GO. The XPS spectra of G–SO_3 and GO–SO_3 showed a single S 2p peak centred at 168 ± 0.8 eV which is attributed to –SO_3 groups while the XPS spectra of G-SH and GO-SH showed another S 2p peak located at lower binding energy (164 ± 1.6 eV), assigned to thiol groups (–SH).[19] Peaks of –SO_3 still remained in spectra of thiol-modified analogues (Figure 3-5C and Figure 3-5D), indicating the incomplete thiol functionalisation. Similarly, these characteristic peaks were also present in the S 2p scans of G–$PO(OH)_2$ and GO–$PO(OH)_2$ (Figure 3-5E and Figure 3-5F).

The P 2p scan (Figure 3-6) which has a centre at around 132–133 eV could be found in all phosphonate-modified analogues, showing phosphonate groups.[20] The P 2p spectrum could also be fitted into phosphorus $2p_{3/2}$ and $2p_{1/2}$. The relatively broad peak at higher binding energy (around 136–137 eV) found in the P 2p scan of G–PVPA probably arose from phosphates, but this peak is at a higher binding energy than noted in the literature.[20, 21] The baseline of the P 2p scans for both G–$PO(OH)_2$ and GO–$PO(OH)_2$ is difficult to create accurately due to noise (Figure 3-6A and Figure 3-6C). The change of baseline position could affect the area, roughly 0.3–0.5, and the centre position, approximately 0.02–0.3 eV, of fitted peaks for both G–$PO(OH)_2$ and GO–$PO(OH)_2$.

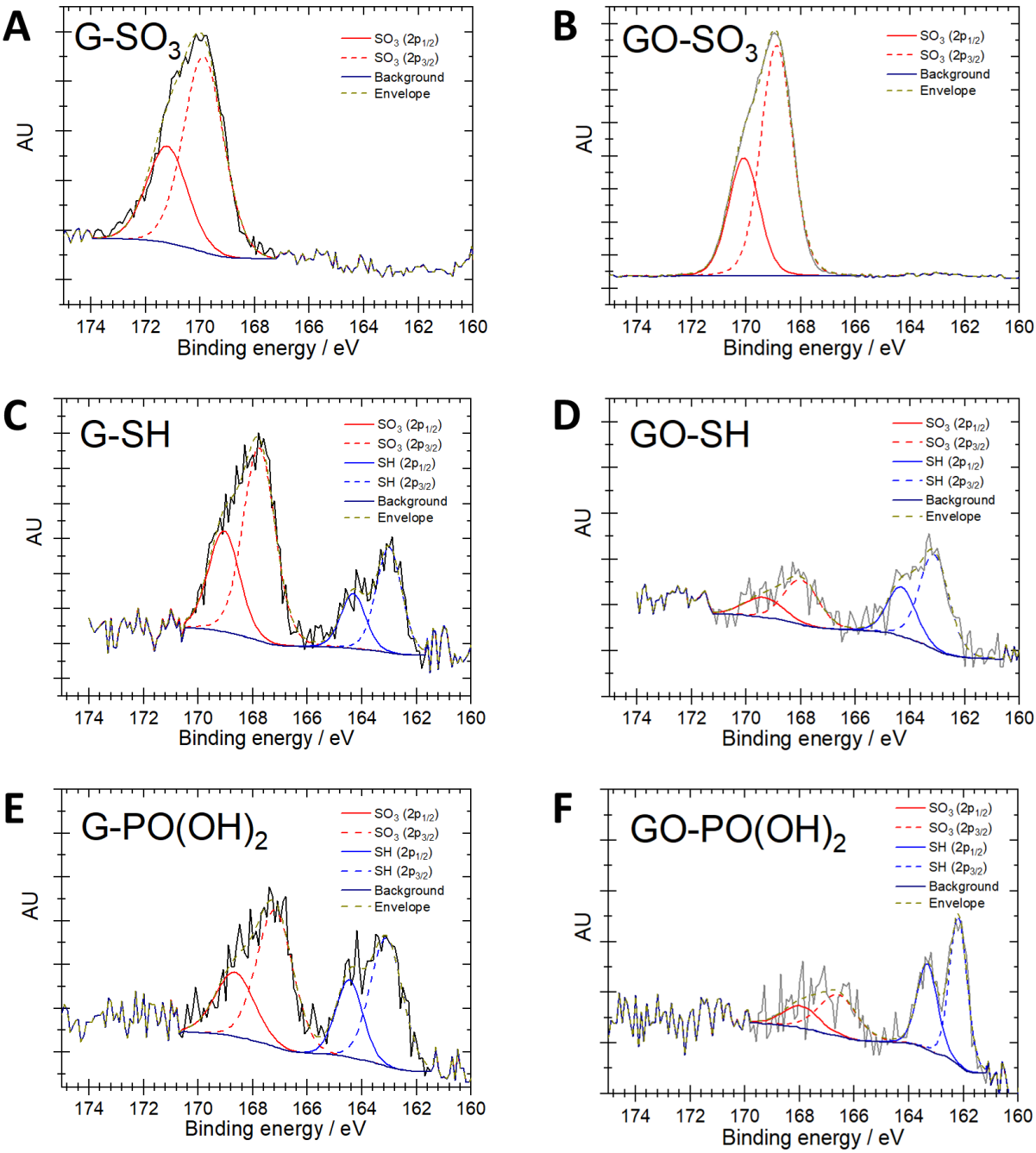

Figure 3-5. S 2p scans with the peak fitting results of unfunctionalised graphene and its derivatives.

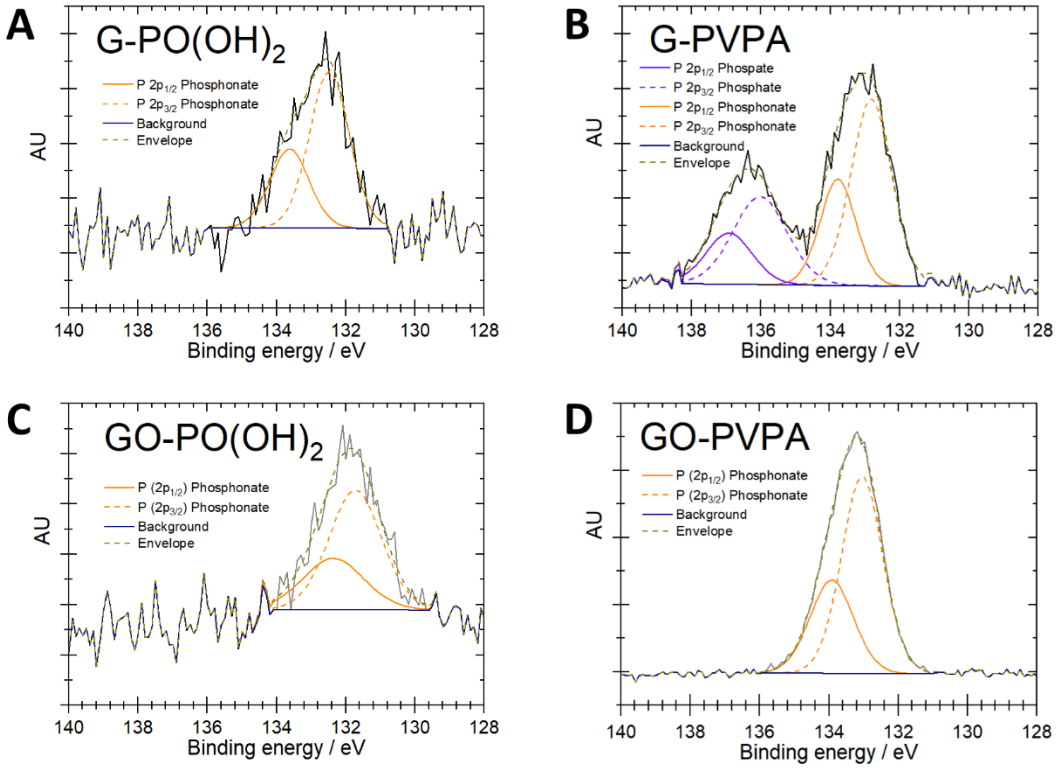

Figure 3-6. P 2p spectrum with the peak fitting results of phosphonate-modified graphene derivatives.

3.2.1.4 Dispersibility assessment

Dispersibility studies of pristine graphene (G), GO, and modified GFNs at a concentration of 0.1 mg mL^{-1} in Milli-Q water are shown in Figure 3-7. The aggregation of G in water was observed 72 hours post-sonication while other functionalised graphene materials still showed an aqueous dispersion, meaning that the functionalisation in this thesis altered dispersibility of pristine graphene. The aggregation was also observed in dispersions of GO–SH and GO–$PO(OH)_2$, likely due to the lack of oxygen-containing functional groups caused by thermal reduction during functionalisation which is consistent with the XPS evidence. The dispersibility of GFNs is consistent with the XPS and FTIR evidence of functionalisation of graphene.

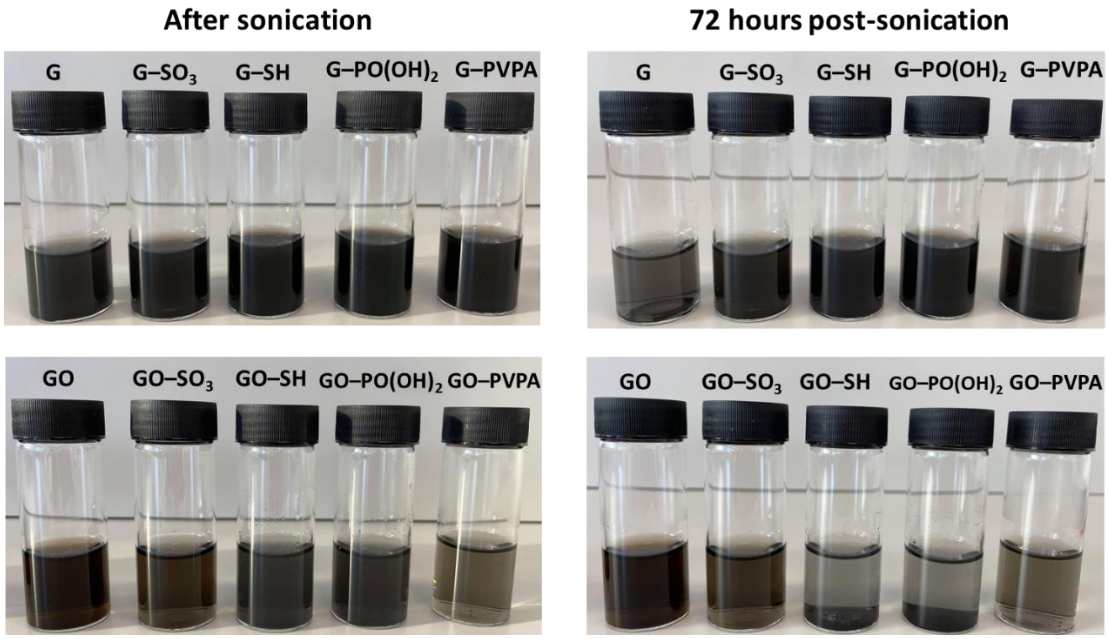

Figure 3-7. Dispersibility studies of functionalised graphene materials in water. Concentration: 0.1 mg mL^{-1}

3.2.1.5 Zeta potential

Zeta potential measurement can provide information about the physical stability of GFNs in dispersions.[22] Large positive or negative values of zeta potential, typically more than +30 mV and -30 mV, indicate to a good stability of dispersions due to electrostatic repulsion of individual particles.[22] The zeta potential of GO and the prepared functionalised graphene analogues in aqueous suspensions was measured and summarised in Table 3-4. All GFN-containing suspensions showed the net surface charge in negative values.

Table 3-4. Zeta potential of modified graphene derivatives and GO at pH 7. The measurement was repeated 6 times per each type of GFN suspensions. Errors are from repeated measurements.

Material	Zeta potential/ mV
G–SO_3	−47.40 (±0.91)
G–SH	−38.50 (±1.06)
G–$PO(OH)_2$	−36.30 (±0.31)
G–PVPA	−51.07 (±1.31)
GO	−50.12 (±1.35)
GO–SO_3	−48.22 (±0.85)
GO–SH	−50.17 (±1.81)
GO–$PO(OH)_2$	−45.28 (±1.04)
GO–PVPA	−52.20 (±0.32)

3.2.1.6 Thermogravimetric analysis

Thermogravimetric analysis (TGA) was applied to determine characteristic decomposition patterns for each material. TGA also allows an estimation of the fraction of functional groups in a material. Figure 3-8 illustrates TGA profiles of graphene, GO, modified GFNs and copolymer. The TGA profile of pristine graphene showed no significant mass loss due to the lack of functional group, in contrast to the major mass loss at about 180°C for GO due to a pyrolysis of the labile oxygen-consisting groups.[23] While graphene showed a steady mass loss over the temperature range (25 °C – 800 °C), TGA curves of modified GFNs, except for G–SO_3 and G–SH, exhibited the significant mass loss (≥30%) below 800 °C. However, G–SO_3 and G–SH only showed approximately 5% mass lost at 180 °C. Additionally, there is a significant difference in the mass-loss profiles of GO–SO_3 and GO–SH, consistent with the recovery of sp^2 carbon in GO–SH during the reduction process and a consequent improved temperature stability. This can be also supported by the derivative weight trace of GO–SH that shows a lower percentage of the peak for a pyrolysis of oxygen-containing groups at 180 °C.

The derivative weight TGA curve of PVPA-*co*-AA (Figure 3-8B) makes the three steps of thermal degradation easier to see. The first step began at around 140–260°C which was attributed to the loss of water formed in the self-condensation of the phosphonic acid groups[24, 25] and the release of CO and CO_2 from decarboxylation reaction.[26] The second stage occurred at approximately 260–380°C which was ascribed to the decomposition of vinyl (CH_2) backbone by chain scission[26, 27] and the third step (400–500°C) likely due to the cleavage of C-P bonds and the degradation of PVPA chains.[25, 27]

The TGA curves of phosphonate-modified graphene (G–PVPA and G–$PO(OH)_2$ in Figure 3-8B) showed the characteristic degradation steps of the copolymer,[24-27] with two peaks (140–260°C and 300–400°C) for G–PVPA and a very broad peak at 140-500°C for G–$PO(OH)_2$. Also, the same results were observed in thermal analysis of GO–PVPA and GO–$PO(OH)_2$ that their TGA curves exhibited two distinct peaks of degradation which are attributed to the degradation of copolymer and GO. Moreover, there were two distinct decomposition steps at approximately 555°C and 720°C for GO–$PO(OH)_2$.

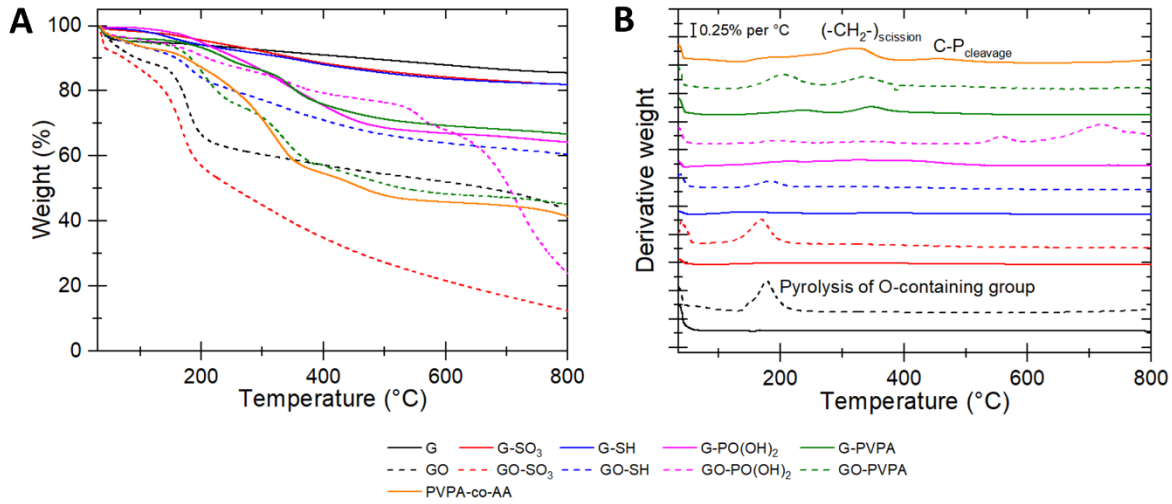

Figure 3-8. Thermogravimetric analysis (TGA) profiles of graphene, copolymer and functionalised graphene-family nanomaterials. A) Percentage of weight loss as a function of temperature. B) Derivative weight as a function of temperature. The scales have been normalised. Experimental conditions: heating rate 10 °C min^{-1}, N_2 atmosphere.

3.2.2 LbL constructs containing phosphonate-modified graphene analogues

3.2.2.1 Brief review of methods

Layer-by-layer (LbL) assembly was selected to prepare surfaces for investigation of cell response to material because it is an easily implemented technique and has started to be used for surface modification of biomedical materials.[28] Phosphonated graphene analogues (G–PVPA, G–$PO(OH)_2$, GO–PVPA, and GO–$PO(OH)_2$) were incorporated into LbL constructs with PEI and the effect of different GFNs on the formation of LbL assemblies was assessed. PEI was selected as the positively charged polymer due to its antimicrobial properties.[29] The PEI/GO, PEI/G–PVPA, PEI/G–$PO(OH)_2$, PEI/GO–PVPA, and PEI/GO–$PO(OH)_2$ LbL constructs are referred to collectively as the GFN-containing LbL constructs throughout this chapter.

3.2.2.2 UV-visible spectroscopy and images of the as-prepared LbL assemblies

The growth of layer-by-layer (LbL) assemblies of PEI and phosphonate-modified graphene and GO was monitored by UV-visible spectroscopy. Figure 3-9 shows that the absorbance of LbL films monotonically increased with an increasing number of bilayers due to the greater amount of GFNs in constructs. With the same number of bilayers, PEI/G–PVPA and PEI/GO exhibited the higher UV-visible absorbance in a comparison to PEI/GO–PVPA, PEI/ G–$PO(OH)_2$, and PEI/ G–PO(OH)2, which is likely due to the greater amount of G–PVPA and GO deposit on

surfaces (Figure 3-10). LbL assemblies of PEI-incorporated with G–$PO(OH)_2$, GO–PVPA, GO and GO–$PO(OH)_2$ exhibit a linear growth which indicate to a high-ordered multilayer films.[30]

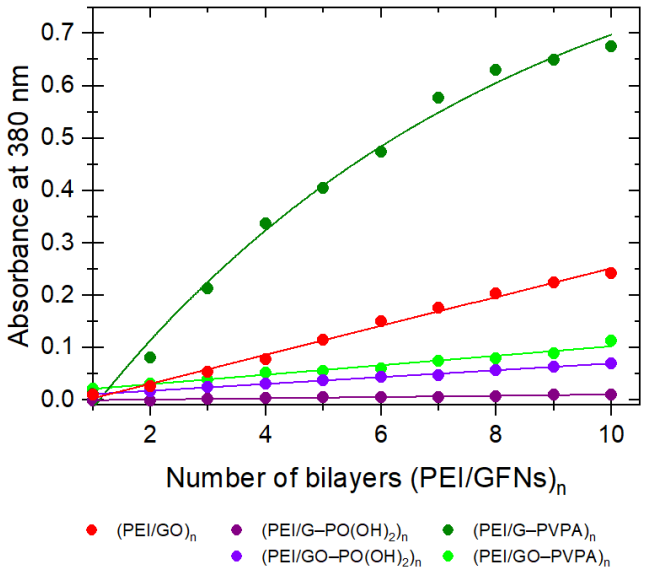

Figure 3-9. The growth of LbL assemblies of cationic polymer with negatively charge GFNs monitored by UV-visible spectroscopy. The absorbance of LbL constructs was collected as a function of layers, up to 10 bilayers.

Images of the as-prepared phosphonated GFNs-containing LbL constructs can be seen in Figure 3-10. The brown, grey, and black spots are characterised as GFN particles, indicative of the incorporation of graphene derivatives into the LbL constructs. PEI/GO, PEI/G–PVPA and PEI/GO–PVPA LbL assemblies appeared to have a greater coverage than LbL constructs made from other types of modified graphene nanomaterials. This is corresponding with the UV-visible absorbance reported in Figure 3-9 by which PEI/G–PVPA and PEI/GO exhibited the first and second highest absorbance, respectively, among all constructs. The agglomeration of GFNs and the inconsistency of surface coverage between different samples can be observed for all types of LbL constructs. Moreover, the homogeneous surface could not be obtained due to an uneven distribution of GFNs among the same piece of samples.

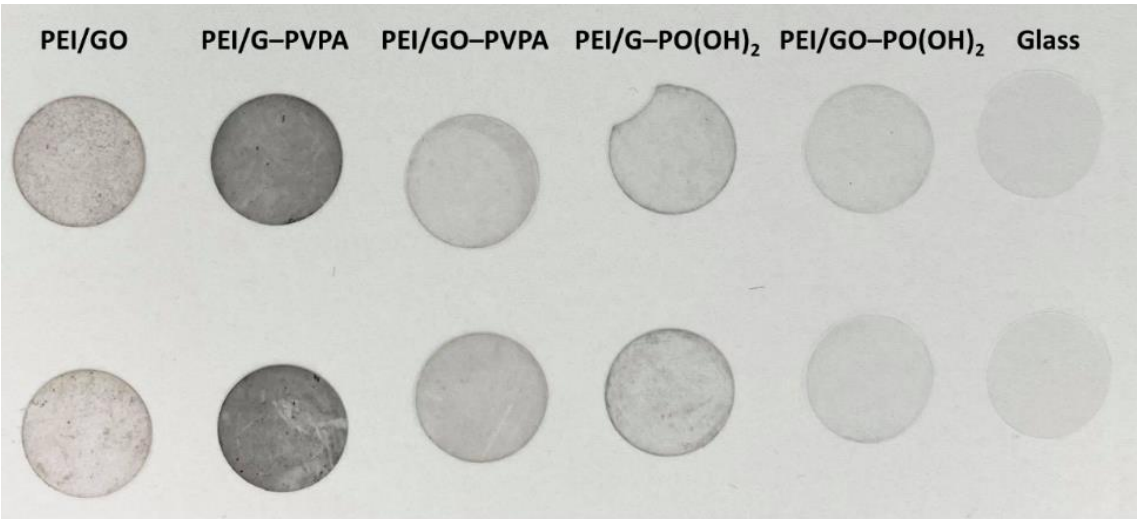

Figure 3-10. Images of as-prepared LbL constructs, grown on glass coverslips. Left to right: PEI/GO, PEI/G–PVPA, PEI/GO–PVPA, PEI/G–$PO(OH)_2$, PEI/GO–$PO(OH)_2$, and glass (3 bilayers, GFN terminated surfaces). The samples in two rows are same, but were prepared at different time, leading to a variation on surface coverage among different samples

3.2.2.3 Atomic force microscopy

Surface topography of the prepared LbL constructs was assessed by atomic force microscopy (AFM) measurement and the recorded images are displayed in Figure 3-11. The average roughness (R_a) and the root mean square roughness (R_{RMS}) were calculated and are reported in Table 3-5.

The AFM images reveal an agglomeration of GFNs on LbL assemblies. The R_a and R_{RMS} values of PEI/GO, PEI/G–PVPA, and PEI/GO–PVPA are higher than PEI/G–$PO(OH)_2$, indicating a greater loading of GO, G–PVPA, GO–PVPA compared to G–$PO(OH)_2$. This result is consistent with the UV-visible absorbance and images of LbL constructs. On the other hand, PEI/GO–$PO(OH)_2$ possessed the greatest roughness due to a large agglomerated GO–$PO(OH)_2$ flakes and was not mean to a greater amount of modified graphene particles deposited on substrate. It can be observed from the AFM images that GO–$PO(OH)_2$ and G–$PO(OH)_2$ could not provide a complete coverage surface. However, the variation occurred during sample preparation, the inconsistency of surface coverage between different samples, and the heterogenous distribution of GFNs , both within the same and among the different surface, could have an influence on characterisation. Consequently, the accurate UV-visible absorbance and surface characteristic obtained from AFM measurement may be hindered.

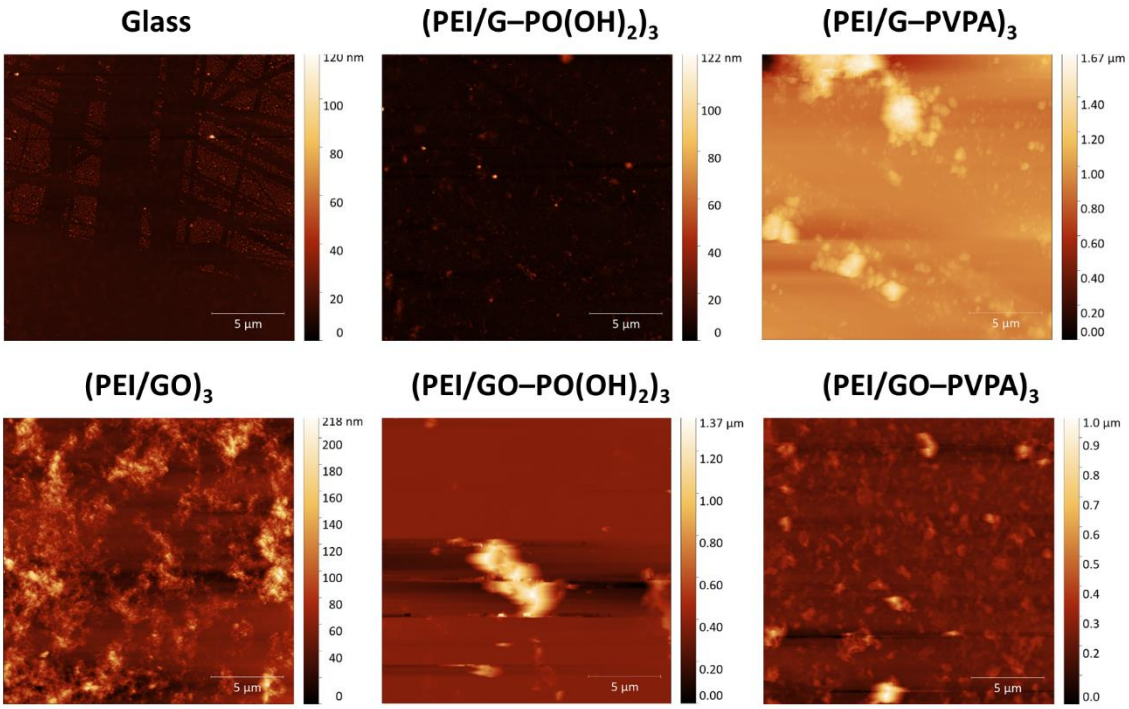

Figure 3-11. AFM height images of graphene-based LbL assemblies acquired in tapping mode.

Table 3-5. Roughness values of graphene-based LbL constructs obtained from AFM measurement.

Material	R_{RMS}/ nm	R_a/ nm
Glass	3.91	2.24
G–PO(OH)$_2$	2.70	1.31
G–PVPA	121.60	67.0
GO	22.96	17.02
GO–PO(OH)$_2$	129.00	52.30
GO–PVPA	60.09	34.82

3.2.2.4 Water contact angle measurements

The wettability of LbL constructs and glass were examined by water contact angle measurements, with the results are shown in Figure 3-12 and Table 3-6. GFNs-based LbL constructs showed a moderate wettability but had a lower contact angle compared to glass. PEI/GO provided the most hydrophilic surface among all materials. However, contact angle of PEI/GO in this study (43.1° ± 4.1°) is slightly higher than the 30° water contact angle of PEI/GO LbL substrates reported by Miyazaki *et al*.[31] This could be due to variability in density and types of oxygen-containing groups in GO.

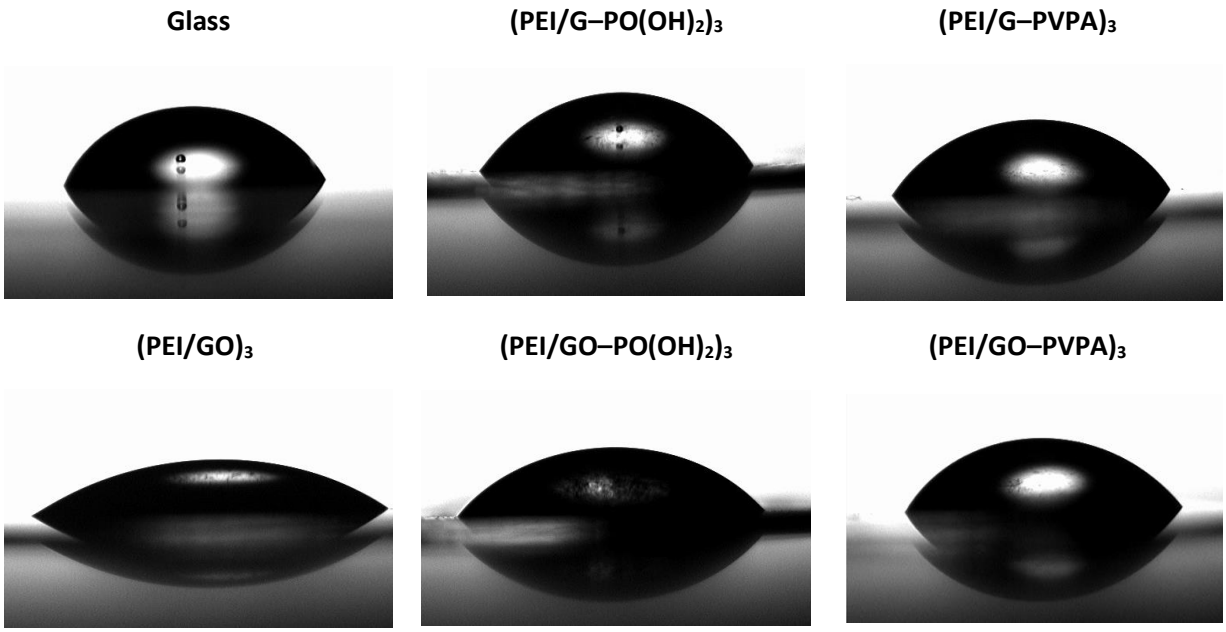

Figure 3-12. Water contact angle representative images of graphene-based LbL assemblies.

Table 3-6. Contact angles of GFNs-based LbL constructs. The averaged values are reported with standard deviation (*n* = 9).

Material	Contact angle
Glass	68.2° ± 2.8°
G–$PO(OH)_2$	57.0° ± 1.8°
G–PVPA	60.5° ± 2.6°
GO	43.1° ± 4.1°
GO–$PO(OH)_2$	54.5° ± 6.7°
GO–PVPA	57.9° ± 3.3°

3.2.2.5 NanoOrange assay of protein adsorption

In this study, bovine serum albumin (BSA) and fibronectin (Fn) were selected as a model for the study of protein adsorption on LbL constructs using NanoOrange assay. The amount of protein adsorbed on surfaces can be calculated from the difference between the starting protein concentration and the concentration of remaining protein in solution. The protein adsorption profiles of LbL are shown in Figure 3-13.

From Figure 3-13, after the incubation period, the amount of adsorbed BSA significantly increased on GFN-containing LbL constructs compared to the control (glass). Similarly, Fn was more significantly adsorbed on all LbL constructs than glass coverslip. Among LbL assemblies, PEI/GO, PEI/G–PVPA, PEI/GO–PVPA, and PEI/G–$PO(OH)_2$ had a significant higher amount of

adsorbed BSA protein compared to PEI/GO-PO(OH)$_2$ while the adsorption of Fn on surfaces was comparable on all GFN-containing LbL constructs.

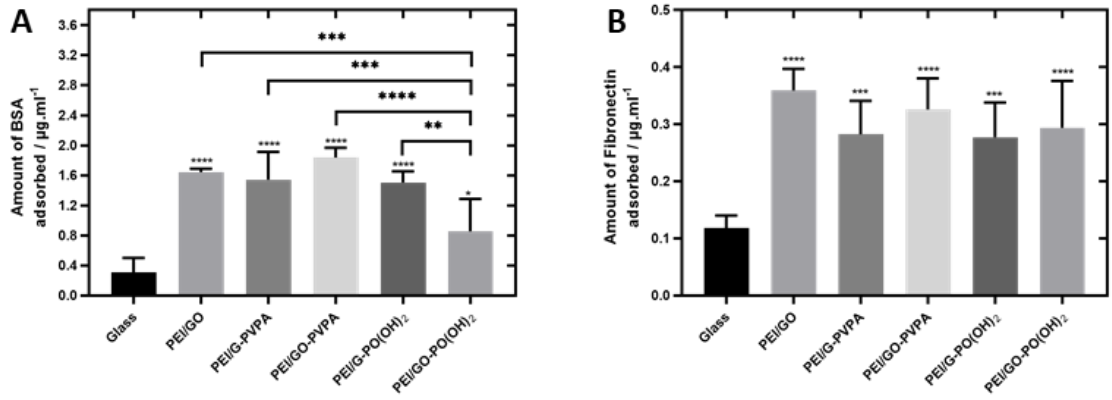

Figure 3-13. The quantification of adsorbed protein on LbL constructs, 3 bilayers (*n* = 3 samples), assessed by NanoOrange assay after 2-hour incubation of materials in 10 µg mL^{-1} protein solutions. A) Bovine serum albumin. B) Fibronectin. Error bars represent standard deviation. Stars above each bar shows statistical significance compared to glass (control) and significant differences between modified GFN-containing LbL constructs are indicated by horizontal lines. **** $p \leq 0.0001$, *** $p \leq 0.001$, ** $p \leq 0.01$, * $p < 0.05$.

3.2.3 Response of human osteoblasts towards GFN-containing LbL constructs

3.2.3.1 Brief review of methods

The LbL assemblies of PEI and phosphonate-modified GFNs (3 bilayers, top surface terminating with GFNs) were selected for culture with primary human osteoblasts (HOBs, passage number 6) and human osteosarcoma cell line (Saos-2, passage number 26) to assess the toxicity and the ability to support cell adhesion and proliferation, including promoting alkaline phosphatase activity and osteogenic mineralisation *in vitro*. Prior to cell seeding, LbL constructs were sterilised under UV light and incubated in culture media at 37 °C and 5% CO_2 overnight to enhance protein adsorption on surface. Cells were then seeded on constructs at a density of 10,000 cell per cm^2 (or 20,000 cells per well), for both HOBs and Saos-2, and cultured for a period of 21 days under standard conditions (37 °C, 5% CO_2) and media replenished every 2–3 days. LIVE/DEAD staining, AlamarBlue cell viability assay, PicoGreen DNA quantification assay, alkaline phosphatase (ALP) activity colorimetric assay, and alizarin red staining were performed at 7 days, 14 days and 21 days post-seeding.

3.2.3.2 LIVE/DEAD assay

The representative images obtained from LIVE/DEAD staining of HOBs on LbL constructs at 7, 14 and 21 days post-seeding are displayed in Figure 3-14. A different cell morphology between LbL constructs was observed, by which HOBs on glass (control) and PEI/GO LbL assemblies showed an elongated shape at 7 days post-seeding and remained elongated morphology throughout the culture period. In contrast, HOBs on PEI/GO–PVPA and PEI/G–$PO(OH)_2$ LbL constructs exhibited mostly rounded morphology with cell clumps and became more elongation at 21 days of culturing. HOBs on PEI/G–PVPA and PEI/GO-$PO(OH)_2$ remained rounded throughout the 21-day culture period. As compared to glass (control), it can be clearly seen that only PEI/GO LbL construct could support cell attachment with typical morphology of primary osteoblasts.

Cell coverage on each LbL construct was estimated at each time point by analysis of several LIVE/DEAD images (n = 6), with results presented in Figure 3-15. The percentage of cell coverage was calculated from viable cells (green) only. The area of HOBs coverage on surface increased over time throughout the culture period for PEI/GO and glass (control). At 7 days and 14 days post-seeding, there was no significant differences between phosphonate modified GFN-containing LbL constructs. At 21 days post-seeding, cell coverage of HOBs on PEI/GO–PVPA significantly higher than other types of phosphonated GFNs-containing LbL constructs. In a comparison between each GFN-containing LbL construct, PEI/GO possessed the significant highest cell coverage among all surfaces at every time points, with a comparable result to control.

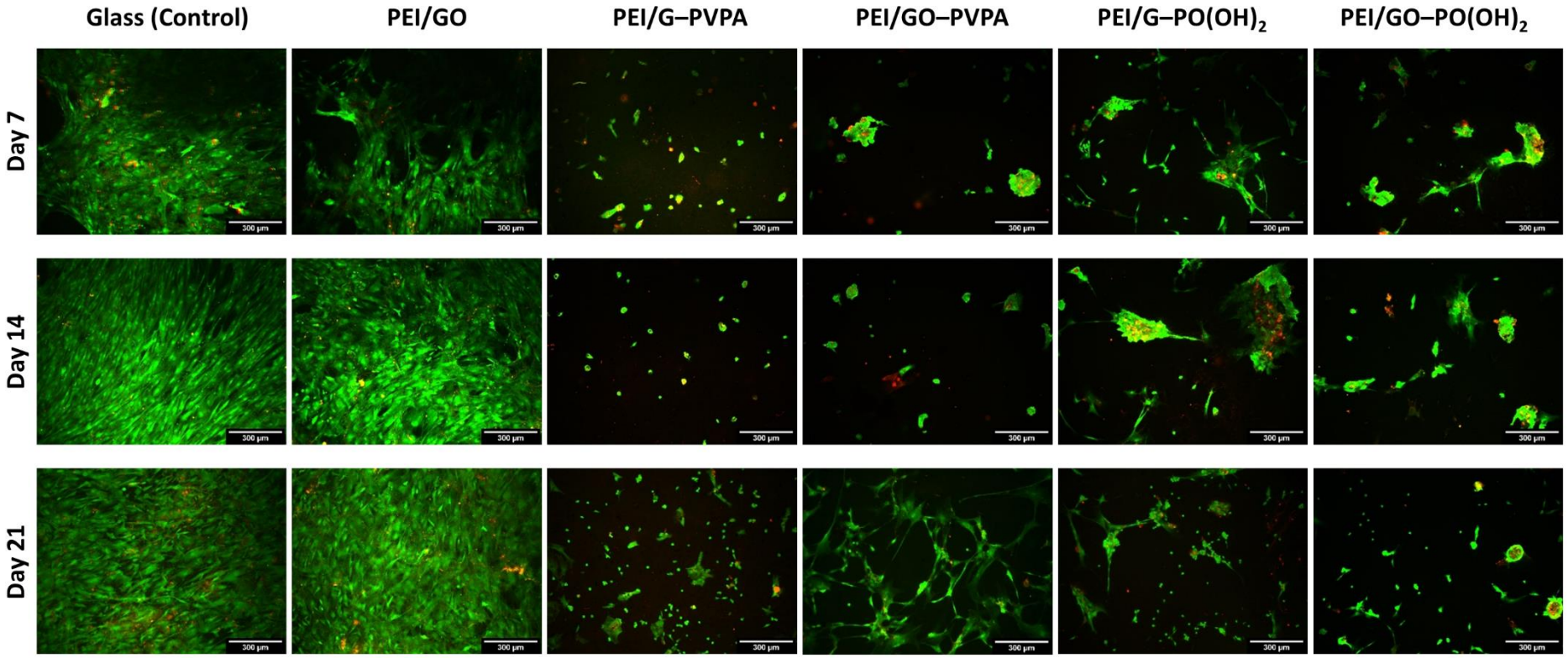

Figure 3-14. Live/Dead images of HOBs seeded onto LbL constructs in basal growth medium, stained with calcein AM (live cells: green) and EthD-1 (dead cells: red) reagent at 7, 14, and 21 days after seeding. Scale bar represents 300 µm.

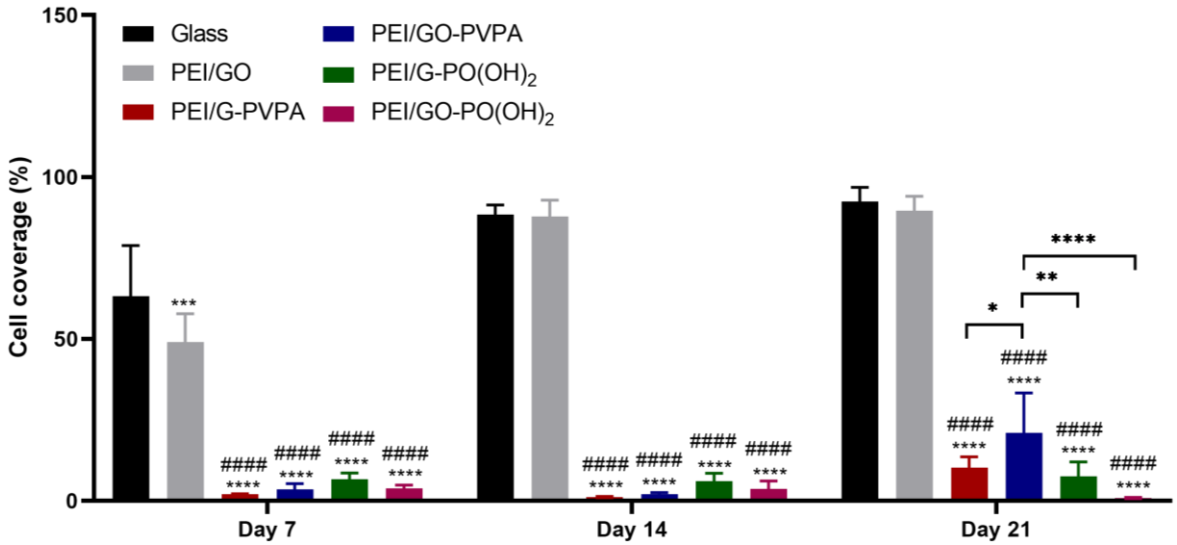

Figure 3-15. Cell covarage quantification (of live/dead staining) of HOBs seeded onto LbL constructs, 3 bilayers (*n* = 6 images). Stars and hash symbols above bars show results with statistical significance compared to glass (control) and GO, respectively, at the same time point. Error bars represent standard deviation. Significant differences between GFN-containing LbL constructs at the same time point are indicated by horizontal lines. **** $p \leq 0.0001$, *** $p \leq 0.001$, ** $p \leq 0.01$, * $p < 0.05$. #### $p \leq 0.0001$.

In contrast to HOBs, GFN-containing LbL constructs could support cell adhesion of Saos-2 throughout the culture period (Figure 3-16). Saos-2 seeded on glass and PEI/GO exhibited typical morphology at 7 days post-seeding and remained elongated until 21 days after culturing. Big clumps of rounded cells can be observed on glass at 14 days post-seeding and on all GFN-containing LbL constructs at Day 21 because cells became over confluent. Saos-2 on PEI/G–PVPA, PEI/GO–PVPA, PEI/G–$PO(OH)_2$, and PEI/GO–$PO(OH)_2$ displayed rounded morphology at Day 7 of the culture period. Cells on PEI/GO–PVPA and PEI/GO–$PO(OH)_2$ became more elongated shape at 14 days and 21 days post-seeding, respectively, whereas cells on PEI/G–PVPA and PEI/G–$PO(OH)_2$ remained rounded throughout the culture period. The number of cells on GFN-containing LbL assemblies proliferated over time. This was further quantified by AlamarBlue cell viability and PicoGreen DNA quantification assays.

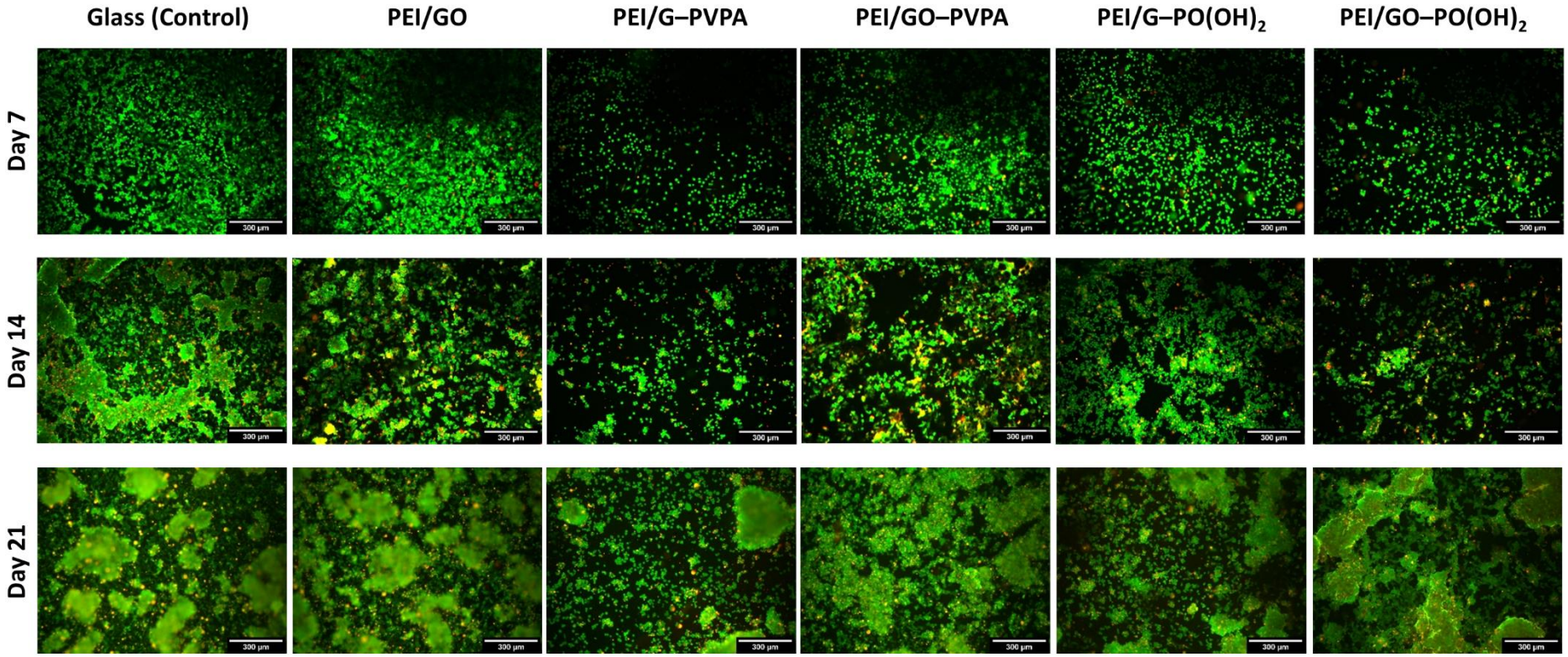

Figure 3-16. Live/Dead images of Saos-2 seeded onto LbL constructs in basal growth medium, stained with calcien AM (live cells: green) and EthD-1 (dead cells: red) reagent at 7, 14, and 21 days after seeding. Scale bar represents 300 µm.

Quantification of Saos-2 coverage area is displayed in Figure 3-17. All GFN-containing LbL surfaces had the comparable percentage of cell coverage at 7 and 14 days post-seeding, afterward, the significant increment in cell coverage was observed at Day 21. In a comparison between GFN-containing LbL constructs, PEI/G–PVPA and PEI/GO–PO(OH)$_2$ exhibited a significant lower cell coverage than other types of surfaces. All GFN-containing LbL constructs could support Saos-2 attachment with percentage of cell coverage above 60% at 21 days after seeding. It is worth noting that, due to over confluency, layers of cells on surfaces were washed out during washing step of analysis procedure. Consequently, the viability assay's accuracy may be compromised by the loss of cells.

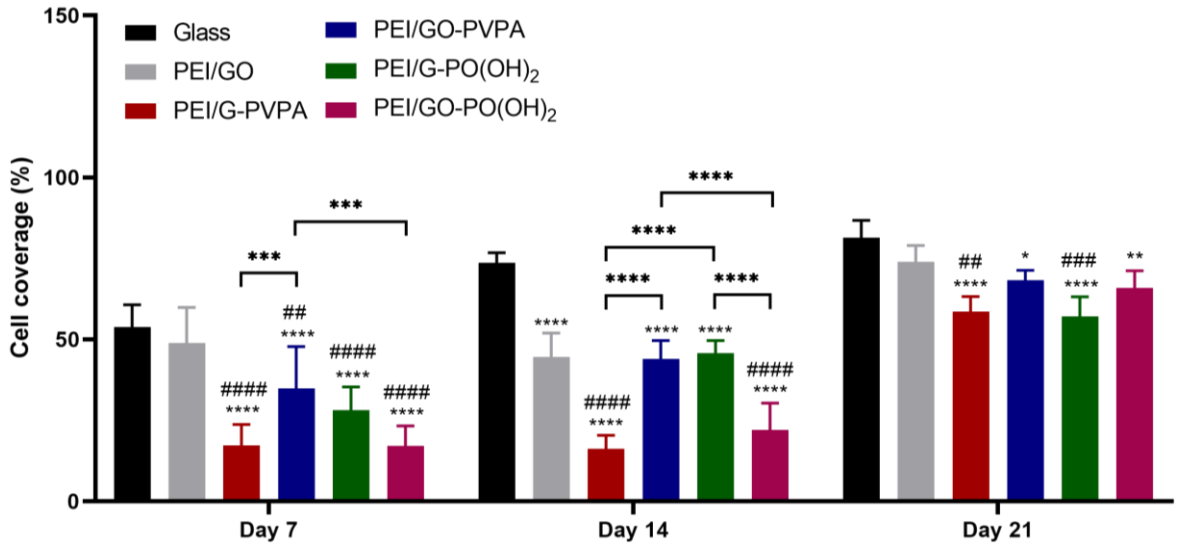

Figure 3-17. Cell coverage quantification of Saos-2 seeded onto LbL constructs, 3 bilayers (*n* = 6 images). Stars and hash symbols above bars show results with statistical significance compared to glass (control) and GO, respectively, at the same time point. Error bars represent standard deviation. Significant differences between GFN-containing LbL constructs at the same time point are indicated by horizontal lines. **** $p \leq 0.0001$, *** $p \leq 0.001$, ** $p \leq 0.01$, * $p < 0.05$. $^{\#\#\#\#}$ $p \leq 0.0001$, $^{\#\#\#}$ $p \leq 0.001$, $^{\#\#}$ $p \leq 0.01$.

3.2.3.3 Cell activity assays

3.2.3.3.1 Brief review of methods

The metabolic activity of osteoblastic cells on each LbL construct was measured over the 21-day period to further assess the effect of each LbL construct upon osteoblasts responses. DNA quantification of osteoblasts cultured on the LbL constructs was assessed using the PicoGreen DNA assay and metabolic activity measured using the AlamarBlue Assay.

3.2.3.3.2 Cell viability and proliferation of HOBs on LbL constructs using AlamarBlue assay

Cell metabolic activity was measured using an AlamarBlue assay to investigate cell viability and proliferation. Metabolically active cells result in the conversion of nonfluorescent resazurin salt to strongly fluorescent resorufin, meaning that a higher fluorescence intensity at 590 nm (I_{590}) is indicative of greater metabolic activity. The fluorescence intensities for HOBs on the LbL constructs are shown in Figure 3-18A. At the same time point, PEI/GO showed no significant difference in I_{590} compared to glass over the test period. In contrast, fluorescence intensities were found to decrease significantly for HOBs on PEI/G–PVPA, PEI/GO–PVPA, PEI/G–$PO(OH)_2$, and PEI/GO–$PO(OH)_2$, as compared to glass and PEI/GO.

The increases in cell metabolic activity of HOBs on LbL constructs are shown in Figure 3-18B. There was no significant difference in cell activity between 1 day and 7 days post-seeding for all LbL constructs and glass. PEI/GO and glass showed the significant development in cell activity after 14 days post-seeding. However, in a comparison between Day 7 and Day 21, the increase in cell activity on PEI/GO did not differ significantly, implying that HOBs on PEI/GO reached confluency after 14 days post-culturing. On the other hand, PEI/G–$PO(OH)_2$, and PEI/GO–$PO(OH)_2$ had a significant difference in cell activity after 21 days post-seeding, as the I_{590} at day 14 did not differ significantly from Day 1 and Day 7. The was no significant difference in cell metabolic activity for PEI/G–PVPA and PEI/GO–PVPA over the culture period although the absolute values of the fluorescence intensity increased since 14 days after seeding, meaning to no cell proliferation.

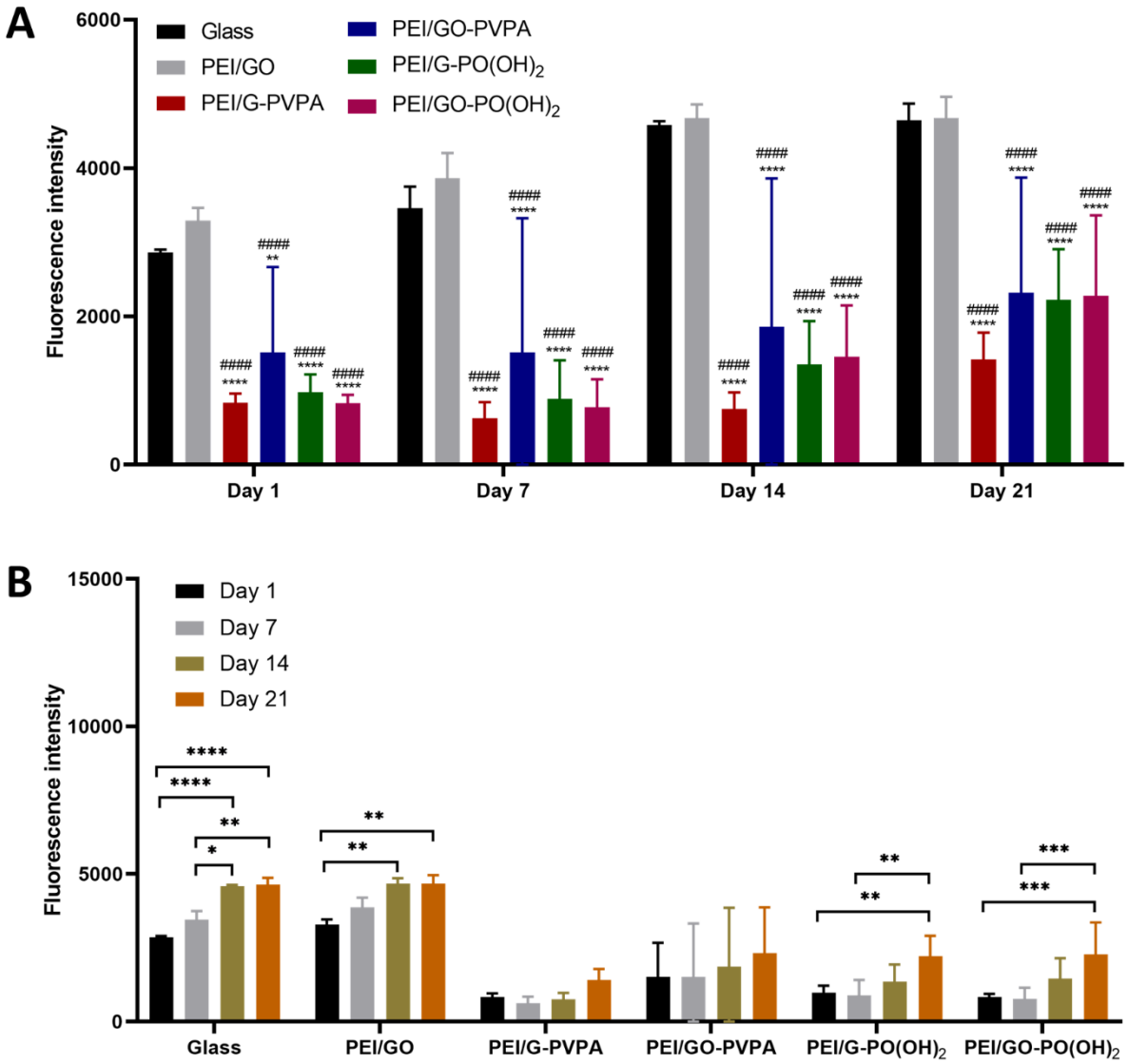

Figure 3-18. Quantification of metabolic activity of HOBs seeded onto LbL constructs in growth medium using AlamarBlue assay (*n* = 3 samples). Fluorescence intensities generated from blanks were excluded from each measurement. Error bars represent standard deviation. A) A comparison in fluorescence intensities between different surfaces at the same time point. Stars and hash symbols above bars show results with statistical significance compared to glass (control) and GO, respectively, at the same time point. B) A comparison in fluorescence intensities at different time point for the same surface. Significant are indicated by horizontal lines. **** $p \leq 0.0001$, *** $p \leq 0.001$, ** $p \leq 0.01$, * $p < 0.05$. #### $p \leq 0.0001$.

The effect of chemical osteogenic inducers towards cell metabolism of HOBs on LbL constructs was assessed at 7 days, 14 days, and 21 days post-seeding. Fluorescence intensities from AlamarBlue assay of HOBs on LbL constructs incubated in basal growth medium and osteogenic medium are reported in Figure 3-19. At 7 days after seeding, a significant difference in cell activity between cells incubated in growth medium and osteogenic medium was only found in HOBs seeded on PEI/GO–PVPA. HOBs cultured on LbL constructs (except

PEI/GO–$PO(OH)_2$) and glass incubated in osteogenic medium showed an increase in fluorescence intensities at 14 days and 21 days post-seeding, as compared to growth medium, meaning to enhanced cell metabolism. In contrast, PEI/GO–$PO(OH)_2$ had a comparable fluorescence intensities for HOBs cultured in both growth medium and osteogenic medium.

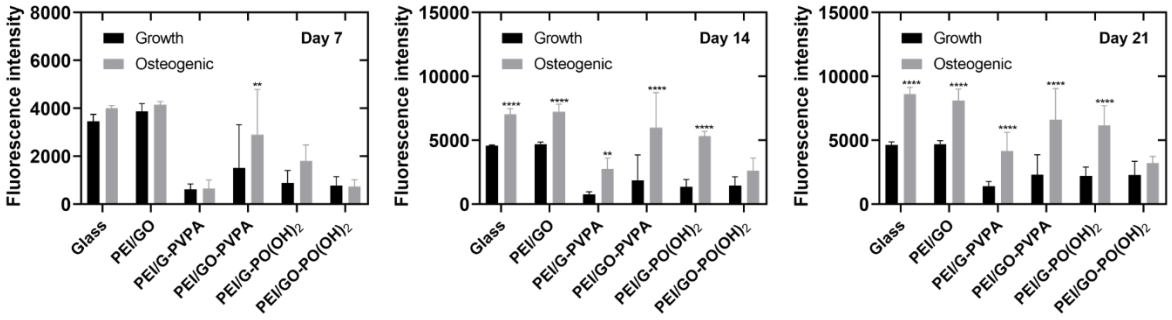

Figure 3-19. Quantification of metabolic activity of HOBs seeded on LbL constructs incubated in basal growth medium and osteogenic induction medium (*n* = 3 samples). Fluorescence intensities generated from blanks were excluded from each measurement. Fluorescence intensities of HOBs on LbL constructs incubated in growth medium are the same values as reported in Figure 3-18. Stars above bars show results with statistical significance of GFN-containing LbL constructs incubated in osteogenic medium compared to samples incubated in growth medium. **** $p \leq 0.0001$, *** $p \leq 0.001$, ** $p \leq 0.01$.

3.2.3.3.3 Cell viability and proliferation of Saos-2 on LbL constructs using AlamarBlue assay

The fluorescence intensities for Saos-2 on LbL constructs are shown in Figure 3-20A. All LbL constructs and controls showed an increase in absolute values of I_{590} (and hence cell metabolism) over the culture period, indicating the proliferation of Saos-2 cells. From Figure 3-20A, fluorescence intensities of cells on PEI/GO and control did not differ significantly over the test period, suggesting the same level of cell metabolism. On the other hand, PEI/G–PVPA showed a significant reduction in I_{590} when compared to PEI/GO at 1 day after culturing and compared to control at 7 days and 14 days post-seeding. Similarly, at 7 days post-seeding, I_{590} was only found to decrease significantly for Saos-2 cells on PEI/G–PVPA constructs as compared to other GFN-containing LbL constructs. At 21 days post-seeding, there was no significant difference in cell activity for Saos-2 on LbL constructs and glass.

The increment in cell metabolic activity of Saos-2 on LbL constructs, are presented in Figure 3-20B. The increases in cell activity between each time point differed significantly for all LbL constructs, evidencing that GFN-containing LbL assemblies were able to support cell metabolic activity, viability, and proliferation up to 21 days post-seeding.

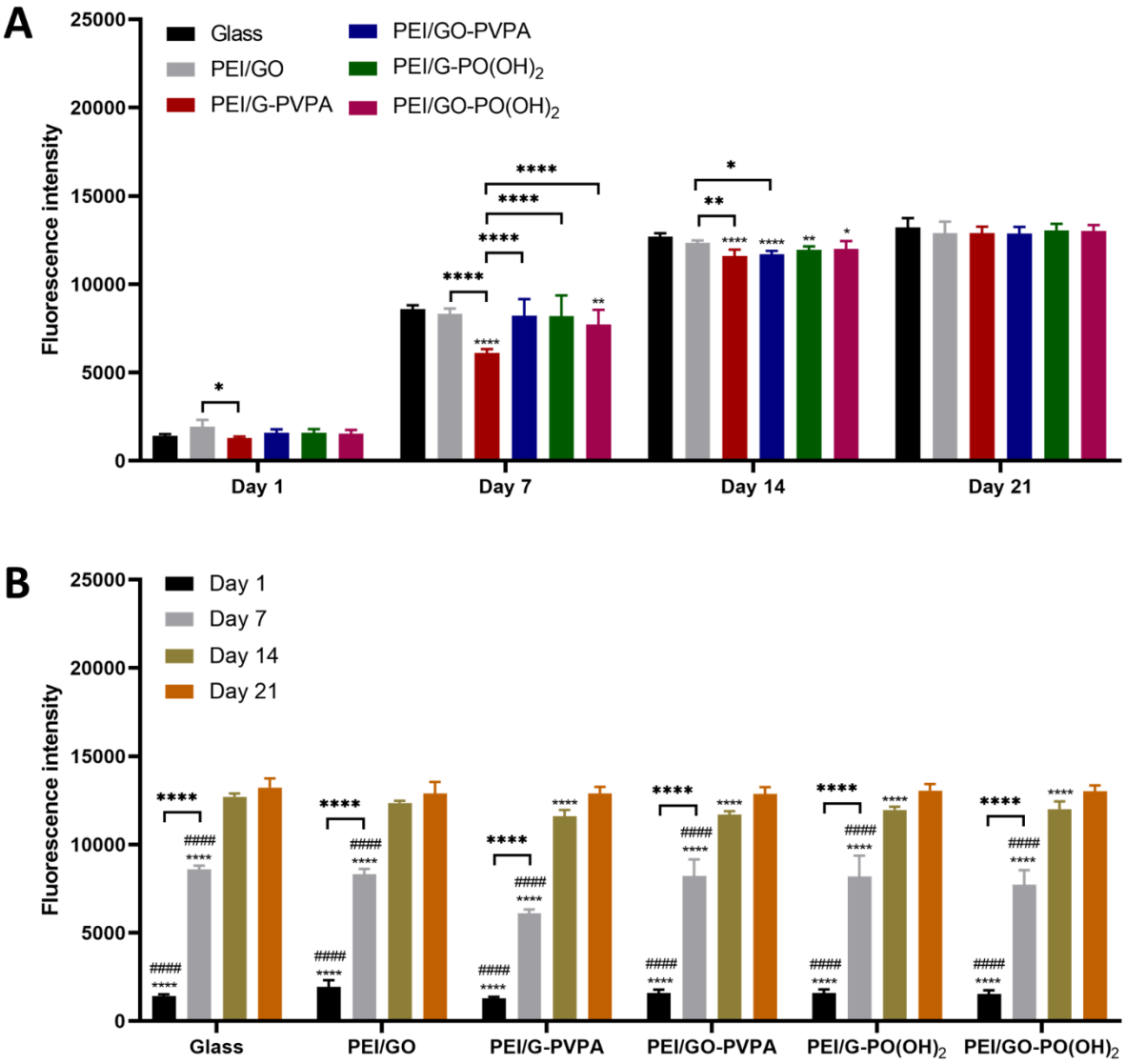

Figure 3-20. Quantification of metabolic activity of Saos-2 seeded onto LbL constructs in growth medium using AlamarBlue assay (*n* = 3 samples). Fluorescence intensities generated from blanks were excluded from each measurement. Error bars represent standard deviation. A) A comparison in fluorescence intensities between different surfaces at the same time point. Stars above bars show results with statistical significance compared to glass (control) at the same time point. Significant differences between GFN-containing LbL constructs at the same time point are indicated by horizontal lines. B) A comparison in fluorescence intensities at different time point for the same surface. Stars and hash symbols above bars show results with statistical significance compared to Day 21 and Day 14, respectively, for the same surfaces. Significant differences between Day 1 and Day 7 are indicated by horizontal lines. **** $p \leq 0.0001$, ** $p \leq 0.01$, * $p < 0.05$. #### $p \leq 0.0001$.

The effect of osteogenic medium towards cell activity for Saos-2 on LbL constructs was investigated at 7 days, 14 days, and 21 days post-seeding, by a comparison of fluorescence intensities I_{590} between samples incubated in growth medium and in osteogenic medium (Figure 3-21). Metabolism of Saos-2 on PEI/G–PVPA cultured with osteogenic medium was

found to develop significantly, when compared to cells incubated in growth, at 7 days and 14 days post-seeding while PEI/G–$PO(OH)_2$ showed a significant difference in cell activity between two culture media at 14 days post-seeding. In contrast, Saos-2 cultured on other GFN-containing LbL constructs and controls displayed equivalent values of I_{590} for Saos-2 cultured in both basal and osteogenic media at 21 days post-seeding.

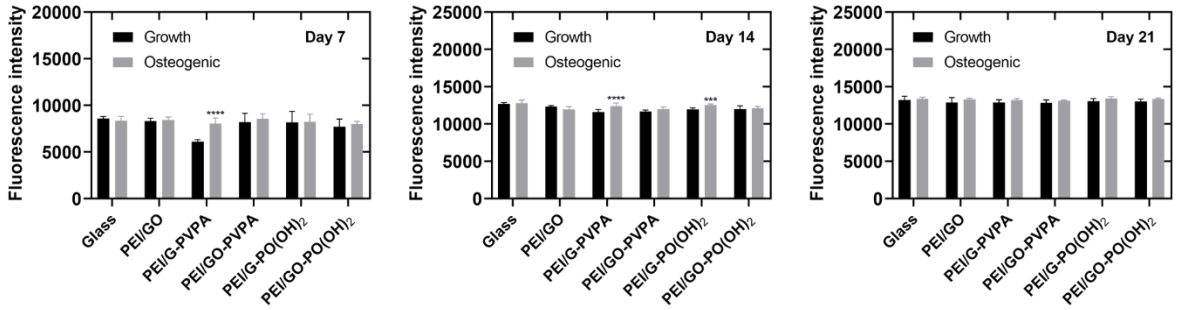

Figure 3-21. Quantification of metabolic activity of Saos-2 seeded on LbL constructs incubated in basal growth medium and osteogenic induction medium (*n* = 3 samples). Fluorescence intensities generated from blanks were excluded from each measurement. Fluorescence intensities of Saos-2 on LbL surfaces incubated in growth medium are the same values as reported in Figure 3-20. Stars above bars show results with statistical significance compared to growth medium for the same type of GFN-containing LbL constructs. **** $p \leq 0.0001$, *** $p \leq 0.001$.

3.2.3.3.4 DNA quantification of HOBs on LbL constructs using PicoGreen assay

The PicoGreen assay was used to quantify the amount of DNA extracted from HOBs seeded on each surface. The worked up PicoGreen data is displayed in Figure 3-22, clearly showing an increase in HOBs DNA concentration over the test period, for all LbL constructs.

From Figure 3-22A, there were no significant differences in the amount of DNA extracted from HOBs on any of the LbL constructs in comparison to the control for 14 days post-seeding, except the PEI/GO and PEI/G–$PO(OH)_2$ LbL construct that showed a statistically significant increase in DNA concentration extracted from cells than control at 7 days post-seeding. Moreover, at 21 days post-seeding, the DNA concentration expressed by HOBs seeded on PEI/G–PVPA and PEI/GO–PVPA was significantly lower than other LbL constructs and control. No significant difference in DNA concentration was observed for PEI/GO, PEI/G–$PO(OH)_2$, and PEI/GO–$PO(OH)_2$ in comparison to the control at 21 days after culturing. The DNA concentration could not detected for PEI/G–PVPA at 7 days and 14 days post-seeding as the values were lower than the limit of detection.

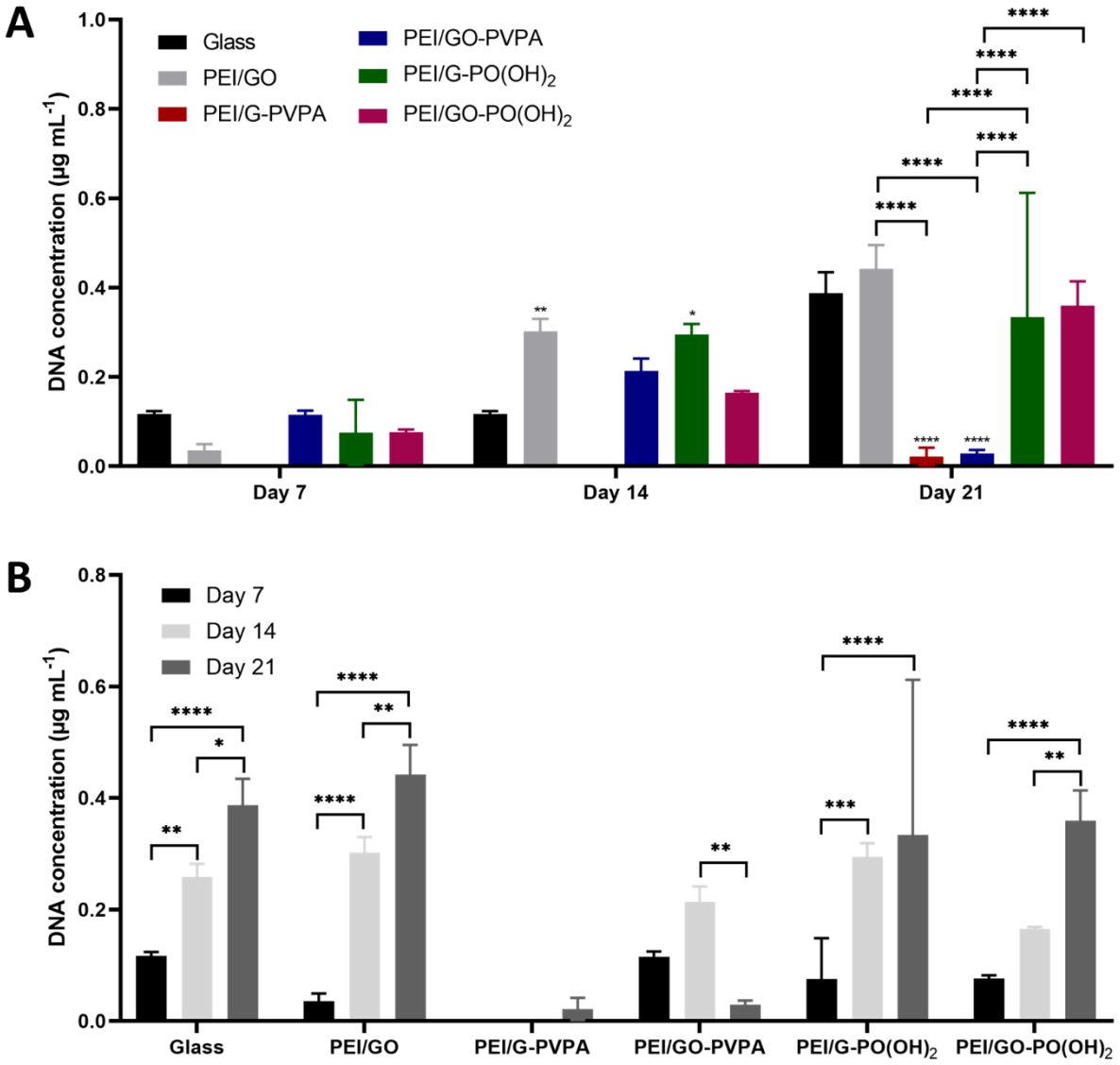

Figure 3-22. DNA quantification of HOBs seeded onto LbL constructs in growth medium using PicoGreen assay. Error bars represent standard deviation (*n* = 3 samples). A) A comparison in DNA concentration of HOBs seeded on different surfaces at the same time point. Stars above bars show results with statistical significance compared to glass (control) at the same time point. Significant differences between GFN-containing LbL constructs at the same time point are indicated by horizontal lines. B) A comparison in DNA concentration of HOBs seeded on the same surface at different time point. Significant differences indicated by horizontal lines. **** $p \leq 0.0001$, ** $p \leq 0.01$, * $p < 0.05$.

The increases in DNA concentration for HOBs on LbL constructs are presented in Figure 3-22B. Lysed primary human osteoblasts on all LbL constructs, except for PEI/G–PVPA, showed an increment in DNA concentration from 7 days to 14 days post-seeding, and from 14 days to 21 days post-seeding. There was a significant increase in the amount of extracted DNA for HOBs on PEI/GO and control over the test period while PEI/GO–PVPA showed a significant decrease in DNA concentration after 14 days post-seeding. The amount of expressed DNA was greater

over time for 14 days after seeding, for HOBs on PEI/G–$PO(OH)_2$. On the other hand, PEI/GO–$PO(OH)_2$ showed a statistically significant increment in DNA concentration after 14 days post-seeding.

The amount of DNA expressed by HOBs on LbL constructs cultured in basal growth medium and osteogenic medium is shown in Figure 3-23. In a comparison to cells incubated in basal growth medium, DNA concentration was found to significantly increase for HOBs on PEI/GO and PEI/GO–$PO(OH)_2$ cultured in osteogenic medium at 7 days post-seeding while there was a significant enhancement in the amount of extracted DNA only for PEI/GO at 14 days post-seeding. In contrast, PEI/GO–PVPA exhibited a significant decrease in DNA concentration for cells grown in osteogenic medium, as compared to control (growth medium), at 7 days post-culturing. The greater amount of DNA extracted was found HOBs seeded on glass and LbL constructs cultured in osteogenic medium, except for PEI/GO–$PO(OH)_2$, at 21 days post-seeding. The DNA concentration of PEI/G–PVPA at Day 7 was not reach the limit of detection for both growth and osteogenic media.

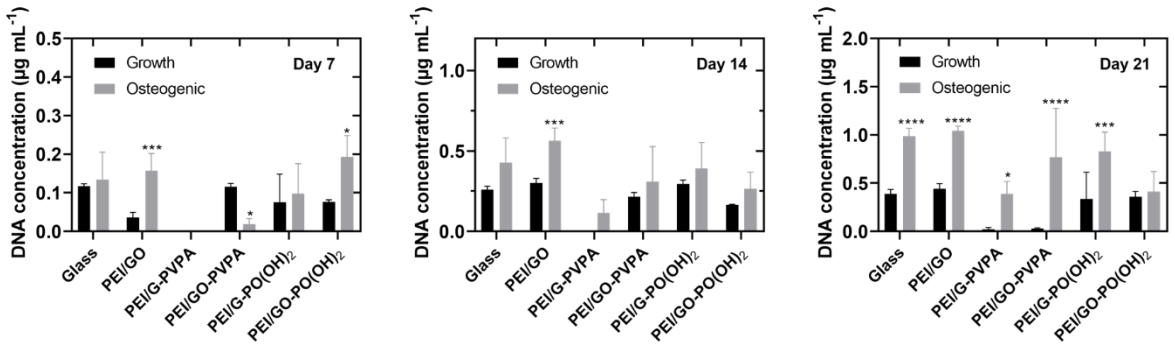

Figure 3-23. DNA quantification of HOBs seeded on LbL constructs incubated in basal growth medium and osteogenic induction medium (n = 3 samples). DNA concentration of HOBs on LbL constructs incubated in growth medium are the same values as reported in Figure 3-22. Stars above bars show results with statistical significance compared to growth medium for the same type of GFN-containing LbL constructs. **** $p \leq 0.0001$, *** $p \leq 0.001$, * $p < 0.05$.

3.2.3.3.5 DNA quantification of Saos-2 on LbL constructs using PicoGreen assay

DNA quantification of Saos-2 seeded onto LbL constructs in growth medium using PicoGreen assay over the 21-day culture period is shown in Figure 3-24. All phosphonated GFN-containing LbL constructs showed a statistically significant decrease in DNA concentration in a comparison with PEI/GO and control at 7 days post-seeding. Among all surfaces, PEI/G–PVPA and PEI/GO–PVPA had the significant lowest amount of DNA extracted from Saos-2 at

7 days post-culturing. No significant difference in DNA concentration between LbL constructs and control was observed at 14 days and 21 days post-feeding.

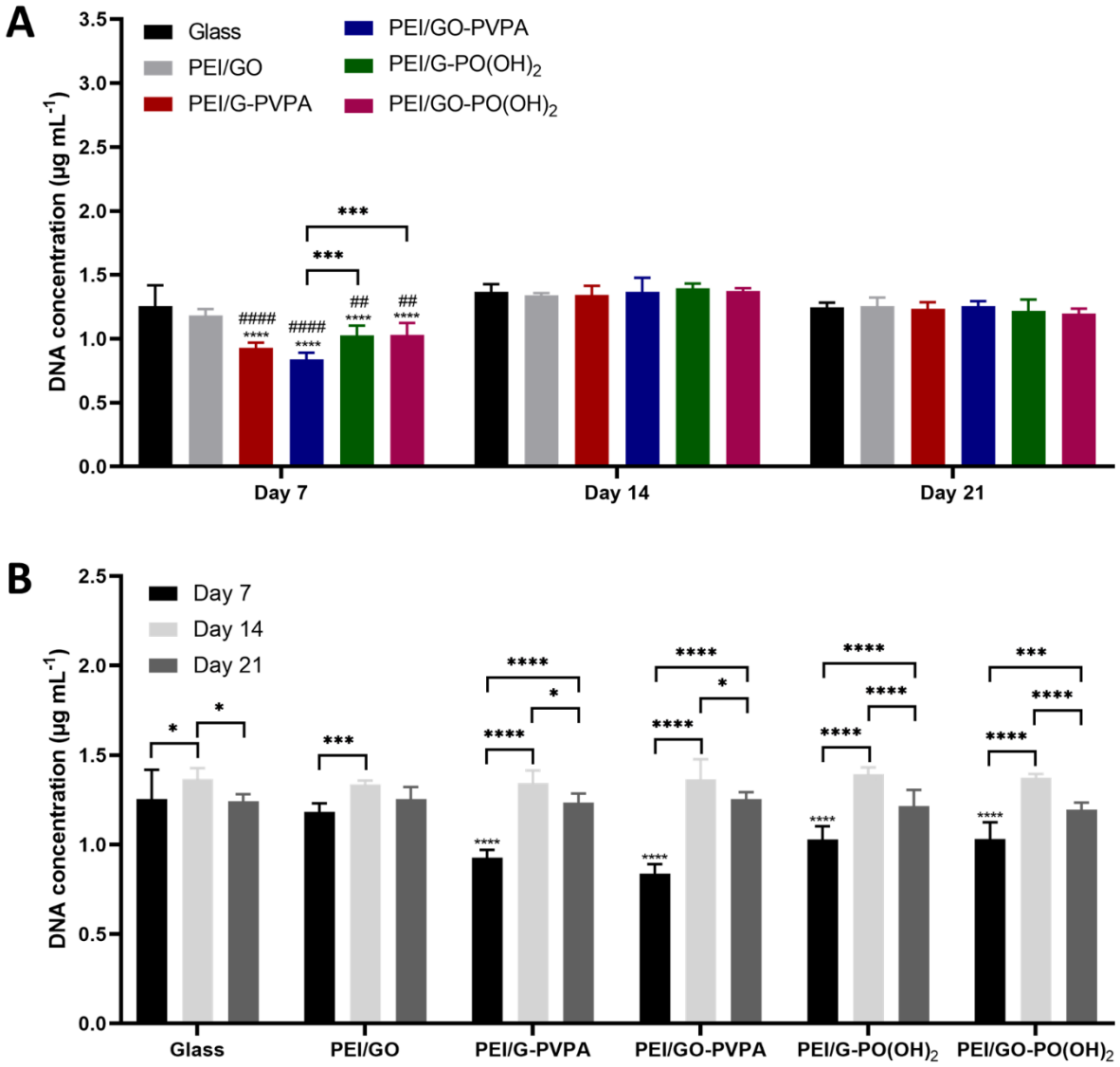

Figure 3-24. DNA quantification of Saos-2 seeded onto LbL constructs in growth medium using PicoGreen assay. Error bars represent standard deviation (*n* = 3 samples). A) A comparison in DNA concentration of Saos-2 seeded on different surfaces at the same time point. Stars above bars show results with statistical significance compared to glass (control) at the same time point. Significant differences between GFN-containing LbL constructs at the same time point are indicated by horizontal lines. B) A comparison in DNA concentration of HOBs seeded on the same surface at different time point. Significant differences indicated by horizontal lines. **** $p \leq 0.0001$, *** $p \leq 0.001$, ** $p \leq 0.01$, * $p < 0.05$. #### $p \leq 0.0001$, ## $p \leq 0.01$.

The increases in DNA concentration over the test period is displayed in Figure 3-24B. Glass and PEI/GO showed a significant increase in DNA concentration form 7 days to 14 days post-seeding, after that a decrease in the amount of DNA was observed at 21 days post-seeding. Similarly, the amount of DNA extracted from Saos-2 seeded on PEI/G–PVPA, PEI/GO–PVPA,

PEI/G–PO(OH)2, and PEI/GO–$PO(OH)_2$ were found to increase significantly over time until 14 days post-seeding. Thereafter, the amount of DNA expressed by cells significantly reduced at 21 days post-seeding for phosphonated GFN-containing LbL constructs.

Concentration of DNA expressed by Saos-2 on LbL constructs cultured in basal growth medium and osteogenic induction medium is displayed in Figure 3-25. All GFN-containing LbL constructs had significantly higher DNA concentrations for Saos-2 incubated in osteogenic medium, as compared to growth medium, at 7 days post-seeding. All LbL constructs, except PEI/GO–$PO(OH)_2$, and control showed a statistically significant reduction in the amount of extracted DNA for cells cultured in osteogenic medium at 14 days after culturing, in a comparison with cells cultured in basal growth medium. Likewise, the amount of DNA expressed by Saos-2 grown osteogenic medium was significantly lower than cells incubated in growth medium for all LbL constructs and glass substrate at 21 days post-seeding.

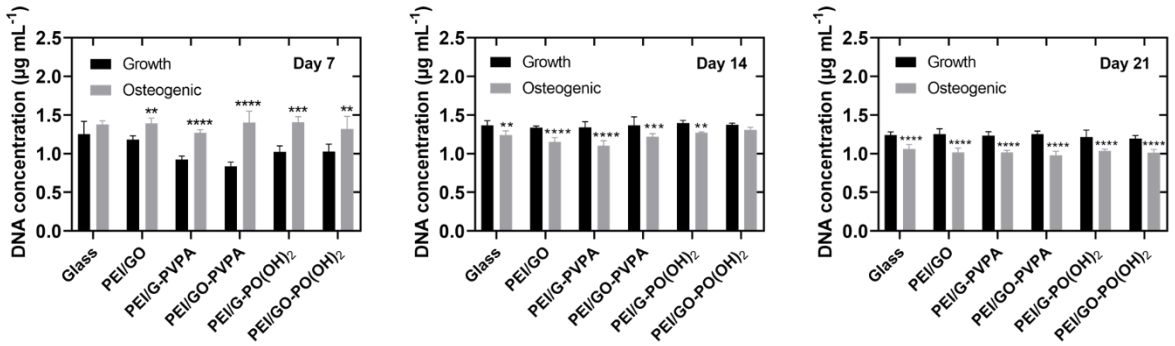

Figure 3-25. DNA quantification of Saos-2 seeded on LbL constructs incubated in basal growth medium and osteogenic induction medium (*n* = 3 samples). DNA concentration of Saos-2 on LbL constructs incubated in growth medium are the same values as reported in Figure 3-24. Stars above bars show results with statistical significance compared to growth medium for the same type of GFN-containing LbL constructs. **** $p \leq 0.0001$, *** $p \leq 0.001$, ** $p \leq 0.01$.

3.2.3.4 Osteogenic mineralisation of human osteoblasts on GFN-containing LbL constructs

3.2.3.4.1 Brief review of methods

Primary human osteoblasts (HOBs) and human osteosarcoma cell line (Saos-2) were seeded separately onto GFN-containing LbL constructs including glass and cultured in both osteogenic induction and standard growth media up to 21 days. The osteogenic mineralisation of osteoblasts was evaluated using ALP assay and alizarin red S staining. Alkaline phosphatase assay is a quantitative assay for measuring ALP enzyme activity expressed from cells *in vitro*. This method uses *p*-nitrophenyl phosphate (*p*NPP) as a phosphatase substrate which turns

yellow (λ_{max}= 405 nm) when dephosphorylated by ALP. Alizarin red S staining is a common histological technique used for detection of calcium deposits in tissue. Alizarin red S reacts with calcium through its sulfonic groups and/or OH groups to form calcium salts.[32] The ALP assay and alizarin red S staining were performed on osteoblasts at 7-day, 14-day and 21-day culturing in both cultured conditions (with and without osteogenic induction).

3.2.3.4.2 Alkaline phosphatase activity of HOBs on LbL constructs

ALP assay is used to measure ALP activity, a marker expressed during osteoblastic maturation. ALP activity of HOBs on LbL constructs incubated in standard growth medium is shown in Figure 3-26. ALP activity of HOBs cultured in growth medium was found to increase over time up to 14 days post-seeding, and then decrease at 21 days of the culture period. However, this is not a case for PEI/GO–PVPA and PEI/GO–$PO(OH)_2$ by which the highest ALP activity of HOBs was observed at 7 days post-seeding, after this time point, the ALP activity deceased. Also, HOBs cultured on surfaces of PEI/G–PVPA and PEI/G–$PO(OH)_2$ showed no significant difference in ALP activity throughout the test period.

HOBs on GFN-containing LbL constructs, except PEI/GO–$PO(OH)_2$, exhibited a significant drop in ALP activity as compared to control at 7 days post-seeding. ALP activity of HOBs seeded on phosphonated GFN-containing LbL films showed a significant decrease in a comparison with PEI/GO at 14 days and 21 days post-seeding. During the test period, PEI/G–PVPA showed the significant lowest ALP activity among all surfaces.

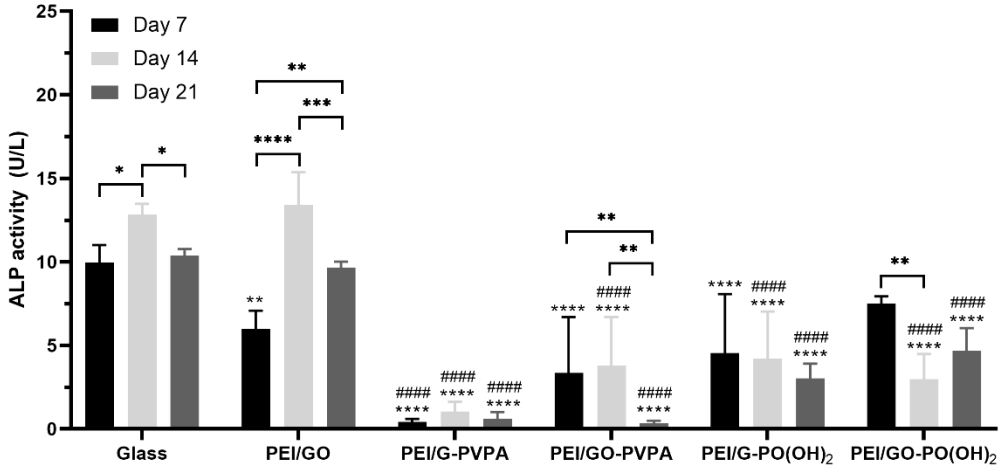

Figure 3-26. Alkaline phosphatase activity of HOBs on LbL constructs, incubated in basal growth medium (*n* = 3 samples). Stars and hash symbols above bars show results with statistical significance compared to glass (control) and GO, respectively, at the same time point. Error bars represent standard deviation. Significant differences within the same surface but different time point are indicated by horizontal lines. Significant differences between phosphonated GFN-containing LbL constructs at the same time point are not displayed for clarity. **** $p \leq 0.0001$, *** $p \leq 0.001$, ** $p \leq 0.01$, * $p < 0.05$. #### $p \leq 0.0001$.

On the other hand, ALP activity of HOBs on all LbL constructs cultured in osteogenic medium relatively increased over time throughout the test period, as can be seen in Figure 3-27. There were no significant differences in ALP activity of HOBs on GFN-containing LbL constructs in a comparison with control, with the exception of PEI/G–PVPA, at 7 days and 14 days post-seeding. PEI/G–PVPA showed a significant lower ALP activity than PEI/GO and control throughout the 21-day culture period whereas PEI/GO–$PO(OH)_2$ had lower ALP activity significantly than PEI/GO, PEI/G–$PO(OH)_2$, and control at 21 days post-seeding. PEI/GO–PVPA showed a significant development in ALP activity in a comparison with PEI/G–PVPA at Day 14 of analysis while possessed a lower ALP activity than control at 21 days post-seeding.

From Figure 3-28, ALP activity of HOBs cultured in osteogenic medium was found to increase significantly, in a comparison to standard growth medium, for all GFN-containing LbL constructs at 14 days and 21 days post-seeding. Only PEI/GO and control showed a significant difference between HOBs incubated in growth and osteogenic media at Day 7 of analysis, by which a greater ALP activity was found in cells cultured with osteogenic medium.

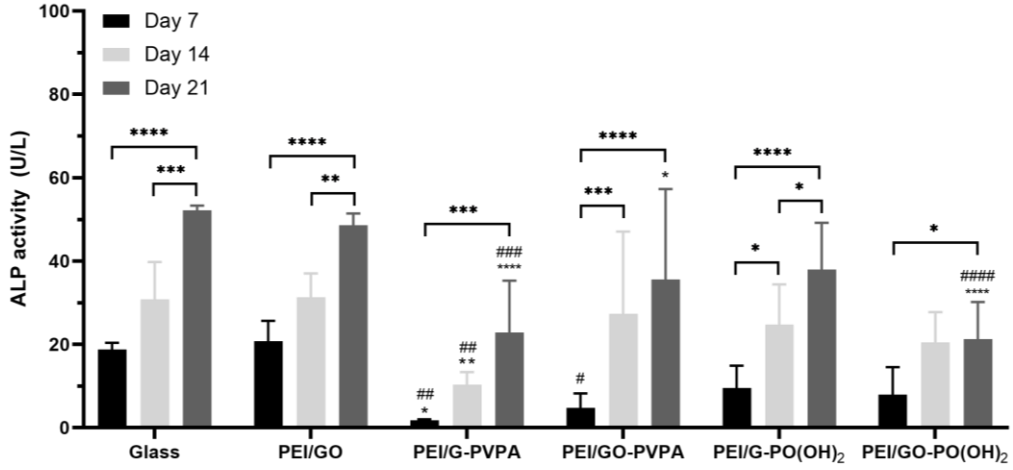

Figure 3-27. Alkaline phosphatase activity of HOBs on LbL constructs, incubated in osteogenic medium (*n* = 3 samples). Stars and hash symbols above bars show results with statistical significance compared to glass (control) and GO, respectively, at the same time point. Error bars represent standard deviation. Significant differences within the same surface but different time point are indicated by horizontal lines. Significant differences between phosphonated GFN-containing LbL constructs at the same time point are not displayed for clarity. **** $p \leq 0.0001$, *** $p \leq 0.001$, ** $p \leq 0.01$, * $p < 0.05$. #### $p \leq 0.0001$, ### $p \leq 0.001$, ## $p \leq 0.01$, # $p < 0.05$.

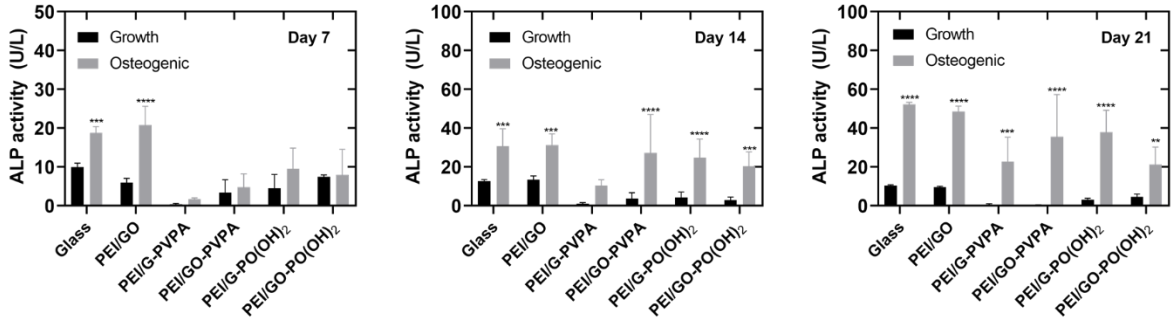

Figure 3-28. A comparison of ALP activity of HOBs on LbL constructs incubated in basal growth medium and osteogenic induction medium (*n* = 3 samples). Results are obtained from Figure 3-26 and Figure 3-27. Stars above bars show results with statistical significance compared to growth medium for the same type of GFN-containing LbL constructs. **** $p \leq 0.0001$, *** $p \leq 0.001$, ** $p \leq 0.01$.

3.2.3.4.3 Alkaline phosphatase activity of Saos-2 on LbL constructs

ALP activity of Saos-2 on LbL constructs incubated in standard growth medium is presented in Figure 3-29. Similar to HOBs, ALP activity of Saos-2 on LbL constructs cultured in growth medium was found to increase over time up to 14 days post-seeding and decrease after this time point. At 7 days post-seeding, PEI/GO–$PO(OH)_2$ exhibited a significant greater in ALP activity of HOBs than PEI/GO and PEI/G–PVPA. Furthermore, a significant reduction in ALP activity was observed for HOBs seeded on PEI/GO–PVPA, in a comparison with PEI/GO and

control at 21 days post-seeding. There were no significant differences in ALP activity for Saos-2 seeded on surfaces between glass, PEI/GO, PEI/G–PVPA, and PEI/G–$PO(OH)_2$ throughout the test period.

On the other hand, as can be seen from Figure 3-30, ALP activity of Saos-2 on PEI/GO and glass cultured in osteogenic medium showed a relative decrease over the test period. A significant decrease in ALP activity after 7 days post-seeding was found for Saos-2 on phosphonated GFN-containing LbL constructs. ALP activity of Saos-2 on PEI/GO was found to significantly increase, as compared to PEI/GO–PVPA, PEI/G–$PO(OH)_2$, and PEI/GO–$PO(OH)_2$ at 21 days post-seeding. No significant difference in ALP activity of Saos-2 was observed among phosphonated GFN-containing LbL constructs throughout the test period. Also, all LbL constructs demonstrated a comparable ALP activity to control.

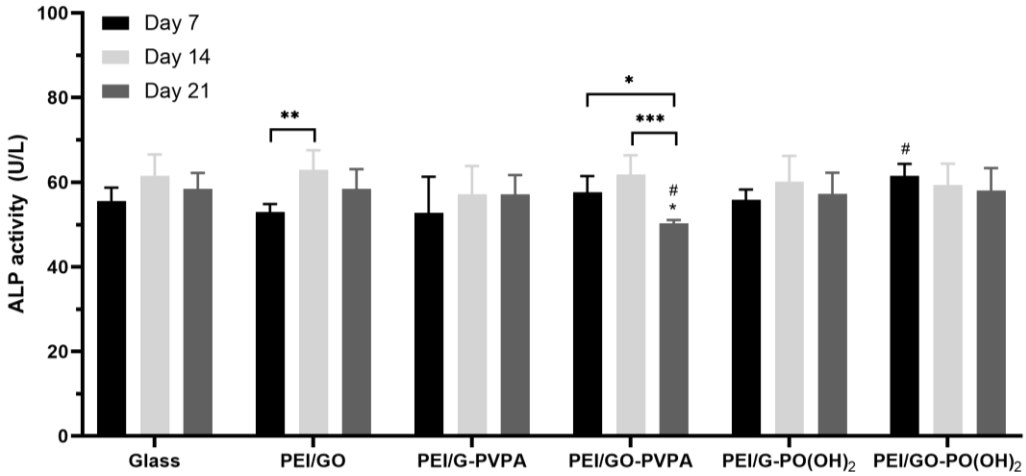

Figure 3-29. Alkaline phosphatase activity of Saos-2 on LbL constructs, incubated in basal growth medium (*n* = 3 samples). Stars and hash symbols above bars show results with statistical significance compared to glass (control) and GO, respectively, at the same time point. Error bars represent standard deviation. Significant differences within the same surface but different time point are indicated by horizontal lines. Significant differences between phosphonated GFN-containing LbL constructs at the same time point are not displayed for clarity. *** $p \leq 0.001$, ** $p \leq 0.01$, * $p < 0.05$. $^{\#}$ $p < 0.05$.

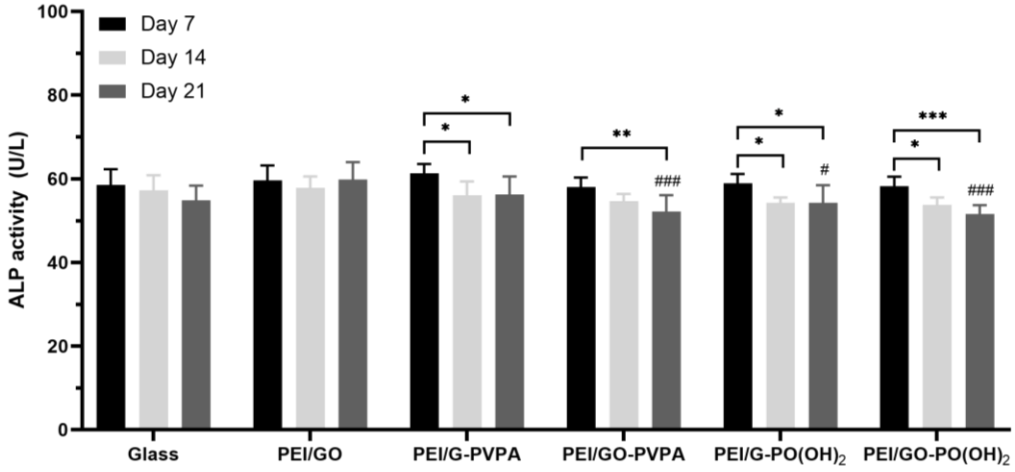

Figure 3-30. Alkaline phosphatase activity of Saos-2 on LbL constructs, incubated in osteogenic medium (*n* = 3 samples). Hash symbols above bars show results with statistical significance compared to and GO at the same time point. Error bars represent standard deviation. Significant differences within the same surface but different time point are indicated by horizontal lines. Significant differences between phosphonated GFN-containing LbL constructs at the same time point are not displayed for clarity. *** $p \leq 0.001$, ** $p \leq 0.01$, * $p < 0.05$. ### $p \leq 0.001$, # $p < 0.05$.

A comparison of ALP activity for Saos-2 on LbL constructs cultured in growth and osteogenic media is displayed in Figure 3-31. At 7 days post-seeding, a significant difference in ALP activity of Saos-2 cultured in different media was found only for PEI/GO and PEI/G–PVPA, by which a greater ALP activity was observed for cells cultured in osteogenic medium. In contrast, ALP activity of HOBs incubated in osteogenic medium showed a significant decrease, in a comparison with standard growth medium, for PEI/GO–$PO(OH)_2$ at Day 14 and Day 21 of the test period, and for PEI/GO–PVPA at 14 days post-seeding.

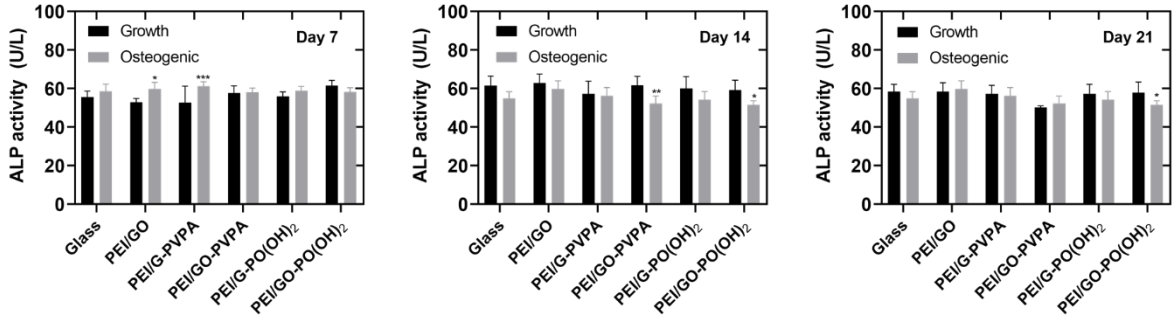

Figure 3-31. A comparison of ALP activity of Saos-2 on LbL constructs incubated in basal growth medium and osteogenic induction medium (*n* = 3 samples). Results are obtained from Figure 3-29 and Figure 3-30. Stars above bars show results with statistical significance compared to growth medium for the same type of GFN-containing LbL constructs. *** $p \leq 0.001$, ** $p \leq 0.01$, * $p < 0.05$.

3.2.3.4.4 Alizarin red S staining of HOBs on LbL constructs

In addition to ALP assay, the osteogenic mineralisation of osteoblasts on GFN-containing LbL constructs was also measured using the alizarin red S stain, which detects calcium deposited in the mineralised matrix. The images of HOBs stained with the alizarin red S in basal growth medium and osteogenic medium are illustrated in Figure 3-32 and Figure 3-33, respectively.

In the absence of osteogenic induction (Figure 3-32), HOBs on all surfaces including the control did not show a positive alizarin red S staining over the test period, although the proliferation of HOBs was observed on glass (control) and PEI/GO at 21 days post-seeding.

On the other hand, HOBs on LbL constructs and glass cultured in osteogenic media (Figure 3-33) exhibited a qualitatively positive stain with alizarin red S at 21 days post-seeding, indicating the calcium deposited in mineralised matrix. However, it was only PEI/GO that showed a qualitatively much greater positive staining at this time point. A positive staining of alizarin red S was observed for HOBs seeded on glass and PEI/GO at 14 days post-seeding, but was very faint and insignificant, implying to an earlier stage of osteogenic mineralisation of HOBs. There was no positive staining observed for HOBs seeded on PEI/G–PVPA, PEI/GOPVPA, PEI/G–$PO(OH)_2$, and PEI/GO–$PO(OH)_2$ throughout the culture period.

The alizarin red staining for HOBs with lower passage number seeded on LbL constructs and incubated in osteogenic medium was also studied with results shown in Figure 3-34. HOBs seeded on glass, PEI/GO and PEI/GO–$PO(OH)_2$ showed the mineralisation at 14 days post-seeding and continued mineralising until 21-day culturing, but the staining detected in HOBs on PEI/GO–$PO(OH)_2$ was faint. PEI/GO–PVPA could induce the mineralisation of HOBs since 7 days post-seeding but it was a weak staining. HOBs seeded on PEI/GO–PVPA released more calcium deposits in matrix, with stronger alizarin red stain at 14 days after seeding. However, at 21-day testing, no positive staining was observed which may be due to the loss of cell attachment. PEI/G–$PO(OH)_2$ showed the mineralised matrix with positive stain only at 21-day culturing whereas the alizarin red staining of HOBs on PEI/G-PVPA could be observed at 14 days post-culturing. According to results shown in Figure 3-33 and Figure 3-34, it is evident that the passage number of cell (or cell senescence) have an influence on cell function.

Alizarin red S staining of Saos-2 seeded on GFN-containing LbL constructs and glass, after incubation in basal growth medium in the absence and the presece of osteogenic inducers

are displayed in Figure 3-35 and Figure 3-36, respectively. In contrast to HOBs, a strong and significantly positive staining of alizarin red S could be observed for Saos-2 seeded on LbL constructs and control, cultured in medium with the presence of osteogenic inducers (Figure 3-36), since 14 days post-seeding. This means that all GFN-containing LbL constructs could induce and support the mineralisation of Saos-2. PEI/GO showed a relative stronger of alizarin red stains in a comparison with the rest of Lbl constructs and controls, indicative of the greater amount of calcium deposited in mineralised matrix. On the other hand, no positive staining was observed on all LbL constructs and controls for Saos-2 cultured in standard growth medium without osteogenic induction throughout the 21-day test period. This can be seen in Figure 3-35.

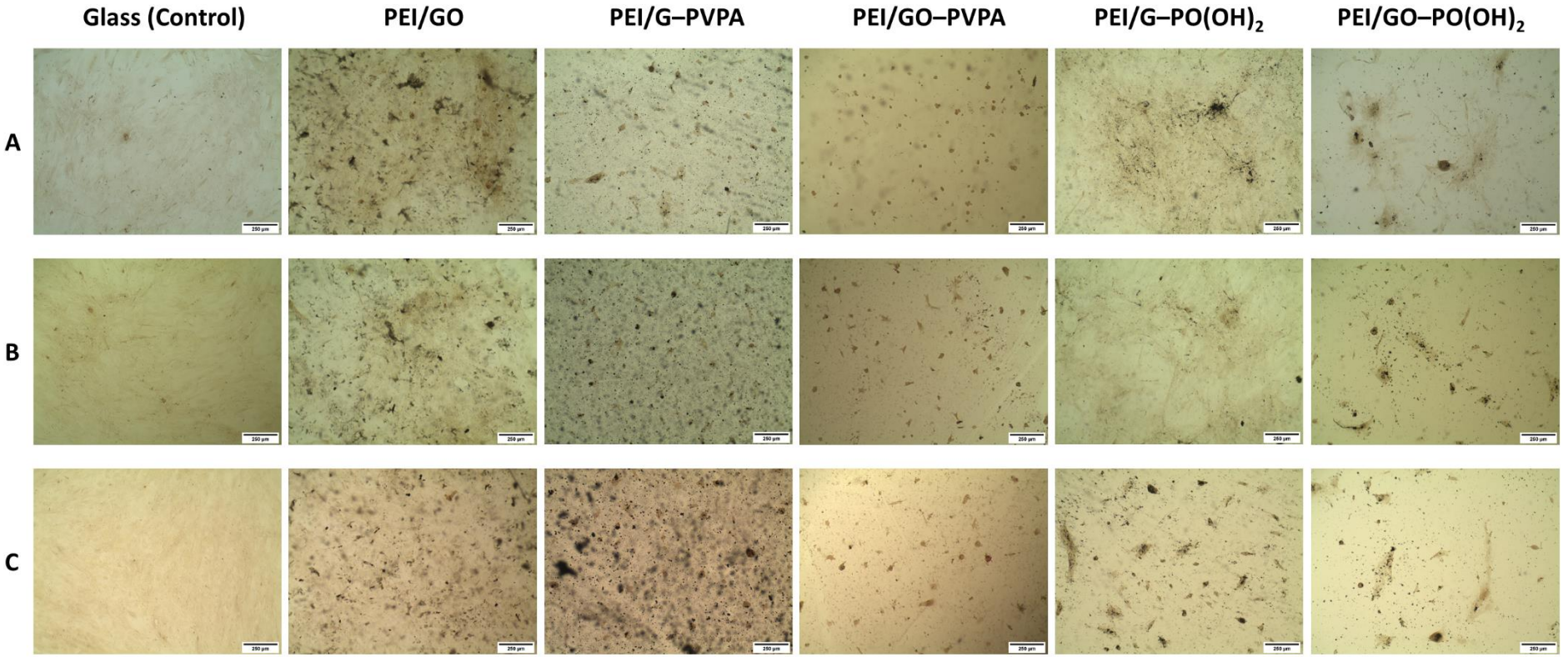

Figure 3-32. Alizarin red S staining of HOBs (passage number 6) on GFN-containing LbL constructs, after incubation with basal growth (non-induction) medium for A) 7 days B) 14 days and C) 21 days. Scale bar represents 250 µm.

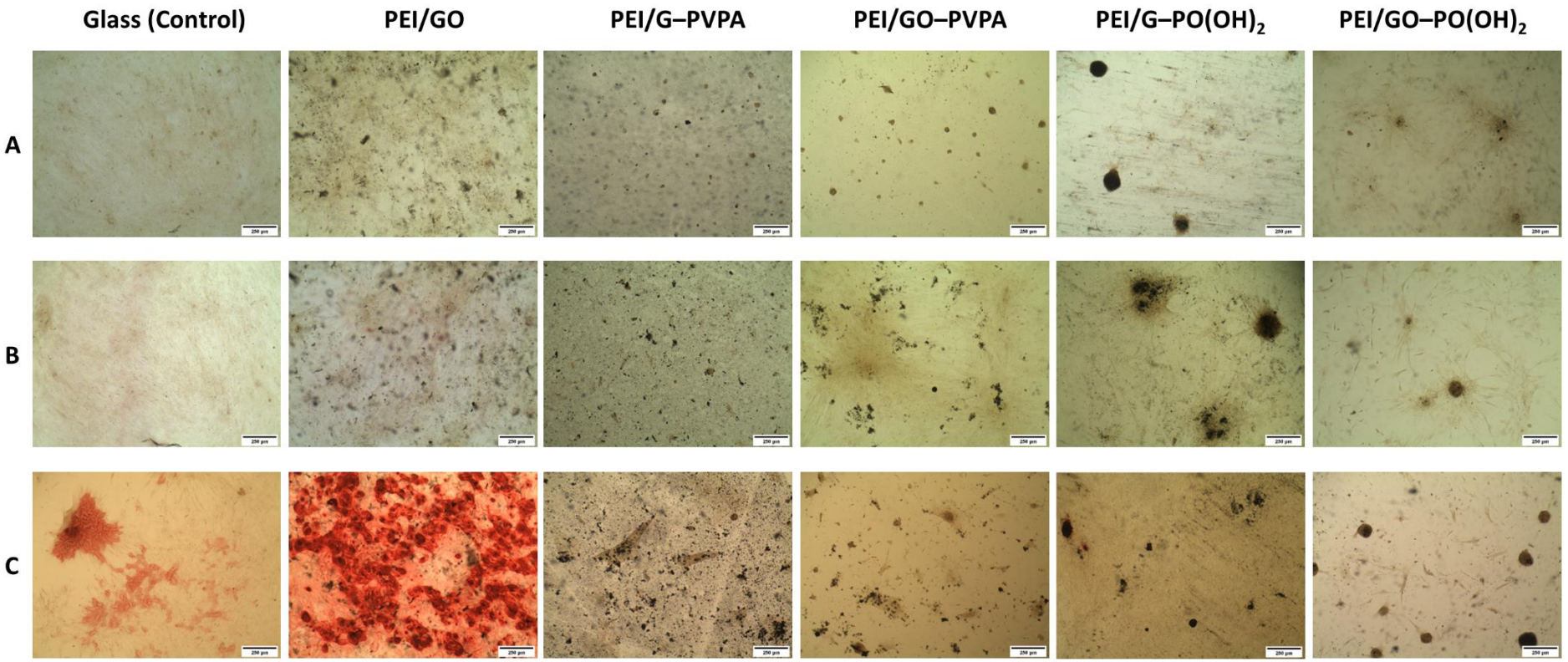

Figure 3-33. Alizarin red S staining of HOBs (passage number 6) on GFN-containing LbL constructs, after incubation with osteogenic induction medium for A) 7 days B) 14 days and C) 21 days. Scale bar represents 250 µm.

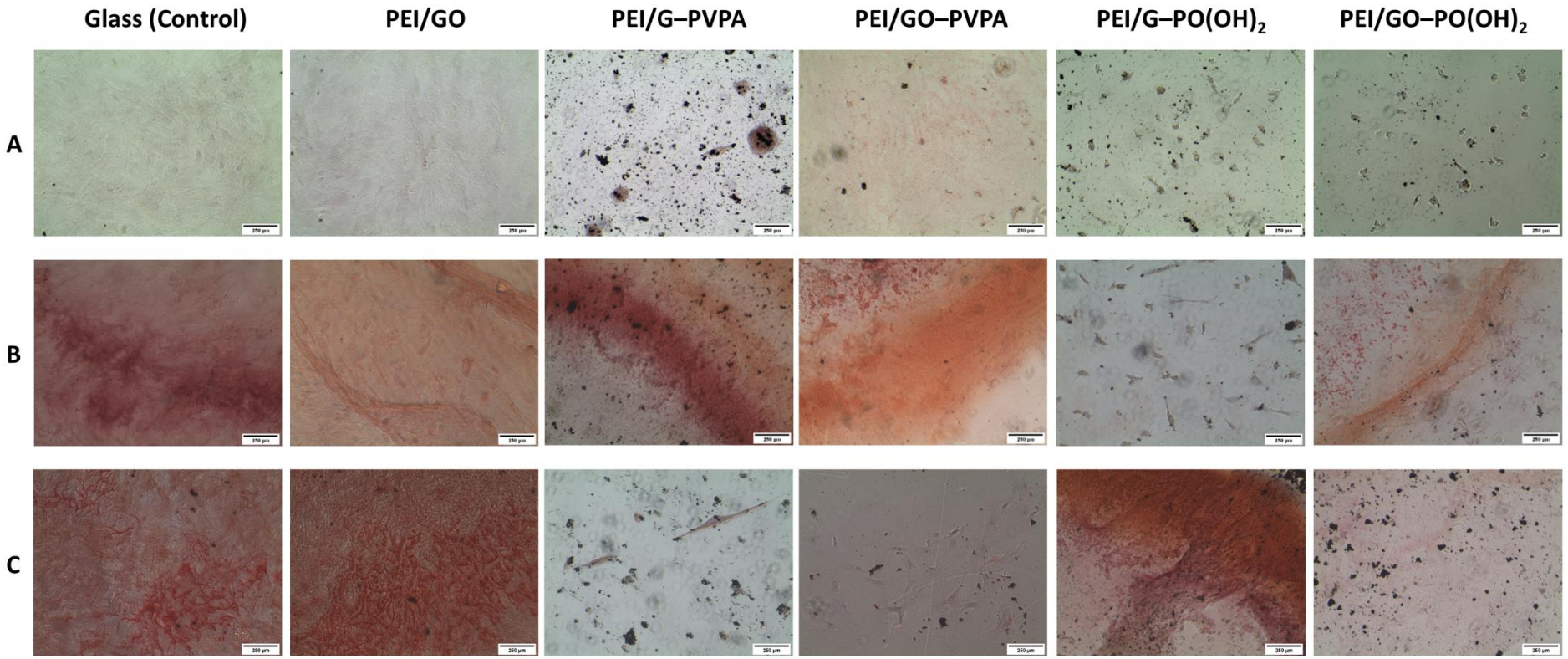

Figure 3-34. Alizarin red S staining of HOBs (passage number 3) on GFN-containing LbL constructs, after incubation with osteogenic induction medium for A) 7 days B) 14 days and C) 21 days. Scale bar represents 250 µm.

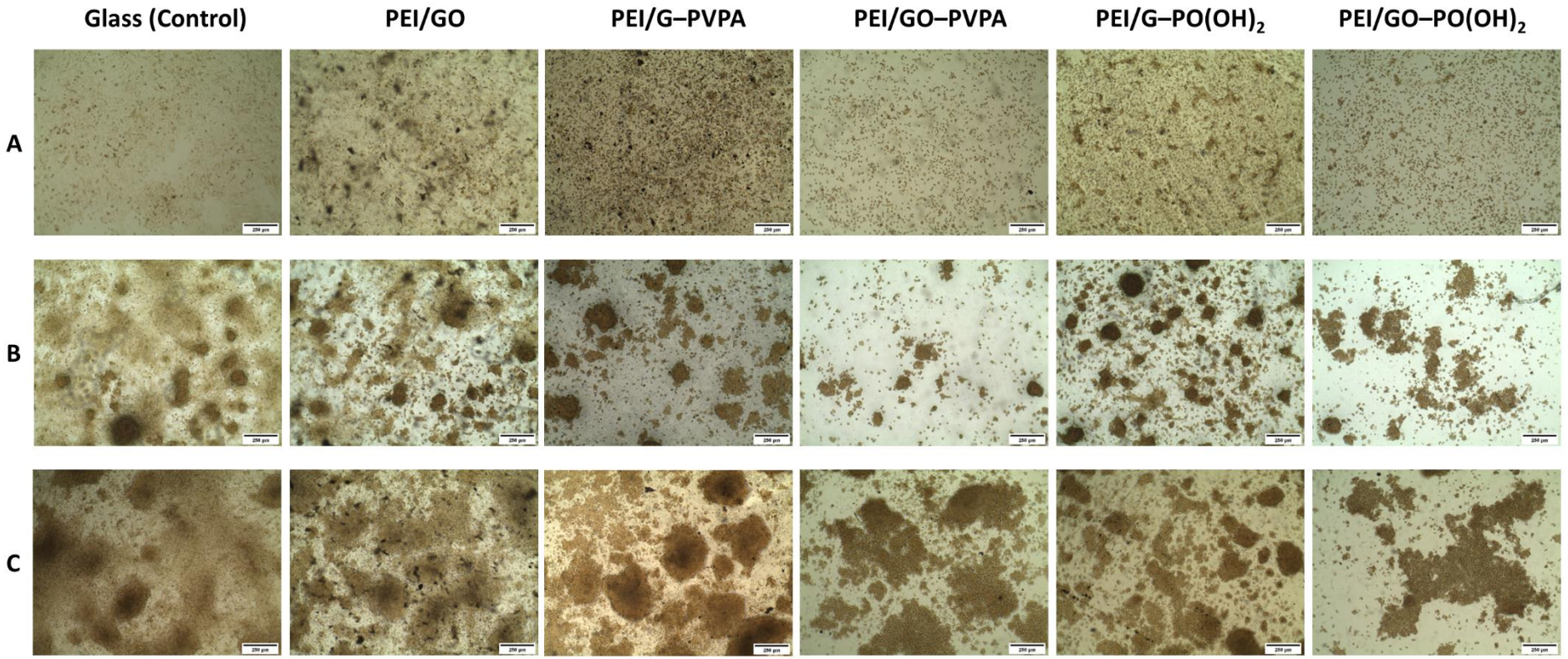

Figure 3-35. Alizarin red S staining of Saos-2 on GFN-containing LbL constructs, after incubation with basal growth (non-induction) medium for A) 7 days B) 14 days and C) 21 days. Scale bar represents 250 µm.

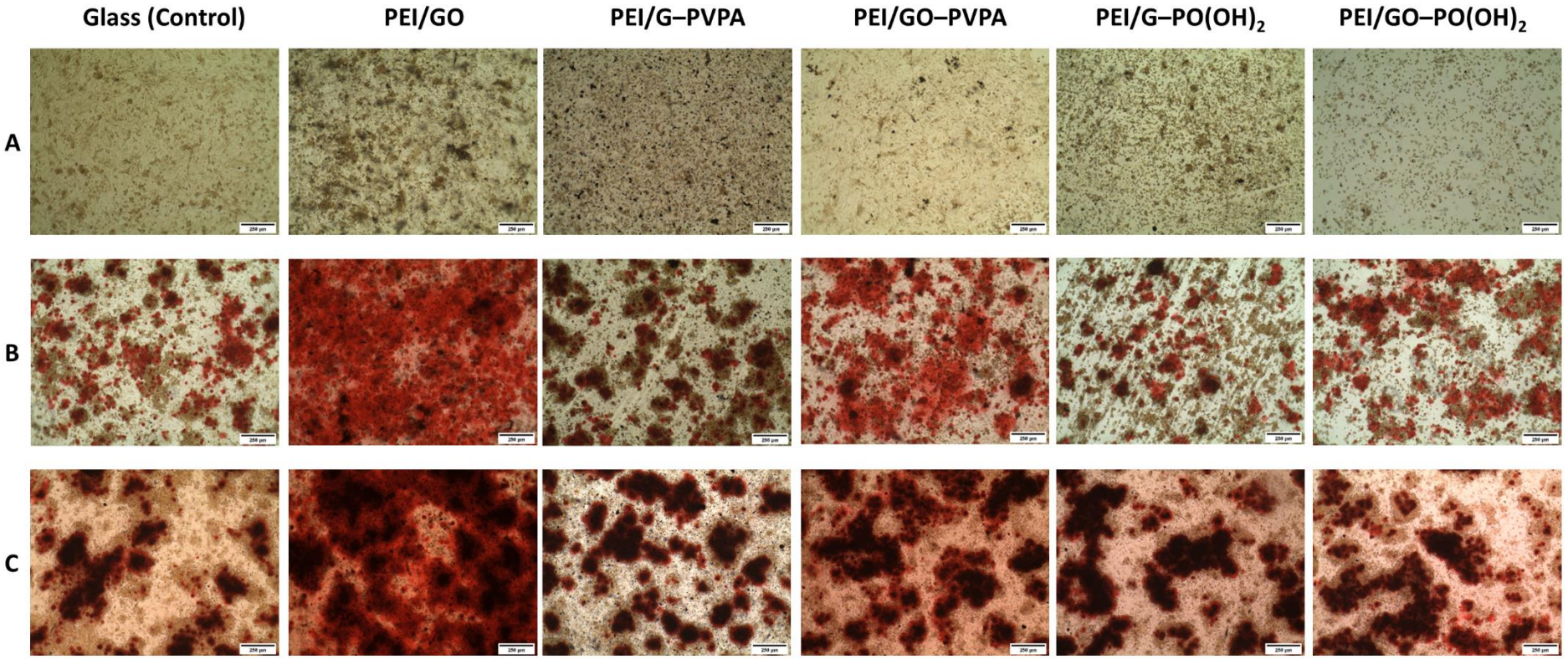

Figure 3-36. Alizarin red S staining of Saos-2 on GFN-containing LbL constructs, after incubation with osteogenic induction medium for A) 7 days B) 14 days and C) 21 days. Scale bar represents 250 µm.

3.3 Discussion

3.3.1 Functionalisation of graphene-family nanomaterials and graphene-based LbL constructs

The XPS data and FTIR spectra of modified graphene derivatives confirmed the presence of functional groups attached to graphene and GO as well as indicating the chemical identity. The functionalisation in this thesis has shown to improve aqueous dispersibility of pristine graphene, by which the aggregation of graphene in suspensions was reduced for all modified-graphene derivatives in a comparison to pristine graphene.

From the characterisation of phosphonate-containing graphene derivatives, it is most likely that GO can be used as a starting material for functionalisation better than pristine graphene nanoplatelets because it has functional groups consisting oxygen whereas the chemical modification of graphene may occur on the reactive edges.[33] It is hypothesised that, after the vinyl monomer's polymerisation has been initiated, propagating radicals can attack sp^2 carbon or double bonds of GO and new radicals are form at its surface, resulting in further propagation and termination.[34] Moreover, the oxygen-containing functional groups on GO surface and edges such as hydroxyl and carboxylic groups can form ionic interactions and hydrogen bonds with the analogous sites of macromolecules or polymers.[35]

Besides, it seems that the functionalisation via copolymerisation in the presence of graphene or GO provides better results than edge-modification that uses only VPA monomers in feed. VPA polymerises slowly and with difficulty. Phosphonic acids readily form anhydrides in water at polymerisation temperatures. The steric bulk of the VPA anhydride impedes itself to diffuse through the medium for forming polymer chains, leading to a lower rate of reactivity and subsequently difficulty to achieve a high molecular weight homopolymer.[36] On the other hand, copolymerisation of VPA with a reactive monomer such as acrylic acid can give the higher obtained amount of VPA.[3]

From the C 1s spectrum of G–PVPA in Figure 3-4I, two distinct peaks were observed which may be attributed to the structure of graphene and copolymer (PVPA-*co*-AA). It is possible that the functionalisation via copolymerisation could produce the free copolymer chains of PVPA-*co*-AA which did not attach to graphene structure and left in suspension. PVPA-*co*-AA

could be considered as an anionic polymer that is soluble in water. The free chains of PVPA-*co*-AA occurred from copolymerisation may interact with graphene flakes through van der Waals forces and stay in suspension by electrostatic repulsion as same as the mechanism of ionic surfactants that stabilise graphene sheets.[37]

The amount of sulfur in edge-modified G-SO_3 was approximately 1 wt% whereas edge-specific sulfonated graphene (SGnP) produced by chemical synthesis of graphite and by Jeon's ball milling process had 5% and 9% sulfur, respectively. The higher percentage of sulfur in SGnP indicated to the introduction of a significant number of new defects which could arise from the damage of graphene structure from the fabrication process. This was evidenced by the Raman spectra, as the I_D/I_G ratio was 2.72 for SGnP made by chemical synthesis of graphite[1] and was 2.3 for by Jeon's ball milling process,[38] in comparison to a ratio of 0.9 for the edge-modified G–SO_3 characterised in this study. Therefore, the production of SGnP by those two methods introduced significant defects to the graphene structure, to the extent that the defect-induced D peak was larger in magnitude than the G peak, while the sulfonation presented here caused little change in defect density.

The XPS data of GFNs reveal that the reduction of oxygenous groups on GO sheets occurs under functionalisation. It can be seen from the C 1s peak fitting results that the C-O peak fit of GO–SH and GO–PVPA decreases in amplitude compared to GO–SO_3 and GO, respectively. This suggests that the reducing condition used to achieve GO-SH could also reduce any oxygen-containing defects on graphene sheets. Moreover, the temperature used in the production of GO–SH and GO–PVPA, which is about 80–90 °C, can accelerate the thermal reduction of GO.[17]

3.3.2 GFN-containing LbL constructs

The more negative zeta potential of GO, G–PVPA and GO–PVPA arises from additional ionised functional groups (–OH, –COOH and –$PO(OH)_2$) attached on graphene sheets, subsequently providing a more stable dispersion.[39] The more negative zeta potential of GO, G–PVPA and GO–PVPA also contributed the enhanced electrostatic interaction with the PEI, leading to higher deposition amount, as shown by UV absorbance (Figure 3-9), images of GFN-containing LbL constructs (Figure 3-10), and AFM images (Figure 3-11).

The LbL constructs of PEI incorporated with G–$PO(OH)_2$ and GO–$PO(OH)_2$ were found to have a lower coverage on surfaces. This may arise from lower amount of functional groups attached on graphene edges and the poor dispersibility of edge-modified graphene derivatives in aqueous media. Furthermore, the AFM images of LbL assemblies exhibited the aggregation of GFNs on surfaces which has an effect to the roughness values. The distribution of GFN-based LbL constructs should be further studied by Raman mapping.

The fabrication technique used in this thesis, which was a dip coating, could not provide homogeneous surfaces (Figure 3-10). To improve the homogeneity of LbL surfaces, a spray-LbL process may be used to increase contact times between polyelectrolyte and surface and avoid the cross-contamination of opposite charged polyelectrolytes. It was found that film prepared by spraying can be controlled and reliable.[40]

3.3.3 Protein adsorption

Protein adsorption is the initial process that occurs when materials are immersed to biological environment such as serum-supplemented culture media, subsequently mediating cell adhesion with materials.[41, 42] Following protein adsorption, cells can interact to adsorbed protein on surface via integrins (heterodimeric receptors in the cell membrane) which take part in cellular signalling, promoting cell proliferation and differentiation, and the secretion of proteins.[42, 43] BSA is the major protein component in fetal bovine serum (FBS) used for supplement in culture media and is predicted to adhere initially to surfacess.[44] Fn is a serum protein which can promote cell attachment through integrins.[44]

Proteins can be adsorbed on surface through hydrophobic, electrostatic, hydrogen bonding or van der Waals interactions, meaning that the adsorption of proteins depends on many factors include surface charge, wettability and topography.[42] Wallace and co-workers described that BSA adsorption was greater with the increased surface roughness whereas Fn adsorption was independent with roughness of substrates.[41] Also, after the initial adsorption, BSA can rearrange its structure to a more dehydrated and compact conformation which supports a further adsorption of protein on material interfaces.[41] This evident explains the BSA adsorption profile of GFN-containing LbL constructs which that PEI/GO, PEI/G–PVPA, PEI/GO–PVPA, and PEI/GO–$PO(OH)_2$ possessed greater surface roughness as can be seen from AFM measurements, so the amount of adsorbed BSA was higher than glass. However, this

was not the case for PEI/G–$PO(OH)_2$ of which the surface roughness was lower but the amount of adsorbed proteins was higher than glass. Moreover, PEI/GO–$PO(OH)_2$ exhibited the highest surface roughness through AFM measurements but there was a lower amount of graphene attached to the surface, leading to a significant decrease in BSA adsorption in comparison with other types of LbL constructs. These findings imply that the presence and amount of modified GFNs deposited on surface contributed to the protein adsorption of LbL constructs more than the surface roughness.

Fn can be adsorbed to materials via both hydrophobic and hydrophilic surfaces but, at low concentrations, it binds better to hydrophobic surfaces than hydrophilic surfaces.[45] As a consequence of deposited GFNs on surfaces, adsorbed Fn was significantly increased in all GFN-containing LbL constructs compared to glass which possesses a more hydrophilic surface (Figure 3-13B). Although PEI/GO, PEI/G–PVPA, and PEI/GO–PVPA showed larger amounts of GFNs deposited on surfaces among all LbL constructs, no significant difference in Fn adsorption was observed. All LbL constructs exhibited the greater adsorption of BSA compared to Fn, possibly due to the ability of BSA to rearrangement its structure to a more dehydrated and compact conformation that facilitates a further adsorption of protein on material interfaces and forms multilayers of protein.[41]

3.3.4 Human osteoblasts on GFN-containing LbL constructs

3.3.4.1 Cell adhesion and morphology

The LIVE/DEAD images revealed that LbL constructs could support the attachment of HOBs. However, there were the differences in cell morphology and the area of cell coverage between materials (Figure 3-14 and Figure 3-15). The little cell spreading and the low number of HOBs could be observed on PEI/G–PVPA, PEI/GO–PVPA, PEI/G–$PO(OH)_2$ and PEI/GO–$PO(OH)_2$ over the test period. Also, HOBs seeded on PEI-incorporated with phosphonate-modified graphene analogues mostly exhibited a rounded shape. In contrast, HOBs seeded onto PEI/GO showed greater cell proliferation and spreading with the characteristic morphology of osteoblasts (spindle-like or elongated shape).

On the other hand, all LbL constructs could support cell adhesion and expansion for Saos-2 throughout the culture period with greater cell coverage, as can be seen from Figure 3-16 and

Figure 3-17. A large amount of cells were found on surfaces of LbL constructs and increased over time with cell coverage on surfaces 20–50 % at Day 7 to 60–75% at Day 21, indicative of cell proliferation. With respect to cell morphology, only PEI/GO and control provided the appropriate surface that enhanced the typical spindle-like shape of Saos-2 over the test period. In contrast, the spherical morphology of Saos-2 was mainly observed on PEI/G–PVPA, PEI/GO–PVPA, PEI/G–$PO(OH)_2$ and PEI/GO–$PO(OH)_2$. The findings obtained from LIVE/DEAD images of HOBs and Saos-2 suggest that the surface properties of LbL constructs containing phosphonate-modified GFNs are different from GO-based film and can alter the cell behaviour towards materials, such as the difference in cell adhesion and morphology of osteoblasts observed among LbL constructs. However, the variation of sample preparation and the discrepancy in surface appearance, as shown in Figure 3-10, could hinder the accurate results because different samples were used in the LIVE/DEAD assay.

Cell adhesion on materials is dependent on surface properties such as surface chemistry, topography and protein adsorption.[42, 46] It has been established that different surface-terminating chemistry has effects on cell adhesion.[46, 47] Surfaces terminated by carboxyl (–COOH), hydroxyl (–OH) and amine ($–NH_2$) were found to be favourable for adhesion of human mesenchymal stem cells (hMSCs) and human fibroblasts while more hydrophobic surface terminated by methyl group ($–CH_3$) exhibited little cell adhesion.[46, 47] Similarly, in this research, a greater cell attachment and spreading were observed on PEI/GO which has –COOH and –OH terminated surface from GO. Other LbL constructs that contain phosphonate-modified graphene derivatives showed poor cell attachment because these graphene analogues had lower hydrophilic functional groups, with $–CH_3$ terminal group. This can be supported by the wettability of LbL substrates acquired by contact angle measurements (Figure 3-12).

Many studies have reported the effect of surface topography on cell adhesion. Surfaces with increased roughness or disorders can promote cell adhesion, proliferation and differentiation of stem cells[48, 49] and osteoblast-like cells.[50] As can be seen from AFM measurements, PEI/G–$PO(OH)_2$ had the low roughness values, correlating to the low level of cell attachment and spreading. Interestingly, PEI/G–PVPA, PEI/GO–PVPA and PEI/GO–$PO(OH)_2$ exhibited rougher surfaces than PEI/GO and glass but the lack of cell adhesion and proliferation of HOBs was observed on these surfaces. This means that the other surface properties such as the

distribution of GFNs on LbL constructs, the wettability and terminal groups on the surface have more influence than topography.

In this study, BSA and Fn were selected as a model for the study of protein adsorption of LbL constructs. BSA is considered as a non-adhesive protein which can hinder cell attachment to materials, however, it can regulate the conformation and cell adhesion activity of other adhesive proteins (e.g., fibronectin and vitronectin) to promote cell attachment.[51] From the study of protein adsorption, all LbL constructs showed more adsorbed BSA than Fn. This is because BSA can form multilayers of protein and it is a major component of supplemented serum in culture media and thought to adhere initially to surface.[41] Although PEI/G–PVPA, PEI/GO–PVPA and PEI/GO–$PO(OH)_2$ had the amount of adsorbed protein comparable to PEI/GO, the attachment and spreading of cells were still poor. This may be due to other additional controls such as the functional groups terminated surfaces and the aggregation of modified-GFNs on surfaces.

3.3.4.2 Cell activity

The LIVE/DEAD images cannot be used alone for cytocompatibility assessment and/or to indicate the viability and proliferation of cells on LbL constructs, since only small selected areas from samples were acquired for analysis compared to the total area occupied by cells on the surfaces. The data, therefore, must be supplemented by assays which reflect the whole surfaces. Accordingly, AlamarBlue and PicoGreen assays were performed to determine the proliferation and the amount of DNA expressed from osteoblasts on the LbL constructs.

HOBs seeded on LbL constructs showed an increase in cell metabolism and DNA concentration over time throughout the test period, suggesting cell proliferation. PEI/G–PVPA, PEI/GO–PVPA, PEI/G–$PO(OH)_2$ and PEI/GO–$PO(OH)_2$ showed a significant lower cell metabolism in a comparison with PEI/GO, owing to the lack of cell adhesion and subsequent lower cell number attached on surfaces. The cell metabolic activity of HOBs between 14 days and 21 days post-seeding did not differ significantly for PEI/GO and glass, suggesting to no proliferation of HOBs after 14 days of the culture period. This is probably because cells have reached confluency. The results obtained from AlamarBlue assay correlate with the data from LIVE/DEAD assay, by which PEI/GO exhibited the most suitable and acceptable surface to support cell attachment, spreading, and proliferation of HOBs.

On the other hand, the significant increment in fluorescence intensities could be observed throughout the test period for Saos-2 seeded on LbL assemblies containing phosphonate-modified GFNs while the fluorescence intensities for PEI/GO and control did not increase significantly after 14 days post-seeding. This suggests that Saos-2 on PEI/GO and glass could reach the confluence since Day 14 of the culture period, meaning to greater cell proliferation than other LbL constructs. However, the amount of DNA extracted from Saos-2 seeded on LbL constructs showed a significant increase up to 14 days post-seeding, after that, a decrease of DNA concentration was observed. The reduction of DNA concentration at 21 days post-seeding may arise from the loss of cell layers during washing step after removing culture media. This can be supported from the LIVE/DEAD images of Saos-2 on LbL constructs (Figure 3-16), by which cells exhibited the over confluence and formed the large clumps of cell layers at 21 days post-seeding. The DNA concentration of Saos-2, consequently, is not corresponding with the data obtained from the AlamarBlue and LIVE/DEAD assays. It is worth considering that the process of cell lysis during the analysis of PicoGreen assay may be incomplete and subsequently hinder the accurate DNA concentration obtained from samples.

PVPA-*co*-AA was found to affect the metabolic activity and proliferation of osteoblasts in a dose-dependent manner. A high concentration could have a negative effect towards cell viability due to a too high content of phosphorus, leading to cell death.[52, 53] In this thesis, G–PVPA and GO–PVPA had the higher content of phosphorus as compared to GO–$PO(OH)_2$ and G–$PO(OH)_2$ (Table 3-1 and Table 3-3) as well as the amount of G–PVPA and GO–PVPA deposited on LbL surfaces were greater than GO–$PO(OH)_2$ and G–$PO(OH)_2$ (Figure 3-9 and Figure 3-10). Therefore, the high amount of phosphorus may be having an inhibitory effect on proliferation, resulting in low metabolic activity (Figure 3-18 and Figure 3-20) and very low DNA concentration (Figure 3-22 and Figure 3-24) of osteoblasts on PEI/G–PVPA and PEI/GO–PVPA LbL constructs. A huge range of standard deviation observed in AlamarBlue and PicoGreen assays could be the results of the discrepancy in surface appearance and the effect from the process of cell lysis.

In the study of osteogenic mineralisation of osteoblasts, chemical inducers including β-glycerophosphate, dexamethasone, and L-ascorbic acid are required for preparing osteogenic medium. Hence, the effect of these chemicals on cell activity was also investigated using the AlamarBlue and PicoGreen assays. The metabolic activity (Figure 3-19) and DNA

concentration (Figure 3-23) exhibited a significant increase for HOBs seeded on LbL constructs and incubated in osteogenic medium, in a comparison with normal growth medium. On the other hand, the metabolic activity of Saos-2 on LbL constructs were comparable for cells incubated in culture media with the presence and the absence of osteogenic inducers (Figure 3-21). As compared to standard growth medium, Saos-2 on LbL constructs cultured in osteogenic medium showed a significant greater in the DNA concentration at 7 days post-seeding, but a significant drop was observed after this time point (Figure 3-25). It is known that ascorbic acid, when supplied to culture medium, can stimulate cell growth, leading to an increase in cell proliferation and the amount of DNA expressed by cells.[54] This may be a reason for an increase in cell activities of osteoblasts cultured in osteogenic medium.

3.3.4.3 Osteoblastic matrix mineralisation

In this study, the osteogenic mineralisation of osteoblast cultures on GFNs-containing LbL constructs was investigated by a detection of ALP activity and a visualisation of mineralised matrix using alizarin red S staining. All LbL constructs and control (glass) did not show the alizarin red stain for HOBs cultured in standard growth media (without osteogenic inducers), meaning no calcium deposited in the matrix (Figure 3-32). On the contrary, in the presence of osteogenic induction, the alizarin red S positive stains could be detected in HOBs on PEI/GO LbL construct and glass at 21 days post-seeding (Figure 3-33), suggesting calcium deposited in the matrix. This corresponds to literature reports by which GFNs have a potential to support osteogenic differentiation in the presence of chemical inducers due to the ability to adsorb dexamethasone through π-π stacking of graphene sheets whereas oxygen-consisting functional groups of GO tends to bind with OH moieties of acid via hydrogen bonding interaction.[55-58] However, no positive alizarin red staining was observed for HOBs on phosphonated GFNs-containing LbL constructs cultured in osteogenic medium, throughout the test period, due to the lack of cell attachment.

Although no positive staining of alizarin red S was observed, the ALP activity of HOBs on surfaces could be detected for both conditions (Figure 3-26 and Figure 3-27, respectively). The expression of ALP enzyme activity of HOBs on LbL constructs and its increase over time, found in this study, suggest to the matrix maturation stage of osteoblasts. The ALP activity expressed by HOBs on samples cultured in osteogenic medium was significantly higher than

samples incubated in growth medium. This suggests that HOBs cultured in osteogenic medium may progress to the mineralisation stage before HOBs grown in standard growth culture medium.

Similar to HOBs, no positive staining of alizarin red S was observed on all LbL constructs and controls for Saos-2 cultured in standard growth medium without osteogenic induction throughout the 21-day test period. On the other hand, a strongly and significantly positive staining of alizarin red S could be detected for Saos-2 seeded on LbL constructs and control cultured in osteogenic medium (Figure 3-36) at 14 days post-seeding, indicative of calcium deposited in the mineralised matrix. The ALP activity was also detected for Saos-2 on LbL constructs incubated in growth and osteogenic media (Figure 3-29 and Figure 3-30). The ALP activity of Saos-2 cultured in osteogenic medium exhibited an absolute decrease after 7 days post-seeding for GFN-containing LbL constructs. This is corresponding with the positive alizarin red S staining found in all LbL constructs, incubated in osteogenic medium, since Day 14 of the culture period. In addition, the quantity of extracted DNA had a significant drop over culture time since 7 days post-seeding (Figure 3-25), implying to the lower cell proliferation. The data obtained from alizarin red S staining, ALP activity, and PicoGreen assay suggest that Saos-2 on GFN-containing LbL constructs in osteogenic medium are stimulated toward the mineralisation stage of osteoblasts, by which the expression of ALP enzyme decreases with down-regulation of DNA synthesis while the mineral deposition is detected.[59, 60]

Although all GFN-containing LbL constructs showed the positive staining of alizarin red S for Saos-2 at 14 days and 21 days post-seeding, it was only PEI/GO that could support osteogenic mineralisation of HOBs whereas LbL constructs containing phosphonate-modified graphene analogues did not show the calcium deposition within the matrix. One of principal objectives of this research is to produce modified graphene containing phosphonate moieties for use in BTE application because it is hypothesised that the P–C bond in PVPA can mimic the P–C–P backbone found in bisphosphonates and can induce osteoclast apoptosis and osteoblast maturation subsequently improving mineralisation.[3, 61] Nevertheless, no calcium deposition in the mineralised matrix was observed for HOBs on PEI/G–PVPA, PEI/GO–PVPA, PEI/G–$PO(OH)_2$ and PEI/GO–$PO(OH)_2$ throughout the culture period, especially in the presence of osteogenic inducers. This is possibly due to the lack of cell adhesion and little proliferation on surfaces. Even though the high level of metabolic activity and DNA expression could be

observed, but there were a little cell population attached on surfaces for LbL constructs containing phosphonate-modified graphene derivatives. This is probably a consequence of the variation in surface properties among constructs (Figure 3-10) as the different samples were used in each analysis and time point.

Another possible factor to explain the lack of proliferation and osteogenesis of HOBs on LbL constructs, as compared to Saos-2, is variability from the cell donors of primary cells. The quality of primary cells is highly dependent on the individual donor and sources of variability include the sex, age, and health condition of the cell donors.[62, 63] The genetic stability during the passaging process also raises the significant concern for use of primary cells.[63] On the other hand, cell lines have advantages over primary cells regarding unlimited expansion, no isolation required, ease of culture, and more stable characteristics.[64] Moreover, the increase of HOBs senescence with increasing passage number could be a reason for the lack of osteogenesis found in this study. Figure 3-34 shows the alizarin red S staining of HOBs (passage number 3) on GFN-containing LbL constructs, which is the initial data obtained in this study. It can be seen that the positive alizarin red S staining was observed since 14 days post-seeding for PEI/GO LbL constructs and controls while HOBs with passage number 6 on PEI/GO and glass (Figure 3-33) showed the positive staining of alizarin red S only at 21 days post-seeding. This could indicate to the effect of senescence on osteogenic mineralisation of HOBs on LbL constructs. In addition, Geissler *et al*. demonstrated that hMSCs with increasing passage number completely lose osteogenic differentiation potential, with accompanied increased expression of senescence-associated genes.[65]

3.4 Conclusion

The functionalisation of graphene derivatives could be confirmed by FTIR, XPS, elemental analysis and TGA. Also, the functionalisation changed dispersibility of graphene in aqueous suspension by reducing the aggregation of pristine graphene. Phosphonate-modified graphene analogues synthesised by copolymerisation possess the greater amount of phosphorus, which could refer to the phosphonic acid groups, than by edge-modification. GO, as compared to pristine graphene, was a good starting material for functionalisation due to the presence of oxygen-containing functional groups on the edges and surface with more defects structure. LbL constructs of cationic PEI and anionic GFNs suspension were prepared

by dipped coating and possessed a moderate wettability, with rougher surfaces than glass. However, the aggregation of modified graphene derivatives was observed by AFM images.

LbL constructs made in this study had the ability to adsorb bovine serum albumin greater than fibronectin, with the comparable amount of adsorbed proteins found in all LbL constructs. From the *in vitro* study of osteoblasts (HOBs and Saos-2) on LbL constructs by alizarin red S staining, LIVE/DEAD, AlamarBlue, PicoGreen, and ALP assays, PEI/GO provided the most acceptable and suitable surface that could support cell adhesion, proliferation and osteoblast mineralisation with the presence of typical morphology of osteoblasts, whereas LbL constructs containing phosphonate-modified GFNs showed the lack of cell attachment, little proliferation, and the absence of the matrix mineralisation throughout the culture period. Consequently, GO was selected for the incorporation with Laponite nanoclay to produce nanocomposite hydrogels in the next chapter. Together, Saos-2 cell line was selected as a model for *in vitro* cell encapsulation within Laponite-based gels because of the more genetic stability and unlimited expansion.

3.5 References

1. Abdolmaleki, A.; Mallakpour, S.; Mahmoudian, M., Preparation and Evaluation of Edge Selective Sulfonated Graphene by Chlorosulfuric Acid as an Active Metal-Free Electrocatalyst for Oxygen Reduction Reaction in Alkaline Media. *ChemistrySelect* **2017,** *2* (34), 11211-11217.
2. Silverstein, R. M.; Bassler, G. C., Spectrometric identification of organic compounds. *Journal of Chemical Education* **1962,** *39* (11), 546.
3. Dey, R. E.; Zhong, X.; Youle, P. J.; Wang, Q. G.; Wimpenny, I.; Downes, S.; Hoyland, J. A.; Watts, D. C.; Gough, J. E.; Budd, P. M., Synthesis and Characterization of Poly (vinylphosphonic acid-*co*-acrylic acid) Copolymers for Application in Bone Tissue Scaffolds. *Macromolecules* **2016,** *49* (7), 2656-2662.
4. Ferrari, A. C.; Meyer, J.; Scardaci, V.; Casiraghi, C.; Lazzeri, M.; Mauri, F.; Piscanec, S.; Jiang, D.; Novoselov, K.; Roth, S., Raman spectrum of graphene and graphene layers. *Physical Review Letters* **2006,** *97* (18), 187401.
5. Roghani-Mamaqani, H.; Haddadi-Asl, V.; Khezri, K.; Salami-Kalajahi, M., Edge-functionalized graphene nanoplatelets with polystyrene by atom transfer radical polymerization: grafting through carboxyl groups. *Polymer International* **2014,** *63* (11), 1912-1923.
6. Wang, G.; Yang, J.; Park, J.; Gou, X.; Wang, B.; Liu, H.; Yao, J., Facile synthesis and characterization of graphene nanosheets. *Journal of Physical Chemistry C* **2008,** *112* (22), 8192-8195.
7. Kudin, K. N.; Ozbas, B.; Schniepp, H. C.; Prud'Homme, R. K.; Aksay, I. A.; Car, R., Raman spectra of graphite oxide and functionalized graphene sheets. *Nano Letters* **2008,** *8* (1), 36-41.
8. Sundara, R.; Varrla, E.; Sasikaladevi, J.; Sasidharannair, A., Production of graphene using electromagnetic radiation. US20140356277 A1: 2014.
9. Park, S.; Ruoff, R. S., Chemical methods for the production of graphenes. *Nature nanotechnology* **2009,** *4* (4), 217-224.
10. Malard, L.; Pimenta, M.; Dresselhaus, G.; Dresselhaus, M., Raman spectroscopy in graphene. *Physics Reports* **2009,** *473* (5), 51-87.

11. Kaniyoor, A.; Ramaprabhu, S., A Raman spectroscopic investigation of graphite oxide derived graphene. *AIP Advances* **2012,** *2* (3), 032183.
12. Krishnamoorthy, K.; Veerapandian, M.; Yun, K.; Kim, S.-J., The chemical and structural analysis of graphene oxide with different degrees of oxidation. *Carbon* **2013,** *53*, 38-49.
13. Ferrari, A. C., Raman spectroscopy of graphene and graphite: Disorder, electron–phonon coupling, doping and nonadiabatic effects. *Solid State Communications* **2007,** *143* (1), 47-57.
14. Tuinstra, F.; Koenig, J. L., Raman spectrum of graphite. *The Journal of chemical physics* **1970,** *53* (3), 1126-1130.
15. Ferrari, A. C.; Robertson, J., Interpretation of Raman spectra of disordered and amorphous carbon. *Physical review B* **2000,** *61* (20), 14095.
16. Coleman, J. N., Liquid exfoliation of defect-free graphene. *Accounts of Chemical Research* **2012,** *46* (1), 14-22.
17. Lin, Z.; Yao, Y.; Li, Z.; Liu, Y.; Li, Z.; Wong, C.-P., Solvent-assisted thermal reduction of graphite oxide. *The Journal of Physical Chemistry C* **2010,** *114* (35), 14819-14825.
18. Shellard, P. Functionalised graphene for biomedical applications. PhD Thesis, University of Manchester, 2017.
19. Siril, P.; Shiju, N.; Brown, D.; Wilson, K., Optimising catalytic properties of supported sulfonic acid catalysts. *Applied Catalysis A: General* **2009,** *364* (1-2), 95-100.
20. Siow, K. S.; Britcher, L.; Kumar, S.; Griesser, H. J., Deposition and XPS and FTIR analysis of plasma polymer coatings containing phosphorus. *Plasma Processes and Polymers* **2014,** *11* (2), 133-141.
21. Song, J.; Yu, Z.; Gordin, M. L.; Hu, S.; Yi, R.; Tang, D.; Walter, T.; Regula, M.; Choi, D.; Li, X., Chemically bonded phosphorus/graphene hybrid as a high performance anode for sodium-ion batteries. *Nano Letters* **2014,** *14* (11), 6329-6335.
22. Joseph, E.; Singhvi, G., Chapter 4 - Multifunctional nanocrystals for cancer therapy: a potential nanocarrier. In *Nanomaterials for Drug Delivery and Therapy*, Grumezescu, A. M., Ed. William Andrew Publishing: 2019; pp 91-116.
23. Shen, J.; Hu, Y.; Li, C.; Qin, C.; Ye, M., Synthesis of amphiphilic graphene nanoplatelets. *Small* **2009,** *5* (1), 82-85.
24. Perrin, R.; Elomaa, M.; Jannasch, P., Nanostructured proton conducting polystyrene−poly(vinylphosphonic acid) block copolymers prepared via sequential anionic polymerizations. *Macromolecules* **2009,** *42* (14), 5146-5154.
25. Ingratta, M.; Elomaa, M.; Jannasch, P., Grafting poly (phenylene oxide) with poly (vinylphosphonic acid) for fuel cell membranes. *Polymer Chemistry* **2010,** *1* (5), 739-746.
26. Dubinsky, S.; Grader, G. S.; Shter, G. E.; Silverstein, M. S., Thermal degradation of poly (acrylic acid) containing copper nitrate. *Polymer Degradation and Stability* **2004,** *86* (1), 171-178.
27. Jiang, D. D.; Yao, Q.; McKinney, M. A.; Wilkie, C. A., TGA/FTIR studies on the thermal degradation of some polymeric sulfonic and phosphonic acids and their sodium salts. *Polymer Degradation and Stability* **1999,** *63* (3), 423-434.
28. Gong, Y.; Zhu, Y.; Liu, Y.; Ma, Z.; Gao, C.; Shen, J., Layer-by-layer assembly of chondroitin sulfate and collagen on aminolyzed poly (L-lactic acid) porous scaffolds to enhance their chondrogenesis. *Acta Biomaterialia* **2007,** *3* (5), 677-685.
29. Fan, Z.; Po, K. H. L.; Wong, K. K.; Chen, S.; Lau, S. P., Polyethylenimine-modified graphene oxide as a novel antibacterial agent and its synergistic effect with daptomycin for methicillin-resistant Staphylococcus aureus. *ACS Applied Nano Materials* **2018,** *1* (4), 1811-1818.
30. Yang, M.; Hou, Y.; Kotov, N. A., Graphene-based multilayers: Critical evaluation of materials assembly techniques. *Nano Today* **2012,** *7* (5), 430-447.
31. Miyazaki, C. M.; Mishra, R.; Kinahan, D. J.; Ferreira, M.; Ducrée, J., Polyethylene imine/graphene oxide layer-by-layer surface functionalization for significantly improved limit of detection and binding kinetics of immunoassays on acrylate surfaces. *Colloids and Surfaces B: Biointerfaces* **2017,** *158*, 167-174.

32. PUCHTLER, H.; Meloan, S. N.; TERRY, M. S., On the history and mechanism of alizarin and alizarin red S stains for calcium. *Journal of Histochemistry & Cytochemistry* **1969,** *17* (2), 110-124.
33. Allen, M. J.; Tung, V. C.; Kaner, R. B., Honeycomb carbon: a review of graphene. *Chemical Reviews* **2009,** *110* (1), 132-145.
34. Kan, L.; Xu, Z.; Gao, C., General avenue to individually dispersed graphene oxide-based two-dimensional molecular brushes by free radical polymerization. *Macromolecules* **2010,** *44* (3), 444-452.
35. Georgakilas, V.; Tiwari, J. N.; Kemp, K. C.; Perman, J. A.; Bourlinos, A. B.; Kim, K. S.; Zboril, R., Noncovalent functionalization of graphene and graphene oxide for energy materials, biosensing, catalytic, and biomedical applications. *Chemicals Review* **2016,** *116* (9), 5464-5519.
36. Bingöl, B.; Meyer, W. H.; Wagner, M.; Wegner, G., Synthesis, microstructure, and acidity of poly (vinylphosphonic acid). *Macromolecular Rapid Communications* **2006,** *27* (20), 1719-1724.
37. Nazari, B.; Ranjbar, Z.; Hashjin, R. n. R.; Rezvani Moghaddam, A.; Momen, G.; Ranjbar, B., Dispersing graphene in aqueous media: Investigating the effect of different surfactants. *Colloids and Surfaces A: Physicochemical and Engineering Aspects* **2019,** *582*, 123870.
38. Jeon, I.-Y.; Choi, H.-J.; Jung, S.-M.; Seo, J.-M.; Kim, M.-J.; Dai, L.; Baek, J.-B., Large-Scale Production of Edge-Selectively Functionalized Graphene Nanoplatelets via Ball Milling and Their Use as Metal-Free Electrocatalysts for Oxygen Reduction Reaction. *Journal of the American Chemical Society* **2013,** *135* (4), 1386-1393.
39. Konkena, B.; Vasudevan, S., Understanding aqueous dispersibility of graphene oxide and reduced graphene oxide through p K a measurements. *The Journal of Physical Chemistry Letters* **2012,** *3* (7), 867-872.
40. Izquierdo, A.; Ono, S.; Voegel, J. C.; Schaaf, P.; Decher, G., Dipping versus Spraying: Exploring the Deposition Conditions for Speeding Up Layer-by-Layer Assembly. *Langmuir : the ACS journal of surfaces and colloids* **2005,** *21*, 7558-67.
41. Molino, P. J.; Higgins, M. J.; Innis, P. C.; Kapsa, R. M.; Wallace, G. G., Fibronectin and bovine serum albumin adsorption and conformational dynamics on inherently conducting polymers: a QCM-D study. *Langmuir* **2012,** *28* (22), 8433-8445.
42. Wilson, C. J.; Clegg, R. E.; Leavesley, D. I.; Pearcy, M. J., Mediation of biomaterial–cell interactions by adsorbed proteins: a review. *Tissue Engineering* **2005,** *11* (1-2), 1-18.
43. Aplin, A.; Howe, A.; Alahari, S.; Juliano, R., Signal transduction and signal modulation by cell adhesion receptors: the role of integrins, cadherins, immunoglobulin-cell adhesion molecules, and selectins. *Pharmacological Reviews* **1998,** *50* (2), 197-264.
44. Kobayashi, J.; Arisaka, Y.; Yui, N.; Akiyama, Y.; Yamato, M.; Okano, T., Effect of Temperature Changes on Serum Protein Adsorption on Thermoresponsive Cell-Culture Surfaces Monitored by A Quartz Crystal Microbalance with Dissipation. *International Journal of Molecular Sciences* **2018,** *19* (5), 1516.
45. Grinnell, F.; Feld, M., Fibronectin adsorption on hydrophilic and hydrophobic surfaces detected by antibody binding and analyzed during cell adhesion in serum-containing medium. *Journal of Biological Chemistry* **1982,** *257* (9), 4888-4893.
46. Phillips, J. E.; Petrie, T. A.; Creighton, F. P.; García, A. J., Human mesenchymal stem cell differentiation on self-assembled monolayers presenting different surface chemistries. *Acta Biomaterialia* **2010,** *6* (1), 12-20.
47. Faucheux, N.; Schweiss, R.; Lützow, K.; Werner, C.; Groth, T., Self-assembled monolayers with different terminating groups as model substrates for cell adhesion studies. *Biomaterials* **2004,** *25* (14), 2721-2730.
48. Mazón, P.; García-Bernal, D.; Meseguer-Olmo, L.; Cragnolini, F.; Piedad, N., Human mesenchymal stem cell viability, proliferation and differentiation potential in response to ceramic chemistry and surface roughness. *Ceramics International* **2015,** *41* (5), 6631-6644.
49. Deligianni, D. D.; Katsala, N. D.; Koutsoukos, P. G.; Missirlis, Y. F., Effect of surface roughness of hydroxyapatite on human bone marrow cell adhesion, proliferation, differentiation and detachment strength. *Biomaterials* **2000,** *22* (1), 87-96.

50. Rosales-Leal, J.; Rodríguez-Valverde, M.; Mazzaglia, G.; Ramón-Torregrosa, P.; Diaz-Rodriguez, L.; Garcia-Martinez, O.; Vallecillo-Capilla, M.; Ruiz, C.; Cabrerizo-Vílchez, M., Effect of roughness, wettability and morphology of engineered titanium surfaces on osteoblast-like cell adhesion. *Colloids and Surfaces A: Physicochemical and Engineering Aspects* **2010,** *365* (1-3), 222-229.
51. Koblinski, J. E.; Wu, M.; Demeler, B.; Jacob, K.; Kleinman, H. K., Matrix cell adhesion activation by non-adhesion proteins. *Journal of Cell Science* **2005,** *118* (13), 2965-2974.
52. Ghag, A. K.; Gough, J. E.; Downes, S., The osteoblast and osteoclast responses to phosphonic acid containing poly (ε-caprolactone) electrospun scaffolds. *Biomaterials science* **2014,** *2* (2), 233-241.
53. Wang, Q. G.; Wimpenny, I.; Dey, R. E.; Zhong, X.; Youle, P. J.; Downes, S.; Watts, D. C.; Budd, P. M.; Hoyland, J. A.; Gough, J. E., The unique calcium chelation property of poly (vinyl phosphonic acid-co-acrylic acid) and effects on osteogenesis in vitro. *Journal of Biomedical Materials Research Part A* **2018,** *106* (1), 168-179.
54. Choi, K.-M.; Seo, Y.-K.; Yoon, H.-H.; Song, K.-Y.; Kwon, S.-Y.; Lee, H.-S.; Park, J.-K., Effect of ascorbic acid on bone marrow-derived mesenchymal stem cell proliferation and differentiation. *Journal of Bioscience and Bioengineering* **2008,** *105* (6), 586-594.
55. Lee, W. C.; Lim, C. H. Y.; Shi, H.; Tang, L. A.; Wang, Y.; Lim, C. T.; Loh, K. P., Origin of enhanced stem cell growth and differentiation on graphene and graphene oxide. *ACS Nano* **2011,** *5* (9), 7334-7341.
56. Akhavan, O.; Ghaderi, E.; Shahsavar, M., Graphene nanogrids for selective and fast osteogenic differentiation of human mesenchymal stem cells. *Carbon* **2013,** *59*, 200-211.
57. Borghi, F. F.; Bean, P. A.; Evans, M. D. M.; van der Laan, T.; Kumar, S.; Ostrikov, K., Nanostructured Graphene Surfaces Promote Different Stages of Bone Cell Differentiation. *Nano-Micro Lett.* **2018,** *10* (3), 12.
58. Dubey, N.; Bentini, R.; Islam, I.; Cao, T.; Castro Neto, A. H.; Rosa, V., Graphene: A Versatile Carbon-Based Material for Bone Tissue Engineering. *Stem Cells International* **2015**, 1-12.
59. Lian, J. B.; Stein, G. S., Development of the osteoblast phenotype: molecular mechanisms mediating osteoblast growth and differentiation. *The Iowa orthopaedic journal* **1995,** *15*, 118.
60. Stein, G. S.; Lian, J. B.; Owen, T. A., Relationship of cell growth to the regulation of tissue-specific gene expression during osteoblast differentiation. *The FASEB journal* **1990,** *4* (13), 3111-3123.
61. Thi-Hiep, N.; Van Hoa, D.; Van Toi, V., Injectable in situ crosslinkable hyaluronan-polyvinyl phosphonic acid hydrogels for bone engineering. *Journal of Biomedical Science and Engineering* **2013,** *6* (08), 854-862.
62. Zaim, M.; Karaman, S.; Cetin, G.; Isik, S., Donor age and long-term culture affect differentiation and proliferation of human bone marrow mesenchymal stem cells. *Annals of hematology* **2012,** *91* (8), 1175-1186.
63. National Academies of Sciences, E.; Medicine, *Exploring Sources of Variability Related to the Clinical Translation of Regenerative Engineering Products: Proceedings of a Workshop*. The National Academies Press: Washington, DC, 2019; p 132.
64. Kartsogiannis, V.; Ng, K. W., Cell lines and primary cell cultures in the study of bone cell biology. *Molecular and cellular endocrinology* **2004,** *228* (1-2), 79-102.
65. Geissler, S.; Textor, M.; Kühnisch, J.; Könnig, D.; Klein, O.; Ode, A.; Pfitzner, T.; Adjaye, J.; Kasper, G.; Duda, G. N., Functional comparison of chronological and in vitro aging: differential role of the cytoskeleton and mitochondria in mesenchymal stromal cells. *PloS one* **2012,** *7* (12), e52700.

Chapter 4

Fabrication and characterisation of Laponite-based hydrogels as a scaffold for BTE

4.1 Chapter abstract

This chapter describes how Laponite-based hydrogels were produced with two different concentrations of Laponite, 2.5% and 5% by weight. Mechanical and rheological properties of hydrogels were studied using shear rheometry in oscillatory and flow modes. Measurement was performed in oscillatory mode to acquire limit of linear viscoelastic (LVE) region, storage modulus (G'), loss modulus (G''), and yield point of hydrogels. Flow mode was used to measure shear thinning behaviour, that is, decrease in hydrogel viscosity with increasing shear rate. Injectability and structural recovery of hydrogels were determined by a time-dependent behaviour by alternating between rotational flow and oscillatory modes. The results show that the addition of PVPA-*co*-AA ($M_n \approx 24200$ g mol^{-1}) solution (0.05 wt%) increased G' with lower yield point of Laponite-based gels while the addition of GO suspension (0.09 wt%) did not significantly affect mechanical properties of gels. Rheological characteristics of Laponite-based gels did not influenced by the incorporation of PVPA-*co*-AA and GO.

Osteoblast-like cells were encapsulated within nanoclay-gel discs and nanoclay-gel beads. Cytoskeleton staining was performed to assess cell shape and spreading. Cell functions and expressions such as calcium deposition, fibronectin and collagen type I, were determined using histological staining of encapsulated samples. The addition of both PVPA-*co*-AA and GO showed no significant effect on osteoinductive activity and cytoskeleton organisation of osteoblasts within Laponite-based gels due to a low concentration.

The aims of research discussed in this chapter were to:

- Investigate the effect of GO and phosphonate polymer on properties of hydrogels and compare to bare Laponite.
- Assess cell viability and metabolic activity of cells within hydrogels.
- Determine and compare cell functions within Laponite and composite hydrogels using 3D encapsulation model.
- Highlight interesting conclusions and potential of Laponite-based scaffolds for BTE and further research.

4.2 Results

4.2.1 Mechanical and rheological properties of Laponite-based gels

4.2.1.1 Brief review of methods

Laponite dispersions (2.5 wt% and 5 wt%) were mixed with GO suspension (0.09 wt%) and/or PVPA-*co*-AA solution (0.05 wt%) in deionised water as described in Section 2.6.1. Briefly, Laponite XLG powder was smoothly added in Milli-Q water at the desired concentration, with stirring. In preparation of composite hydrogels, Laponite powder was added into water-based GO suspension with stirring, after which PVPA-*co*-AA solution was added into mixture. All dispersions were stirred for 2 hours prior further use in research. Rheological properties of Laponite-based hydrogels were investigated using DHR-2 rheometer (TA Instrument).

4.2.1.2 Storage and loss moduli of Laponite-based gels

Amplitude strain sweep under oscillatory test was carried out over the range of 0.01% – 100% strain at a constant frequency of 1 Hz (or 6.28 rad s–1) and temperature of 37 °C to determine the limit of linear viscoelastic (LVE) region of hydrogels. Figure 4-1 illustrates storage (G') and loss (G'') modulus of Laponite-based gels as a function of oscillatory strain at two different concentrations of Laponite. All nanoclay-based hydrogels exhibited the LVE region with a steady G'. After the LVE region, G' of hydrogels started to drop, meaning to a deformation of hydrogel structure.[1] Taking into account, all hydrogels showed an increase of G'' with decreasing G' until the yield point or crossover point (G' = G'' or tan δ = 1) was reached, after which G'' was greater than G' (fluid state) for all samples. This indicates that the viscous

portion dominates and samples start to flow, resulting in a liquid-like behaviour of materials. The yield point of each sample is reported in Figure 4-2.

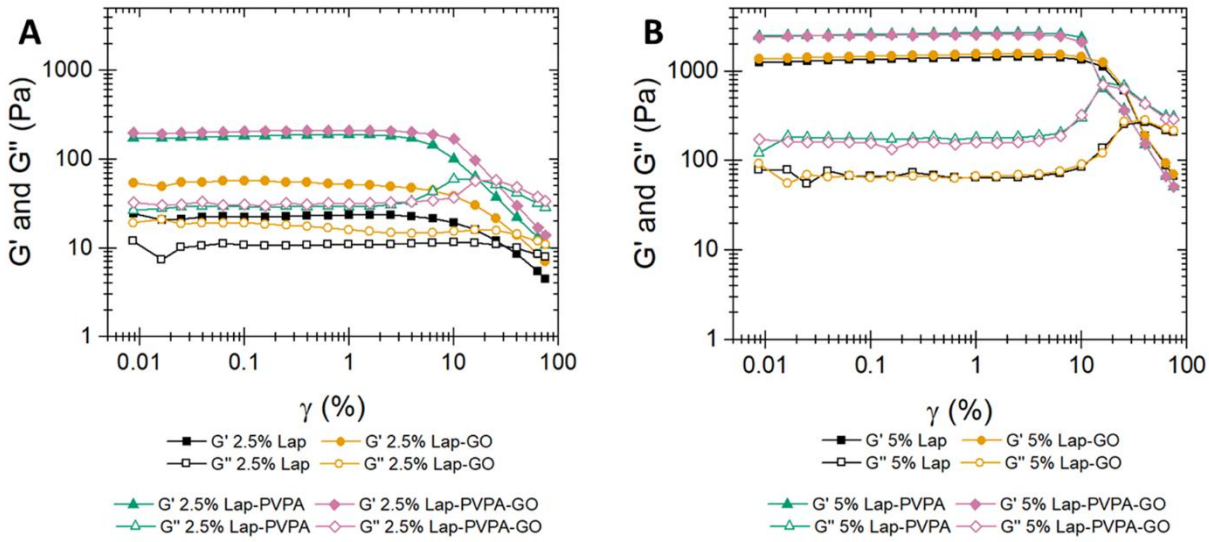

Figure 4-1. Storage (G') and loss (G'') moduli, shown on a log-log plot, of (A) 2.5 wt% and (B) 5 wt% Laponite-based hydrogels as a function of oscillatory strain at a constant frequency of 1 Hz (or 6.28 rad s^{-1}) and temperature of 37 °C. All samples were soaked at 37 °C for 2 minutes before measurement started. Measurement was performed in oscillatory mode with 20 mm parallel plate. Laponite suspensions were mixed with GO suspension and PVPA-*co*-AA solution at 0.09% and 0.05% by weight, respectively, in deionised water. After preparation, all samples were left overnight at room temperature for aging prior testing.

Comparison of yield point (τ_f) and storage modulus (G') of Laponite-based hydrogels in LVE region are shown in Figure 4-2. The addition of PVPA-*co*-AA altered rheological and mechanical properties of Laponite-based hydrogels. Laponite-based hydrogels with the presence of PVPA-*co*-AA had a higher storage modulus (Figure 4-2A, left), but a lower yield point in comparison to Laponite-based gels without addition of PVPA-*co*-AA (Figure 4-2B, left). On the other hand, the incorporation of GO showed no significant difference towards storage modulus and yield point of hydrogels (Figure 4-2, left). Moreover, the set of 5 wt% Laponite-based gels exhibited had the significantly higher G' values in a comparison with to 2.5 wt% Laponite-based gels (Figure 4-2A, right). In contrast, the yield point of hydrogels was not significantly dependent with the concentration of nanoclay (Figure 4-2B, right).

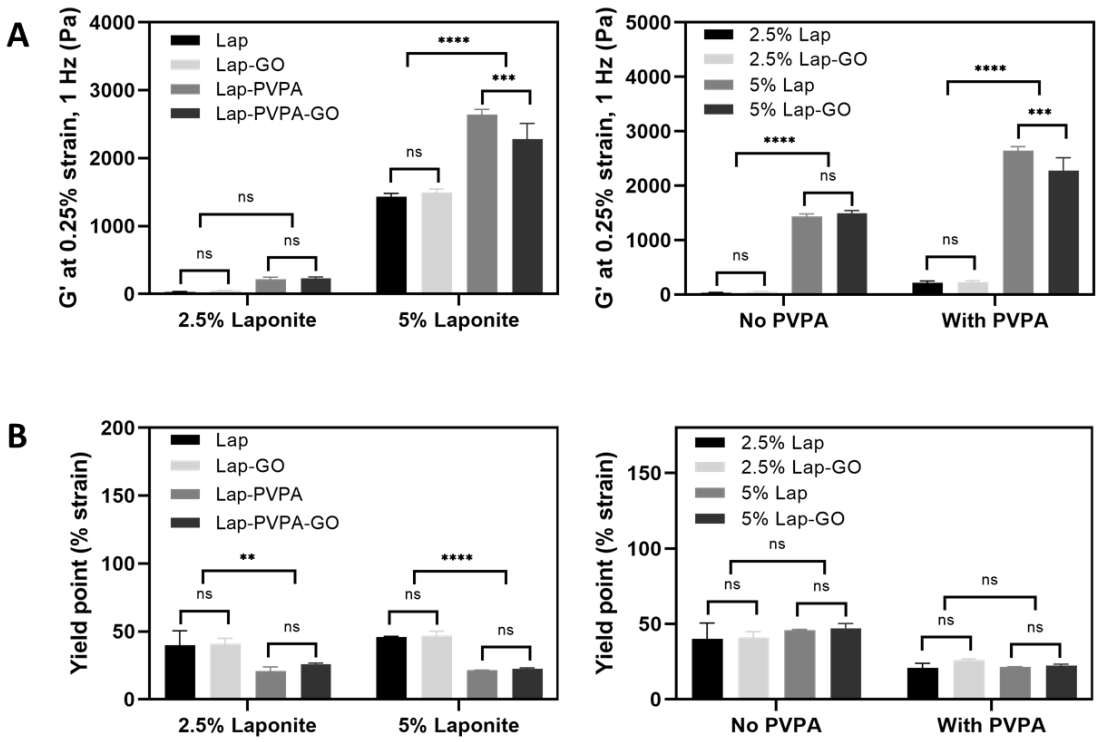

Figure 4-2. Comparison of (A) storage modulus (G') of nanoclay gels at 0.25% strain, 1 Hz and (B) yield point (τ_f) at different components (left panel) and different concentrations of Laponite (right panel). Data were obtained from measurement reported in Figure 4-1.

Frequency sweep oscillatory test was performed in the LVE region at 1% strain to determine the frequency-dependent behaviour of Laponite-based hydrogels. As presented in Figure 4-3, storage modulus (G') of all Laponite-based gels was dominant over loss modulus (G'') for the entire range of frequency. This indicates that all samples exhibited a gel-like behaviour over the frequency range. The linear fit curve was performed at a frequency range of 0.1–63 rad s^{-1} for G' and G'' to determine the slope which are reported in Table 4-1. The slopes are all close to zero but still significantly different from zero (i.e., $p > 0.05$), with the exception of G' of 5% Lap-GO, which is statistically indistinguishable from zero slope. Consequently, it can be considered that G' and G'' of Laponite-based hydrogels were dependent on the frequency, especially at the high region (≥100 rad s^{-1}). Furthermore, some Laponite-based gels exhibited a decrease in moduli with increasing frequency or the slope of plot was negative, indicative of shear-thinning behaviour.

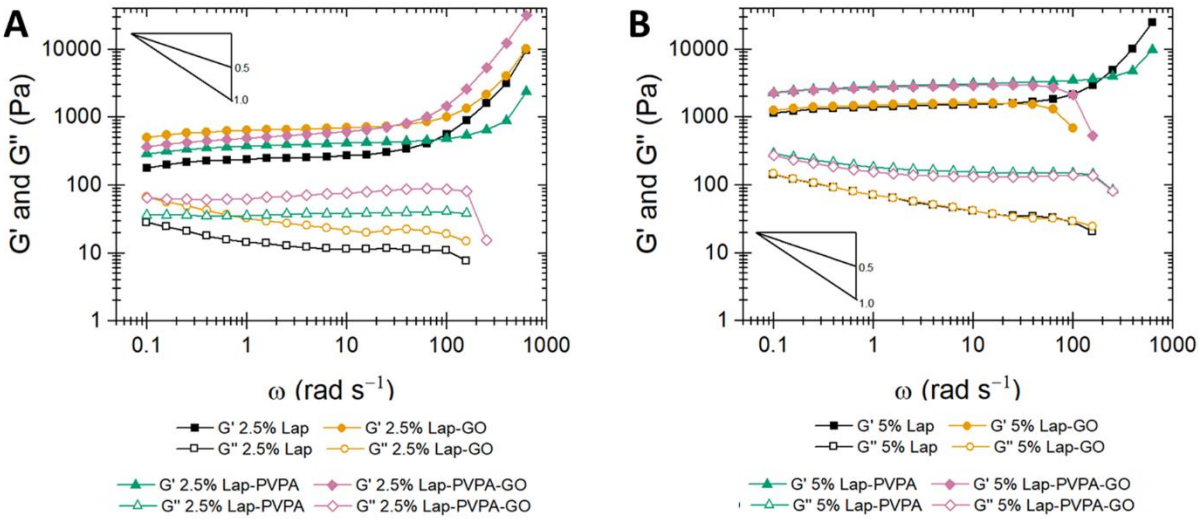

Figure 4-3. Representative data of storage (G') and loss (G'') moduli, shown on a log-log plot, of (A) 2.5 wt% and (B) 5 wt% Laponite-based hydrogels as a function of oscillatory frequency at a constant 1% strain and temperature of 37 °C. All samples were soaked at 37 °C for 2 minutes before measurement started. Measurement was performed in oscillatory mode with 20 mm parallel plate. Laponite suspensions were mixed with GO suspension and PVPA-*co*-AA solution at 0.09% and 0.05% by weight, respectively, in deionised water. After preparation, all samples were left overnight at room temperature for aging prior testing.

Table 4-1. Slope of the linear fit curve on a log-log plot of storage (G') and loss (G'') modulus reported in Figure 4-3. The ± values represent the 95% confidence level. The fit curve was performed at a frequency range of 0.1–63 rad s^{-1}.

Samples	Slope of G'	Slope of G''
2.5% Lap	0.094 ± 0.018	−0.134 ± 0.036
2.5% Lap-GO	0.062 ± 0.009	−0.179 ± 0.037
2.5% Lap-PVPA	0.061 ± 0.010	0.019 ± 0.006
2.5% Lap-PVPA-GO	0.129 ± 0.019	0.060 ± 0.013
5% Lap	0.054 ± 0.008	−0.233 ± 0.021
5% Lap-GO	0.019 ± 0.020	−0.241 ± 0.018
5% Lap-PVPA	0.052 ± 0.006	−0.097 ± 0.023
5% Lap-PVPA-GO	0.034 ± 0.012	−0.100 ± 0.033

4.2.1.3 Shear-thinning behaviour and thixotropy of Laponite-based gels

A continuous rotational flow test was performed to study shear-thinning behaviour of Laponite-based gels. Shear thinning behaviour is characterised by decreasing of viscosity under shear force.[2, 3] The characteristic of shear-thinning behaviour is that the viscosity was found to decrease with increase in shear rate, whilst in the limit of very low shear rates, the viscosity is constant.[3] Viscosity of samples as a function of shear rate is shown in Figure 4-4. Laponite-based hydrogels showed a decrease of viscosity when shear rate increased,

exhibiting shear-thinning behaviour. The set of 5 wt% Laponite-based gels had significantly greater viscosity compared to 2.5 wt% Laponite-based gels. The addition of PVPA-*co*-AA increased viscosity of 2.5 wt% Laponite, but not significant, while the addition of GO had a slight influence on viscosity. This is corresponding to G' obtained from oscillatory test (Figure 4-1 and Figure 4-2). The addition of both GO and PVPA-*co*-AA significantly increased viscosity of 5 wt% Laponite gels (Figure 4-4B). The injection of 2.5% Lap-PVPA-GO through syringe with 21G needle was demonstrated in Figure 4-4C. Laponite-based suspensions stiffen into gels instantaneously when applied to PBS buffer or culture medium.

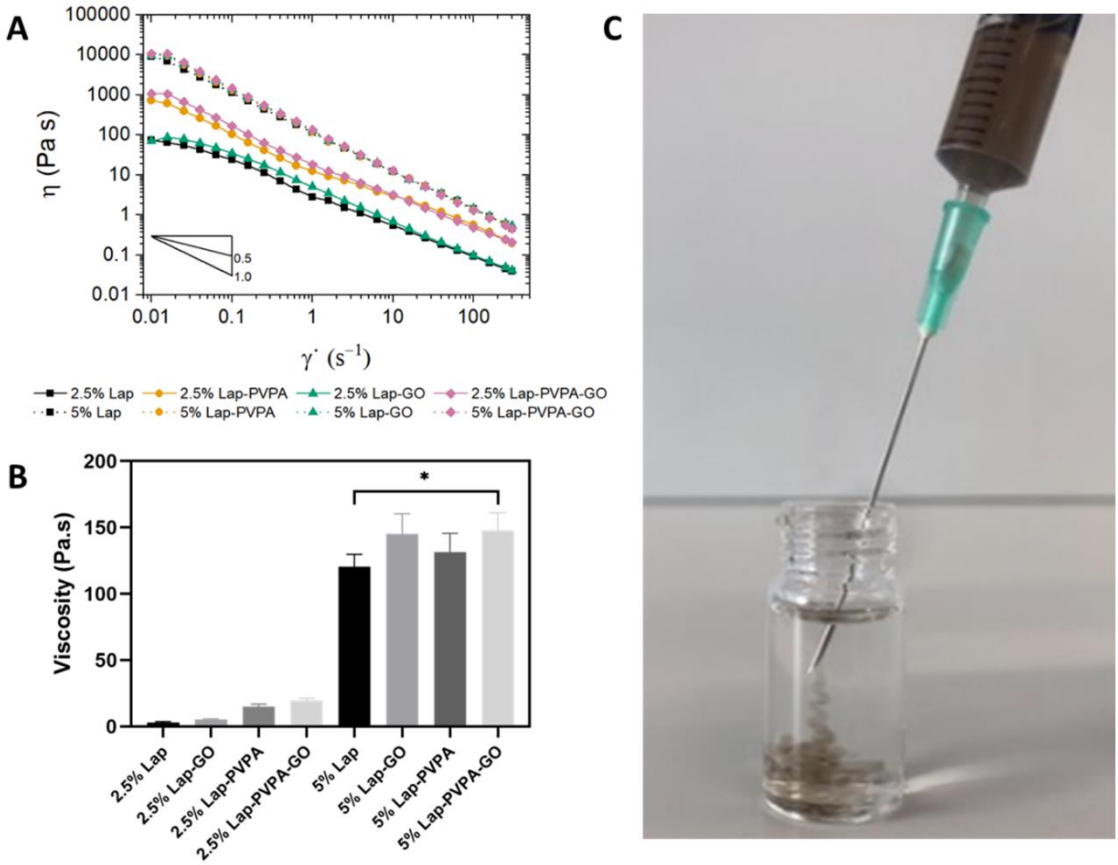

Figure 4-4. (A) Variations of viscosity, shown on a log-log plot, as a function of shear rate 0.01–300 s^{-1} at 37 °C to investigate a shear-thinning behaviour of Laponite-based hydrogels. Representative data were chosen to plot. (B) viscosity of gels at shear rate 1 s^{-1} obtained from (A). All samples were soaked at 37 °C for 2 minutes before measurement started. Measurement was performed in flow mode with 20 mm parallel plate. Laponite concentration was 2.5 wt% and 5 wt% mixed with GO suspension and PVPA-*co*-AA solution at 0.09 wt% and 0.05 wt%, respectively, in deionised water. After preparation, all samples were left overnight at room temperature for aging prior testing. (C) Injection of 2.5 wt% Lap-PVPA-GO into PBS buffer using a syringe with 21G needle.

Time-dependent behaviour can be performed through rotational test and oscillatory test. The rheological behaviour obtained from the rotational test is related to only viscous behaviour (shear viscosity and shear stress) while the oscillation test characterise both viscous (G'') and elastic (G') portions of materials, describing the complete viscoelastic behaviour.[4]

The shear viscosity and shear stress obtained from time-dependent rotational step tests are presented in Figure 4-5. Laponite-based hydrogels exhibited thixotropic behaviour in which a significant increase in shear viscosity was observed at every interval of low shear rate, indicating to the structural recovery after deformation. The shear viscosity of hydrogels decreased with an increase of shear stress under high shear rate, meaning to the structural decomposition and a liquid-like behaviour of hydrogels. After the strong shear was removed, some hydrogels (Lap, Lap-GO, and Lap-PVPA) exhibited an instantaneous increase of viscosity which was close to the original level, indicating a rapid recovery.[5] Unexpectedly, after deformation, shear viscosity of Lap-PVPA-GO gradually increased towards equilibrium and eventually reached the original viscosity at the end of intervals.

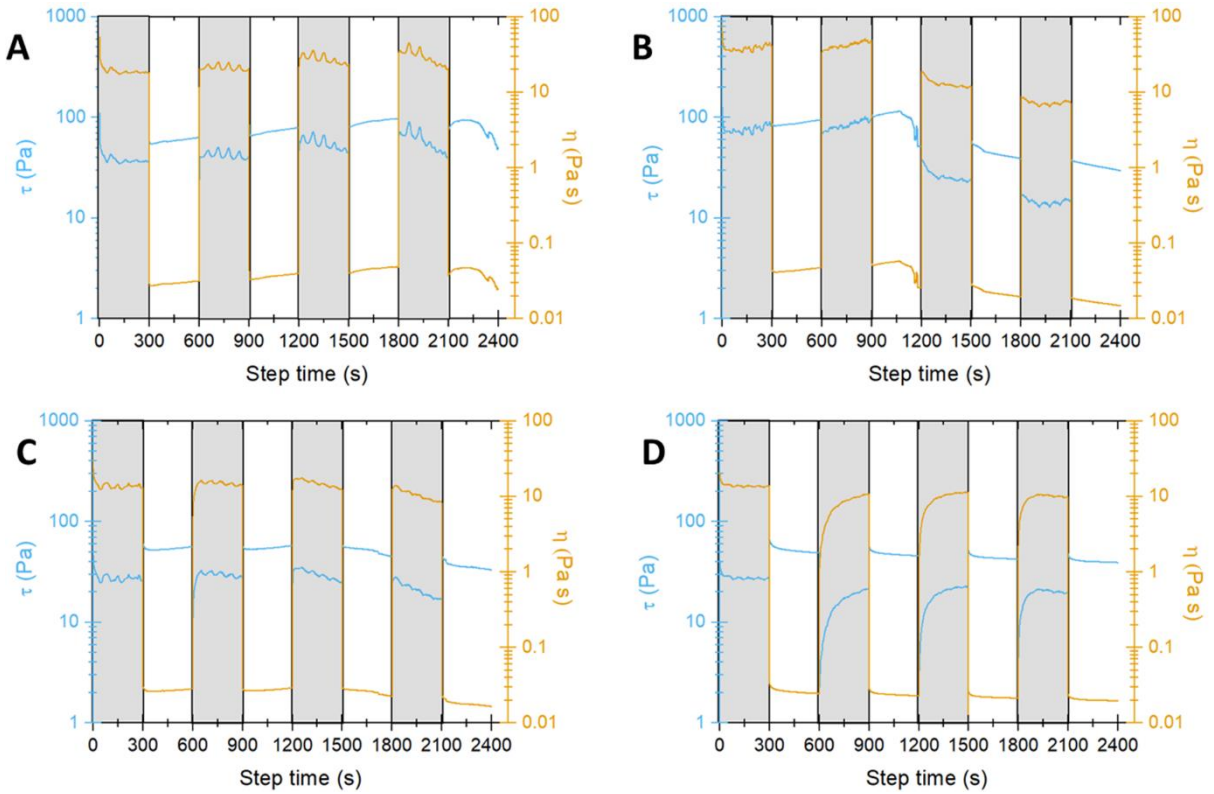

Figure 4-5. Stress and viscosity of Laponite-based hydrogels in which hydrogels were subjected to alternating cycles of low shear rate (2 s^{-1}, 5 minutes) and high shear rate (200 s^{-1}, 5 minutes) at 37 °C. All samples were soaked at 37 °C for 2 minutes before measurement started. Intervals of low shear rate are identified with vertical grey boxes. Measurement was performed in flow mode with 20 mm parallel plate. Laponite concentration was 3 wt% mixed with GO suspension and PVPA-*co*-AA solution at 0.09 wt% and 0.05 wt%, respectively, in deionised water. After preparation, all samples were left overnight at room temperature for aging prior testing. A) Laponite, B) Laponite-GO, C) Laponite-(PVPA-*co*-AA), and D) Laponite-(PVPA-*co*-AA)-GO.

In contrast to characterisation of viscous portion evaluated in the rotational step test, the oscillatory test provides determination of both elastic and viscous potions, describing viscoelastic behaviour. Storage (G') and loss (G'') moduli are then obtained to present elastic and viscous behaviours, respectively.[4] G' and G'' of Laponite-based hydrogels measured from the oscillatory step test are described in Figure 4-6. Laponite-based gels exhibited a solid-like behaviour where G' > G'' at a low shear strain. On the other hand, G' of hydrogels decreased immediately when a high shear was applied, indicating a liquid-like behaviour (G'' > G') of hydrogels due to structural breakdown at this strain. A solid-like behaviour was observed again when a high shear was removed in which G' significantly increased at this stage, demonstrating a rapid recover of structural network.

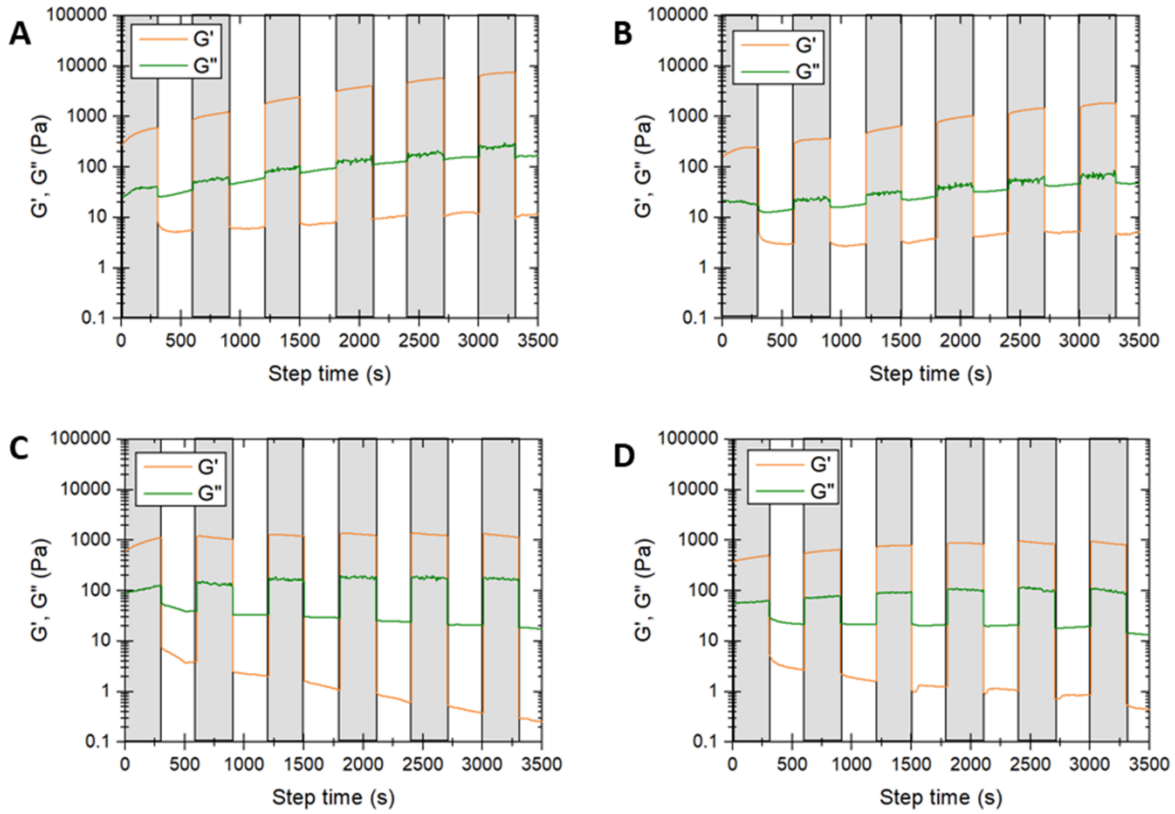

Figure 4-6. Storage (G') and loss (G'') moduli of Laponite-based hydrogels in which hydrogels were subjected to alternating cycles of low strain (0.25% strain, 5 minutes) and high strain (150% strain, 5 minutes) at 37 °C. All samples were soaked at 37 °C for 2 minutes before measurement started. Measurement was performed in oscillatory time-sweep mode with 20 mm parallel plate. Laponite concentration was 3 wt% mixed with GO suspension and PVPA-*co*-AA solution at 0.09 wt% and 0.05 wt%, respectively, in deionised water. After preparation, all samples were left overnight at room temperature for aging prior testing. A) Laponite, B) Laponite-GO, C) Laponite-(PVPA-*co*-AA), and D) Laponite-(PVPA-*co*-AA)-GO.

The rotational step test was performed on Laponite-based suspensions which were injected through culture medium prior measurement to investigate the effect of ions present in culture medium towards thixotropic behaviour. The injection of dispersions into culture medium is to simulate the conditions used in application. Shear viscosity and shear stress of Laponite-based dispersions in culture medium which were obtained from time-dependent rotational step tests are presented in Figure 4-7. Hydrogels exhibited the uniform structural regeneration after deformation as the same with those in native state, meaning that the presence of culture medium did not influence thixotropic properties of Laponite-based gels.

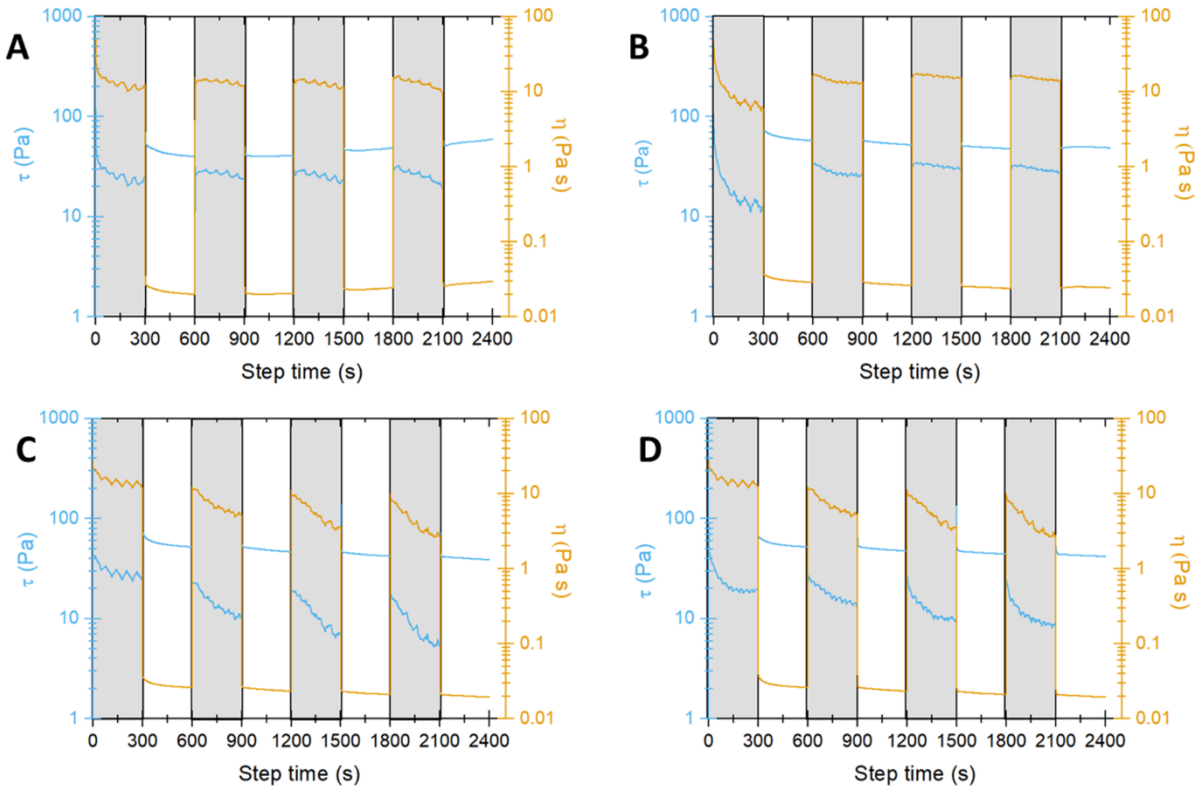

Figure 4-7. Stress and viscosity of Laponite-based hydrogels in which gels were subjected to alternating cycles of low shear rate (2 s^{-1}, 5 minutes) and high shear rate (200 s^{-1}, 5 minutes). All samples were soaked at 37 °C for 2 minutes before measurement started. Intervals of low shear rate are identified with vertical gray boxes. Measurement was performed in flow mode with 20 mm parallel plate. Laponite concentration was 3 wt% mixed with GO suspension and PVPA-*co*-AA solution at 0.09 wt% and 0.05 wt%, respectively, in deionised water. After preparation, all samples were immediately injected through cell culture medium, after which the hydrogels were transferred to measurement straightaway without further aging. A) Laponite, B) Laponite-GO, C) Laponite-(PVPA-*co*-AA), and D) Laponite-PVPA-*co*-AA)-GO.

4.2.2 Scanning electron microscopy images of Laponite hydrogels

Scanning electron microscopy (SEM) images of 1 wt% and 3% Laponite gels are shown in Figure 4-8. The SEM images revealed a porous structure of 1 wt% Laponite gel with pores of approximately 20–40 µm in diameter whereas 3 wt% Laponite exhibited a non-porous structure. However, pores observed in 1 wt% Laponite gel were potentially defects created through a freeze drying.

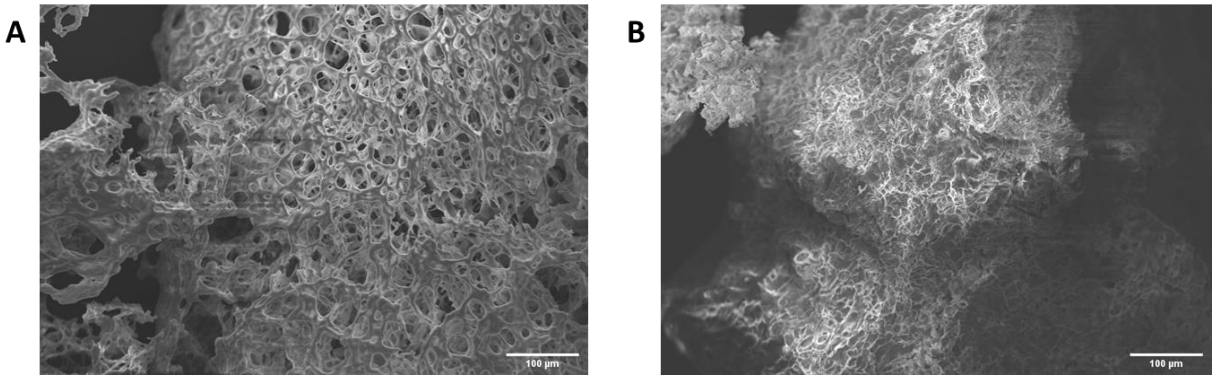

Figure 4-8. SEM images of freeze-dried Laponite gels. (A) 1 wt% Laponite gel and (B) 3 wt% Laponite gel. Scale bar represents 100 µm.

4.2.3 Cell viability and metabolic activity of osteoblastic cells seeded with Laponite-based hydrogels

Following the objectives of this chapter, Laponite-based hydrogels were cultured with osteoblasts and cell viability was assessed using Live/dead assays; live cells were stained with calcein-AM (shown as green), while dead cells were stained with ethidium homodimer (shown as red). A 2D-culture was firstly performed with LIVE/DEAD assays due to its feasibility and ease. Hydrogels without cells were also stained with LIVE/DEAD reagents and used as a control to identify the background of staining generated by hydrogels. Representative LIVE/DEAD images of 2.5% and 5% Laponite-based hydrogels are shown in Figure 4-9 and Figure 4-10, respectively. All Laponite-based hydrogels showed a strong staining with ethidium homodimer (a red fluorescent dye) due to electrostatic interactions between positively charged dye and negatively charged surface of Laponite crystals.[6] There were some green spots visible in both Laponite-based hydrogels seeded with cells and control gels (no cell); however, the size and appearance of those green spots were irregular compared to cell morphology. As a consequence, it is difficult to identify that the green spots found in Laponite-based hydrogels were viable cells. It is also noteworthy that representative bright field images of cells seeded on Laponite-based gels (Figure 4-11) revealed a lot of cells attached on hydrogel surface which was not corresponding to LIVE/DEAD images. Therefore, it is concluded that LIVE/DEAD assays are not suitable to use for cell viability of Laponite-based hydrogels.

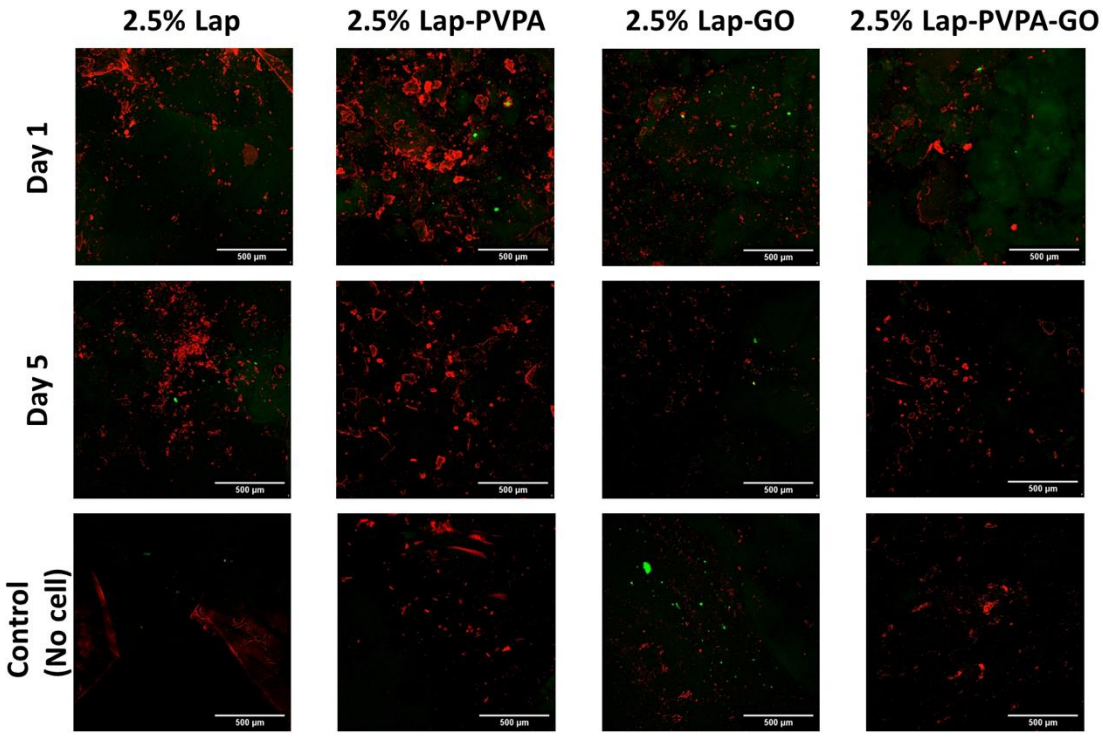

Figure 4-9. LIVE/DEAD images of 2.5 wt% Laponite-based hydrogels with and without Saos-2 at 1 day and 5 days post-seeding. Scale bar represents 500 µm.

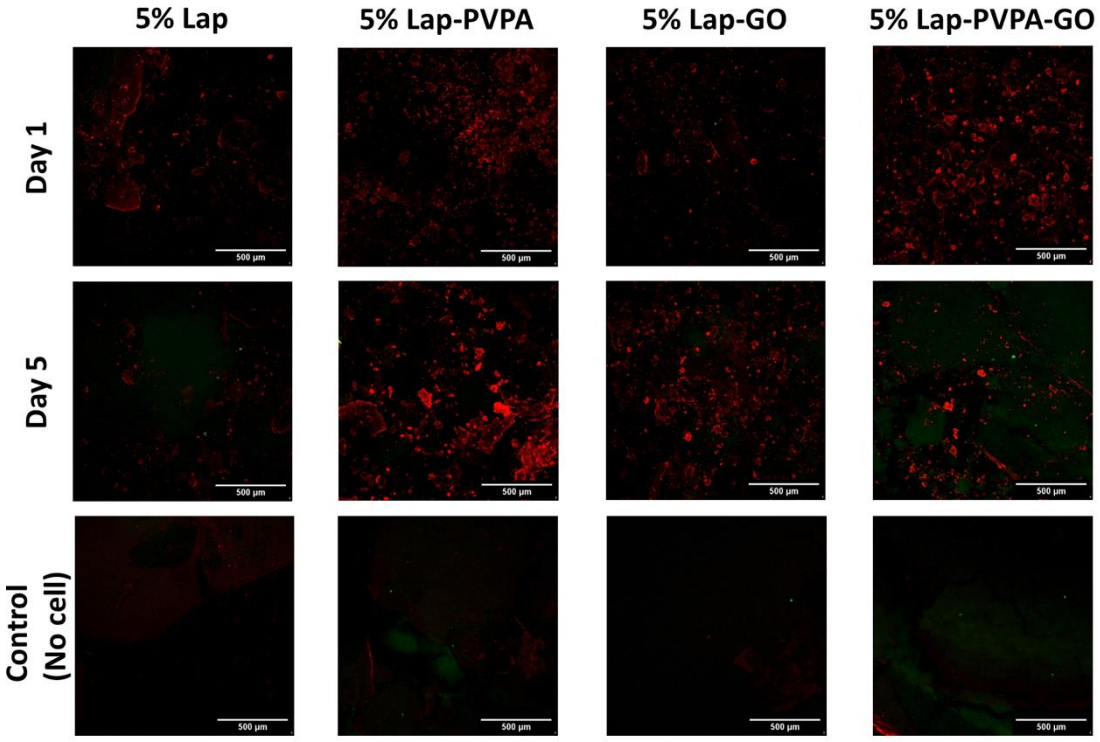

Figure 4-10. LIVE/DEAD images of 5 wt% Laponite-based hydrogels with and without HOBs at 1 day and 5 days post-seeding. Scale bar represents 500 µm.

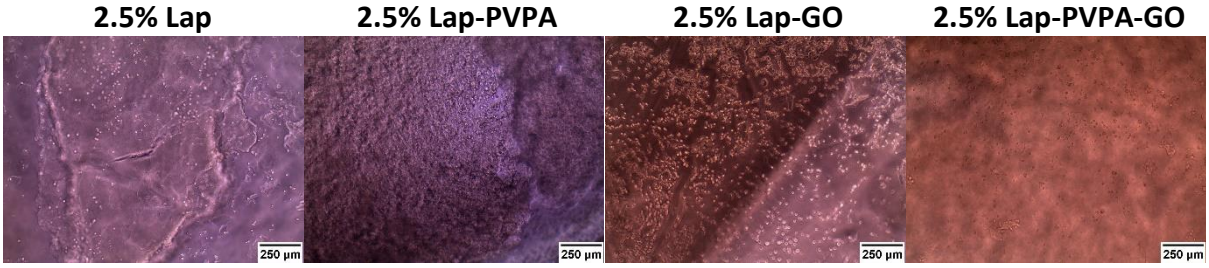

Figure 4-11. Bright field images of osteoblast-like cells (Saos2) seeded on surface of 2.5 wt% Laponite-based hydrogels at 4 days post-seeding. Scale bar represents 250 µm.

The metabolic activity of osteoblasts cultured on the surface (2D culture) and encapsulated within (3D culture) Laponite-based hydrogels was measured over a 7-day period using AlamarBlue assay. Metabolically active cells result in the conversion of nonfluorescent resazurin to fluorescent resorufin, meaning that a greater fluorescence intensity at 590 nm ($I_{590\ nm}$) is indicative of higher metabolic activity. AlamarBlue assay of 2D culture-samples and 3D culture-samples were performed at 1 day, 4 days and 7 days after post-seeding, with results displayed in Figure 4-12A) and Figure 4-12B), respectively. Fluorescence intensity of all acellular hydrogels (without cell seeding) were measured and excluded from fluorescence intensity of samples to remove background intensity generated from each hydrogel. This is shown in Figure 4-13 in which fluorescence intensity of 3D culture-samples and acellular hydrogels are reported.

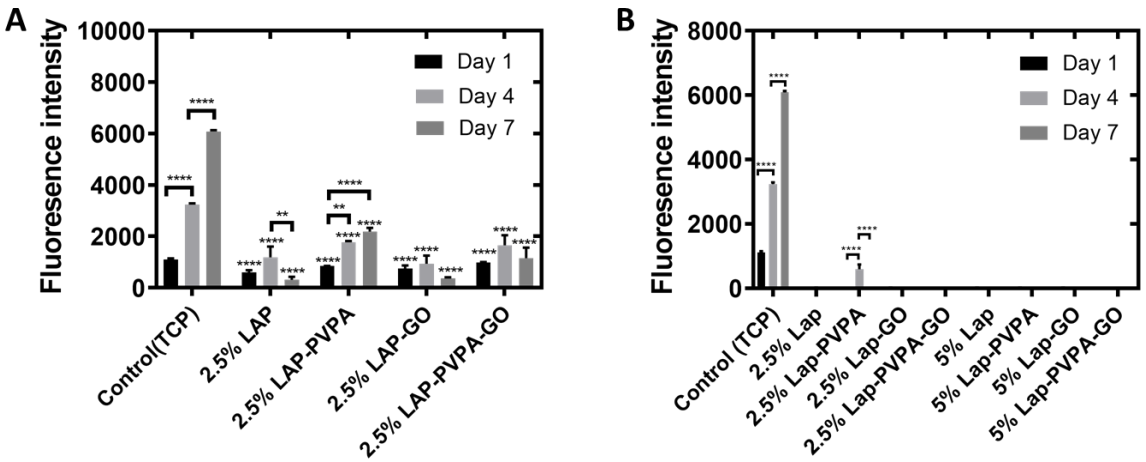

Figure 4-12. Fluorescence intensity measured by AlamarBlue assay of Laponite-based hydrogels with Saos-2 at 1 day, 4 days and 7 days post-seeding (n = 3 samples). Error bars represent standard deviation. A) 2D culture and B) 3D cell encapsulation. All data were obtained and reported without background intensity generated from each acellular hydrogel.

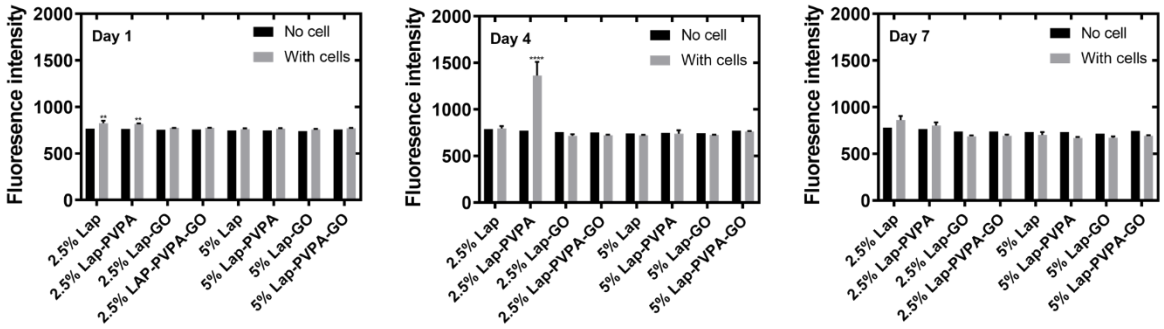

Figure 4-13. Fluorescence intensity measured by AlamarBlue assay of cell encapsulated Laponite-based hydrogels (3D culture) with Saos-2 and hydrogels without cells at 1 day, 4 days and 7 days post-seeding (*n* = 3 samples). Error bars represent standard deviation. **** $p \leq 0.0001$, ** $p \leq 0.01$.

Considering fluorescence intensity of 2D culture-samples (Figure 4-12A), only Lap-PVPA and controls showed a significant increase in I_{590} nm (and hence cell metabolism) over the test period while the rest showed no significant change in I_{590} nm, meaning no cell metabolic activity. Interestingly, all cell encapsulated hydrogels (3D culture) did not show a significant difference in I_{590} nm after background intensity was excluded. The significant difference in fluorescence intensity reported for Lap and Lap-PVPA at 1 day post-seeding, and Lap-PVPA at 4 days post-seeding could be a false positive.

According to results of LIVE/DEAD and AlamarBlue assays, it is convinced that these assays are not suitable to use for measurement of cell viability and activity for Laponite-based hydrogels. Consequently, actin cytoskeleton staining and histological analysis were used to determine cell functions in Laponite-based scaffolds, with results reported in the following sections.

4.2.4 Osteoblast-like cells behaviour within nanoclay-gel discs

4.2.4.1 Actin cytoskeleton organisation

To further investigate cell spreading and morphology within hydrogel structure, phalloidin was performed. Phalloidin binds to F-actin, meaning that phalloidin staining can be used to visualise the actin cytoskeleton. In this section, Saos-2 cells were encapsulated within 3% Laponite and 3% Laponite-PVPA-GO hydrogel discs. The procedure of cell encapsulation is described in Section 2.6.4.1. Briefly, Laponite dispersion was prepared and autoclaved, after which cell-containing culture medium at a density of 5×10^6 cells was mixed with Laponite hydrogels at 1:9 by volume ratio. 100 µL of cell-containing Laponite hydrogels were placed

into inserts in 24-well plates to make hydrogel discs. Phalloidin staining was performed at 1, 3, and 7 days after post-seeding, with representative images displayed in Figure 4-14.

The actin cytoskeleton staining reveals cell morphology and degree of cell spreading within hydrogels. Saos-2 in nanoclay-gel discs exhibited and remained a round morphology over the culture period due to the pore structure of hydrogels. Phalloidin staining also suggests the restricted cytoskeleton organisation and cell spreading of Saos-2 in Laponite-based hydrogels which was contrast to the actin distribution for Saos-2 seeded on TCP (control). The addition of PVPA and GO did not change the extent of cytoskeleton organisation and morphology of Saos-2 within nanoclay gels.

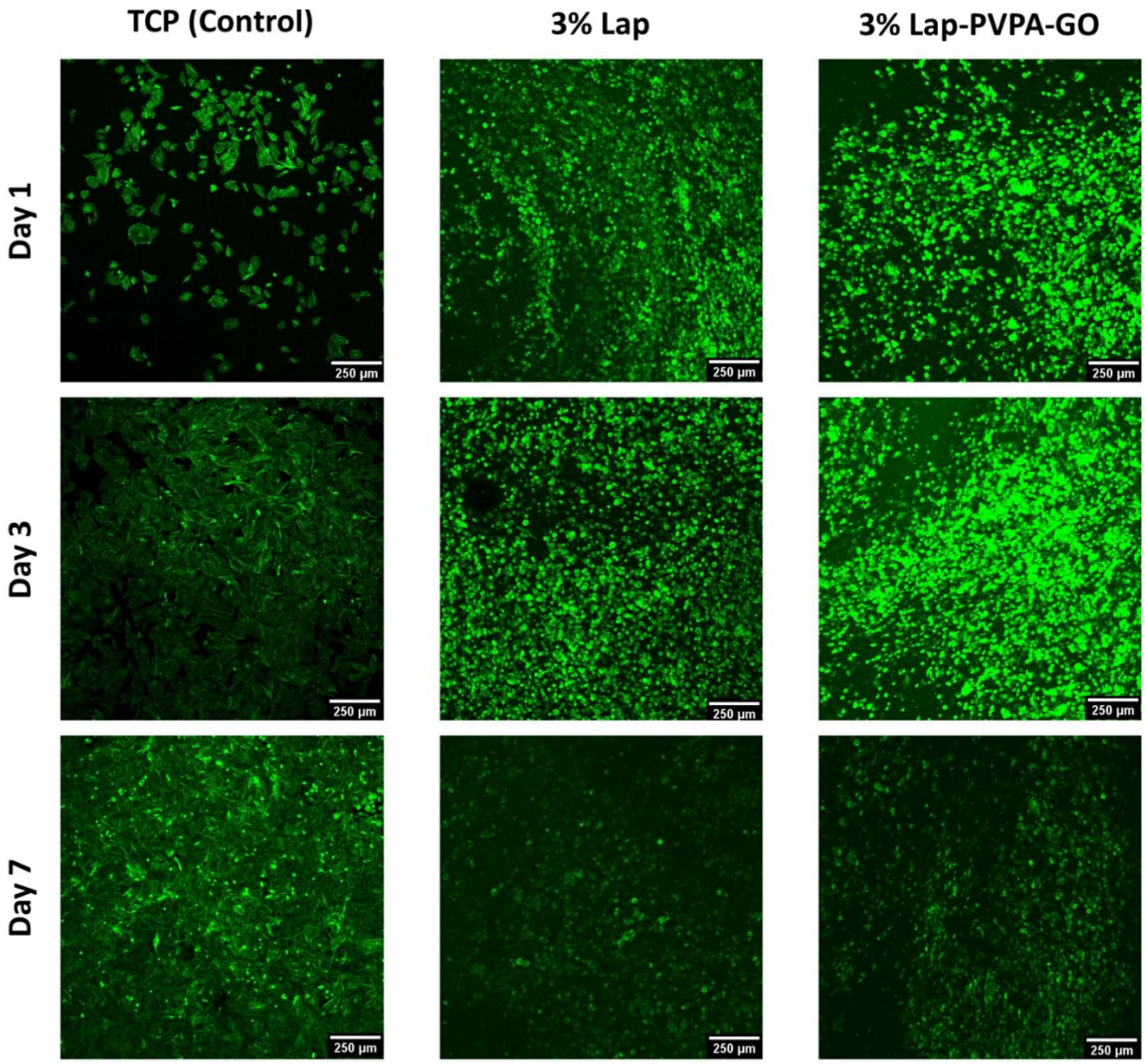

Figure 4-14. Phalloidin staining of osteoblast-like cells Saos-2 (passage number 20) encapsulated in disc-shaped hydrogels at 1, 3, and 7 days post-seeding. Scale bar represents 250 µm.

4.2.4.2 Histological assessment

To investigate cell distribution and activity within hydrogel scaffolds, samples were stained with haematoxylin and eosin (H&E), alizarin red S, and von Kossa which are stains used in histology. H&E stain is the gold standard[7] and widely used in nuclear and cytoplasm stains. Alizarin red S and von Kossa are common stains to either visualise mineralised nodules or detect calcium deposit in mineralised matrix. The von Kossa stain is the method that relates to the binding of silver ions to anions (phosphates, sulphates, or carbonates) of calcium salts and the reduction of silver salts to form dark brown or black staining. Unlike the von Kossa, alizarin red S reacts with calcium cation to form a chelate that is orange to red in colour.[8] Cells seeded on cell-culture treated plastic coverslips were used as controls. H&E, alizarin red S, and von Kossa stains of Saos-2 seeded on controls were presented in Figure 4-15.

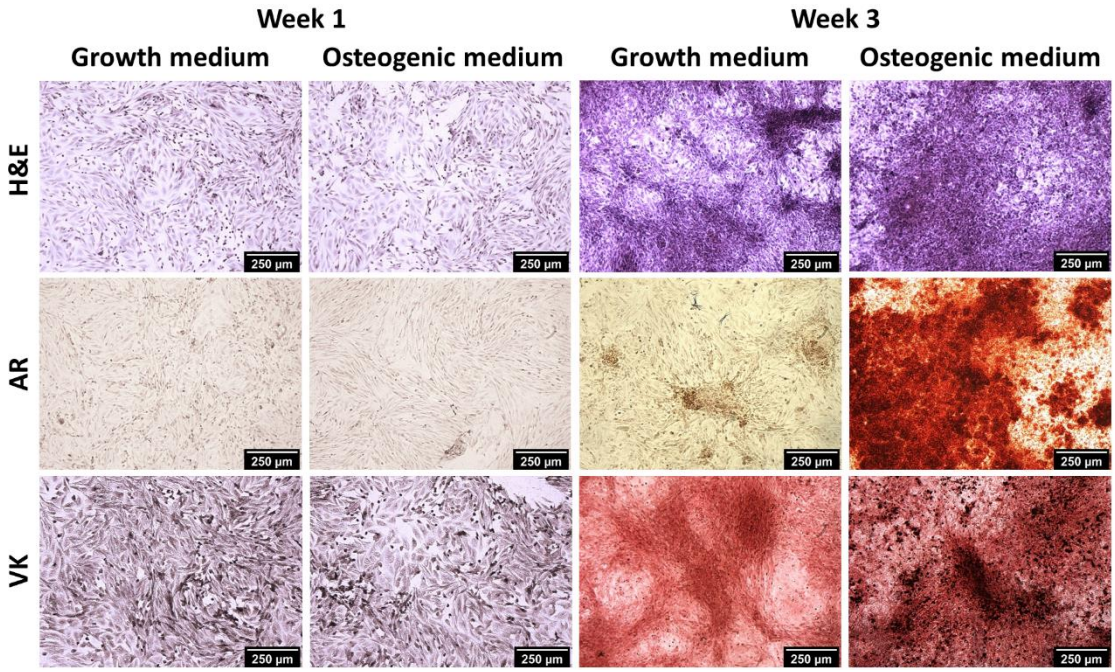

Figure 4-15. Haematoxylin and eosin (H&E), alizarin red S (AR), and von Kossa (VK) stains of *in vitro* Saos-2 (passage number 20) seeded on cell-culture treated plastic coverslips at 1 week and 3 weeks post-seeding. Scale bar represents 250 µm. Frame size: 1295×945 µm.

Representative images of H&E stain of Saos-2 encapsulated within nanoclay gels at 1 and 3 weeks post-seeding are displayed in Figure 4-16. Unlike the noticeable cytoplasm around nuclei of Saos-2 on controls in Figure 4-15, cell nuclei of Saos-2 encapsulated in nanoclay-gel discs, which were stained in dark blue, were surrounded by voids. Cell morphology observed from H&E stain corresponded with results obtained from phalloidin staining. H&E stain also revealed degree of cell distribution and cell clusters within nanoclay-gel discs.

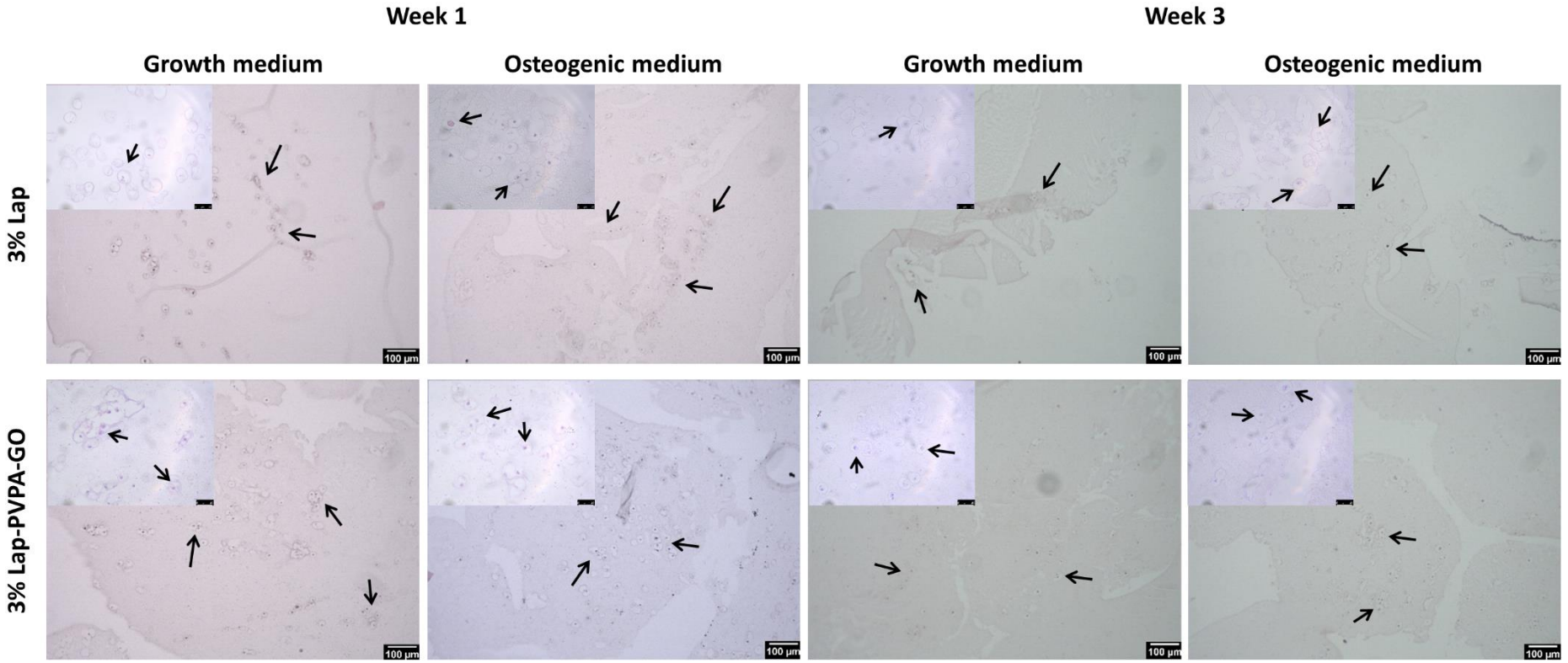

Figure 4-16. Haematoxylin and eosin (H&E) staining of cross-sections from *in vitro* osteoblast-like cells Saos-2 (passage number 20) encapsulated within disc-shaped hydrogels at 1 week and 3 weeks post-seeding. Scale bar represents 100 µm. Inset: the higher magnification images that show stained nuclei of cells within scaffolds. Scale bar of inset images represent 25 µm.

To investigate osteoinductive ability of Laponite-based scaffolds and the synergetic effect of nanoclay, GO, and phosphonates, *in vitro* osteogenic mineralisation of Saos-2 was examined using alizarin red S and von Kossa stains. Saos-2 seeded in nanoclay-gel discs were cultured in basal growth medium and osteogenic medium which contained the osteogenic-induced supplements (ascorbate-2-phosphate, β-glycerophosphate, and dexamethasone). Samples were harvested and analysed at 1 and 3 weeks post-seeding.

Alizarin red S staining and von Kossa staining images for Saos-2 encapsulated in nanoclay-gel discs incubated in the presence and absence of osteogenic induction media are presented in Figure 4-17 and Figure 4-18, respectively. The alizarin red S staining images were analogous to the von Kossa staining images. Neither the control (Figure 4-15) nor the cross-sections of Saos-2 seeded in nanoclay-gel discs displayed positive staining after 1 week post-seeding, in both basal growth and osteogenic media. The Saos-2 encapsulated in 3% Laponite showed positive staining after 3 weeks post-seeding, only in the presence of osteogenic induction. Interestingly, positive staining was observed in the Saos-2 encapsulated in 3% Lap-PVPA-GO after 3 weeks post-seeding, even in the absence of osteogenic supplements. It is noteworthy that staining tended to be stronger in cells at the peripheral of the gel samples for both alizarin red S and von Kossa.

According to the recently research from Dawson's group,[9] hBMSCs seeded in 3D Laponite gel beads showed a strong staining for alizarin red S at 3 weeks post-seeding. Unlike the previous research, Saos-2 seeded in Laponite gel discs exhibited small parts of positive staining across samples. The difference may be due to the procedure of encapsulation and the thickness of gel discs which might affect the diffusion of protein and nutrients into scaffold. Consequently, the procedure of cell encapsulation in this study was improved.

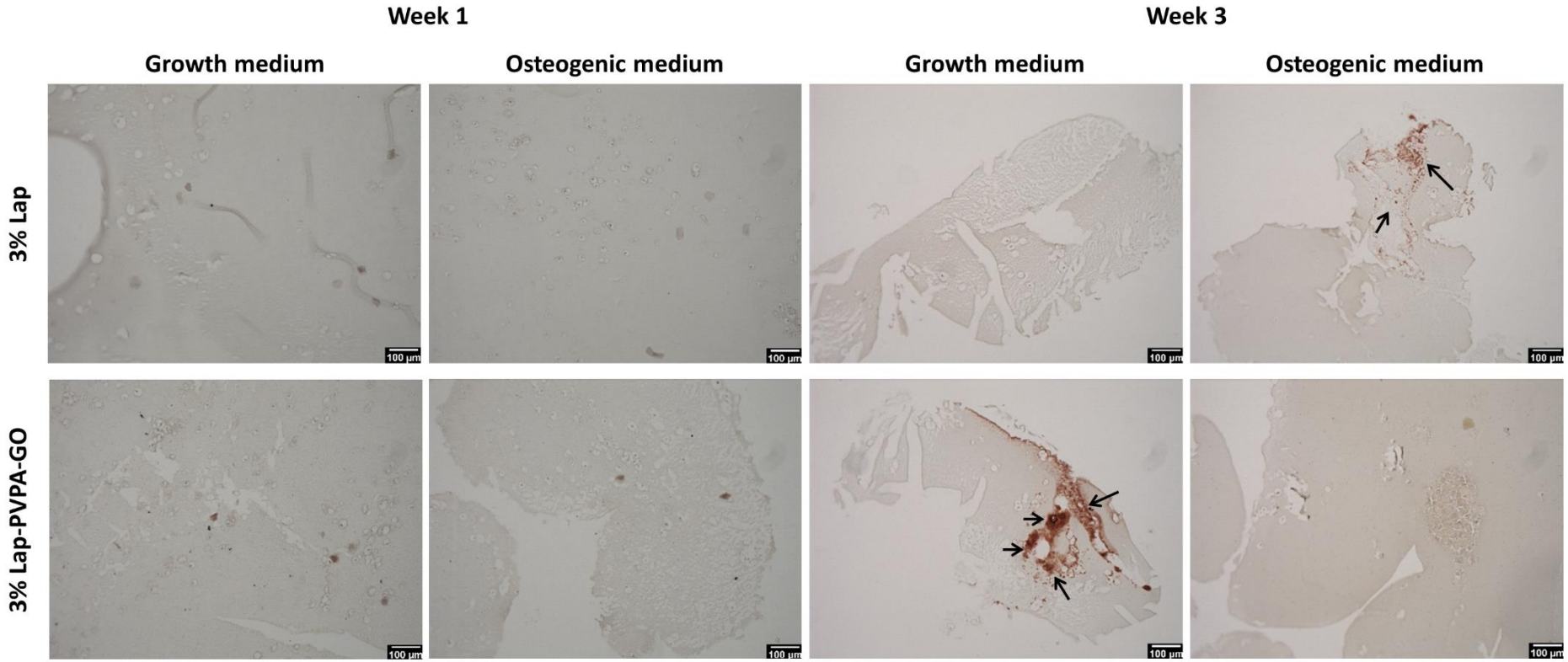

Figure 4-17. Alizarin red S staining of cross-sections from *in vitro* osteoblast-like cells Saos-2 (passage number 20) encapsulated within disc-shaped hydrogels at 1 week and 3 weeks post-seeding. Arrows indicate the positive staining area. Scale bar represents 100 µm.

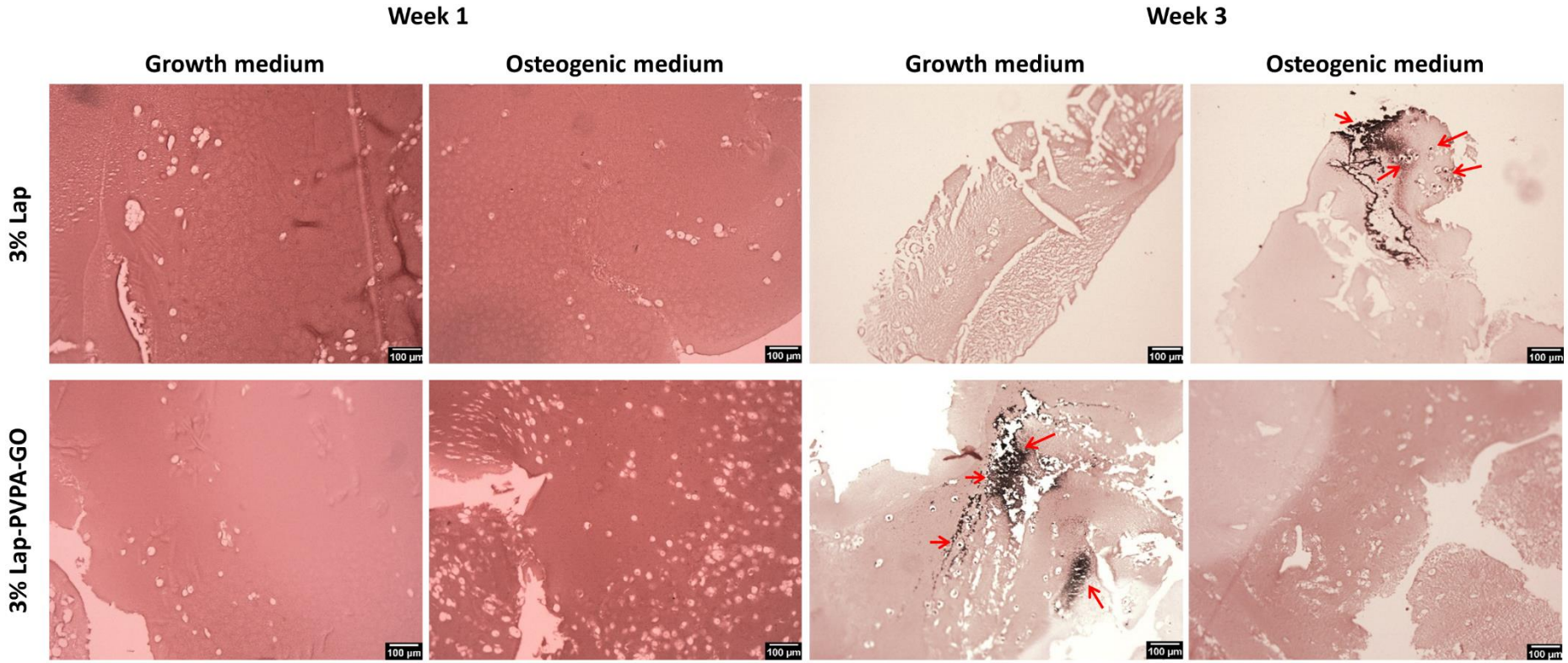

Figure 4-18. Von Kossa staining of cross-sections from *in vitro* osteoblast-like cells Saos-2 (passage number 20) encapsulated within disc-shaped hydrogels at 1 week and 3 weeks post-seeding. Arrows indicate the positive staining area. Scale bar represents 100 µm.

4.2.5 Osteoblast-like cells behaviour within nanoclay-gel droplets

4.2.5.1 Brief review of methods

The procedure of cell encapsulation was improved and adapted from Dawson's group which is described in Section 2.6.4.2. Briefly, Laponite was dispersed in Milli-Q water and vigorously mixed using stirrer. The concentration of Laponite dispersions were 3% by weight. Laponite dispersions were sterilised under UV for 2 hours and used for cell encapsulation immediately. 100 µL of cell-containing culture medium at a density of 5×10^6 cells was homogenously dispersed in 900 µL Laponite suspensions. Cell-containing Laponite hydrogels were then added drop-wise as 10 µL volume into culture medium in 24-well plates with a droplet per well. Cytoskeleton organisation and cell expression of cell-encapsulated nanoclay-gel beads were determined using phalloidin staining and histological assessment.

4.2.5.2 Actin cytoskeleton organisation

4.2.5.2.1 Phalloidin staining

Phalloidin staining was performed at 1, 3, and 7 days after encapsulation to visualise actin cytoskeleton, with representative images shown in Figure 4-19. Cell morphology and degree of cell spreading within nanoclay-gel beads were similar to those found in nanoclay-gel discs; Saos-2 in nanoclay-gel droplets exhibited and remained a round morphology over the culture period due to the pore structure of hydrogels. Phalloidin staining revealed the restricted actin cytoskeleton organisation and cell spreading of cells within Laponite-based hydrogels whereas the actin distribution was observed for Saos-2 seeded on TCP (control). The addition of PVPA and GO did not significantly change the actin cytoskeleton organisation and morphology of Saos-2 within nanoclay-gel droplets.

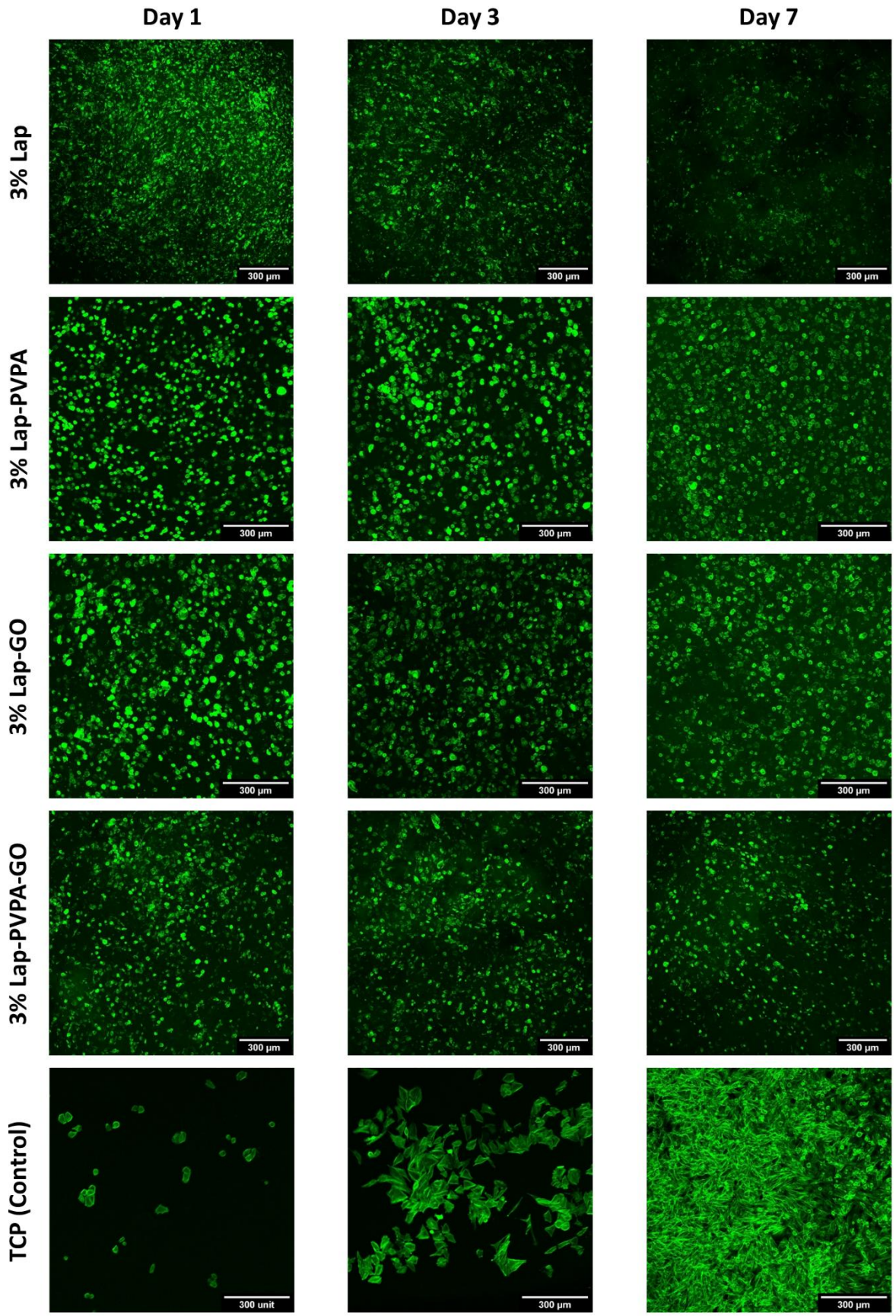

Figure 4-19. Phalloidin staining of osteoblast-like cells Saos-2 (passage number 17) encapsulated in gel droplets at 1, 3, and 7 days post-seeding. Scale bar represents 300 µm.

4.2.5.2.2 Cell area and cell eccentricity analysis

The average cell area was analysed for Saos-2 encapsulated within Laponite-based gel droplets with data shown in Figure 4-20. At different time point, the Saos-2 encapsulated in each nanoclay-based gel did not show any significant change in average cell areas throughout the 7-day test period. At 3 days post-seeding, Saos-2 seeded within Lap-PVPA and Lap-GO showed a significant increase in cell areas, as compared to Saos-2 within Lap and Lap-PVPA-GO.

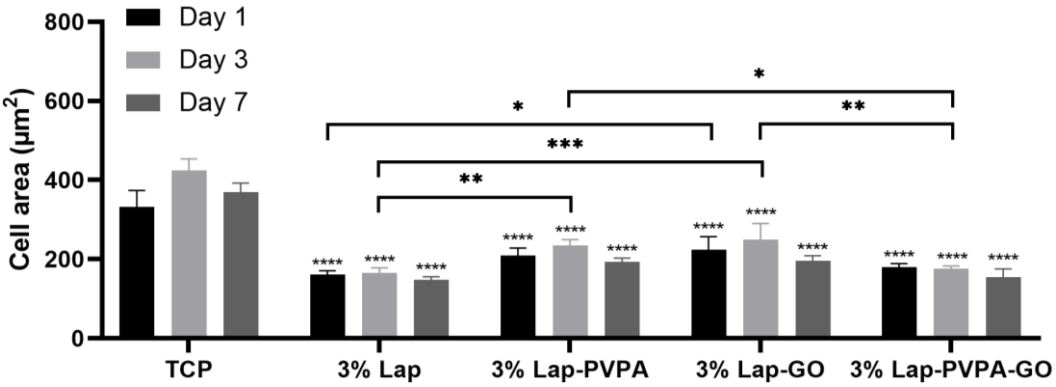

Figure 4-20. Average cell areas of Saos-2 (passage number 17) encapsulated within Laponite-based gel droplets. Data were obtained from phalloidin staining images and analysed using CellProfiler software with the 'measure cell shape/size' feature. Stars above bars show results with statistical significance compared to TCP (control) at the same time point. Error bars represent standard deviation. Significant differences between Laponite-based gels are indicated by horizontal lines. **** $p \leq 0.0001$, *** $p \leq 0.001$, ** $p \leq 0.01$, * $p < 0.05$.

In addition to cell area, cell eccentricity or cell shape analysis was also performed on Saos-2 encapsulated within Laponite-based gel droplets with data shown in Figure 4-21. Eccentricity, *e*, refers to the ratio of the distance between the foci of the ellipse, *c*, and its major axis length, *a*. Eccentricity can also be defined in terms of the ratio of the minor and major axes, *b*/*a*:

$$e = \frac{c}{a} = \sqrt{1 - \frac{b^2}{a^2}} \tag{4-1}$$

Eccentricity has a value between 0 and 1; 0 represents a circle and 1 represents a line segment (Figure 4-22).

Saos-2 seeded on TCP showed a significant increase in cell eccentricity at 3 days and 7 days post-seeding in a comparison with 1 day post-seeding, indicating a more elongated

morphology. There were no significant change in cell eccentricity for all Laponite nanoclay-based gels over the test period.

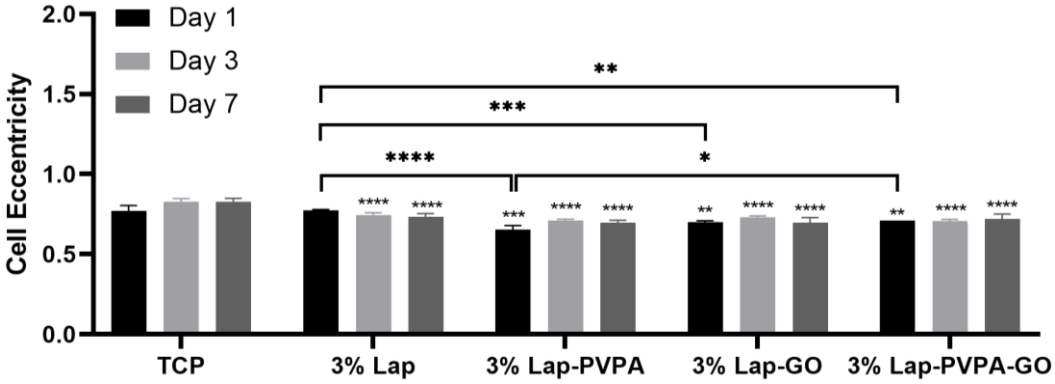

Figure 4-21. Cell shape analysis of Saos-2 (passage number 17) encapsulated within Laponite-based gel droplets. Data were obtained from phalloidin staining images and analysed using CellProfiler software with the 'measure cell shape/size' feature. Stars above bars show results with statistical significance compared to TCP (control) at the same time point. Error bars represent standard deviation. Significant differences between Laponite-based gels are indicated by horizontal lines. **** $p \leq 0.0001$, *** $p \leq 0.001$, ** $p \leq 0.01$, * $p < 0.05$.

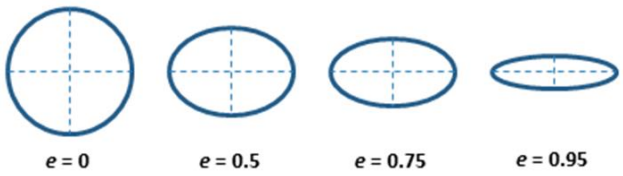

Figure 4-22. Examples of eccentricity values with the shape of objects.

At 1 day post-seeding, there was a significant higher average cell eccentricity for Saos-2 encapsulated in neat Laponite gel in a comparison to other Laponite-based gels, suggesting to a more elongated morphology of Saos-2 seeded in Laponite gel without the addition of copolymer and GO. Also, the average cell eccentricity for Saos-2 within Lap-PVPA was significantly lower than Lap-PVPA-GO at 1 day post-seeding.

4.2.5.3 Histological analysis

Histological analysis was performed at 1 and 3 weeks after post-seeding to determine matrix mineralisation of Saos-2 within nanoclay-gel beads using H&E, alizarin red S, fibronectin and collagen I stains. Saos-2 seeded on cell-culture treated plastic coverslips were used as controls. H&E and alizarin red S stains of controls were displayed in Figure 4-23, with the strongly positive staining of alizarin red S observed on controls cultured in osteogenic medium

at 3 weeks post-seeding. Saos-2 on coverslips exhibited the typical spindle-like morphology of osteoblasts in both standard growth and osteogenic media over the test period.

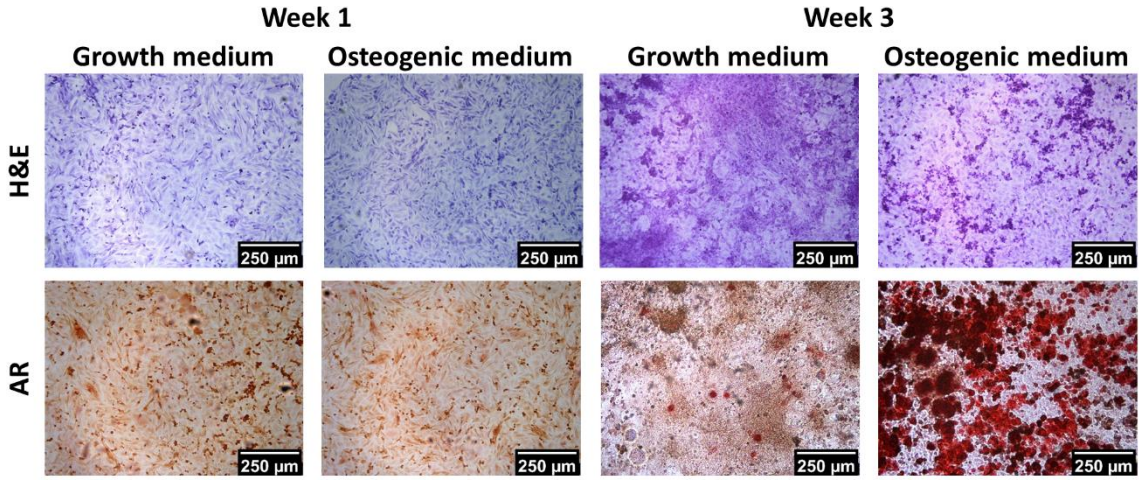

Figure 4-23. Haematoxylin and eosin (H&E) and alizarin red S (AR) stains of *in vitro* Saos-2 (passage number 17) seeded on cell-culture treated plastic coverslips at 1 week and 3 weeks post-seeding. Scale bar represents 250 µm. Frame size: 1100×825 µm.

Representative images of H&E stain of Saos-2 encapsulated within nanoclay gels, at 1 and 3 weeks post-seeding, incubated in growth and osteogenic media are displayed in Figure 4-24 and Figure 4-25, respectively. Unlike the typical morphology of Saos-2 seeded on controls, Saos-2 encapsulated in nanoclay-gel droplets exhibited a rounded shape, with cell nuclei stained in dark blue and the absence of surrounded cytoplasm. Instead, cells within gel droplets were surrounded by voids, suggesting to the occupancy of cells within scaffolds. Cell morphology observed from H&E stain corresponded with results obtained from phalloidin staining. H&E stain also revealed degree of cell distribution and cell clusters within nanoclay-gel droplets, by which a greater cell population was observed within gel droplets at 3 weeks post-seeding, in a comparison with samples cultured for 1 week.

The calcium deposition in the mineralised matrix was determined using alizarin red S staining. The representative images of cross sections from *in vitro* Saos-2 encapsulated nanoclay gels stained with alizarin red S are shown in Figure 4-26 and Figure 4-27 for the incubation in standard growth medium and osteogenic medium, respectively. Interestingly, all Laponite-based nanoclay gels, cultured in standard growth medium without osteogenic induction, showed the positive stains of alizarin red S at 3 weeks post-seeding (Figure 4-26), meaning to calcium deposition within scaffolds. Only Laponite incorporated with GO (Lap-GO), in normal growth medium, exhibited the positive alizarin red staining at 1 week post-seeding.

Unexpectedly, no nanoclay gels which were incubated in osteogenic medium showed any positive alizarin red S stained area throughout the culture period (Figure 4-27). It is noteworthy that the loss of hydrogels occurred during the test period, probably due to dissolution of Laponite gels in culture medium.

Images of type I collagen and fibronectin staining of cell encapsulated Laponite gels are shown in Figure 4-28 – Figure 4-31. A soft brown staining of type I collagen was consistently observed in all samples, cultured in both growth and osteogenic medium, at 1 week and 3 weeks post-seeding (Figure 4-28 and Figure 4-29). Similarly, strong brown stained areas were detected for fibronectin staining for all samples, both in growth and osteogenic media, throughout the test period (Figure 4-30 and Figure 4-31).

Figure 4-32 represents images of type I collagen and fibronectin staining of hydrogel droplets without cells (blank gels) at 1 week post-incubation in normal growth medium. A weak, soft brown stain could be observed at the edge of acellular Laponite-based gels for type I collagen staining. In contrast, a dark brown stain of fibronectin could be detected in acellular Laponite-based gels.

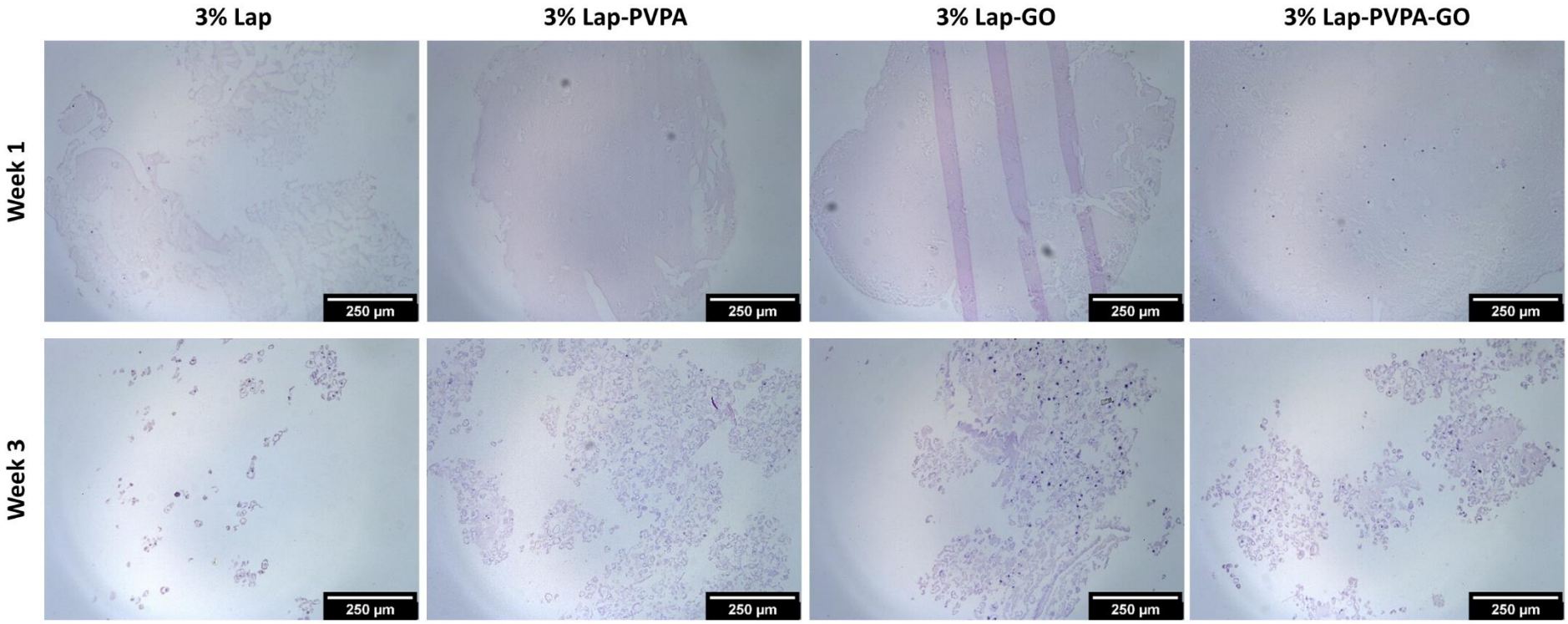

Figure 4-24. Haematoxylin and eosin (H&E) staining of cross-sections from *in vitro* osteoblast-like cells Saos-2 (passage number 17) encapsulated within hydrogel droplets at 1 week and 3 weeks post-seeding. Samples were incubated in basal growth medium without osteogenic inducers. Scale bar represents 250 µm.

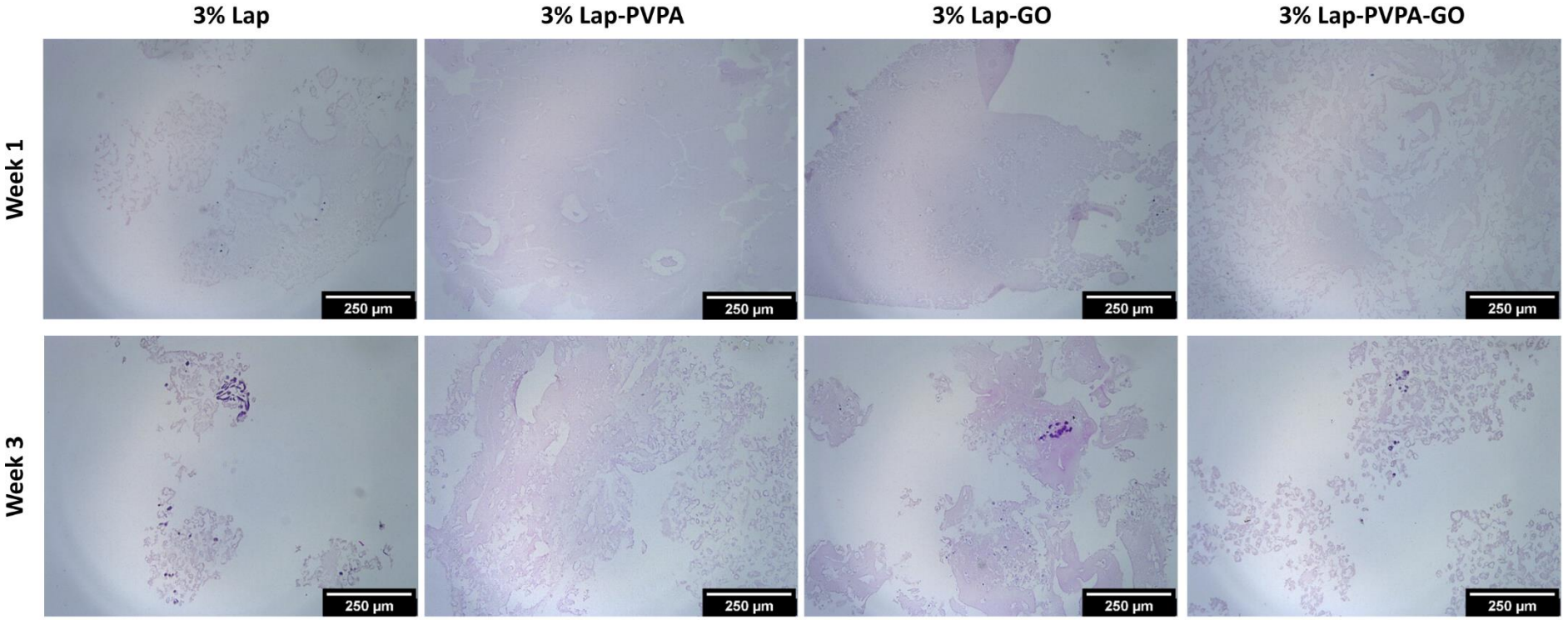

Figure 4-25. Haematoxylin and eosin (H&E) staining of cross-sections from *in vitro* osteoblast-like cells Saos-2 (passage number 17) encapsulated within hydrogel droplets at 1 week and 3 weeks post-seeding. Samples were incubated in basal growth medium supplemented with osteogenic inducers. Scale bar represents 250 µm.

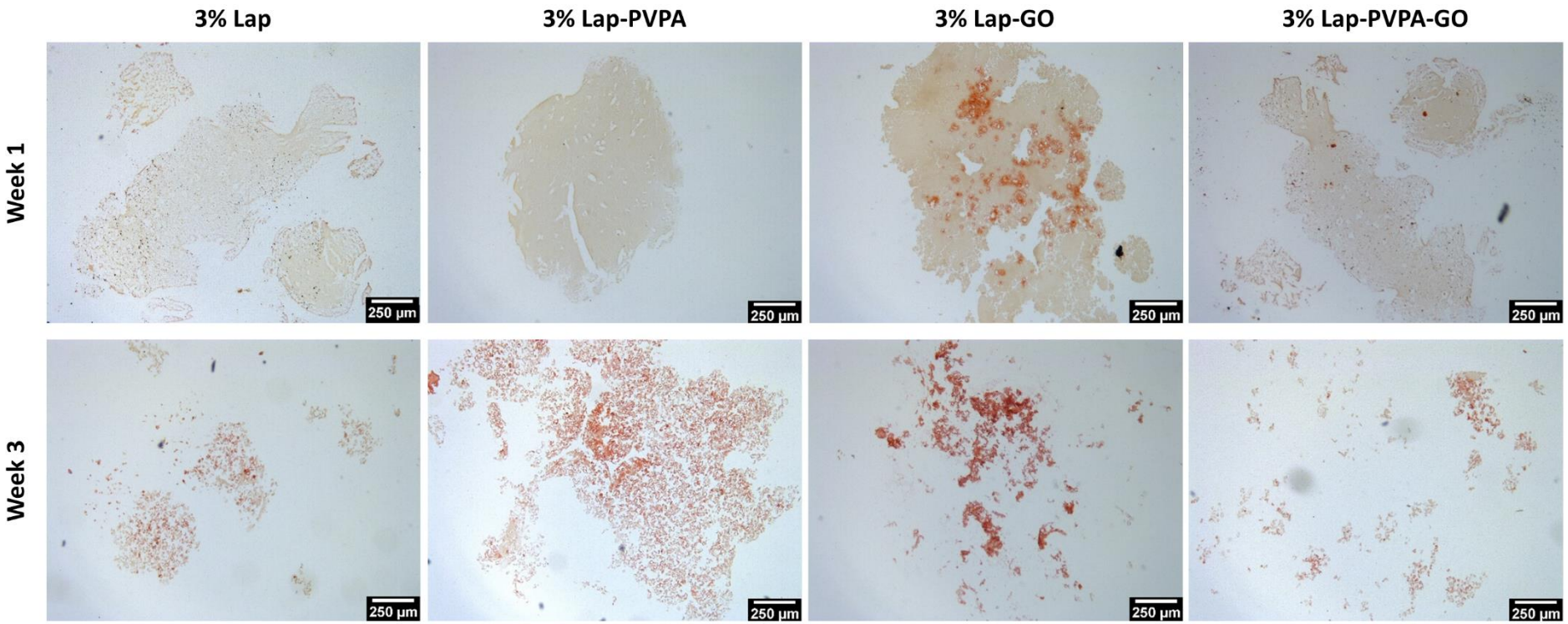

Figure 4-26. Alizarin red S staining of cross-sections from *in vitro* osteoblast-like cells Saos-2 (passage number 17) encapsulated within hydrogel droplets at 1 week and 3 weeks post-seeding. Samples were incubated in basal growth medium without osteogenic inducers. Scale bar represents 250 µm.

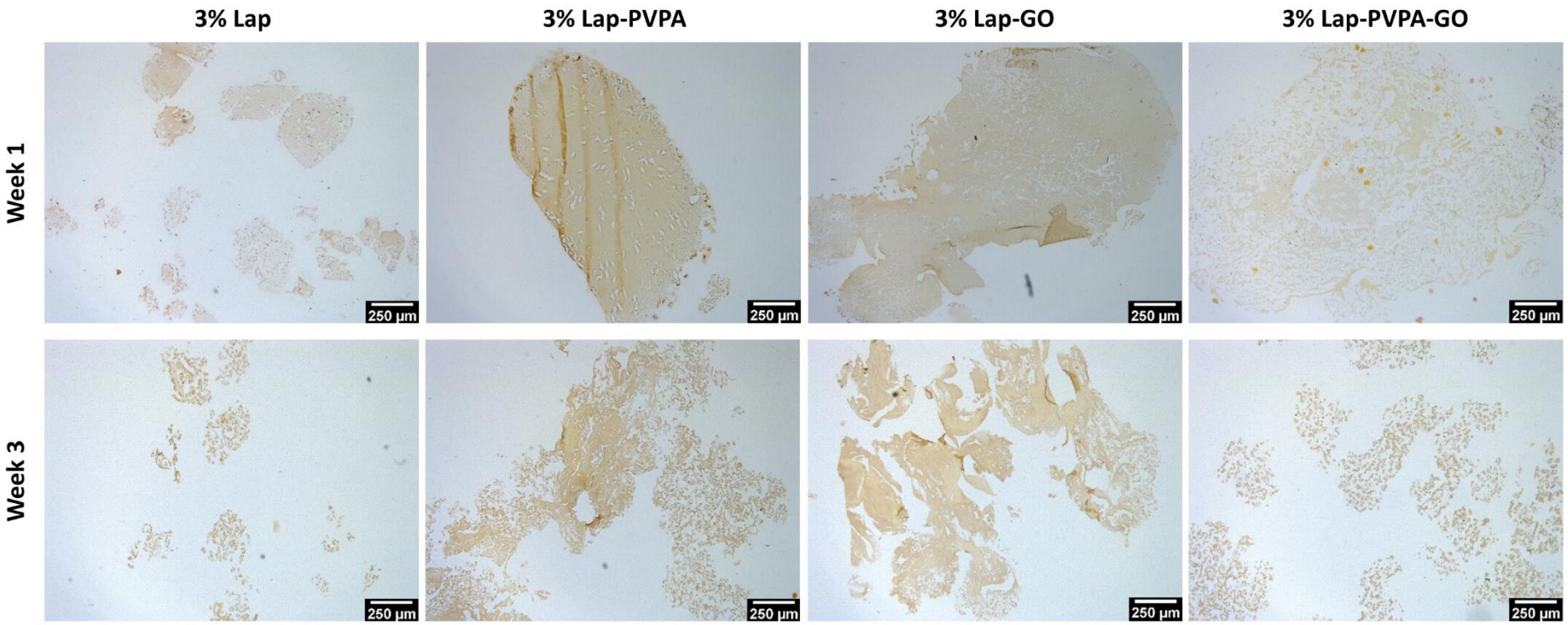

Figure 4-27. Alizarin red S staining of cross-sections from *in vitro* osteoblast-like cells Saos-2 (passage number 17) encapsulated within hydrogel droplets at 1 week and 3 weeks post-seeding. Samples were incubated in basal growth medium supplemented with osteogenic inducers. Scale bar represents 250 µm.

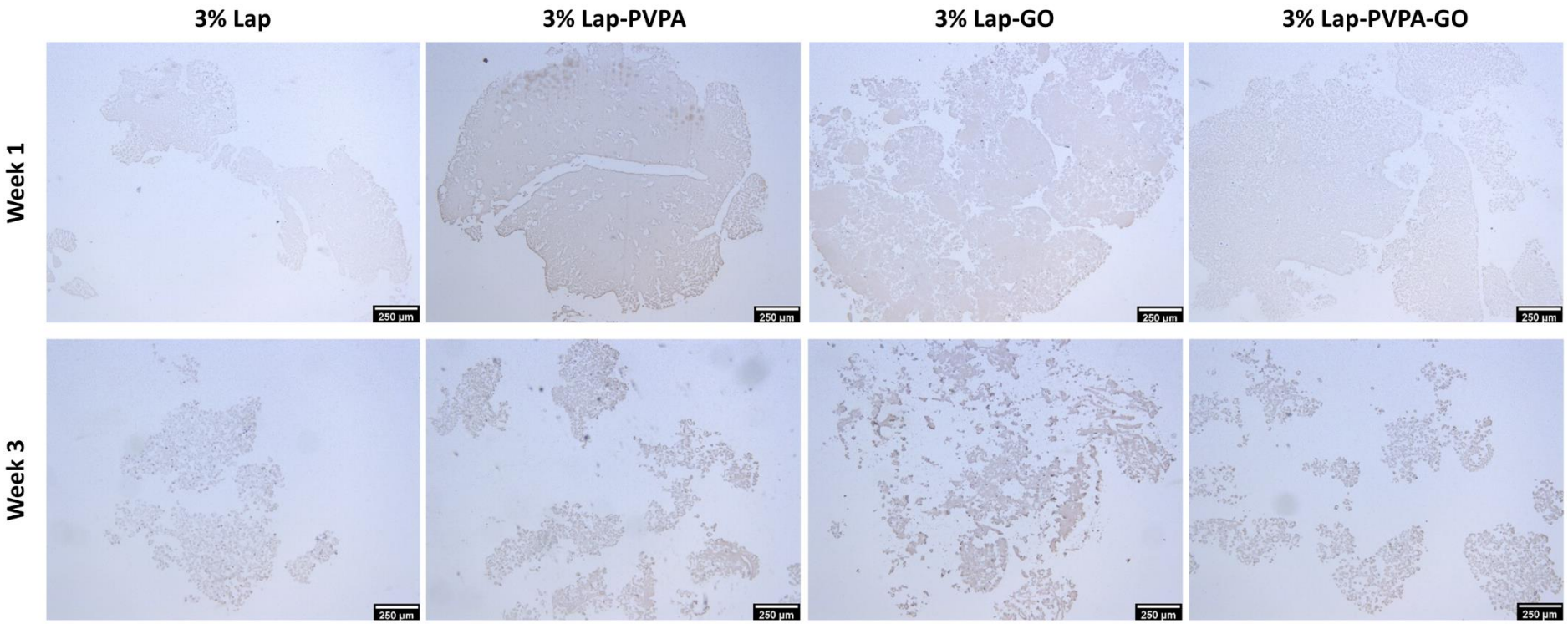

Figure 4-28. Immunohistochemistry staining of Collagen type I of cross-sections from *in vitro* osteoblast-like cells Saos-2 (passage number 17) encapsulated within hydrogel droplets at 1 week and 3 weeks post-seeding. Samples were incubated in basal growth medium without osteogenic inducers. Scale bar represents 250 µm.

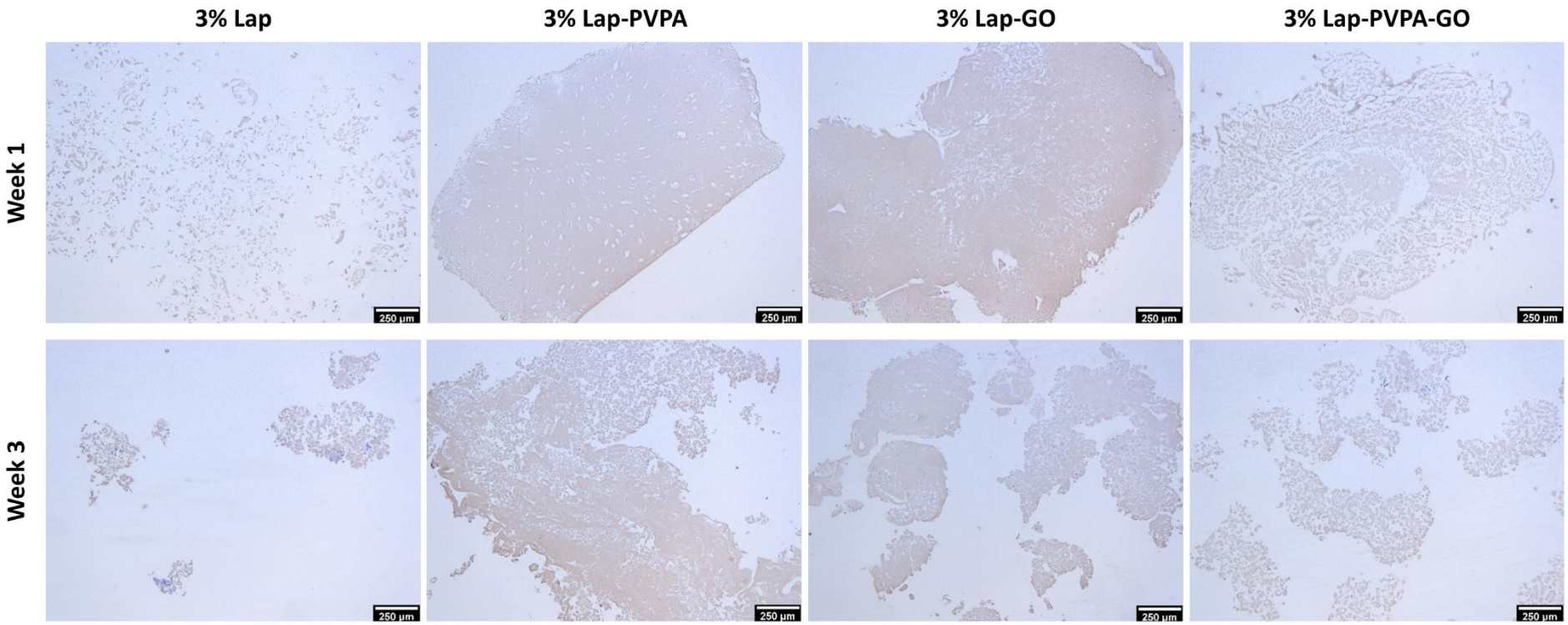

Figure 4-29. Immunohistochemistry staining of Collagen type I of cross-sections from *in vitro* osteoblast-like cells Saos-2 (passage number 17) encapsulated within hydrogel droplets at 1 week and 3 weeks post-seeding. Samples were incubated in basal growth medium supplemented with osteogenic inducers. Scale bar represents 250 µm.

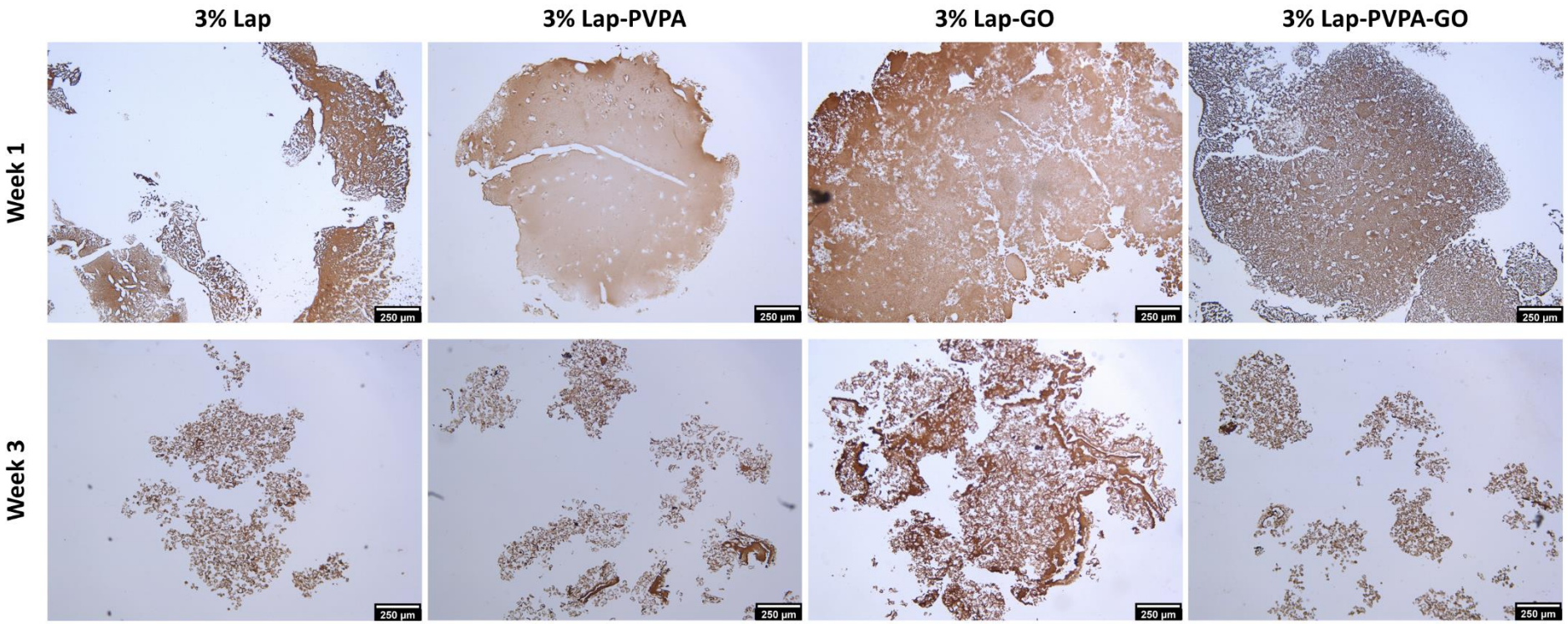

Figure 4-30. Immunohistochemistry staining of fibronectin of cross-sections from *in vitro* osteoblast-like cells Saos-2 (passage number 17) encapsulated within hydrogel droplets at 1 week and 3 weeks post-seeding. Samples were incubated in basal growth medium without osteogenic inducers. Scale bar represents 250 µm.

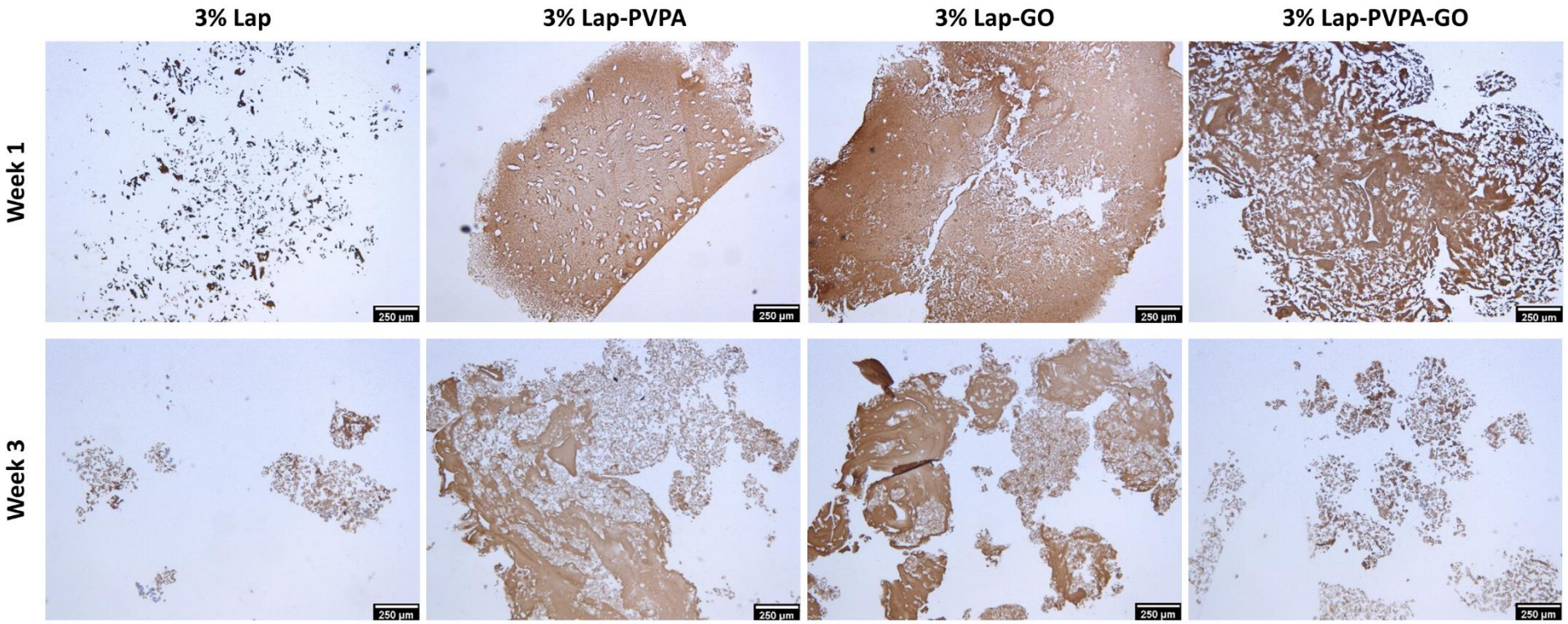

Figure 4-31. Immunohistochemistry staining of fibronectin of cross-sections from *in vitro* osteoblast-like cells Saos-2 (passage number 17) encapsulated within hydrogel droplets at 1 week and 3 weeks post-seeding. Samples were incubated in basal growth medium supplemented with osteogenic inducers. Scale bar represents 250 µm.

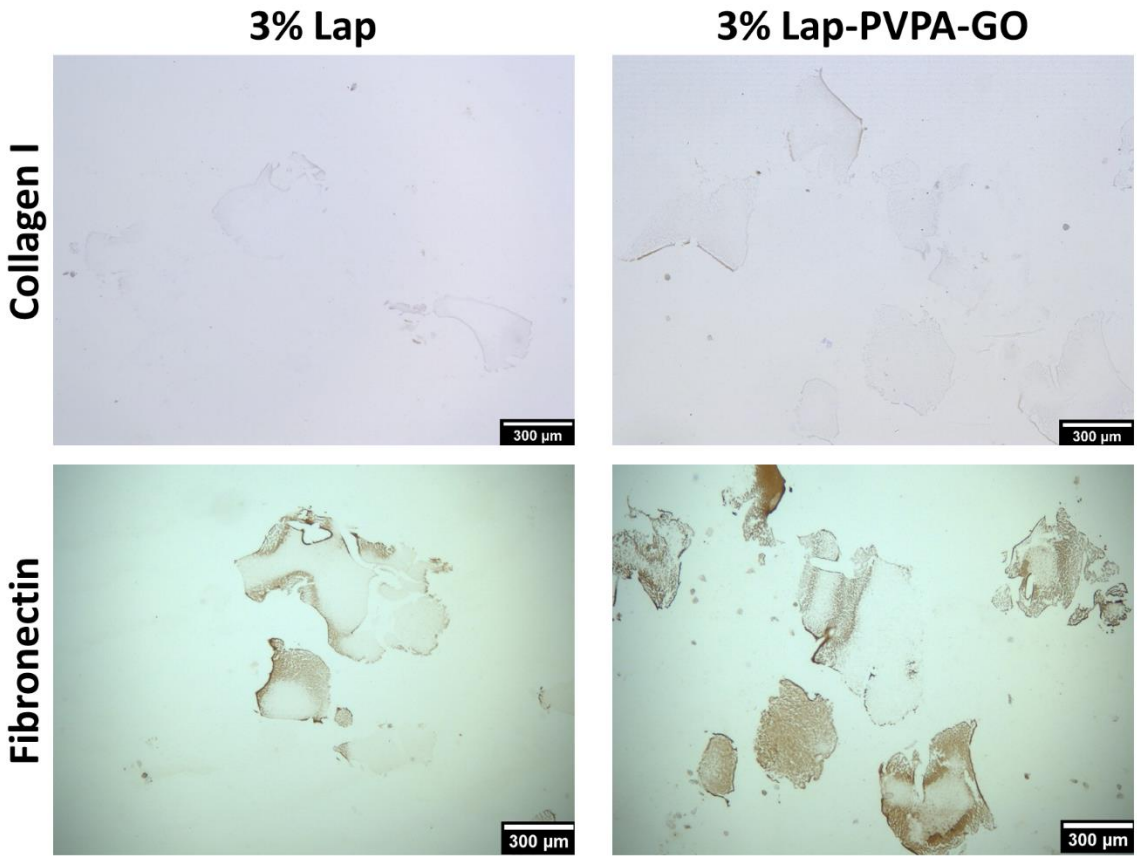

Figure 4-32. Type I collagen and fibronectin immunohistochemical staining of cross-sections from hydrogel droplets without cells (blank gels) at 1 week post-incubation. Samples were incubated in basal growth medium. Scale bar represents 300 µm.

4.2.6 Stability of hydrogel droplets during culture period

The stability of nanoclay gel droplets was investigated using a light microscope to observe the change in the appearance of gel droplets over time for 19 days. It can be seen from Figure 4-33 that all Laponite-based gel droplets had a significant change in the appearance at 15 days post-culturing. Nanoclay gels appeared to swell at 7 days post-culturing and subsequently were not able to maintain their shape as in spherical droplets, probably due to dissolution of Laponite in culture medium after 15 days of the test period. The addition of PVPA-*co*-AA and GO did not significantly alter the stability of Laponite-based gels.

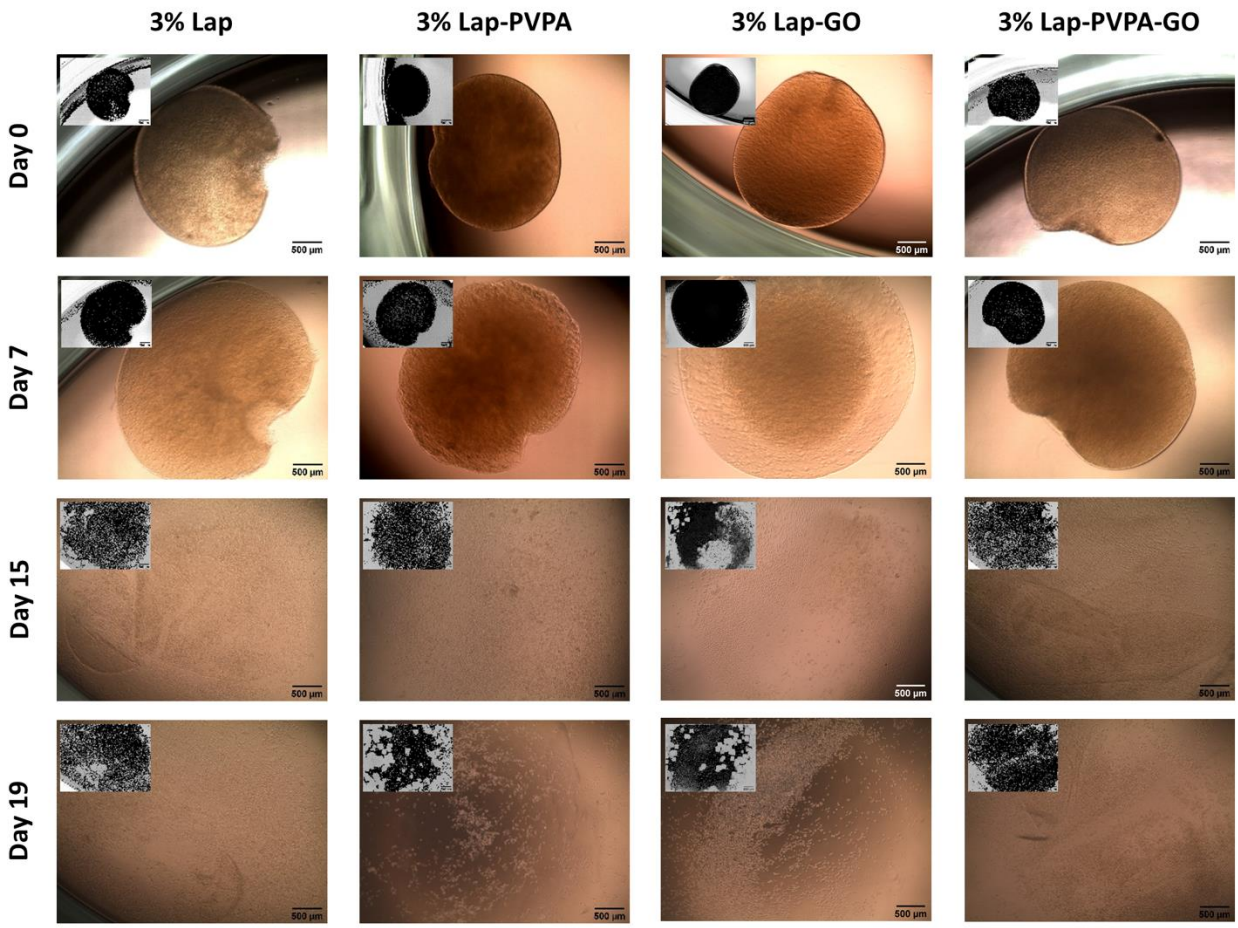

Figure 4-33. Bright field images of Saos-2 (passage number 17) encapsulated 3 wt% Laponite-based hydrogel droplets in osteogenic medium changing over culture period. Scale bar represents 500 µm. Inset: contrast-enhanced greyscale images to help distinguish drop edges. The range of intensity levels on the red channel was adjusted manually. Frame size is the same as the main image.

4.3 Discussion

4.3.1 Effect of phosphonate additions and GO on mechanical and rheological properties of Laponite-based hydrogels

In the context of biomedical applications, clay nanoparticles have been increasingly incorporated with polymers to enhance mechanical, rheological, and degradation properties. For example, clay nanoparticles act as a physical cross-linker in polymer-based hydrogels, providing advantages of shear-thinning and thixotropic behaviours with significantly improved mechanical strength and toughness.[10, 11] The addition of nanoclay particles can also modulate degradation profile with enhancing physiological stability of scaffolds.[12] Nanoclay dispersions possess the complex phase diagram and microscopic interactions.[13-16] The addition of polymers further complicates the sol-gel behaviour of nanoclay, leading to a

challenge in determining precise interactions between polymer chains and nanoclay particles. Polymer chains are hypothesised to interact with nanoclay crystals through electrostatic interactions and hydrogen bonding.[17, 18] For example, charged functional groups presented on polymer structure probably interact with a charged surface or edge of nanoclay discs through electrostatic attractions or repulsions. In addition, polymer chains can be physically adsorbed on surface of nanoclay crystals.[19] If polymers are physically adsorbed on nanoclay surfaces without formation of covalent bonds, shear-thinning characteristics of composite is imparted by nanoclay.[18]

Figure 4-1 and Figure 4-2 show that the addition of a phosphonate copolymer (PVPA-*co*-AA) enhanced the greater storage modulus (G') but lowered the elongation of Laponite-based gels. This is probably because a regeneration of interactions between nanoclay crystals and polymer chains does not easily occur during the stretching due to repulsive interactions.[20] The evolution of G' can be a result from an enhancing rigidity of the network. The elastic or storage modulus (G') can be related to bond strength (E) and the characteristic length-scale (b, leading to b^{-3} as the network density) as $G = Eb^{-3}$.[16, 21] Based on this scaling law, the evolution of G' can occur through an increase of bond strength and/or through a decrease of the characteristic length-scale. Considering that aqueous PVPA-*co*-AA solution can be considered as the anionic polyelectrolyte, polymer chains could generate electrostatic interactions with opposite charged edges of Laponite platelets. This may introduce more rigidity to the network and the strength of bond interactions between Laponite particles and polymer chains, leading to higher G'. Additionally, the increment in storage modulus of Laponite suspension incorporated with PVPA-*co*-AA could be a result from elastic portions in polymer chains responded toward oscillatory shear. The addition of a phosphonate copolymer increased absolute values of viscosity, as reported in Figure 4-4, probably due to polymer chains entanglement. Interestingly, the addition of PVPA-*co*-AA slightly changed shear thinning characteristic behaviour of Laponite-based gels, wherein two steps of viscosity reduction could be observed in Lap-PVPA and Lap-PVPA-GO. This may be referred to polymer chains disentanglement and the arrangement of Laponite platelets in flow direction.

The influence of a phosphonate copolymer toward mechanical and rheological properties of Laponite-based gels presented in this research corresponded to the findings in Laponite/alginate solutions[22] as they are anionic polyelectrolytes. Despite PVPA-*co*-AA being

considered a polyelectrolyte, the microscopic structure of Laponite incorporated with PVPA-*co*-AA does not form a house-of-cards structure as suggested in the literature[14, 20, 23] because there are no positive counter ions to screen repulsive forces between Laponite particles.

Further from electrostatic interactions between charged polymer and opposite charged Laponite platelets, another possible interaction between polymers and clay nanoparticles is that polymer chains could be adsorbed on surface of Laponite crystals and bridge between multiple nanoclay discs.[18] Atmuri *et al*. demonstrated that the addition of a non-adsorbing anionic polymer, PAA, into 3 wt% Laponite retarded the aging of clay dispersion, by which after 30 days aging, neat Laponite dispersion aged quicker to form an arrested state and possessed the greater elastic modulus (G') while Laponite dispersion with the presence of PAA still remained in a fluid state.[24] This behaviour was attributed to the formation of particle clusters in the suspensions with PAA, which decreased the effective volume fraction of particles in the samples, enabling a liquid-like behaviour.[24] This is contrary to this study by which the addition of PVPA-*co*-AA provided a soft solid (3 wt% Laponite) and a gel-like solid (5 wt% Laponite) with greater G' than Laponite suspensions without copolymer. This behaviour may be a consequence of polymer adsorption on Laponite surfaces via hydrogen bonds and formation of polymer bridging between nanoclay particles, resulting in a formation of physically crosslinked network, as shown in Figure 4-34.[18, 19, 22] However, the particular interactions between polymers and nanoclay particles in this study should be further investigates from rheology using, for example, TEM, small angle X-ray scattering (SAXS), dynamic light scattering (DLS), and optical birefringence.[15, 24]

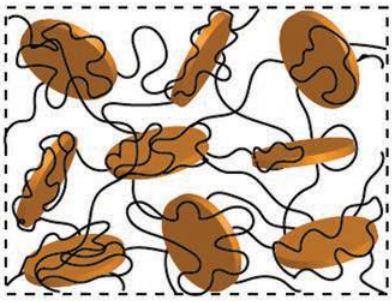

Figure 4-34. The proposed interactions between polymer chains and nanoclay discs through polymer bridging and its subsequent physically crosslinked network.[18]

In addition, the soft solid materials with higher Laponite concentration possess the greater G' and viscosity. This could be a result from a rapid formation of arrested state induced by the

more density of particles in the suspensions, coupled with the hindrance of clusters movement.[24] Also, the increase of G' in the higher concentration of Laponite could be a result of jamming nanoclay particles. Jamming is a physical process by which an increase of particle density results in an increase of viscosity. This phenomenon can be found in some mesoscopic materials. for example, granular particles, glasses, polymers, emulsion, and foams.[25] Srivastava *et al*. studied rheology of a typical jammed suspension using oscillatory shear rheology in strain amplitude and frequency sweep tests to measure G' and G'' of suspension.[26] The result showed that the material had a predominantly elastic (G' >> G'') at low strain and transformed to a dominantly viscous (G'' >> G') when strain increased beyond a certain value. Also, at strain near the transition point, G'' exhibited the evolution to maximum value, indicative of a highly dissipation within material microstructure. These behaviours are considered as a signature of jamming systems by which shear can un-jam the systems. In addition, another signature of jammed systems is that both G' and G'' are only slightly dependent on frequency in the LVE region.[26] This is corresponding with the characteristics of G' and G'' of 5 wt% Laponite-based gels obtained from oscillatory amplitude and frequency sweep tests in this study (Figure 4-1B and Figure 4-3B), consequently, the greater G' in the 5 wt% Laponite-based gels could be contributed to jamming effect of nanoparticles.

Important characteristics of injectable hydrogels related to rheology are shear-thinning and thixotropy.[2, 27] All Laponite-based gels exhibited shear-thinning characteristic as it can be seen from Figure 4-4. Laponite is considered as a thixotropic material in which a reduction in magnitude of rheological parameters (such as viscosity, storage modulus and shear stress) occurs when flow is applied to material at rest state and its subsequent recovery in magnitude happens after the cessation of flow and return to a rest state. In other words, thixotropy refers to a phenomenon of structural deformation under high shear and its subsequent structural build-up at rest state.[28, 29] In this study, thixotropy of Laponite-based hydrogels was characterised through rotational test and oscillatory test. All Laponite-based gels exhibited thixotropic behaviour in by which viscosity, stress, and storage modulus dropped under high shear and subsequently recovered to the rest state after the cessation of shear

The addition of copolymer and graphene did not change thixotropic property of Laponite gels. However, from a time-dependent oscillatory step test (Figure 4-6), Laponite-based gels with the absence of PVPA-*co*-AA showed an evolution in magnitude of G' after the cessation of

shear. This phenomenon may be contributed to physical jamming or percolation of randomly distributed silicate layers. The addition of energy by oscillatory shear may be causing an arrangement of particles toward the direction of shear process and increase physical jamming by inducing inter-particle interactions to prevent free rotation of nanoclay sheets.[30, 31] Rate of thixotropic rebuilding of clay-modified cement pastes was investigated.[32] Clay-modified pastes exhibit a lower relaxation time compared to plain cement pastes, indicating that the jammed state of clay particles and high rate of instantaneous structural rebuilding after shear.[32] Also, it was evident that suspensions with higher degree of jamming exhibited smaller tan δ values.[26] It can be seen from Figure 4-6 that the tan δ value of Laponite-based gels without copolymer was smaller than Laponite-based gels with the addition of copolymer. This finding could be another evidence to suggest that physical jamming of nanoclay particles may happen during a time-dependent oscillatory step test.

In contrast, the evolution of G' did not observed for Laponite-based gels with the presence of PVPA-*co*-AA. It could be speculated that the addition of polymer creates new slippery surfaces that prevent the jamming behaviour by allowing the particles to slide pass each other.

On the other hand, the addition of GO did not significantly influence rheological and mechanical properties of Laponite-based gels. It was expected that the incorporation of GO into Laponite-based suspensions would improve moduli of gels due to its remarkable mechanical properties, with Young's modulus 200–500 GPa.[33] Zhang *et al*. demonstrated that the addition of 0.8 wt% GO improved tensile strength and compressive modulus of PVA hydrogels by 132% and 36%, respectively.[34] The –COOH and –OH groups on GO nanosheet could form strong interactions with PVA via hydrogen bonds, leading to mechanical enhancement.[34] Piao and Chen also produced gelation-GO nanocomposite hydrogels using chemical crosslink agents and found that the incorporation of 3% w/v of GO into gelatin hydrogels enhanced mechanical properties of nanocomposite hydrogels, by which compressive strength and storage modulus increased respectively for 288% and 160%, due to chemical crosslinking and electrostatic interactions between gelatin and GO.[35] The neglected effect of GO towards mechanical and rheological properties of Laponite-based gels acquired from rheometer may be due to a very low amount of GO (0.09% by weight) used in this study, in a comparison to those studies.[34, 35] Interactions between GO platelets and Laponite disc-shaped crystals could be the formation of hydrogen bonds between hydroxyl groups

presented on nanoclay lamellae surface and oxygen-containing moieties of GO, resulting in the adsorption of GO on nanoclay surface.[36] Although both polymer chains and GO flakes could be adsorbed on nanoclay surfaces, the reinforced mechanism and effects toward mechanical and rheological properties were different, probably owing to the different structure (chain-like and sheet-like structures).

4.3.2 Behaviours of osteoblast-like cells within Laponite-based hydrogels

4.3.2.1 Cell morphology and cell spreading

LIVE/DEAD and AlamarBlue assays are not suitable to use for measurement of cell viability and activity of Laponite-based hydrogels due to electrostatic interactions between charged Laponite particles and reagents, hence, there is little reagent left to react with cells.[37] Also, the contrast between stained cells and stained Laponite platelets was difficult to work out. Consequently, phalloidin staining was used to visualise the actin cytoskeleton of Saos-2 within hydrogel structure. From Figure 4-19, phalloidin staining showed the restricted actin cytoskeleton organisation and cell spreading of cells within Laponite-based hydrogels. The addition of PVPA and GO did not significantly change the actin cytoskeleton organisation and morphology of Saos-2 within nanoclay-gel droplets. Degree of cell spreading can be determined from cell size and shape.[38] Cell size and shape of Saos-2 encapsulated within Laponite-based gels were analysed using CellProfiler software with the 'measure cell shape/size' feature to quantified cell area and eccentricity. The average areas occupied by cells and eccentricity within hydrogel structure did not significantly changed over time for all Laponite-based gels. There was a slightly significant increase in the average cell area for Lap-PVPA and Lap-GO in a comparison with Lap and Lap-PVPA-GO at 3 days post-seeding (Figure 4-20), which could be a result of cell clumps. At 1 day post-seeding, Saos-2 seeded in neat Laponite gels showed a significant higher eccentricity in comparison with other gels, suggesting a more elongated morphology of cells (Figure 4-21). This is corresponding with the representative Phalloidin staining images of Laponite by which some elongated cells were observed (Figure 4-19). Li *et al*. demonstrated that stiffness of hydrogels have an effect on cell morphology.[39] It was found that chondrocytes encapsulated within GelMA hydrogels with higher stiffness exhibited a round morphology with restricted actin cytoskeleton organisation whereas elongated cells with distributed F-actin filaments were observed in low stiffness

GelMA hydrogels, indicative of more degree of cell spreading.[39] This reason could explain the presence of more elongated cells observed in neat Laponite gels, by which Laponite gel possessed lower G' (hence, lower stiffness) than other Laponite gels with the addition of copolymer and GO (Figure 4-1).

4.3.2.2 Osteogenic mineralisation and protein expression

Laponite has been used to incorporate with various polymer-based hydrogels for the purpose of rheological improvement, reinforcement and enhancement osteogenic differentiation of stem cells and osteoblasts.[40-42] Research works related to the use of Laponite as a main matrix or neat Laponite hydrogels for osteogenic microenvironments are still limited. In this study, Laponite-based hydrogels encapsulated with osteoblasts were assessed the ability of Laponite gels to serve as an osteogenic microenvironment. Histological assessment with alizarin red S staining reveals that all Laponite-based gel droplets cultured in standard growth medium showed a positive stain of alizarin red S (Figure 4-26), suggesting the mineralised matrix formation or accelerated osteogesis of Saos-2 osteoblastic cells in the absence of osteoinductive factors. The accelerated osteogenesis of Saos-2 within clay gels in the absence of osteogenic inducers could be due to the inherent bioactive of degradative products (Mg^{2+}, Li^{+}, and orthosilicic acid) of Laponite. This finding also corresponds to research studies demonstrated by Gaharwar's group, by which the addition of nanosilicates into gelatin-based hydrogels enhanced the formation of mineralised matrix and ALP activity of pre-osteoblasts MC3T3 cells and hMSCs in normal growth medium without the addition of osteogenic supplements.[10, 40]

The addition of phosphonate-containing copolymer and GO did not significantly accelerate or up-regulate the osteogenic mineralisation of Saos-2, probably due to a low concentration added into nanoclay gels. A positive staining could be observed at 7 days post-seeding for Lap-GO in growth medium, but this did not show for Lap-PVPA-GO. However, further from the qualitatively histological assessments, the quantitative measurements and the analysis at 14 days post-seeding should be performed to confirm the acceleration or up-regulation of mineralised matrix formation. Unexpectedly, no positive staining of alizarin red S was not observed for all Laponite-based gels incubated in osteogenic medium (Figure 4-27) whereas Saos-2 seeded on TCP exhibited a significantly strong positive stain (Figure 4-23). The reason

for no positive staining could be a result of inappropriate and heterogeneous mixing procedure during the encapsulation, leading to a possibility to lose cell population in gel droplets.

Another possible reason for no staining is the effect of osteogenic supplements towards proliferation and mineralisation of osteoblasts. Dexamethasone, a synthetic glucocorticoid, was reported to suppress cell growth or proliferation towards hMSCs and osteoblastic cells in time- and dose-dependent manner, resulting in a decrease in the number of cells.[43-45] It was reported that glucocorticoid increased glycogen synthase kinase 3 beta (GSK3β), the β-catenin destruction complex, resulting in c-Myc down-regulation and inhibition of the G_1/S cell cycle transition.[44] However, the concentration of dexamethasone used in this study was as same as the concentration used for standard preparation of osteogenic medium.[9, 46] Moreover, the initial results of Saos-2 encapsulated within neat Laponite and Lap-PVPA-GO hydrogels in this study exhibited a positive alizarin red S staining for both growth and osteogenic media at 3 weeks post-seeding (Figure 4-35). Therefore, it seems that a negative staining of alizarin red S staining observed for samples cultured in osteogenic medium (Figure 4-27) is a result of variation occurred from encapsulation technique.

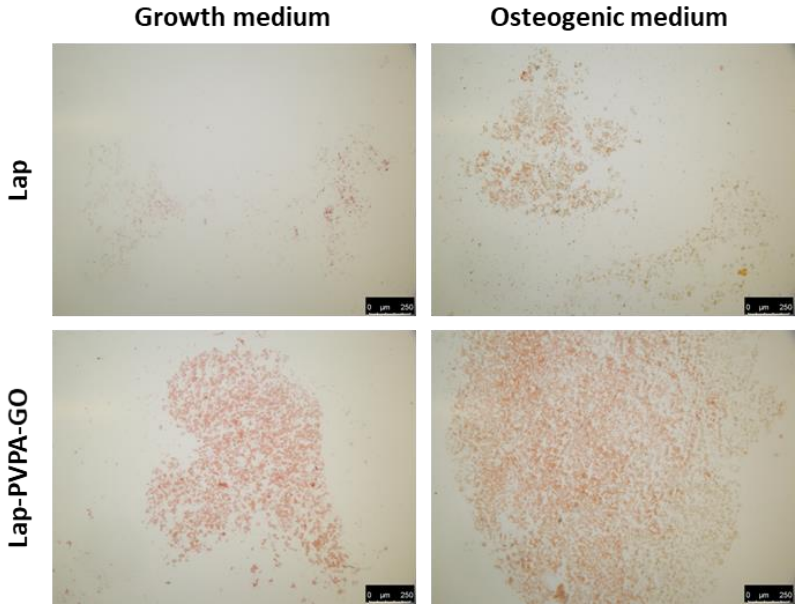

Figure 4-35. Alizarin red S staining of cross-sections from *in vitro* osteoblast-like cells Saos-2 (passage number 15) encapsulated within hydrogel droplets at 3 weeks post-seeding. Samples were incubated in basal growth medium supplemented with osteogenic inducers. Scale bar represents 250 µm.

Further from alizarin red S staining, immunohistochemistry staining of type I collagen and fibronectin was also determined. Type I collagen and fibronectin are classified as bone matrix proteins and abundant components of ECM that are maximal synthesised during cell proliferation phase.[47-50] In this study, histological assessment of Saos-2 encapsulated within Laponite-based gels revealed a consistently soft brown stain detected for all samples with independent of osteogenic inducers (Figure 4-28 and Figure 4-29). Likewise, all Laponite-based gels with Saos-2 incubated in both growth and osteogenic media exhibited a strong brown staining of fibronectin throughout the culture period (Figure 4-30 and Figure 4-31). However, nanoclay gels appeared to generate an interaction with fibronectin primary antibody, resulting in a dark brown stain as a background. This can be seen from fibronectin staining of nanoclay blank gels (Figure 4-32), of which dark brown stained areas could be observed. Although it is difficult to distinguish between positive stained areas and background, fibronectin staining could be observed around cell nuclei for Laponite-based gels incubated in growth medium at 3 weeks post-seeding (Figure 4-30).

The brown staining detected in all samples over the test period suggests that fibronectin and collagen type I were secreted by Saos-2 encapsulated in Laponite-based gels although the calcium deposition was not observed in some samples. This finding is corresponding to results published by Shi *et al*.,[9] by which the expression of type I collagen in Laponite-cell scaffolds, cultured in osteogenic conditions, did not show a significantly difference between 1 week and 3 weeks post-culture. The different finding between this thesis and the study of Shi et al. is the results of alizarin red S staining. Shi and collaborators demonstrated a significant increase in alizarin red S staining was observed from week 1 to week 3 for samples incubated in osteogenic medium while an increase in alizarin red S staining was observed in samples incubated in growth medium for this thesis. Histological assessment is a qualitative method which is sometimes not enough to confirm osteogenic mineralisation of cells. Hence, other quantification analysis, such as alkaline phosphatase activity assay, real-time polymerase chain reaction to measure osteogenic genes expression, and calcium quantification colorimetric assay should be further performed.

Interestingly, in a comparison with nanoclay gel droplets, positive staining areas of alizarin red S and von Kossa detected in Laponite-based gel discs seemed to be smaller and weaker (Figure 4-17 and Figure 4-18). This could be due to a depletion of protein and/or oxygen within

gel discs. Brown *et al*. investigated an oxygen transport within cylindrical gels with the 1.2 mm height.[51] The authors found that a high cell density increased the rate of oxygen consumption, along with a greater physical impediment of oxygen and a lower degree of oxygen replenishment. Moreover, the concentration gradients developed within hydrogels by which oxygen most existed at the boundary of constructs and depleted inside hydrogels as cells consumed oxygen, replenishment is limited by diffusion from the bulk solution. The dimension of hydrogels showed a large effect on oxygen transport profile. By decreasing the dimension of hydrogels to reduce the path length of diffusion, cell will experience a more sufficient supply due to a reduction in transit time with a greater degree of oxygen diffusion.[51] Nanoclay gel discs in this research could have a low degree of oxygen replenishment due to a longer path length of diffusion with a larger dimension, in a comparison to nanoclay gel droplets. Also, cell density within gel discs was greater than gel droplets because gel discs required a higher amount of total suspension, leading to higher cell density inside constructs. For these reasons, cells within nanoclay gel discs may experience insufficient oxygen and/or protein supplies, leading to cell death and no cell functions. Cylindrical gels take an advantage over gel droplets with respect to the ability to maintain the integrity of scaffolds during culture period. Nanoclay gel discs may be utilised as an acellular scaffold in a subcutaneous implantation and allow for cell infiltration. In this regard, the ability of Laponite gels to support cell migration was studied and described in the next chapter.

4.3.3 Stability and dissociation of nanoclay gel droplets

In this study, stability of Laponite-based hydrogels was investigated through the change in droplet shape over time. Figure 4-33 shows that all Laponite-based gels exhibited a swelling and subsequently fell apart. It has been stated that, in serum-containing culture medium, Laponite platelets can interact with proteins through adsorption mechanism, generating clay-protein bridges that introduce a greater stability to nanoclay gels due to an increase of network stiffness.[9] However, in the environment of culture conditions (37 °C, 5% CO_2) and pH 7.4 of culture medium, degradation of Laponite tends to occur due to a dissociation in acidic environment promoted by carbonic acid from CO_2 dissolution.[52] Moreover, cells typically release CO_2 as a waste product after consumption of oxygen and nutrients. This could explain a falling apart of gel droplets observed in Figure 4-33 by which Laponite-based gels may experience dissociation during culture caused by cells and environment, resulting in

disintegration. Also, Laponite droplets could be disrupted during changing medium, leading to falling apart into small pieces. The addition of phosphonate copolymer and GO did not significantly alter stability of Laponite-based gels, probably due to a very low amount adding to nanoclay suspensions. The degradation of Laponite gels shows a good sign for biodegradability of scaffolds, suggesting a potential use for research studies regarding *in vivo* implantation. Degradation of Laponite should be further investigated using other techniques such as quantification of leached ions from Laponite into culture medium and weight loss of gels over time during culture period.[5, 53] The degradation profile of Laponite gels is a crucial parameter for designing BTE scaffolds, by which scaffolds should be able to maintain their integrity in sufficient time to allow for new tissue formation. To improve mechanical stiffness and stability of Laponite-based gels, the incorporation of polymers, nanomaterials, and proteins with adequate concentration can be further researched. Numerous studies have demonstrated the positive effect of adding clay nanoparticles towards mechanical and rheological properties of hydrogels. For example, the addition of clay nanoparticles showed a significant enhancement of mechanical strength and toughness with providing shear-thinning and thixotropic behaviours in polymer-based hydrogels.[10, 11] However, in this context, Laponite nanoclay would be a major phase and the addition of other materials or molecules is expected to improve mechanical properties and stability of clay gels. The incorporation of proteins or growth factors could help to improve stability of gels and biological activities as well as cell migration. Page *et al*. reported that 50 µL of 3% Laponite gels containing 2 µg VEGF showed a retention and cohesion of completed gels at the subcutaneous injection site at 21 days after injection.[54] Similarly, Gibb *et al*. demonstrated, by histological images, that fragments of 20 µL of 2.5% Laponite gels containing 1 µg BMP-2 remained in place and embedded within developed tissue. Proliferating cells were also observed enclosed in clay gels, suggesting cell invasion proceeded by BMP-2 mediated response.[55]

4.4 Conclusion

In this chapter, phosphonate-containing copolymer and GO were incorporated into Laponite gels with objectives to improve mechanical properties and promote accelerated osteogenic mineralisation of osteoblasts. The addition of phosphonate-containing copolymer increased storage modulus with lower yield point of Laponite-based gels whereas the incorporation of GO did not show any significant change due to a concentration effect. Cell viability and

metabolic activity could not be assessed using LIVE/DEAD and AlamarBlue assays because of an interference from clay-dye interactions. Osteoinductive activity and cell behaviours were investigated using cytoskeleton staining and histological assessments. The addition of both phosphonated polymer and GO showed no significant effect on osteoinductive activity and cytoskeleton organisation of osteoblasts within Laponite-based gels due to a low concentration.

Interestingly, Laponite-based gels in this study exhibited osteogenic mineralisation of osteoblasts in the absence of chemical inducers (observed by alizarin red S staining), suggesting that Laponite possesses osteoinductive properties. This study further supports a research from Dawson's group[9] by which Laponite gels as a main phase of scaffolds offer a potential host osteogenic microenvironment and opportunity to serve as BTE scaffolds. The degradation profile and mechanical stiffness enhancement of Laponite gels should be further investigated and improved, allowing for a greater stability of gels against dissociation with correspondence to rate of mineralised matrix formation.

The dimensions and shape of gels showed an effect on osteogenic mineralisation: cylindrical gels (or gel discs) exhibited a lower degree of positive histological staining. However, gels with cylindrical shape take an advantage over gel droplets regarding dimensional integrity. Gel discs may be used as an acellular scaffold in an implantation and allow for cell infiltration, and its subsequent tissue formation. Consequently, the ability of nanoclay gels to support cell migration was studied and presented in the next chapter, along with cellular activities in 2D culture on gel surfaces.

4.5 References

1. Gaharwar, A. K.; Kishore, V.; Rivera, C.; Bullock, W.; Wu, C. J.; Akkus, O.; Schmidt, G., Physically Crosslinked Nanocomposites from Silicate-Crosslinked PEO: Mechanical Properties and Osteogenic Differentiation of Human Mesenchymal Stem Cells. *Macromolecular Bioscience* **2012,** *12* (6), 779-793.
2. Chen, M. H.; Wang, L. L.; Chung, J. J.; Kim, Y.-H.; Atluri, P.; Burdick, J. A., Methods to assess shear-thinning hydrogels for application as injectable biomaterials. *ACS biomaterials science & engineering* **2017,** *3* (12), 3146-3160.
3. Barnes, H. A.; Hutton, J. F.; Walters, K., *An introduction to rheology*. Elsevier: 1989; Vol. 3.
4. Mezger, T. G., *The rheology handbook: for users of rotational and oscillatory rheometers*. Vincentz Network GmbH & Co KG: 2006.
5. Samimi Gharaie, S.; Dabiri, S. M. H.; Akbari, M., Smart shear-thinning hydrogels as injectable drug delivery systems. *Polymers* **2018,** *10* (12), 1317.

6. Boyer, C.; Figueiredo, L.; Pace, R.; Lesoeur, J.; Rouillon, T.; Le Visage, C.; Tassin, J.-F.; Weiss, P.; Guicheux, J.; Rethore, G., Laponite nanoparticle-associated silated hydroxypropylmethyl cellulose as an injectable reinforced interpenetrating network hydrogel for cartilage tissue engineering. *Acta biomaterialia* **2018,** *65*, 112-122.
7. Rosai, J., Why microscopy will remain a cornerstone of surgical pathology. *Laboratory Investigation* **2007,** *87* (5), 403-408.
8. Wang, Y.-H.; Liu, Y.; Maye, P.; Rowe, D. W., Examination of mineralized nodule formation in living osteoblastic cultures using fluorescent dyes. *Biotechnol Prog* **2006,** *22* (6), 1697-1701.
9. Shi, P.; Kim, Y. H.; Mousa, M.; Sanchez, R. R.; Oreffo, R. O.; Dawson, J. I., Self-Assembling Nanoclay Diffusion Gels for Bioactive Osteogenic Microenvironments. *Advanced healthcare materials* **2018,** *7* (15), 1800331.
10. Xavier, J. R.; Thakur, T.; Desai, P.; Jaiswal, M. K.; Sears, N.; Cosgriff-Hernandez, E.; Kaunas, R.; Gaharwar, A. K., Bioactive nanoengineered hydrogels for bone tissue engineering: a growth-factor-free approach. *ACS Nano* **2015,** *9* (3), 3109-3118.
11. Nojoomi, A.; Tamjid, E.; Simchi, A.; Bonakdar, S.; Stroeve, P., Injectable polyethylene glycol-laponite composite hydrogels as articular cartilage scaffolds with superior mechanical and rheological properties. *International Journal of Polymeric Materials and Polymeric Biomaterials* **2017,** *66* (3), 105-114.
12. Kerativitayanan, P.; Tatullo, M.; Khariton, M.; Joshi, P.; Perniconi, B.; Gaharwar, A. K., Nanoengineered osteoinductive and elastomeric scaffolds for bone tissue engineering. *ACS Biomaterials Science & Engineering* **2017,** *3* (4), 590-600.
13. Marques, F. A. d. M.; Angelini, R.; Ruocco, G.; Ruzicka, B., Isotopic effect on the gel and glass formation of a charged colloidal clay: Laponite. *The Journal of Physical Chemistry B* **2017,** *121* (17), 4576-4582.
14. Becher, T. B.; Braga, C. B.; Bertuzzi, D. L.; Ramos, M. D.; Hassan, A.; Crespilho, F. N.; Ornelas, C., The structure–property relationship in LAPONITE® materials: from Wigner glasses to strong self-healing hydrogels formed by non-covalent interactions. *Soft matter* **2019,** *15* (6), 1278-1289.
15. Suman, K.; Joshi, Y. M., Microstructure and soft glassy dynamics of an aqueous laponite dispersion. *Langmuir* **2018,** *34* (44), 13079-13103.
16. Suman, K.; Mittal, M.; Joshi, Y. M., Effect of sodium pyrophosphate and understanding microstructure of aqueous LAPONITE® dispersion using dissolution study. *Journal of Physics: Condensed Matter* **2020,** *32* (22), 224002.
17. Thompson, D. W.; Butterworth, J. T., The nature of laponite and its aqueous dispersions. *Journal of Colloid and Interface Science* **1992,** *151* (1), 236-243.
18. Gaharwar, A. K.; Cross, L. M.; Peak, C. W.; Gold, K.; Carrow, J. K.; Brokesh, A.; Singh, K. A., 2D nanoclay for biomedical applications: Regenerative medicine, therapeutic delivery, and additive manufacturing. *Advanced Materials* **2019,** *31* (23), 1900332.
19. Lal, J.; Auvray, L., Interaction of polymer with clays. *Journal of applied crystallography* **2000,** *33* (3), 673-676.
20. Takeno, H.; Nakamura, A., Effects of molecular mass of polymer on mechanical properties of clay/poly (ethylene oxide) blend hydrogels, and comparison between them and clay/sodium polyacrylate blend hydrogels. *Colloid and Polymer Science* **2019,** *297* (4), 641-649.
21. Jones, R. A. L.; Jones, R.; Jones, R. A., *Soft condensed matter*. Oxford University Press: 2002; Vol. 6.
22. Dávila, J. L.; d'Ávila, M. A., Laponite as a rheology modifier of alginate solutions: Physical gelation and aging evolution. *Carbohydrate polymers* **2017,** *157*, 1-8.
23. Savenko, V.; Bulavin, L.; Rawiso, M.; Lebovka, N., Aging of aqueous Laponite dispersions in the presence of sodium polystyrene sulfonate. *arXiv preprint arXiv:1406.2992* **2014**.
24. Atmuri, A. K.; Bhatia, S. R., Polymer-Mediated Clustering of Charged Anisotropic Colloids. *Langmuir* **2013,** *29* (10), 3179-3187.
25. Biroli, G., Jamming: A new kind of phase transition? *Nature Physics* **2007,** *3* (4), 222-223.

26. Srivastava, S.; Shin, J. H.; Archer, L. A., Structure and rheology of nanoparticle–polymer suspensions. *Soft Matter* **2012,** *8* (15), 4097-4108.
27. Zuidema, J. M.; Rivet, C. J.; Gilbert, R. J.; Morrison, F. A., A protocol for rheological characterization of hydrogels for tissue engineering strategies. *Journal of Biomedical Materials Research Part B: Applied Biomaterials* **2014,** *102* (5), 1063-1073.
28. Barnes, H. A., Thixotropy—a review. *Journal of Non-Newtonian fluid mechanics* **1997,** *70* (1-2), 1-33.
29. Mewis, J.; Wagner, N. J., Thixotropy. *Advances in Colloid and Interface Science* **2009,** *147*, 214-227.
30. Yılmaz, O.; Cheaburu, C. N.; Gülümser, G.; Vasile, C., Rheological behaviour of acrylate/montmorillonite nanocomposite latexes and their application in leather finishing as binders. *Progress in Organic Coatings* **2011,** *70* (1), 52-58.
31. Drozdov, A. D.; Jensen, E. A.; Christiansen, J. d. C., Nonlinear time-dependent response of polypropylene/nanoclay melts: Experiments and modeling. *Computational Materials Science* **2010,** *47* (3), 807-816.
32. Kawashima, S.; Chaouche, M.; Corr, D. J.; Shah, S. P., Rate of thixotropic rebuilding of cement pastes modified with highly purified attapulgite clays. *Cement and Concrete Research* **2013,** *53*, 112-118.
33. Liu, L.; Zhang, J.; Zhao, J.; Liu, F., Mechanical properties of graphene oxides. *Nanoscale* **2012,** *4* (19), 5910-5916.
34. Zhang, L.; Wang, Z.; Xu, C.; Li, Y.; Gao, J.; Wang, W.; Liu, Y., High strength graphene oxide/polyvinyl alcohol composite hydrogels. *Journal of Materials Chemistry* **2011,** *21* (28), 10399-10406.
35. Piao, Y.; Chen, B., Synthesis and mechanical properties of double cross-linked gelatin-graphene oxide hydrogels. *International Journal of Biological Macromolecules* **2017,** *101*, 791-798.
36. Sari, M. G.; Abdolmaleki, M.; Rostami, M.; Ramezanzadeh, B., Nanoclay dispersion and colloidal stability improvement in phenol novolac epoxy composite via graphene oxide for the achievement of superior corrosion protection performance. *Corrosion Science* **2020,** *173*, 108799.
37. Boyer, C.; Figueiredo, L.; Pace, R.; Lesoeur, J.; Rouillon, T.; Le Visage, C.; Tassin, J. F.; Weiss, P.; Guicheux, J.; Rethore, G., Laponite nanoparticle-associated silated hydroxypropylmethyl cellulose as an injectable reinforced interpenetrating network hydrogel for cartilage tissue engineering. *Acta Biomaterialia* **2018,** *65*, 112-122.
38. Brugmans, M.; Cassiman, J. J.; Vanderheydt, L.; Oosterlinck, A. J.; Vlietinck, R.; Van Den Berghe, H., Quantification of the degree of cell spreading of human fibroblasts by semi-automated analysis of the cell perimeter. *Cytometry: The Journal of the International Society for Analytical Cytology* **1983,** *3* (4), 262-268.
39. Li, X.; Chen, S.; Li, J.; Wang, X.; Zhang, J.; Kawazoe, N.; Chen, G., 3D Culture of Chondrocytes in Gelatin Hydrogels with Different Stiffness. *Polymers* **2016,** *8* (8), 269.
40. Paul, A.; Manoharan, V.; Krafft, D.; Assmann, A.; Uquillas, J. A.; Shin, S. R.; Hasan, A.; Hussain, M. A.; Memic, A.; Gaharwar, A. K., Nanoengineered biomimetic hydrogels for guiding human stem cell osteogenesis in three dimensional microenvironments. *Journal of Materials Chemistry B* **2016,** *4* (20), 3544-3554.
41. Alarçin, E.; Lee, T. Y.; Karuthedom, S.; Mohammadi, M.; Brennan, M. A.; Lee, D. H.; Marrella, A.; Zhang, J.; Syla, D.; Zhang, Y. S., Injectable shear-thinning hydrogels for delivering osteogenic and angiogenic cells and growth factors. *Biomaterials science* **2018,** *6* (6), 1604-1615.
42. Su, D.; Jiang, L.; Chen, X.; Dong, J.; Shao, Z., Enhancing the gelation and bioactivity of injectable silk fibroin hydrogel with laponite nanoplatelets. *ACS applied materials & interfaces* **2016,** *8* (15), 9619-9628.
43. Kim, C.; Cheng, S.; Kim, G., Effects of dexamethasone on proliferation, activity, and cytokine secretion of normal human bone marrow stromal cells: possible mechanisms of glucocorticoid-induced bone loss. *Journal of endocrinology* **1999,** *162* (3), 371-380.

44. Smith, E.; Coetzee, G. A.; Frenkel, B., Glucocorticoids inhibit cell cycle progression in differentiating osteoblasts via glycogen synthase kinase-3β. *Journal of Biological Chemistry* **2002,** *277* (20), 18191-18197.
45. Weinstein, R. S.; Jilka, R. L.; Parfitt, A. M.; Manolagas, S. C., Inhibition of osteoblastogenesis and promotion of apoptosis of osteoblasts and osteocytes by glucocorticoids. Potential mechanisms of their deleterious effects on bone. *The Journal of clinical investigation* **1998,** *102* (2), 274-282.
46. Cidonio, G.; Alcala-Orozco, C. R.; Lim, K. S.; Glinka, M.; Mutreja, I.; Kim, Y.-H.; Dawson, J. I.; Woodfield, T. B.; Oreffo, R. O., Osteogenic and angiogenic tissue formation in high fidelity nanocomposite Laponite-gelatin bioinks. *Biofabrication* **2019,** *11* (3), 035027.
47. Lian, J. B.; Stein, G. S., Development of the osteoblast phenotype: molecular mechanisms mediating osteoblast growth and differentiation. *The Iowa orthopaedic journal* **1995,** *15*, 118.
48. Owen, T. A.; Aronow, M.; Shalhoub, V.; Barone, L. M.; Wilming, L.; Tassinari, M. S.; Kennedy, M. B.; Pockwinse, S.; Lian, J. B.; Stein, G. S., Progressive development of the rat osteoblast phenotype in vitro: reciprocal relationships in expression of genes associated with osteoblast proliferation and differentiation during formation of the bone extracellular matrix. *Journal of cellular physiology* **1990,** *143* (3), 420-430.
49. Stein, G. S.; Lian, J. B.; Owen, T. A., Relationship of cell growth to the regulation of tissue-specific gene expression during osteoblast differentiation. *The FASEB journal* **1990,** *4* (13), 3111-3123.
50. Wenz, A.; Borchers, K.; Tovar, G. E.; Kluger, P. J., Bone matrix production in hydroxyapatite-modified hydrogels suitable for bone bioprinting. *Biofabrication* **2017,** *9* (4), 044103.
51. Brown, D. A.; MacLellan, W. R.; Laks, H.; CY Dunn, J.; M. Wu, B.; Beygui, R. E., Analysis of oxygen transport in a diffusion-limited model of engineered heart tissue. *Biotechnology and bioengineering* **2007,** *97* (4), 962-975.
52. Mourchid, A.; Levitz, P., Long-term gelation of laponite aqueous dispersions. *Physical Review E* **1998,** *57* (5), R4887.
53. Jatav, S.; Joshi, Y. M., Chemical stability of Laponite in aqueous media. *Applied clay science* **2014,** *97*, 72-77.
54. Page, D. J.; Clarkin, C. E.; Mani, R.; Khan, N. A.; Dawson, J. I.; Evans, N. D., Injectable nanoclay gels for angiogenesis. *Acta biomaterialia* **2019,** *100*, 378-387.
55. Gibbs, D. M. R.; Black, C. R. M.; Hulsart-Billstrom, G.; Shi, P.; Scarpa, E.; Oreffo, R. O. C.; Dawson, J. I., Bone induction at physiological doses of BMP through localization by clay nanoparticle gels. *Biomaterials* **2016,** *99*, 16-23.

Chapter 5

Response of osteoblasts to Laponite-based hydrogels in 2D culture model

5.1 Chapter abstract

In this chapter, response of osteoblasts towards Laponite-based gels and cell migration were investigated. Saos-2 cells were 2D cultured on surfaces of nanoclay gel discs. Cytoskeleton organisation and osteogenic mineralisation were assessed using phalloidin staining and histological assessment with alizarin red S staining. The results showed that cell density of gel surfaces increased over time and all Laponite-based gels could support osteogenic mineralisation of Saos-2.

Cell migration of Saos-2 was studied by seeding fluorescent dye-labelled cells on surfaces of nanoclay gels and using the confocal microscope to acquire stacked images. The migration of osteoblast in 3D scaffolds was reported as 3D stacked images to indicate the difference in distance between cell layers and a stationary reference level. The effect of chemical gradient and growth factors were also studied using culture medium containing Platelet derived growth factor β (PDGF-BB) as followed the protocol described by Movilla *et al*.[1] According to preliminary results, no migration of cells into Laponite gels was observed in all conditions.

The aims of research discussed in this chapter were to:

- Cell adhesion, cytoskeleton organisation, and osteogenic mineralisation on surfaces of Laponite-based gels
- The ability of Laponite gels to support osteoblasts migration
- The effect of chemical gradient and growth factors on osteoblasts migration within Laponite gels matrix

5.2 Results

5.2.1 Osteoblast-like cells behaviour on surface of nanoclay-gel discs

5.2.1.1 Review of methods

The concentration of Laponite dispersions were 3% by weight. 150 µL of Laponite-based dispersions were placed in ThinCert™ Cell Culture Inserts for 24-well plate to make gel discs with approximately 2 mm thick. All samples were sterilised under UV for 2 hours. Saos-2 cells (passage number 16) were seeded on gel surfaces at a density of 2×10^4 cells per well. Cytoskeleton organisation and cell expression of osteoblasts on nanoclay-gel surfaces were determined using phalloidin staining and histological assessment.

5.2.1.2 Actin cytoskeleton organisation

Phalloidin staining was performed at 1, 3, and 7 days after seeding to visualise actin cytoskeleton organisation, with representative images shown in Figure 5-1. Saos-2 on surfaces of Laponite-based gels mostly exhibited a round morphology over the culture period. Phalloidin staining revealed the restricted actin cytoskeleton organisation and cell spreading for majority of cells adhered on Laponite-based hydrogels whereas the actin distribution was observed for Saos-2 seeded on TCP (control). The addition of PVPA and GO did not significantly change the actin cytoskeleton organisation and morphology of Saos-2 attached on surfaces of Laponite-based gels, in a comparison to neat Laponite gels.

The average cell area and shape were analysed for Saos-2 seeded on Laponite-based gel discs with data shown in Figure 5-2 and Figure 5-3, respectively. At different time points, the Saos-2 seeded on Laponite nanoclay-based gels did not show any significant change in average cell areas throughout the 7-day test period with one exception. Cells attached on Lap-GO gel had a small but significant increase in average cell area at 3 days and 7 days post-seeding as compared to day 1. There was no significant difference in cell areas between nanoclay gels at the same time point.

Cell shape analysis was performed and reported as cell eccentricity, with data displayed in Figure 5-3. Saos-2 at 1 day post-seeding cultured on Lap-PVPA and Lap-GO showed a significant higher in cell eccentricity as compared to 7 days post-seeding, indicative to more elongation of osteoblasts at this time point. No significant difference in cell shape was

observed for Saos-2 attached on different Laponite-based gels, implying that the addition of GO and PVPA-*co*-AA did not alter cell shape of osteoblasts.

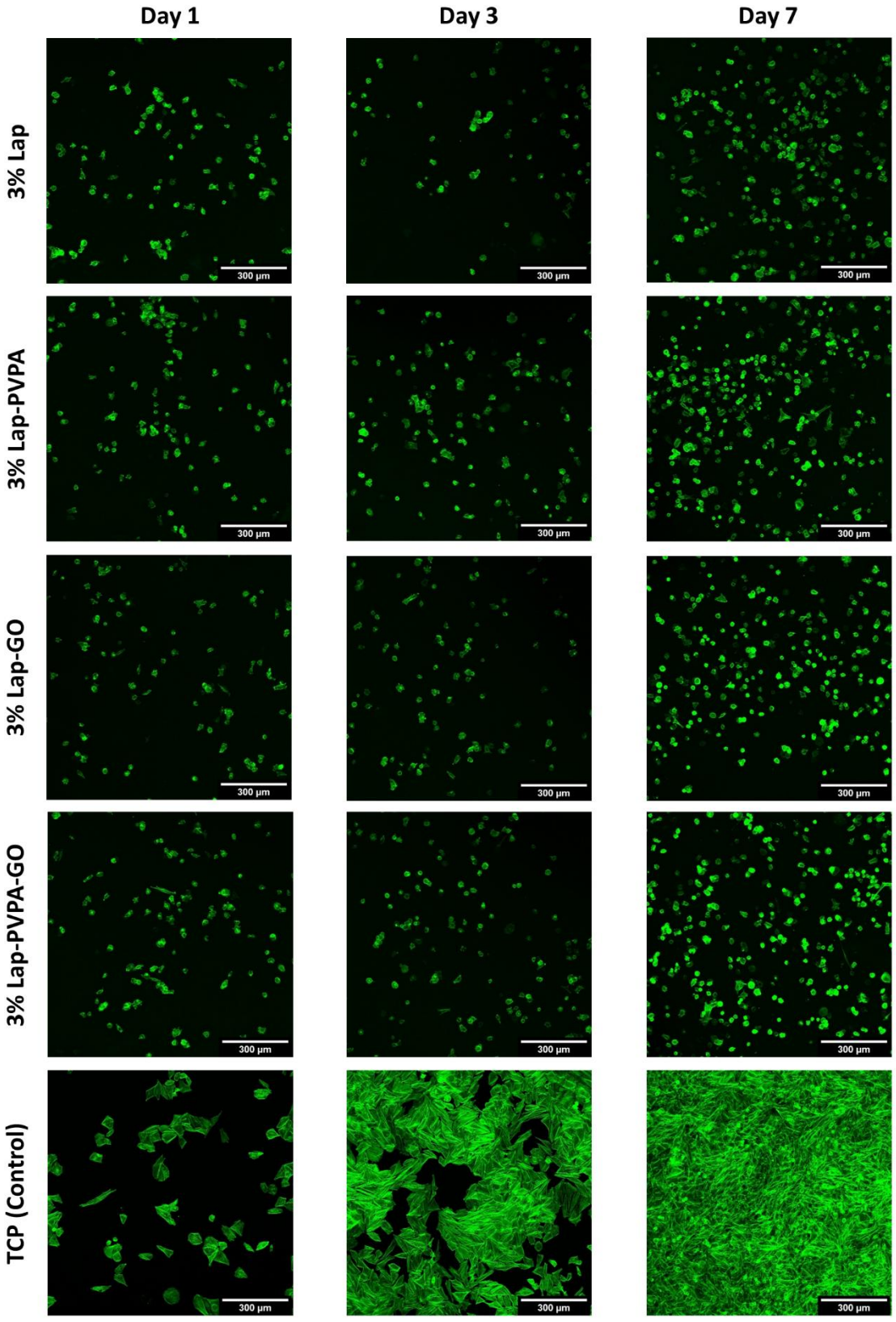

Figure 5-1. Phalloidin staining of osteoblast-like cells Saos-2 (passage number 16) seeded on surfaces of hydrogel discs at 1, 3, and 7 days post-seeding. Scale bar represents 250 µm.

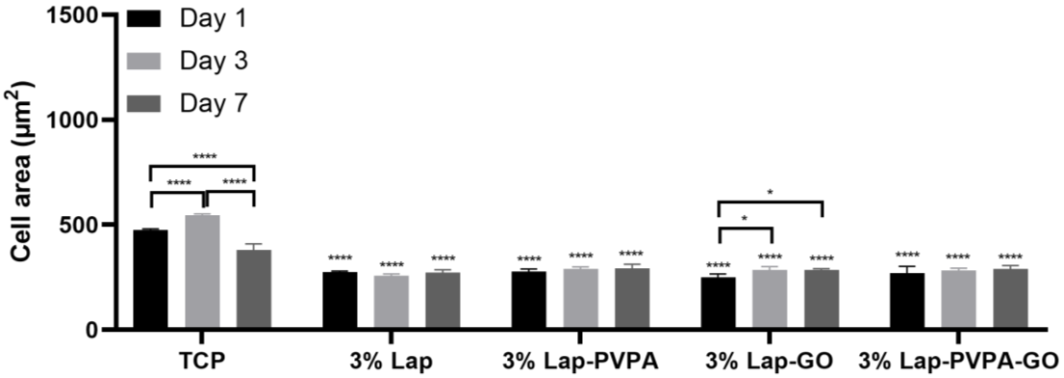

Figure 5-2. Average cell areas of Saos-2 (passage number 16) seeded on Laponite-based gel discs. Data were obtained from phalloidin staining images and analysed using CellProfiler software with the 'measure cell shape/size' feature. Stars above bars show results with statistical significance compared to TCP (control) at the same time point. Error bars represent standard deviation. Significant differences between time points for each Laponite-based gel are indicated by horizontal lines. **** $p \leq 0.0001$, * $p < 0.05$.

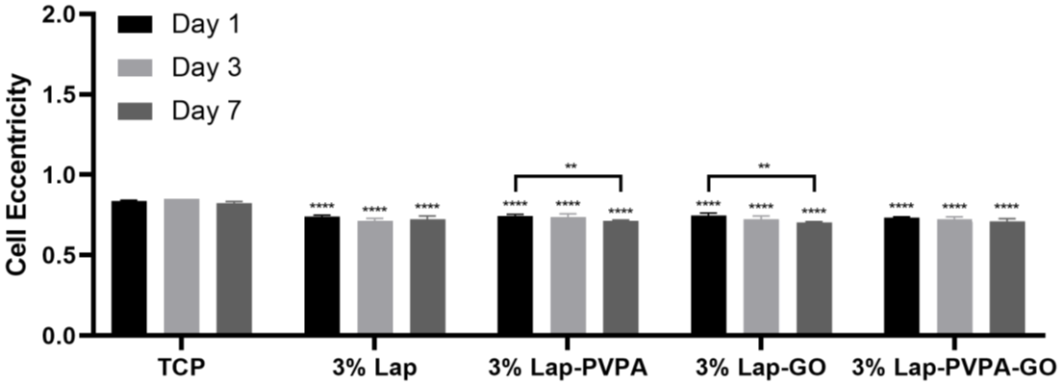

Figure 5-3. Cell shape analysis of Saos-2 (passage number 16) seeded on Laponite-based gel discs. Data were obtained from phalloidin staining images and analysed using CellProfiler software with the 'measure cell shape/size' feature. Stars above bars show results with statistical significance compared to TCP (control) at the same time point. Error bars represent standard deviation. Significant differences between Laponite-based gels are indicated by horizontal lines. **** $p \leq 0.0001$, ** $p \leq 0.01$.

5.2.1.3 Histological assessment

Histological assessment was performed at 1 and 3 weeks after post-seeding to determine matrix mineralisation of Saos-2 cultured on surfaces of Laponite-based gels using haematoxylin and eosin (H&E) and alizarin red S stains. Saos-2 seeded on cell-culture treated plastic coverslips were used as controls. H&E and alizarin red S stains of controls were displayed in Figure 5-4, with the strongly positive staining of alizarin red S observed on controls cultured in osteogenic medium at 3 weeks post-seeding. Saos-2 cells as controls

exhibited the typical elongated morphology of osteoblasts in both basal growth and osteogenic media throughtout the test period.

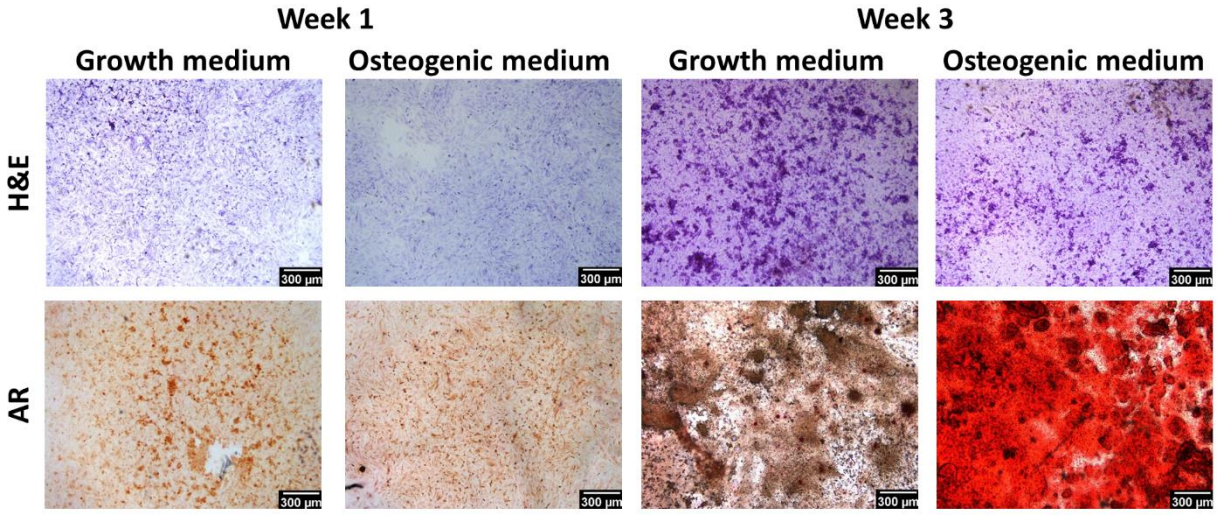

Figure 5-4. Haematoxylin and eosin (H&E) and alizarin red S (AR) stains of in vitro Saos-2 (passage number 16) seeded on cell-culture treated plastic coverslips at 1 week and 3 weeks post-seeding. Scale bar represents 300 µm. Frame size: 2180×1635 µm.

Representative images of H&E stain of Saos-2 cultured on surfaces of nanoclay gels at 1 and 3 weeks post-seeding incubated in growth and osteogenic media are shown in Figure 5-5 and Figure 5-6, respectively. At 1 week post-seeding, unlike the spindle-like morphology of Saos-2 seeded on controls in Figure 5-4, Saos-2 on nanoclay-based gels mostly exhibited a rounded shape, with cell nuclei stained in dark blue and the presence of surrounded cytoplasm. However, it seems that cells on gel surfaces became more elongated at 3 weeks post-seeding by which cytoplasm surrounded cell nuclei lengthen or extended. This cell behaviour was observed for all Laponite-based gels cultured in both growth and osteogenic media. Taking into consideration, some Saos-2 cells seeded on Lap-PVPA, Lap-GO, and Lap-PVPA-GO showed a higher degree of elongation compared to Lap. Haematoxylin and eosin staining also revealed a greater cell population observed on gels at 3 weeks post-seeding in a comparison with samples cultured for 1 week, suggestive of cell proliferation.

Calcium deposition in the mineralised matrix was determined using alizarin red S. The representative images of cross sections from *in vitro* Saos-2 seeded on surfaces of Laponite nanoclay gels stained with alizarin red S are shown in Figure 5-7 and Figure 5-8 for the incubation in standard growth medium and osteogenic medium, respectively. No positive staining of alizarin red S was detected at 1 week post-seeding for Saos-2 on Laponite-based

gels cultured in both growth and osteogenic media. As expected, calcium deposited in mineralised matrix evidenced by a significant positive staining of alizarin red S was detected for Saos-2 seeded on nanoclay-based gels cultured in osteogenic medium at week 3 of culture period (Figure 5-8). A weak positive staining of alizarin red S could be also observed for nanoclay-based gels incubated in growth medium (Figure 5-7). The results suggest that all Laponite-based gels could support cell attachment, proliferation, and osteogenic mineralisation of osteoblast-like cells.

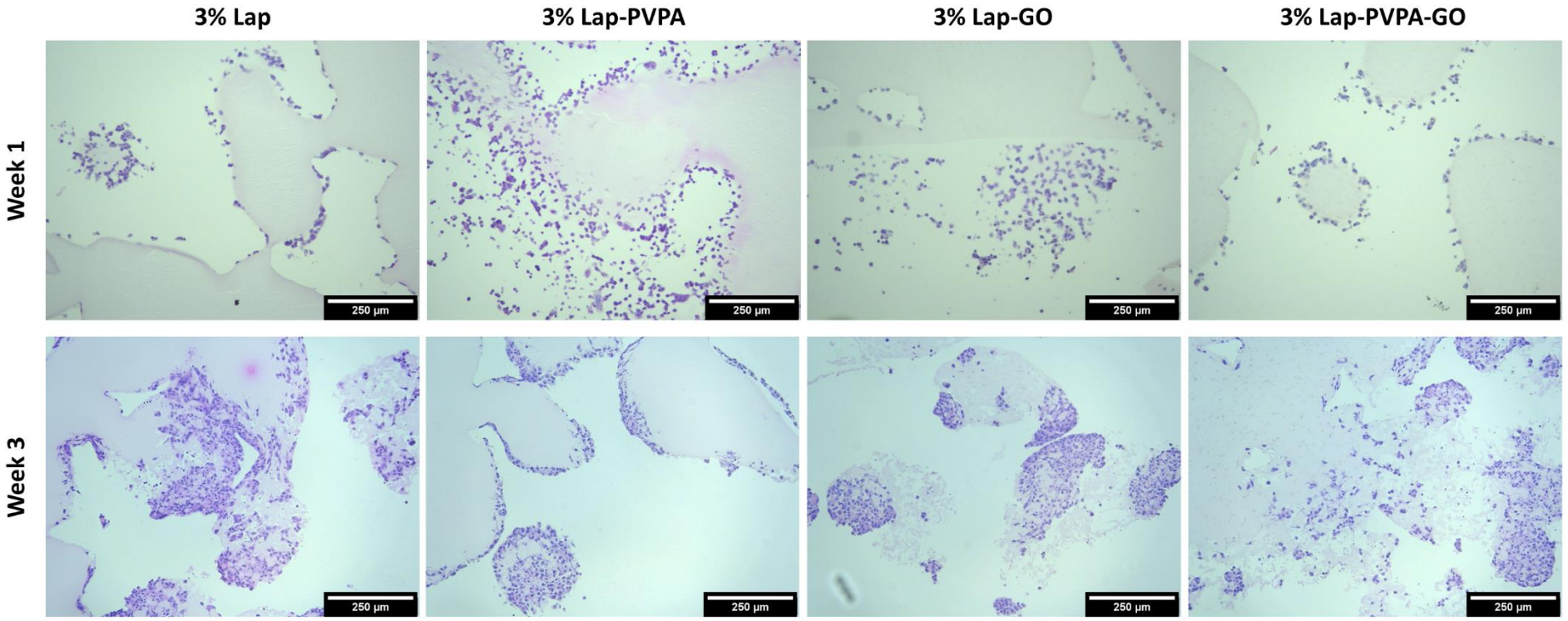

Figure 5-5. Haematoxylin and eosin (H&E) staining of cross-sections from in vitro osteoblast-like cells Saos-2 (passage number 16) cultured on surfaces of Laponite-based gels at 1 week and 3 weeks post-seeding. Samples were incubated in standard growth medium without osteogenic inducers. Scale bar represents 250 µm.

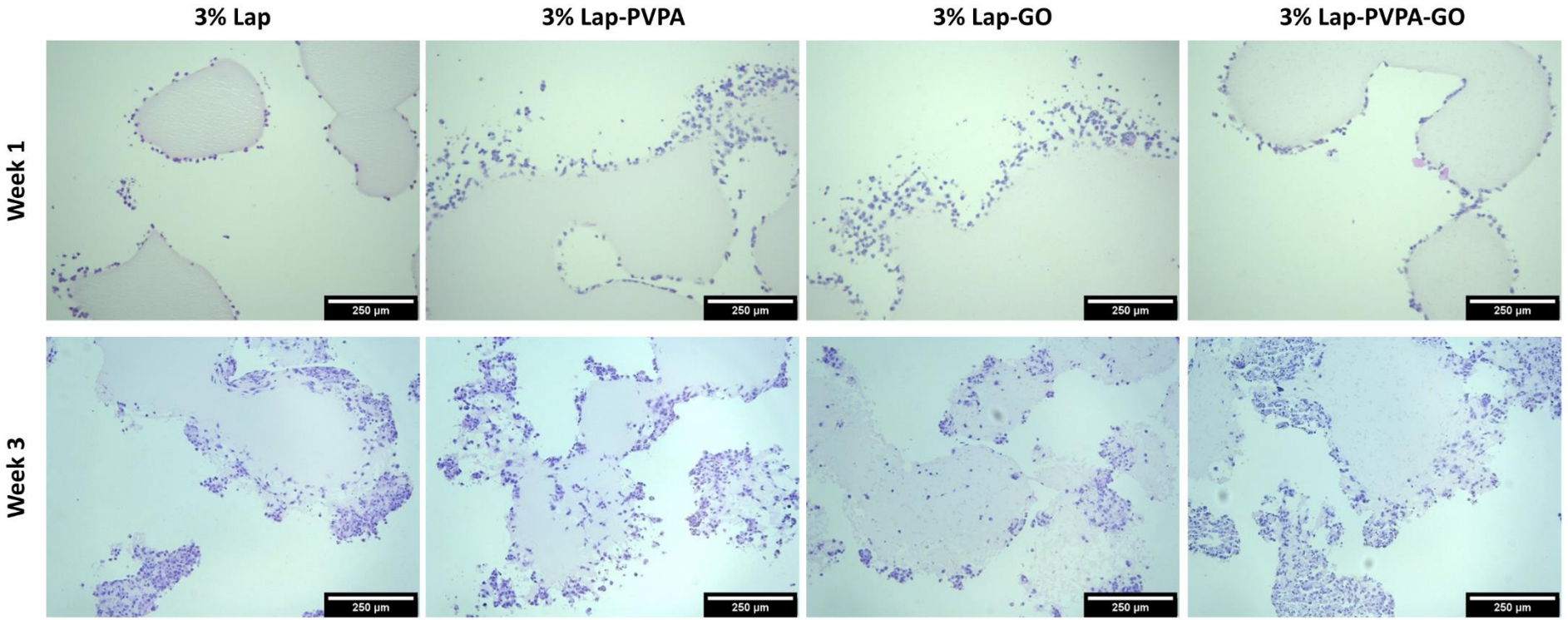

Figure 5-6. Haematoxylin and eosin (H&E) staining of cross-sections from in vitro osteoblast-like cells Saos-2 (passage number 16) cultured on surfaces of Laponite-based gels at 1 week and 3 weeks post-seeding. Samples were incubated in standard growth medium with osteogenic inducers. Scale bar represents 250 µm.

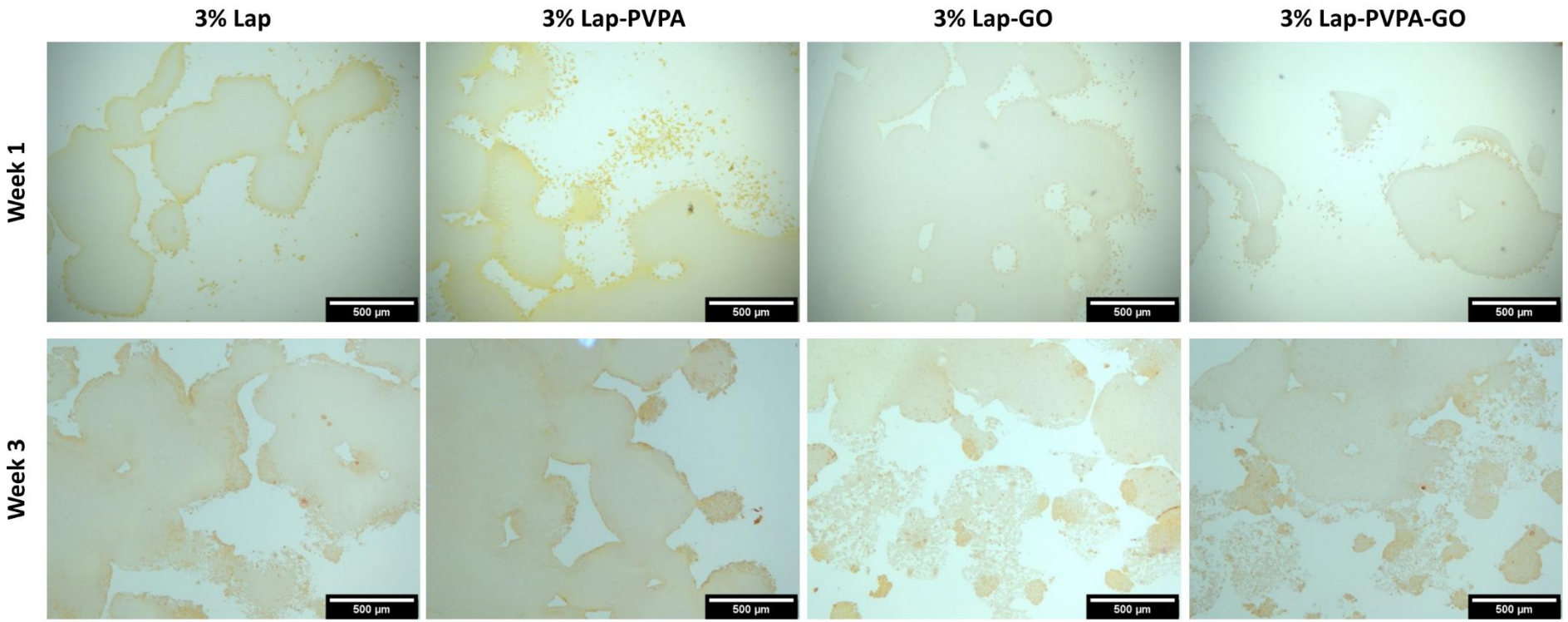

Figure 5-7. Alizarin red S staining of cross-sections from in vitro osteoblast-like cells Saos-2 (passage number 16) cultured on surfaces of Laponite-based gels at 1 week and 3 weeks post-seeding. Samples were incubated in standard growth medium without osteogenic inducers. Scale bar represents 500 µm.

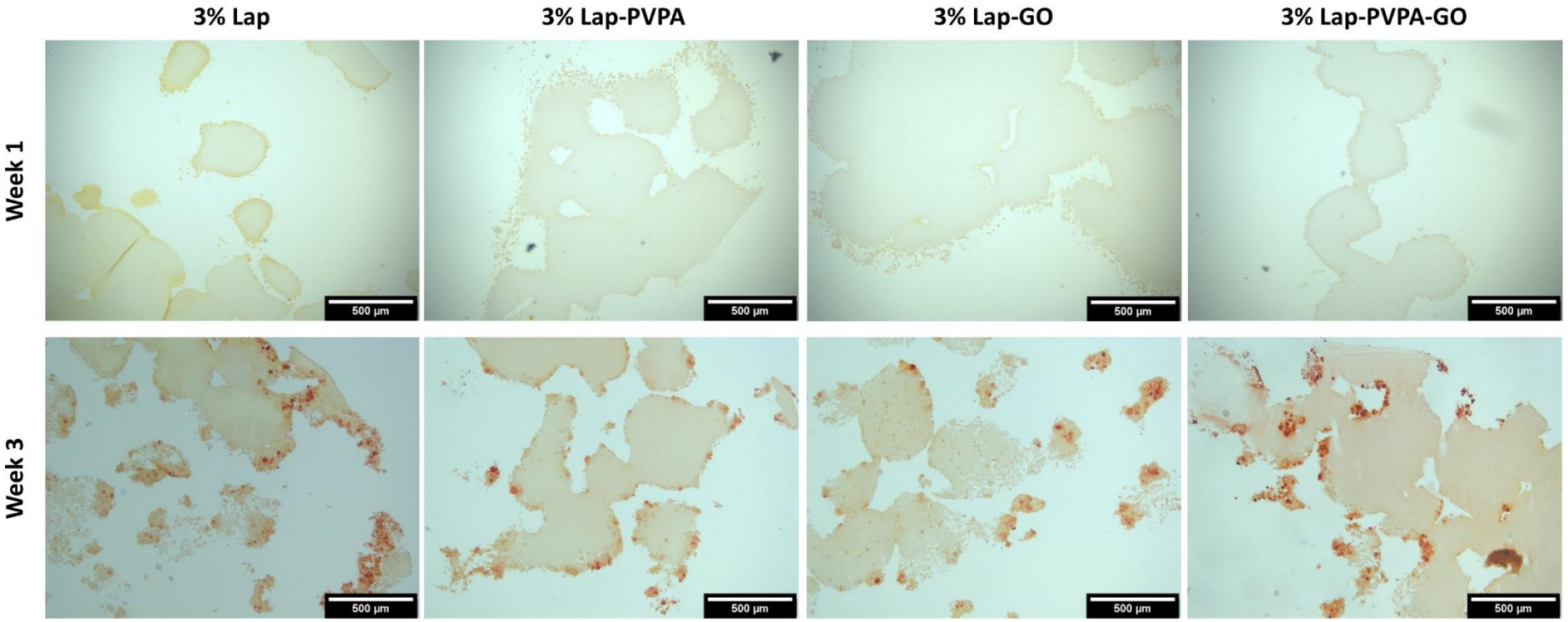

Figure 5-8. Alizarin red S staining of cross-sections from in vitro osteoblast-like cells Saos-2 (passage number 16) cultured on surfaces of Laponite-based gels at 1 week and 3 weeks post-seeding. Samples were incubated in standard growth medium with osteogenic inducers. Scale bar represents 500 µm.

5.2.2 Migration of osteoblast-like cells towards Laponite-gel scaffolds in the environment of protein gradient

The capability of Laponite gels to support cell migration was studied by seeding Saos-2 cells on surface of Laponite gel discs with 0.5 mm thickness, which were placed in ThinCert™ Cell Culture Inserts, at a density of 20,000 cells. Serum-free culture medium was put into an insert while concentrated FBS was put into well to create FBS gradient within hydrogel discs. Cells were labelled with fluorescent dye to facilitate a monitoring of migration using the confocal microscopy. A migration of live Saos-2 cells was performed on the same sample with the same position throughout the test period. Thermanox™ coverslips, which can generate blue autofluorescence were used as a reference level by placing under inserts containing gels during an acquisition of images. Diagram of experimental set up for cell culture and for image acquisition is shown in **Error! Reference source not found.**. Image acquisition was performed at 4 hours, 1 day, 2 days, and 3 days after seeding.

From Figure 5-9, it seems that no sign of cell migration through hydrogel matrix was observed for both concentrations of nanoclay gels. A decrease of the difference in distance between cell layers on top of gels and reference level at 1 day, 2 days, and 3 days in a comparison to 4 hours after seeding was from a shrinkage effect of hydrogels. Uncommonly, layers of cells were found to migrate upward from surface of 1% Laponite gels. This phenomenon was observed at 1 day, 2 days, and 3 days of the study.

PDGF-BB was used to promote osteoblastic cells migration. The PDGF-BB gradient was created in the same direction with FBS gradient, by which cell culture medium containing proteins (10% FBS + 5 ng mL^{-1} PDGF-BB) was added in well whereas a protein-free culture medium was put in an insert. The preliminary results are shown in Figure 5-10. At 4 hours post-seeding, a few cells seeded on 3% Lap were found to locate at downward direction from gel surface. However, there was no more sign of cell movement observed after this time point. Similarly, no cell movement into the gels was found for Saos-2 seeded on surface of 3% Lap-PVPA-GO. It is noteworthy that, in this experiment, different samples were used at different time points.

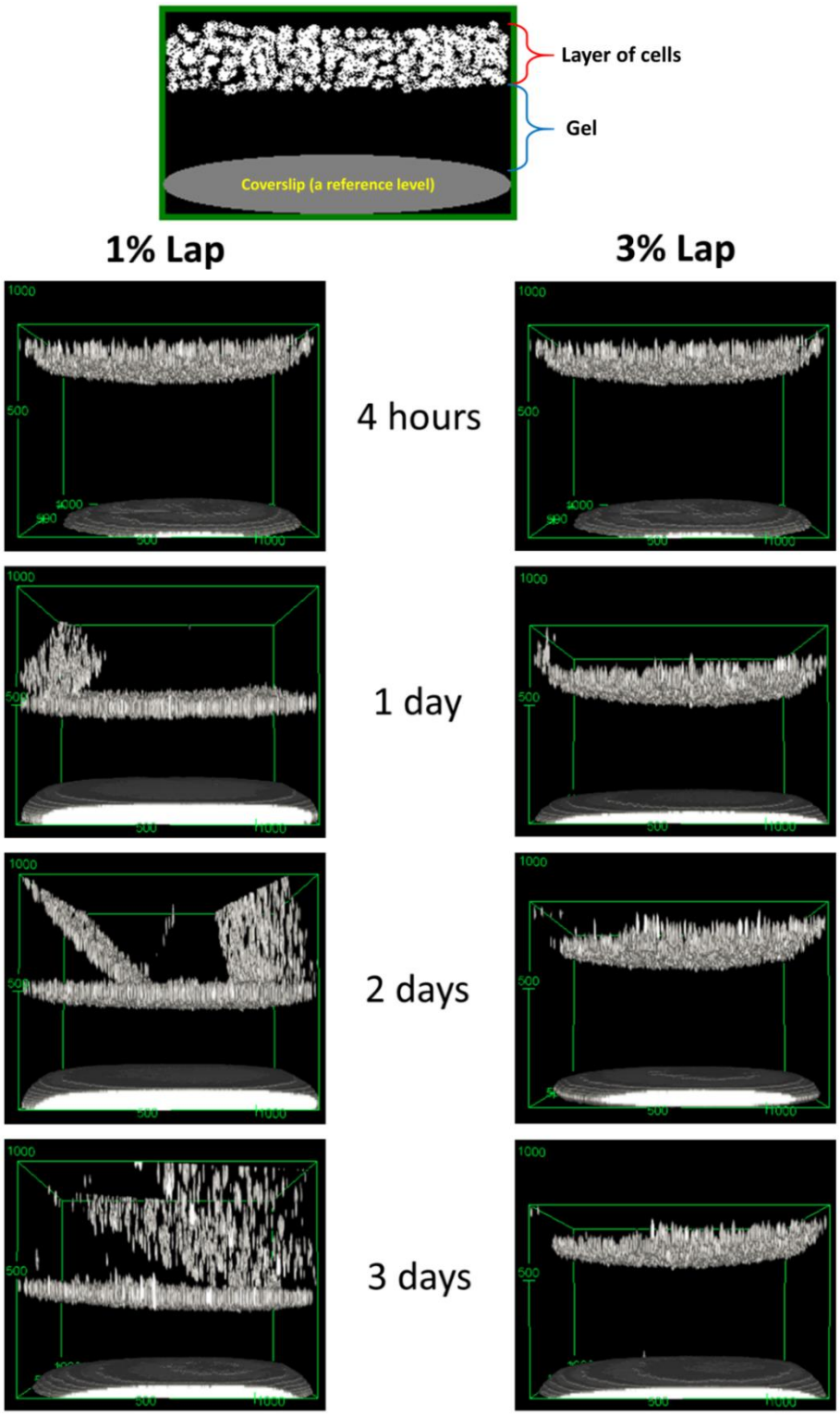

Figure 5-9. 3D renderings of Z stacks in a study of the ability of Laponite gels to support migration of osteoblast-like cells into the gel matrix. The FBS protein gradient was created to induce a migration of cells. Same sample of each gel were used at different time points. 3D images were proceeded using ImageJ software with 3D Viewer plugin. Huang's thresholding algorithm on the blue channel. The bottom plane comes from the fluorescence from the coverslip. Dimensions of green bounding box are in micrometers. Voxel size: 0.6584x0.6584x5 μm^3. The top image is a diagram to describe the position of scaffold, cells, and reference level in 3D images.

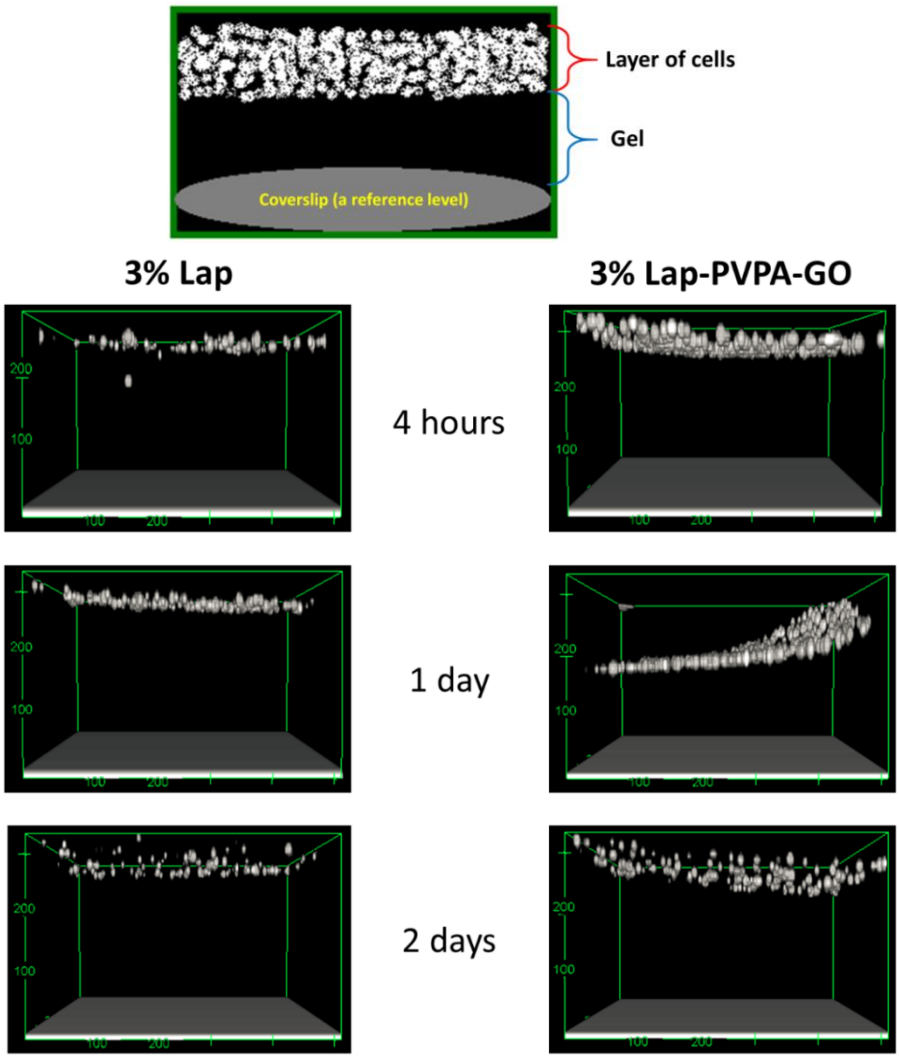

Figure 5-10. 3D renderings of Z stacks in a study of the ability of Laponite gels to support osteoblast-like cells migration. The PDGF-BB protein gradient was created to facilitate and induce a migration of cells. Different samples were used at different time points. 3D images were proceeded using ImageJ software with 3D Viewer plugin. Huang's thresholding algorithm on the blue channel. The bottom plane comes from the fluorescence from the coverslip. Dimensions of green bounding box are in micrometers. Voxel size: 0.6584x0.6584x5 μm^3. The top image is a diagram to describe the position of scaffold, cells, and reference level in 3D images.

5.3 Discussion

5.3.1 Cell behaviours on surface of Laponite-based gels

An *in vitro* two-dimensional (2D) cell culture was used to study osteoblastic response towards Laponite-based hydrogels. Unlike 3D encapsulation, the complications and variations occurred from culture technique such as uneven distribution of cell population could be

reduced or eliminated, hence the certain behaviours and biological activities of osteoblasts towards Laponite-based gels could be assessed.

Firstly, cell adhesion and spreading on gel surfaces were investigated using phalloidin staining to examine actin filaments organisation. Cell adhesion is the initiation process that mediates many subsequent activities such as proliferation, migration, and differentiation within scaffolds.[2] Saos-2 adhered on Laponite gel surfaces mostly exhibited a restricted F-actin organisation with rounded shape while some spreading cells with elongated shape were observed. Histological assessment reveals a positive staining of alizarin red S on all samples at 3 weeks post-seeding for both conditions (with and without osteogenic inducers), but a degree of colour staining was stronger for samples cultured in osteogenic condition (Figure 5-7 and Figure 5-8). H&E staining also suggested a higher cell population, along with a greater degree of cell elongation, at 3 weeks post-seeding as compare to week 1 (Figure 5-5 and Figure 5-6).

The addition of Laponite nanosilicates into non-adhesive polymer-based scaffolds has been reported to enhance cell adhesion and proliferation of hMSCs and osteoblasts.[3, 4] For example, hMSCs seeded on PEO/nanosilicate composite films with silicate content above 60% by weight exhibited a well organised cytoskeleton with stressed fibres while cells cultured on PEO films with low concentration of nanosilicate showed a restricted cytoskeleton with rounded morphology.[3] Moreover, hMSCs seeded on hydrated Laponite clay films showed no significant difference in morphology in a comparison to cells on glass substrates, but the degree of cell spreading on surfaces of Laponite gels was decreased.[5] The difference in cell spreading between surfaces of gel and film is an effect of stiffness of substrates. This effect could explain the difference in the organisation of stress fibres found between Saos-2 seeded on clay gel surfaces and controls, in this thesis, or clay films in those studies.[3, 5] However, cytoskeletal organisation and degree of cell spreading of Saos-2 in this study were apparently corresponding with hMSCs seeded on Laponite clay gels reported by Shi *et al*.[5] The addition of phosphonate-containing polymer and GO did not alter cell spreading which may be due to the effect of low concentration of GO and polymer, resulting in the comparable stiffness among Laponite-based gels. Factors that influence cell adhesion including surface roughness, hydrophilicity, charge, protein adsorption, and mechanical stiffness of substrates.[6-8] In general, most of cell types preferentially adhere and grow on stiffer substrates.[8-10]

With respect to soft hydrogels, many studies investigated the influence of hydrogel stiffness towards cell adhesion using hydrogels with elastic moduli ranging from 10 Pa to 2500 Pa.[8, 9, 11] A decrease in cell attachment with increasing hydrogel elasticity was reported for HeLa cells, fibroblasts and hMSCs.[8, 9, 11] On the other hand, human osteosarcoma showed a well attach with a spread morphology on RGDS-containing PEG hydrogels, independent of stiffness and elasticity.[9] Despite elastic moduli being in the same range, the Saos-2 osteoblastic cells on Laponite-based gels in this study likely exhibited a lower degree of cell spreading in a comparison with those soft hydrogels. The difference is probably due to the inclusion of RGDS peptide motif, cell binding sequence that mediates cell attachment or cell-matrix interaction, into those soft hydrogels to promote cell adhesion. Consequently, to improve cell adhesion along with stiffness of Laponite-based gels, the incorporation of ECM proteins, to increase adhesion ligands or integrins, can be one of a potential method.

In addition to cell adhesion and spreading, other cell functions such as cell growth, migration, and differentiation are also modulated by the matrix stiffness.[12] For example, it has been demonstrated that hMSCs differentiation is dependent on substrate stiffness, by which the culture of hMSCs on soft gels (0.1–1 kPa) induced neuronal differentiation whereas hMSCs differentiated towards myogenic and osteogenic cell lineages when they were cultured on stiffer gel matrixes.[12, 13] Cells on flexible substrates were reported to exhibit a decrease in cell spreading but possessed an increase in cell motility rates as compared to cells on stiff substrates.[14] Moreover, cell proliferation indicated by rates of DNA synthesis was found to decrease for cells seeded on flexible substrates in a comparison to cells on rigid matrixes.[15] Laponite-based gels in this study can be classified as a soft gel with ability to support cell proliferation and osteogenic mineralisation. However, for further research, it is worth investigating the effect of gel stiffness on cell adhesion and cell functions, along with the ability of Laponite-based gels to support osteogenic, chondrogenic, angiogenic, and neurogenic differentiation of stem cells. Mechanical properties of Laponite-based gels can be tuneable by adjusting the concentration of components, but further work is required to evaluate the threshold nanoclay/polymer/graphene ratio towards biocompatibility, porosity and degradation rate of nanoclay-based gels. Also, the incorporation of other molecules into Laponite gel matrixes may be an alternative strategy to improve mechanical properties and biological activities of cells.

5.3.2 Cell migration in Laponite-based gels

In this study, the migration of Saos-2 in 3D environment of Laponite-based gels was examined with preliminary results shown in Figure 5-9 for FBS protein gradient and Figure 5-10 for PDGF-BB protein gradient. No migration of Saos-2 within 3 wt% nanoclay gel matrixes was observed for both environments of FBS protein gradient and PDGF-BB protein gradient. The reason for no migration of cells may be due to the lack of effective porosity within scaffolds or the pores may be too small for cells to infiltrate. Moreover, cells may not be able to migrate through the necks between the pores. Pore size is a factor that influence cell migration. Murphy *et al*. investigated the effect of pore size on cell adhesion and migration of MC3T3-E1 cells, in collagen-glycosaminoglycan (CG) scaffolds with mean pore sizes ranging from 85 mm to 325 mm and the finding suggested that cell migration increased with larger pore sizes.[2] Moreover, Ehrbar *et al*. demonstrated that migration of preosteoblasts within soft gels (G'<100 Pa) was dominated by a non-proteolytic migratory mode and 3D cell migration could occur via existing pores or macroscopic gel defects.[16] According to literatures, it can be assuming that cell migration through 1 wt% Laponite gels, which could be classified as soft gels, may occur via existing pores. However, 1 wt% Laponite gels in this thesis possessed a porous structure with approximate pore size 20–40 μm (Figure 4-8) which may be too small for cells to infiltrate or migrate.

On the other hand, gel with higher stiffness (G'≈120–500 Pa) supported cell migration through a proteolytic mode or matrix degradation induced by matrix metalloproteinases (MMPs).[1, 16] The migratory mode of osteoblast for 3 wt% Laponite-based gels (G'≈200–400 Pa) could be dominated by a proteolytic mode due to its stiffness and lack of pore structure. However, Laponite-based gels may be insensitive to degradation by MMPs, leading to no migration of osteoblasts.

From Figure 5-9, layers of cell clusters were observed in an upward direction from gel surfaces. It is not convinced that these layers of cells found in 1 wt% Laponite gel were a collective migration because cell-matrix interaction is required in cell migration process and there was no scaffold or substrates above gel surfaces. These layers of cells may be cells on fragmented gels attached on the side wall of insert which were a result of shrinkage effect of hydrogels and/or gel surface disruption during changing medium.

For further research, the fabrication of Laponite gel scaffolds with porous interconnected network may be required for directing cell migration. This could be achieved the addition of other natural or synthetic hydrogels or by utilising 3D printed constructs with an engineered microstructure.[17]

5.4 Conclusion

In this chapter, the response of Saos-2 osteoblast-like cells towards Laponite-based gels in 2D culture was studied. The phalloidin staining and histological analysis suggest that all Laponite-based gels supported cell adhesion, proliferation, and osteogenic mineralisation of Saos-2. Degree of cell spreading on surfaces of Laponite-based gels was lower than cells seeded on Laponite-containing films in other studies[3, 4] due to a lower stiffness of Laponite soft gels. The addition of phosphonate-containing copolymer and GO did not alter cell adhesion and functions of Saos-2. The ability of Laponite gels to support migration of osteoblastic cells was investigated. It was found that cells could not migrate through hydrogel matrixes which is probably due to the lack of effective pore structure. The improvement of porosity and mechanical properties are necessarily required for further research to facilitate cell migration together with the capability to support biological functions of cells.

5.5 References

1. Movilla, N.; Borau, C.; Valero, C.; García-Aznar, J., Degradation of extracellular matrix regulates osteoblast migration: a microfluidic-based study. *Bone* **2018,** *107*, 10-17.
2. Murphy, C. M.; Haugh, M. G.; O'brien, F. J., The effect of mean pore size on cell attachment, proliferation and migration in collagen–glycosaminoglycan scaffolds for bone tissue engineering. *Biomaterials* **2010,** *31* (3), 461-466.
3. Gaharwar, A. K.; Kishore, V.; Rivera, C.; Bullock, W.; Wu, C. J.; Akkus, O.; Schmidt, G., Physically Crosslinked Nanocomposites from Silicate-Crosslinked PEO: Mechanical Properties and Osteogenic Differentiation of Human Mesenchymal Stem Cells. *Macromolecular Bioscience* **2012,** *12* (6), 779-793.
4. Gaharwar, A. K.; Schexnailder, P. J.; Kline, B. P.; Schmidt, G., Assessment of using Laponite® cross-linked poly (ethylene oxide) for controlled cell adhesion and mineralization. *Acta biomaterialia* **2011,** *7* (2), 568-577.
5. Shi, P.; Kim, Y. H.; Mousa, M.; Sanchez, R. R.; Oreffo, R. O.; Dawson, J. I., Self-Assembling Nanoclay Diffusion Gels for Bioactive Osteogenic Microenvironments. *Advanced healthcare materials* **2018,** *7* (15), 1800331.
6. Wilson, C. J.; Clegg, R. E.; Leavesley, D. I.; Pearcy, M. J., Mediation of biomaterial–cell interactions by adsorbed proteins: a review. *Tissue Engineering* **2005,** *11* (1-2), 1-18.
7. Phillips, J. E.; Petrie, T. A.; Creighton, F. P.; García, A. J., Human mesenchymal stem cell differentiation on self-assembled monolayers presenting different surface chemistries. *Acta Biomaterialia* **2010,** *6* (1), 12-20.

8. Best, J. P.; Javed, S.; Richardson, J. J.; Cho, K. L.; Kamphuis, M. M.; Caruso, F., Stiffness-mediated adhesion of cervical cancer cells to soft hydrogel films. *Soft Matter* **2013,** *9* (18), 4580-4584.
9. M. Jonker, A.; A. Bode, S.; H. Kusters, A.; van Hest, J. C. M.; Löwik, D. W. P. M., Soft PEG-Hydrogels with Independently Tunable Stiffness and RGDS-Content for Cell Adhesion Studies. *Macromolecular Bioscience* **2015,** *15* (10), 1338-1347.
10. Missirlis, D.; Spatz, J. P., Combined Effects of PEG Hydrogel Elasticity and Cell-Adhesive Coating on Fibroblast Adhesion and Persistent Migration. *Biomacromolecules* **2014,** *15* (1), 195-205.
11. Kyburz, K. A.; Anseth, K. S., Three-dimensional hMSC motility within peptide-functionalized PEG-based hydrogels of varying adhesivity and crosslinking density. *Acta Biomaterialia* **2013,** *9* (5), 6381-6392.
12. Brandl, F.; Sommer, F.; Goepferich, A., Rational design of hydrogels for tissue engineering: impact of physical factors on cell behavior. *Biomaterials* **2007,** *28* (2), 134-146.
13. Engler, A. J.; Sen, S.; Sweeney, H. L.; Discher, D. E., Matrix Elasticity Directs Stem Cell Lineage Specification. *Cell* **2006,** *126* (4), 677-689.
14. Pelham, R. J.; Wang, Y.-l., Cell locomotion and focal adhesions are regulated by substrate flexibility. *Proceedings of the National Academy of Sciences* **1997,** *94* (25), 13661-13665.
15. Wang, H.-B.; Dembo, M.; Wang, Y.-L., Substrate flexibility regulates growth and apoptosis of normal but not transformed cells. *American Journal of Physiology-Cell Physiology* **2000,** *279* (5), C1345-C1350.
16. Ehrbar, M.; Sala, A.; Lienemann, P.; Ranga, A.; Mosiewicz, K.; Bittermann, A.; Rizzi, S.; Weber, F. E.; Lutolf, M., Elucidating the role of matrix stiffness in 3D cell migration and remodeling. *Biophysical journal* **2011,** *100* (2), 284-293.
17. Cidonio, G.; Alcala-Orozco, C. R.; Lim, K. S.; Glinka, M.; Mutreja, I.; Kim, Y.-H.; Dawson, J. I.; Woodfield, T. B.; Oreffo, R. O., Osteogenic and angiogenic tissue formation in high fidelity nanocomposite Laponite-gelatin bioinks. *Biofabrication* **2019,** *11* (3), 035027.

Chapter 6

Summary and future work

6.1 Significant research findings

My thesis work aimed to produce phosphonate-modified graphene derivatives using the synthesis routes that cause a little disruption to the graphene sheet. The modification of phosphonated graphene analogues, by two different synthesis routes which were edge-modification and copolymerisation in graphene-based suspensions, were outlined in Chapter 3. The evidence provided in this chapter indicated the presence of phosphorous-containing functional groups, change in dispersibility, and little alteration in defect density of graphene sheets. Phosphonate-modified graphene analogues possessed negative zeta potential to be stable in suspension, but the charge density varied between analogues from −36.30 mV (G–$PO(OH)_2$) to −52.20 mV (GO–PVPA).

A further objective was to investigate the ability of phosphonate-modified graphene analogues to support cell growth and osteogenic mineralisation. Phosphonate-modified GFNs were incorporated into LbL constructs that were used as surfaces for cell culture study. The LbL assemblies of phosphonate-modified graphene analogues produced from the edge-modification method (PEI/G–$PO(OH)_2$ and PEI/GO–$PO(OH)_2$) were found to have the lower level of incorporation than other LbL constructs, likely due to the lower charge density on G–$PO(OH)_2$ and GO–$PO(OH)_2$. The biocompatibility of the LbL constructs containing GFNs towards osteoblasts, which were HOBs and Saos-2 cells, was assessed. No significant toxicity was observed for all LbL constructs based on a high cell viability and the increase in DNA quantification during culture period. Cell adhesion, especially for HOBs, depended on surface properties including protein adsorption, surface chemistry, and topography which showed a subsequent influence on cell spreading, proliferation, and osteogenic mineralisation. Only HOBs seeded on PEI/GO showed calcium deposition indicated by positive staining of alizarin

red S whereas all GFN-containing LbL substrates could support osteogenic mineralisation of Saos-2. From the *in vitro* study in Chapter 3, PEI/GO was determined to be the most acceptable and suitable surface that could support adhesion and cell activities of osteoblasts with the typical spindle-like morphology. Hence, GO was selected for the incorporation into Laponite-based gels.

The primary aim of this thesis was to create injectable Laponite-based hydrogels and to investigate their ability to serve as a host osteogenic microenvironment. Injectable Laponite gels containing GO and phosphonate copolymer (PVPA-*co*-AA) were fabricated by a simple mixing technique. The effect of GO and PVPA-*co*-AA on properties of hydrogels and compare to bare Laponite was investigated, with results outlined in Chapter 4. The addition of PVPA-*co*-AA increased storage modulus and viscosity of Laponite gels whilst GO did not alter mechanical properties probably because of a low concentration. The increased storage modulus by the incorporation of PVPA-*co*-AA was likely due to a physically crosslinked network occurred from polymer adsorption on Laponite surfaces and subsequent formation of polymer bridging between nanoclay particles. Behaviours of Saos-2 osteoblastic cells within Laponite-based hydrogels were determined to investigate a potential of Laponite-based scaffolds for BTE. Interestingly, positive staining of alizarin red S staining was detected at 3 weeks post-seeding for all samples cultured in basal growth medium without osteogenic inducers, suggesting the osteoinductive property of Laponite nanoclay. The addition of GO and PVPA-*co*-AA did not promote or accelerate osteogenic mineralisation of Saos-2 within Laponite-based gels. Moreover, stability of Laponite-based hydrogels was investigated through the change in droplet shape over time. Laponite-based gels exhibited fragmentation after 2 weeks post-culturing, implying a gradual degradation of nanoclay gels presumably caused by cells and culture environment.

Response of cells towards Laponite-based gels using 2D culture was investigated with results reported in Chapter 5. The majority of Saos-2 seeded on surfaces of nanoclay-based gels showed restricted actin stress fibres and low degree of cell spreading. Calcium deposition identified by positive staining of alizarin red S was detected for Saos-2 cultured on all Laponite-based gels at 3 weeks post-seeding. Cell migration through nanoclay gel scaffolds was also examined in this chapter. The protein gradient was created using FBS and PDGF-BB to study chemotactic properties of Saos-2. The preliminary results showed no sign of cell migration

through gel structure, likely due to the lack of effective porosity within scaffolds or the pores may be too small for cells to infiltrate.

In summary, based on the research objectives, phosphonate-modified GFNs could be produced through both edge-selective modification and radical polymerisation with graphene or GO, but the latter strategy provided a higher content of phosphorous. All LbL constructs containing phosphonate-modified GFNs showed no significant toxicity towards osteoblasts and could support osteogenic mineralisation of Saos-2. Laponite-based gels offer a potential scaffold to serve as host osteogenic microenvironments with biocompatibility and biodegradability. However, Laponite gels lacked the effective porosity to allow cell migration.

6.2 Future work

6.2.1 Modified graphene family-nanomaterials

6.2.1.1 Attachment of biologically relevant molecules to modified graphene derivatives

The modifications of graphene and GO and their characterisations were presented in Chapter 3. Several extensions to this work are outlined in this section, which include additional characterisation of modified graphene materials and potential studies for future application.

One of expectations in functionalisation of graphene in this thesis was to provide functional groups for tethering biomolecules. Graphene-family nanomaterials are promising candidates in biotechnology development including biosensing and detection of biomolecules, drug delivery, and cell imaging.[1-3] Graphene and GO have been modified and functionalised with various biomolecules including DNA, proteins, and peptides to improve biocompatibility, solubility, and selectivity.[1, 2] GO is more likely used in biofunctionalisation due to the enriched oxygen-containing functional groups that provide the possibility for extensive range of reactions, immobilisation, and functionalisation.[1, 2] On the other hand, graphene with the preserved sp^2 carbon network takes advantages over GO, which is disrupted in the extended π-system structure from oxidation, regarding superior electronic properties and conductivity.[4] G–SH produced in this thesis has shown the possibility of tethering biomolecules by radical addition to alkene of thiol groups.[5] Likewise, phosphonate groups existing in G–$PO(OH)_2$ and G–PVPA may be able to react with biomolecules through H-bonds, radical addition, and electrostatic interactions. Biomolecules can also interact with graphene materials via π–π

interaction such as single stranded DNA.[6] Modified graphene derivatives in this thesis may provide opportunities to tether multi biomolecules through both functional groups and π–π stacking, utilising in biotechnology and biomedical applications. Therefore, for the future direction of this work or further research, it is worth investigating the attachment of biomolecules to modified graphene analogues.

6.2.1.2 Electrical conductivity measurement

The high carrier mobility of graphene produced by the edge functionalisation, outlined in this thesis, is expected to preserve. Electrical conductivity of graphene can be measured on CVD graphene thin film using the gated van der Pauw method, with a diagram of device shown in Figure 6-1.[7] G–SO_3 CVD graphene can be used as a representative of edge-specific functionalised graphene, with the functionalisation procedure demonstrated by Shellard *et al*.,[5] for electrical conductivity measurement using the van der Pauw method. Alternatively, nanocomposite films of modified graphene materials with polymers can be produced and measured a conductivity. For example, nanocomposites of modified graphene and PLA can be fabricated via solution casting using the protocol established by Sabzi *et al*.[8] With this regards, a pure PLA film may be used as a control and the homogenous distribution of modified graphene particles within polymer matrix is required.

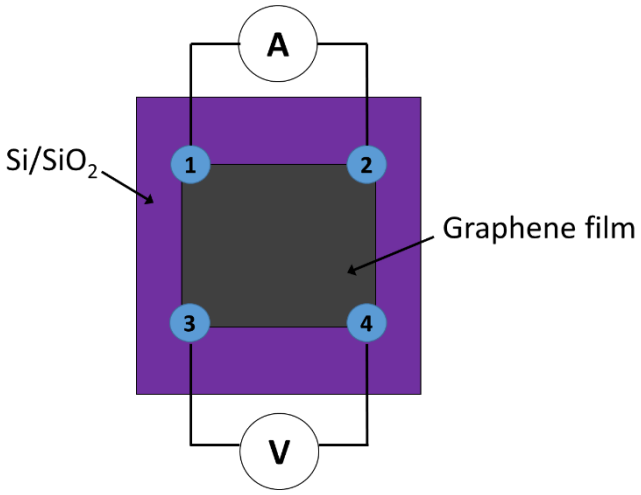

Figure 6-1. Set up for the van der Pauw conductivity measurement on thin film, showing four electrical contacts applied to the corners of graphene film. For electrical measurement, a current flows through one side of film, by sourcing in contact 1 and draining at contact 2. The potential differences across contacts 3 and 4 are measured. Diagram is modified from Sabzi et al.[7] and the thesis of Shellard.[9]

6.2.2 Graphene materials-containing layer-by-layer assemblies

6.2.2.1 Distribution of graphene materials in layer-by-layer constructs

The distribution of GFNs is a crucial parameter that relates to mechanical properties of the composites. A good dispersion of graphene particles in composites leads to high interfacial strength with matrix and uniformity that significantly influence the mechanical properties.[10] Further from AFM measurement and imaging of LbL constructs, distribution of phosphonate-modified GFNs can be also examined using Raman mapping. The Raman mapping images of PEI/GO, PEI/GO–SO_3, PEI/G–SO_3, PLL/GO, PLL/GO–SO_3, and PLL/G–SO_3 LbL constructs, containing 15 bilayers, are presented in Figure 6-2. The Raman maps were created at the G peak (centred at 1597 cm^{-1}) which is the fingerprint of graphene-based materials. Colour bars on the right of each maps indicate the intensity range of the peaks. The agglomeration of graphene materials was observed and identified by the areas of free shape with different colours, meaning that the LbL constructs were not completely homogeneous distributed.

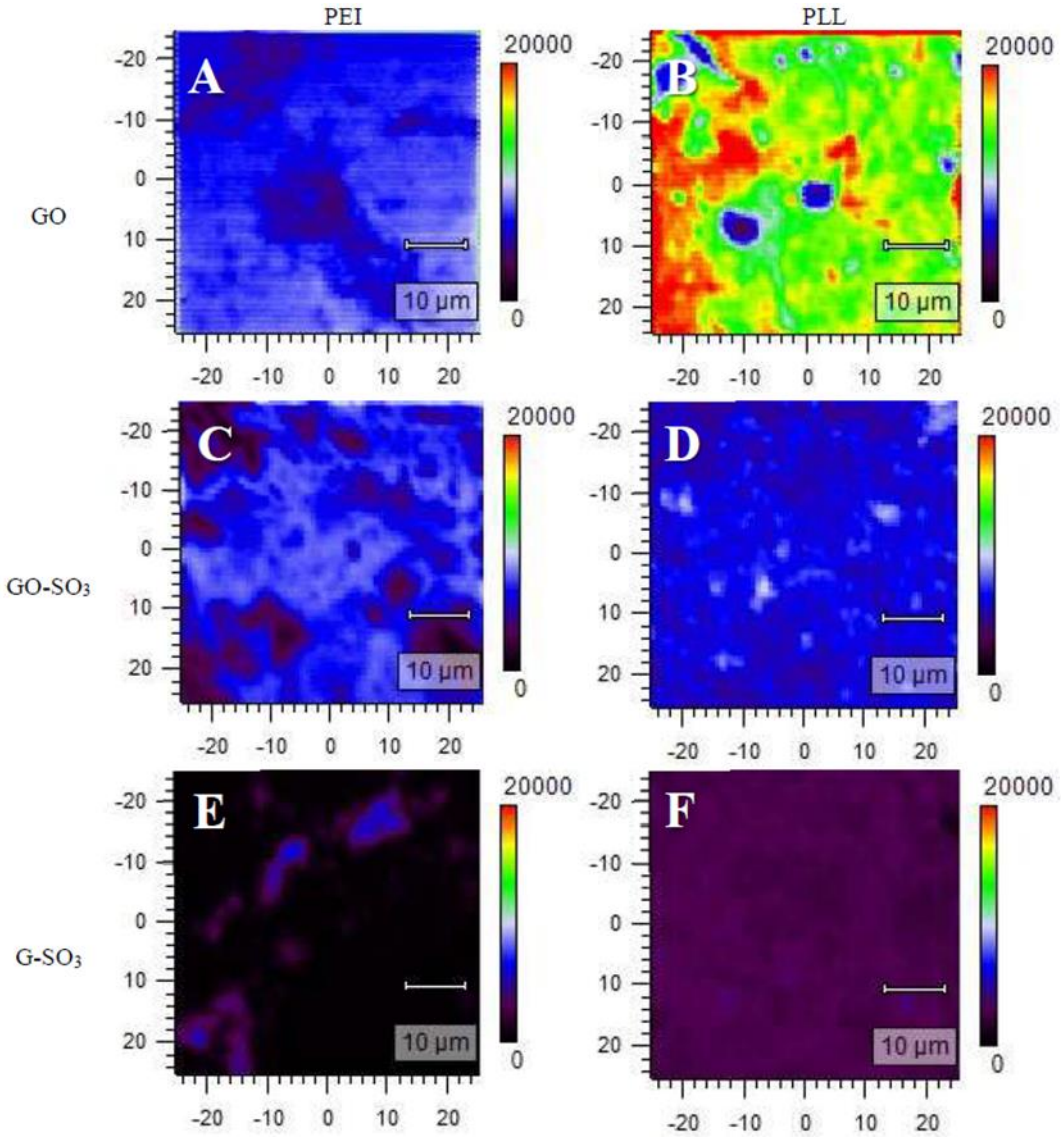

Figure 6-2. G peak (1597 cm^{-1}) Raman intensity maps of LbL constructs on Si/SiO_2 wafers. A:$(PEI/GO)_{15}$, B:$(PLL/GO)_{15}$, C:$(PEI/GO–SO_3)_{15}$, D:$(PLL/GO–SO_3)_{15}$, E:$(PEI/G–SO_3)_{15}$, F:$(PLL/G-SO_3)_{15}$. Data were obtained from my MSc dissertation.[11]

6.2.2.2 Mass measurement by the quartz crystal microbalance with dissipation monitoring

A mass of modified GFNs deposited on LbL constructs can be measured using the quartz crystal microbalance with dissipation (QCM-D), which is a useful technique commonly used for an accurate measurement of the adsorbed amounts of materials (ng cm^{-2}) on surface.[12] According to the Sauerbrey equation,[13] the amount of materials added to the surface of quartz wafer is proportional to the frequency change if the added mass is thin, rigid, and evenly distributed.[12]

6.2.3 Human mesenchymal stem cells response towards layer-by-layer constructs

The behaviour of hMSCs on phosphonate-modified GFN-containing LbL constructs were not studied systematically in this thesis because of COVID-19–related lab closures (see COVID-19 Impact Statement) and lack of availability of viable cells. However, hMSCs differentiation toward osteoblasts was investigated using alizarin red S staining, with preliminary results shown in Figure 6-3. No positive staining was detected for hMSCs seeded on PEI/G–SO_3 over the test period, likely due to the lack of cell adhesion. A weak positive staining was observed for hMSCs on PEI/GO, PEI/GO–SO_3 and control at 14 days and 21 days post-seeding.

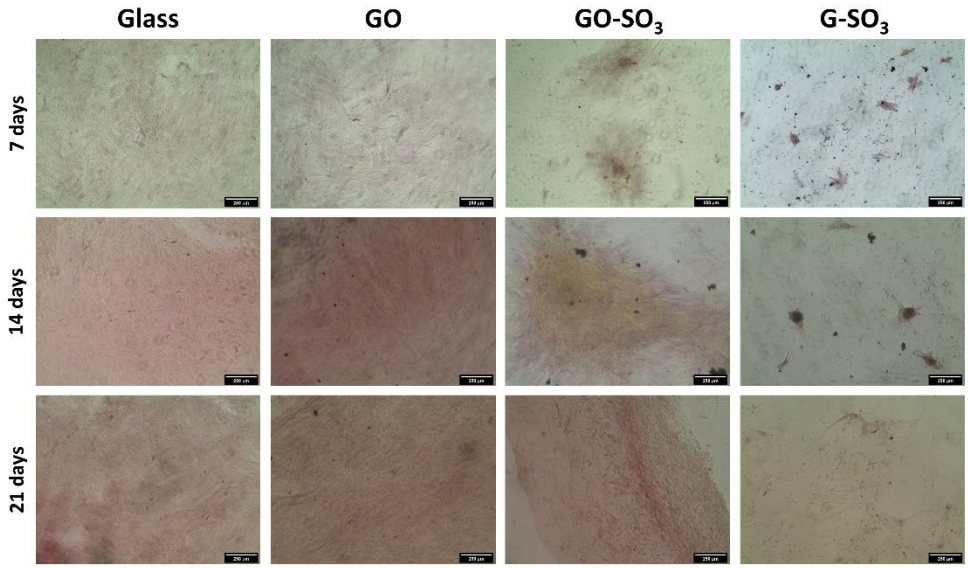

Figure 6-3. Alizarin red S staining of hMSCs on GFN-containing LbL constructs, incubated with osteogenic induction medium for 7 days, 14 days, and 21 days. Scale bar represents 250 µm.

Graphene-based materials have shown potentials to induce stem cell differentiation towards osteogenic, chondrogenic, neurogenic, and cardiomyogenic lineages.[14] Therefore, it is worth determining the effect of phosphonate modified GFN-containing LbL constructs on hMSCs differentiation towards those cell lineages.

6.2.4 Laponite-based gels

6.2.4.1 The effect of concentrations of GO and PVPA-*co*-AA in Laponite gels towards cell behaviours, mechanical and rheological properties

Cell functions of Saos-2 within Laponite-based hydrogels was investigated using 3D cell encapsulation, with results outlined in Chapter 4. Also, the behaviour and migration of osteoblasts were studied in Chapter 5. Several extensions are outlined in this section which

include additional experiments or characterisation techniques, a further research, and other potential studies.

The concentration of GO and PVPA-*co*-AA added into Laponite gels presented in Chapter 4 and 5 was fixed at 0.09% and 0.05% by weight, respectively. The concentrations of GO suspension and PVPA-*co*-AA solution used in this thesis were 100 μg mL^{-1} and 500 μg mL^{-1}, respectively. However, storage moduli (G') of Laponite-based gels did not significantly increase and osteogenic mineralisation of Saos-2 within nanoclay gels did not accelerated or promoted at this concentration of GO and PVPA-*co*-AA. Hence, the concentrations of GO and PVPA-*co*-AA should be optimised to maintain adequate mechanical properties and biocompatibility of nanoclay-based gels with enhancing osteogenic mineralisation of osteoblasts.

Piao and Chen also demonstrated that the incorporation of 3% w/v of GO into gelatin hydrogels increased compressive strength and storage modulus of nanocomposite hydrogels due to chemical crosslinking and electrostatic interactions between gelatin and GO.[15] Saos-2 treated with PVPA-*co*-AA solution at 500 μg mL^{-1} showed a great viability and proliferation.[16, 17] Wang et al. reported that the *in vitro* mineralisation of Saos-2 treated with PVPA-*co*-AA solution in osteogenic medium was observed until the concentration of copolymer reached 25 μg mL^{-1} whilst the concentration of PVPA-*co*-AA solution up to 100 μg mL^{-1} induced osteogenic differentiation of hMSCs.[17]

6.2.4.2 Quantification of calcium deposited in matrix mineralisation

In this thesis, only qualitative histological staining was performed on cross-sections of samples to indicate the mineralisation of Saos-2 within Laponite-based gels. A quantification method, as a relative measure of mineralisation, to represent images from histology is strongly recommended for further research. A quantification of mineralisation within nanoclay gels may be measured by a colorimetric detection using an alizarin red S assay. With this method, the staining protocol must be identical for all the treatments being compared, as well as negative controls (only gel scaffolds) are essentially needed. It may also be worth incorporating some additional controls to test for any interference with gels and the alizarin red S staining or extraction process. For example, some known amounts of calcium may be mixed into nanoclay gels to check for this.

Another concern is that the fragmentation of nanoclay-gel droplets after 2 weeks post-seeding can cause complications to the staining procedure and measurement, for example, samples may be lost during washing step of residual alizarin red S solution. A feasible solution to this complication is coating nanoclay gels with alginate as an outer layer to hold fragmented gels inside alginate gel, with a supposed structure of gel beads shown in Figure 6-4.

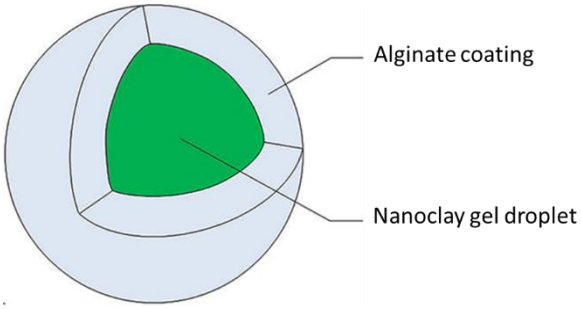

Figure 6-4. A supposed structure of nanoclay gel droplet coated with alginate gel.

6.2.4.3 Degradation of Laponite-based gels

The stability of Laponite-based gels during culture period was studied in in this thesis, with results presented in Chapter 4. The disintegration of nanoclay gel beads was observed. It was speculated that the dissolution of Laponite leads to the fragmentation of gel beads. Laponite in aqueous dispersions tends to dissociate at pH values lower than 9.[18, 19] To confirm the dissolution of Laponite-based gels in culture environment, leached Mg^{2+} from Laponite gels in the culture medium may be detected by complexometric titration with EDTA using eriochromeblack-T as an indicator.[18] The concentrations of Mg^{2+} in culture medium can be used as a negative control.

6.2.4.4 *In vitro* osteoclasts response to Laponite gels containing PVPA-*co*-AA

PVPA-*co*-AA has been thought to mimic the function of bisphosphonates which are acknowledged as the bone resorption inhibitors and known to induce osteoclast apoptosis. The *in vitro* osteoclasts cultured with Laponite gels containing PVPA-*co*-AA should be studied to determine the changes in morphology and number of osteoclasts including the presence of apoptotic cells over the culture period in response to the PVPA-*co*-AA copolymer.

6.2.4.5 *In vivo* study of Laponite-based gels

Based on *in vitro* study performed in this thesis, Laponite-based gels have shown potentials to be used as an osteogenic microenvironment with ability to degrade in physiological

conditions. Non-toxic products released from Laponite dissociation (Mg^{2+}, Li^{+}, $Si(OH)_4$, and Na^{+}) could be also adsorbed in human body.[20, 21] In the future direction of this thesis, acellular or growth factors-loaded Laponite-based gels may be subcutaneous implanted *in vivo* and investigated their ability to support tissue formation and vascularisation. However, biodegradability and toxicity *in vivo* are required for GO-containing Laponite gels as GO showed an accumulation in some organs.[22]

6.2.4.6 Improvement of mechanical properties and porous structure of Laponite gels

To improve mechanical stiffness and stability of Laponite-based gels, the incorporation of polymers, nanomaterials, and proteins with adequate concentration can be further researched. Laponite platelets can interact with proteins through adsorption mechanism, generating clay-protein bridges and account for an increase of network stiffness.[23] Generally, nanoclays are used to incorporate into polymer matrix in order to improve mechanical and rheological properties.[20, 24] However, in this context, Laponite nanoclay would be a major phase and the addition of other molecules is expected to improve mechanical properties and stability of clay gels.

As outlined in Chapter 5, Laponite-based gels lacked the effective pore structure to support cell migration. For further research, the fabrication of Laponite gel scaffolds with porous interconnected network may be required for directing cell migration. In this regard, 3D printing techniques can be utilised to create engineered tissue constructs with controllable pore sizes. The addition of other hydrogels, such as gelatin and collagen hydrogels, can be also applied.

6.3 References

1. Wang, Y.; Li, Z.; Wang, J.; Li, J.; Lin, Y., Graphene and graphene oxide: biofunctionalization and applications in biotechnology. *Trends in Biotechnology* **2011,** *29* (5), 205-212.
2. Mousavi, S. M.; Hashemi, S. A.; Ghasemi, Y.; Amani, A. M.; Babapoor, A.; Arjmand, O., Applications of graphene oxide in case of nanomedicines and nanocarriers for biomolecules: review study. *Drug Metabolism Reviews* **2019,** *51* (1), 12-41.
3. Lerner, M. B.; Pan, D.; Gao, Y.; Locascio, L. E.; Lee, K.-Y.; Nokes, J.; Afsahi, S.; Lerner, J. D.; Walker, A.; Collins, P. G.; Oegema, K.; Barron, F.; Goldsmith, B. R., Large scale commercial fabrication of high quality graphene-based assays for biomolecule detection. *Sensors and Actuators B: Chemical* **2017,** *239*, 1261-1267.
4. Khan, U.; O'Neill, A.; Lotya, M.; De, S.; Coleman, J. N., High-concentration solvent exfoliation of graphene. *small* **2010,** *6* (7), 864-871.

5. Shellard, P. M.; Srisubin, T.; Hartmann, M.; Butcher, J.; Fei, F.; Cox, H.; McNamara, T. P.; McArdle, T.; Shepherd, A. M.; Jacobs, R. M., A versatile route to edge-specific modifications to pristine graphene by electrophilic aromatic substitution. *Journal of Materials Science* **2020,** *55*, 10284-10302.
6. Tang, L. A. L.; Wang, J.; Loh, K. P., Graphene-Based SELDI Probe with Ultrahigh Extraction and Sensitivity for DNA Oligomer. *Journal of the American Chemical Society* **2010,** *132* (32), 10976-10977.
7. Rolin, C.; Kang, E.; Lee, J.-H.; Borghs, G.; Heremans, P.; Genoe, J., Charge carrier mobility in thin films of organic semiconductors by the gated van der Pauw method. *Nature Communications* **2017,** *8* (1), 14975.
8. Sabzi, M.; Jiang, L.; Liu, F.; Ghasemi, I.; Atai, M., Graphene nanoplatelets as poly(lactic acid) modifier: linear rheological behavior and electrical conductivity. *Journal of Materials Chemistry A* **2013,** *1* (28), 8253-8261.
9. Shellard, P. Functionalised graphene for biomedical applications. PhD Thesis, University of Manchester, 2017.
10. Zhao, X.; Zhang, Q.; Chen, D.; Lu, P., Enhanced mechanical properties of graphene-based poly (vinyl alcohol) composites. *Macromolecules* **2010,** *43* (5), 2357-2363.
11. Srisubin, T. Characterising the distribution of functionalised graphene nanoplatelets in layer-by-layer assemblies. University of Manchester, **2016**.
12. Singh, K.; Blanford, C. F., Electrochemical Quartz Crystal Microbalance with Dissipation Monitoring: A Technique to Optimize Enzyme Use in Bioelectrocatalysis. *ChemCatChem* **2014,** *6* (4), 921-929.
13. Sauerbrey, G., Verwendung von Schwingquarzen zur Wägung dünner Schichten und zur Mikrowägung. *Zeitschrift für Physik* **1959,** *155* (2), 206-222.
14. Luong-Van, E. K.; Madanagopal, T. T.; Rosa, V., Mechanisms of graphene influence on cell differentiation. *Materials Today Chemistry* **2020,** *16*, 100250.
15. Piao, Y.; Chen, B., Synthesis and mechanical properties of double cross-linked gelatin-graphene oxide hydrogels. *International Journal of Biological Macromolecules* **2017,** *101*, 791-798.
16. Dey, R. E.; Zhong, X.; Youle, P. J.; Wang, Q. G.; Wimpenny, I.; Downes, S.; Hoyland, J. A.; Watts, D. C.; Gough, J. E.; Budd, P. M., Synthesis and Characterization of Poly (vinylphosphonic acid-*co*-acrylic acid) Copolymers for Application in Bone Tissue Scaffolds. *Macromolecules* **2016,** *49* (7), 2656-2662.
17. Wang, Q. G.; Wimpenny, I.; Dey, R. E.; Zhong, X.; Youle, P. J.; Downes, S.; Watts, D. C.; Budd, P. M.; Hoyland, J. A.; Gough, J. E., The unique calcium chelation property of poly (vinyl phosphonic acid-co-acrylic acid) and effects on osteogenesis in vitro. *Journal of Biomedical Materials Research Part A* **2018,** *106* (1), 168-179.
18. Jatav, S.; Joshi, Y. M., Chemical stability of Laponite in aqueous media. *Applied clay science* **2014,** *97*, 72-77.
19. Thompson, D. W.; Butterworth, J. T., The nature of laponite and its aqueous dispersions. *Journal of Colloid and Interface Science* **1992,** *151* (1), 236-243.
20. Xavier, J. R.; Thakur, T.; Desai, P.; Jaiswal, M. K.; Sears, N.; Cosgriff-Hernandez, E.; Kaunas, R.; Gaharwar, A. K., Bioactive nanoengineered hydrogels for bone tissue engineering: a growth-factor-free approach. *ACS Nano* **2015,** *9* (3), 3109-3118.
21. Tomás, H.; Alves, C. S.; Rodrigues, J., Laponite®: A key nanoplatform for biomedical applications? *Nanomedicine: Nanotechnology, Biology and Medicine* **2017**.
22. Liu, J.-H.; Yang, S.-T.; Wang, H.; Chang, Y.; Cao, A.; Liu, Y., Effect of size and dose on the biodistribution of graphene oxide in mice. *Nanomedicine* **2012,** *7* (12), 1801-1812.
23. Shi, P.; Kim, Y. H.; Mousa, M.; Sanchez, R. R.; Oreffo, R. O.; Dawson, J. I., Self-Assembling Nanoclay Diffusion Gels for Bioactive Osteogenic Microenvironments. *Advanced healthcare materials* **2018,** *7* (15), 1800331.
24. Nojoomi, A.; Tamjid, E.; Simchi, A.; Bonakdar, S.; Stroeve, P., Injectable polyethylene glycol-laponite composite hydrogels as articular cartilage scaffolds with superior mechanical and rheological properties. *International Journal of Polymeric Materials and Polymeric Biomaterials* **2017,** *66* (3), 105-114.

Appendix

A.1 Live/dead images of primary human osteoblasts on LbL constructs

Figure A-1 shows LIVE/DEAD images of HOBs seeded on PEI/G–SO_3, PEI/G–SH, PEI/GO–SO_3, and PEI/GO–SH. HOBs seeded on PEI/G–SO_3, PEI/G–SH, and PEI/GO–SH were rounded and did not spread or proliferate throughout the test period. In contrast, HOBs on PEI/GO–SO_3 showed a spindle-like shape or elongated morphology with proliferation over time.

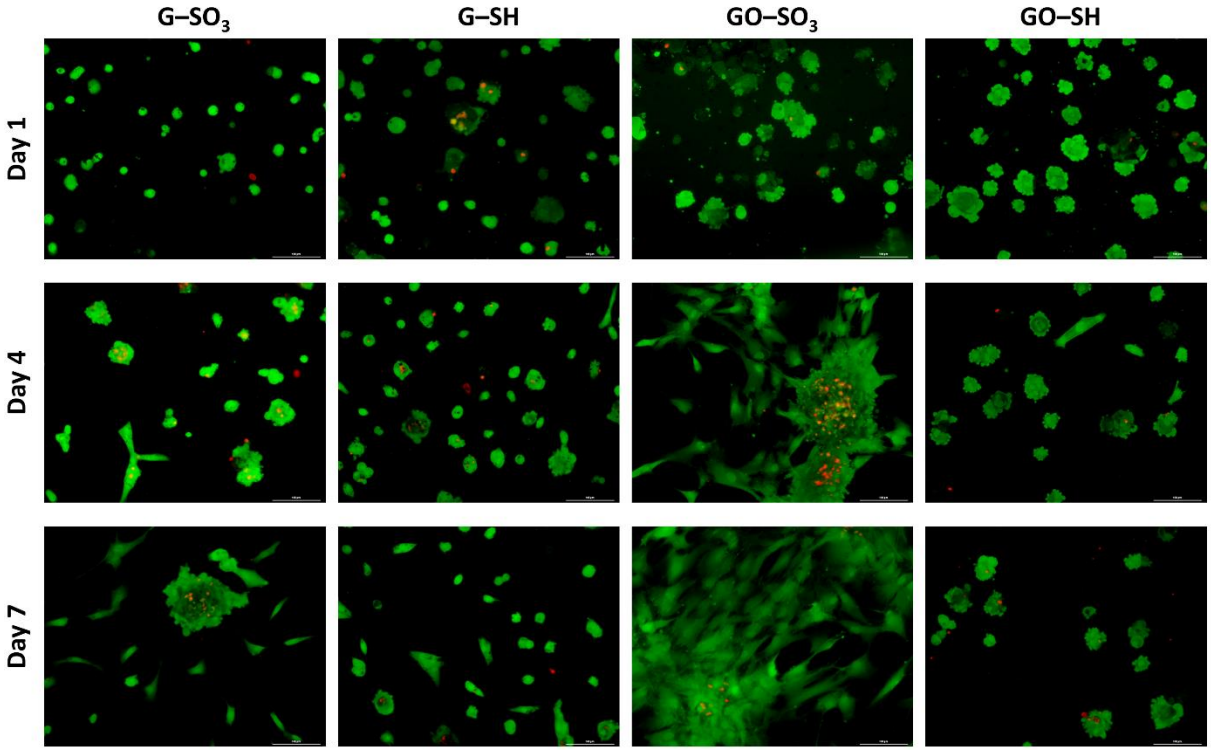

Figure A-1. LIVE/DEAD images of HOBs (passage number 3) seeded on LbL constructs containing functionalised graphene derivatives and PEI, with 3 bilayers.

A.2 Osteogenic mineralisation of primary human osteoblasts on LbL constructs

Representative images of alizarin red S staining of HOBs on PEI/G–SO_3, PEI/G–SH, PEI/GO–SO_3, and PEI/GO–SH cultured in growth and osteogenic media are shown in Figure A-2 and Figure A-3, respectively. No positive staining was observed on any samples, likely due to the lack of cell attachment and proliferation.

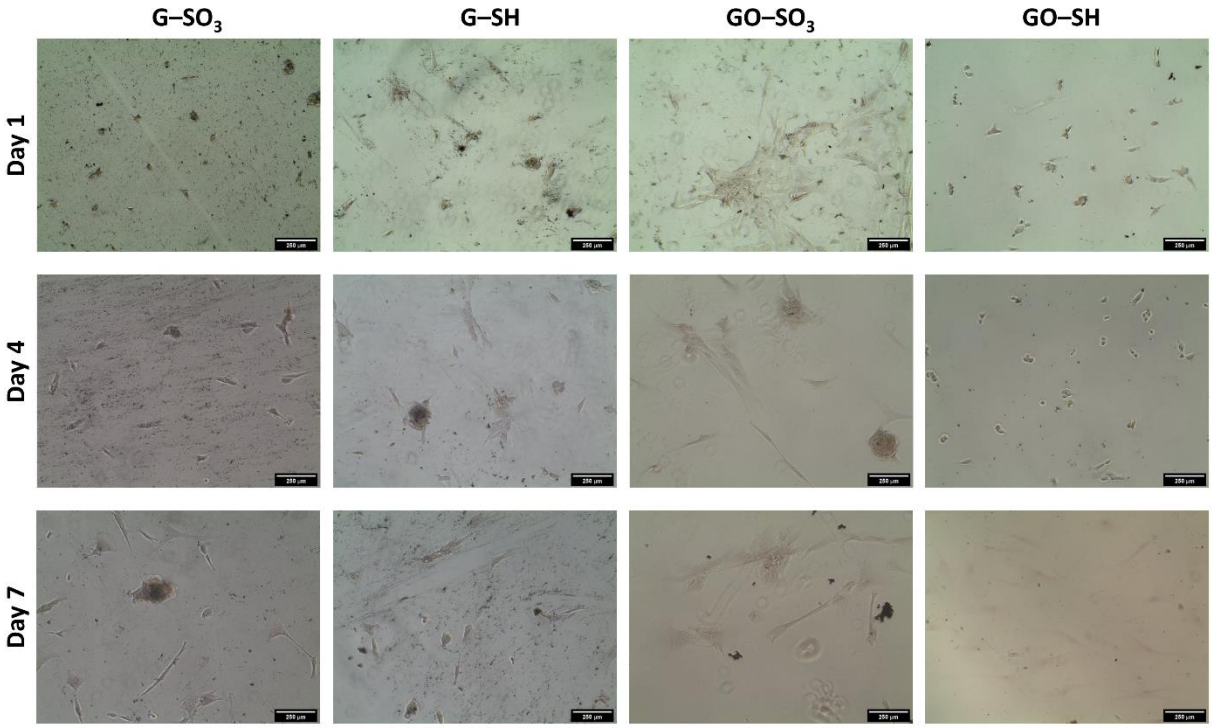

Figure A-2. Alizarin red S staining of HOBs (passage number 3) on GFN-containing LbL constructs, after incubation with basal growth (non-induction) medium over 3 weeks. Scale bar represents 250 µm.

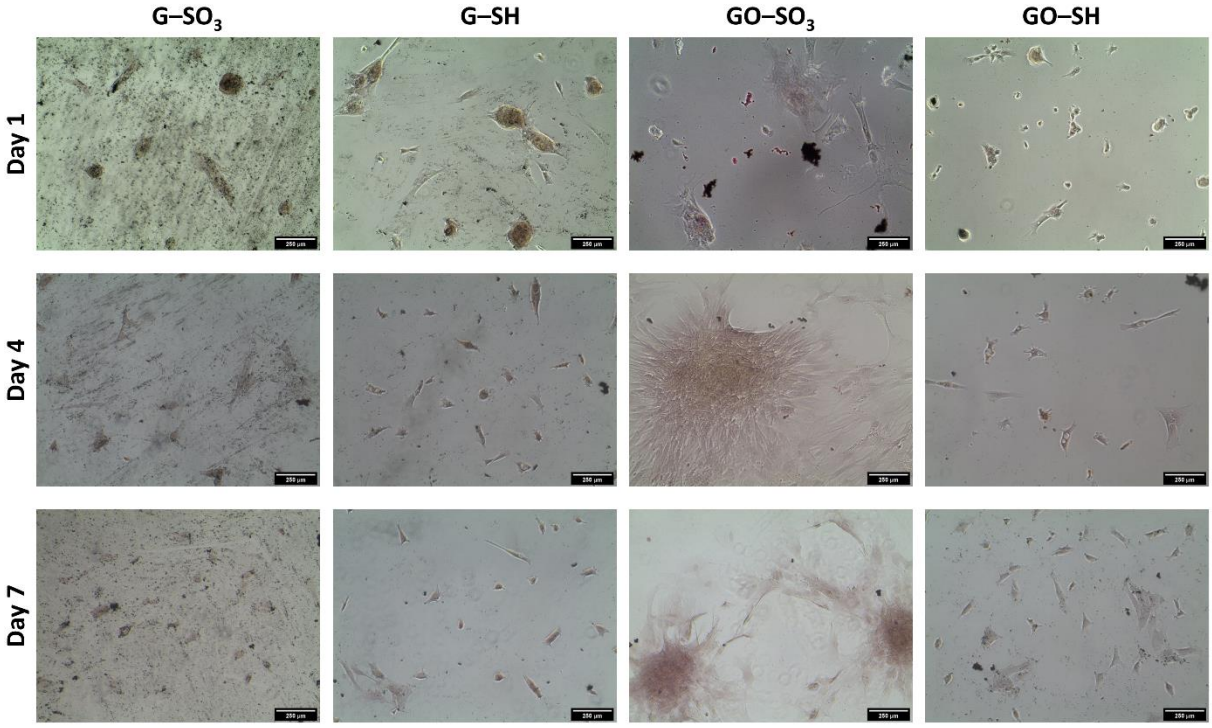

Figure A-3. Alizarin red S staining of HOBs (passage number 3) on GFN-containing LbL constructs, after incubation with osteogenic induction medium over 3 weeks. Scale bar represents 250 µm.

A.3 Osteogenic differentiation of human mesenchymal stem cells within nanoclay-gel discs

hMSCs were encapsulated within Laponite-based gel discs and cultured in growth and osteogenic media for 4 weeks. Osteogenic differentiation of hMSCs was investigated by histological assessment. Alizarin red S and Von Kossa stains were performed on cross-sections of samples, with representative images presented in Figure A-4 – Figure A-7. No positive staining was detected for hMSCs within Laponite-based gel discs, meaning to no osteogenic differentiation or mineralisation.

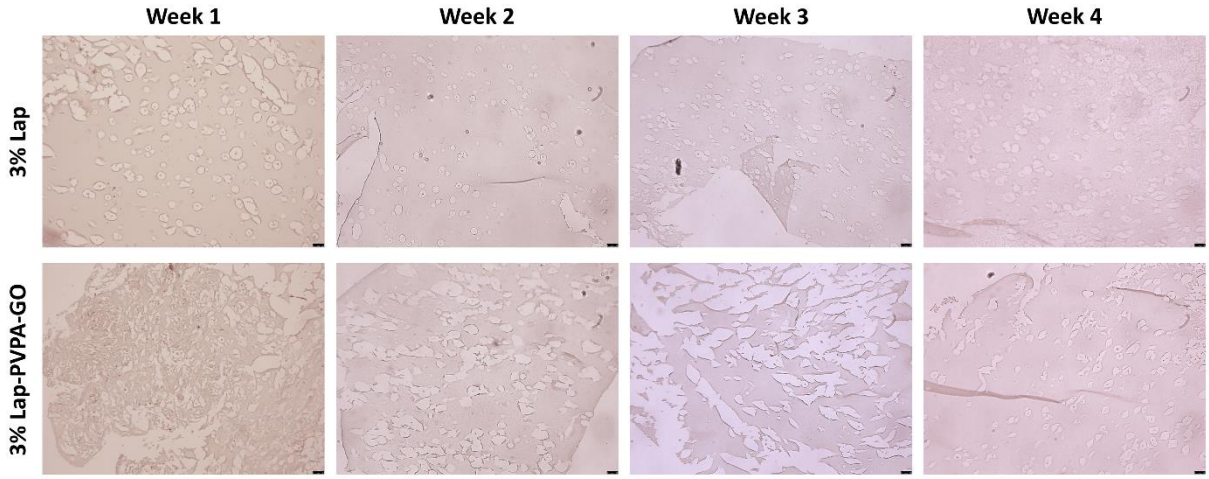

Figure A-4. Alizarin red S staining of cross-sections from in vitro hMSCs (passage number 6) encapsulated within nanoclay-gel discs, incubation in growth medium for 4 weeks. Scale bar represents 50 µm.

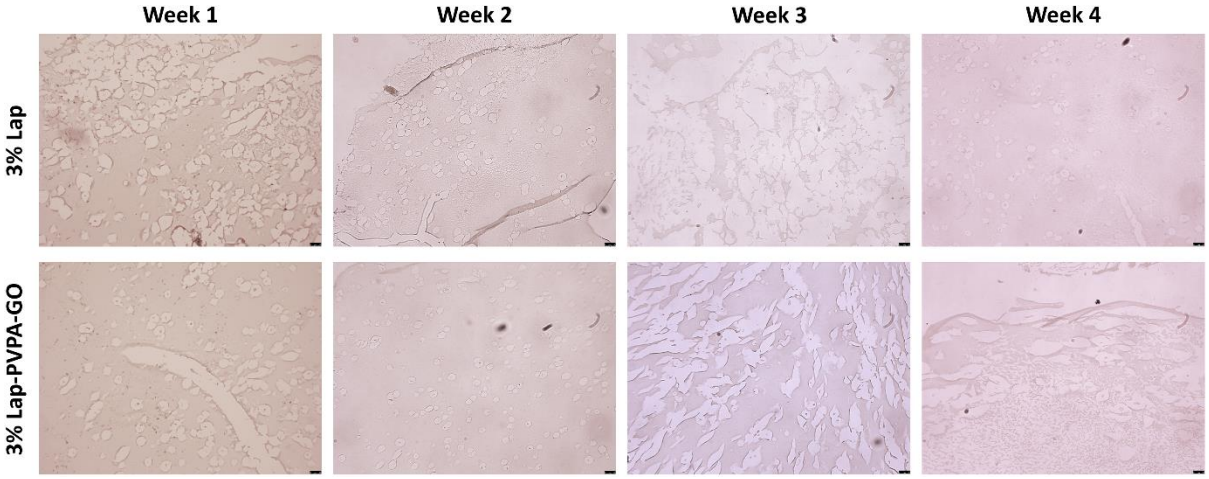

Figure A-5. Alizarin red S staining of cross-sections from in vitro hMSCs (passage number 6) encapsulated within nanoclay-gel discs, incubation in osteogenic medium for 4 weeks. Scale bar represents 50 µm.

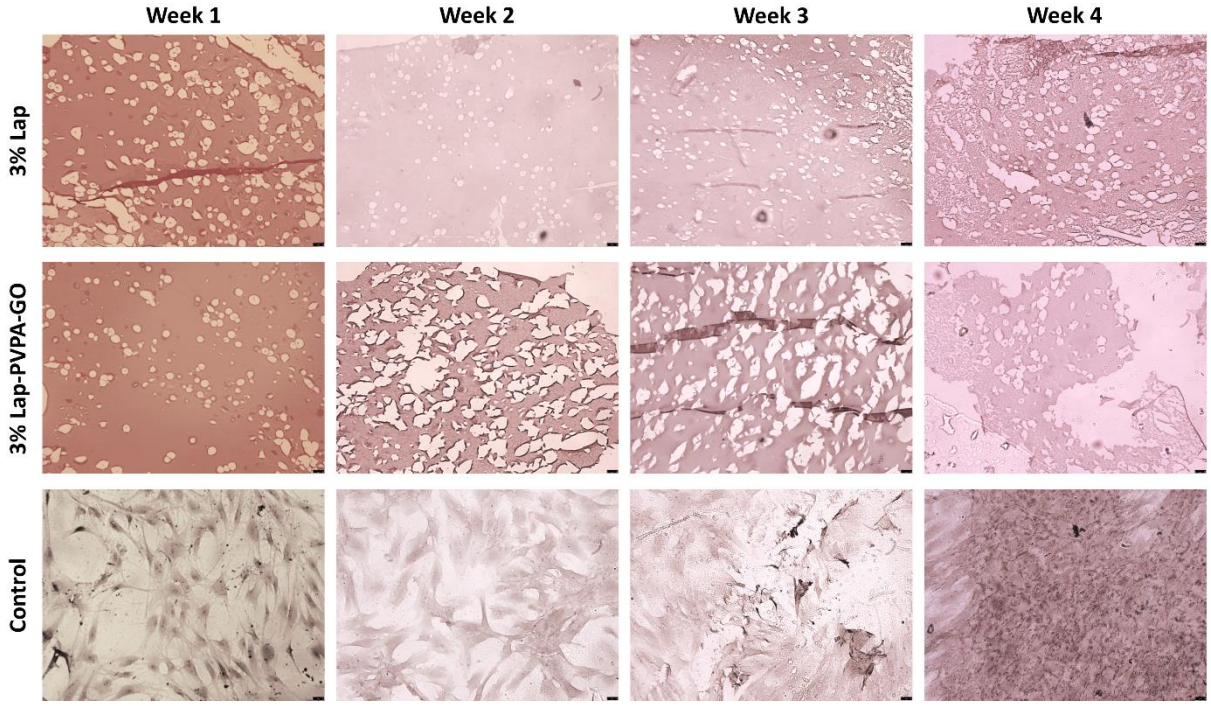

Figure A-6. Von Kossa staining of cross-sections from in vitro hMSCs (passage number 6) encapsulated within nanoclay-gel discs, incubation in growth medium for 4 weeks. Scale bar represents 50 µm.

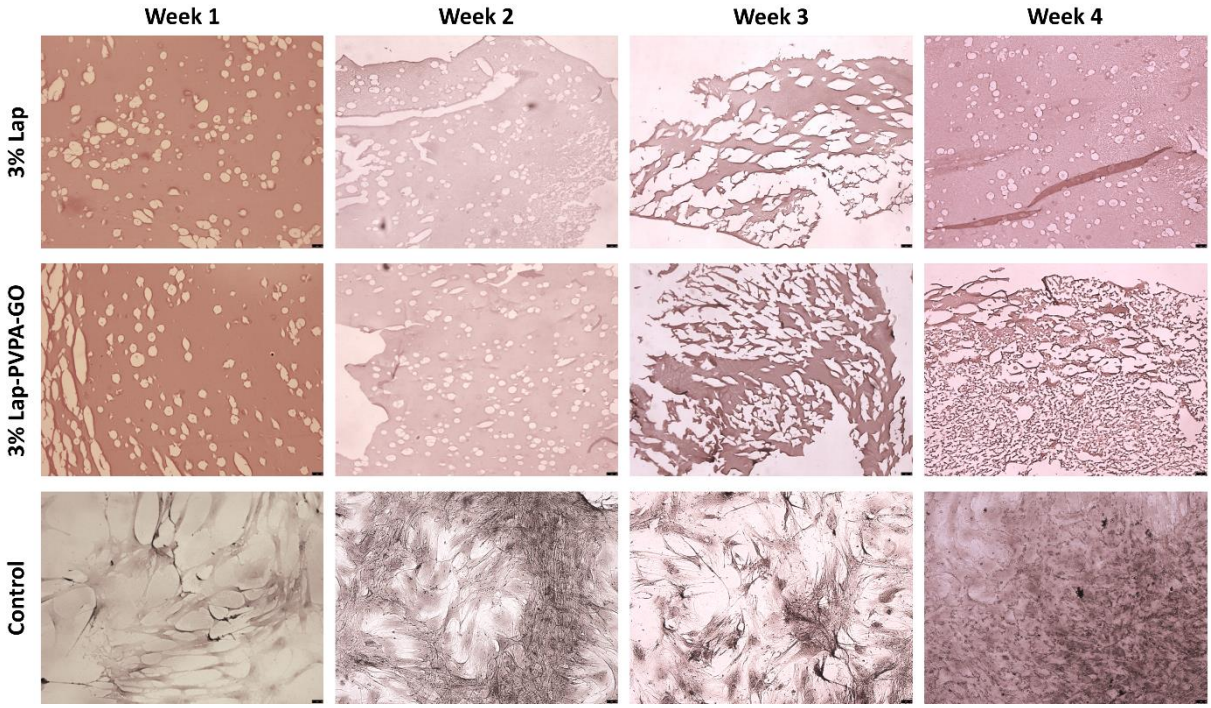

Figure A-7. Von Kossa staining of cross-sections from in vitro hMSCs (passage number 6) encapsulated within nanoclay-gel discs, incubation in osteogenic medium for 4 weeks. Scale bar represents 50 µm.

A.4 Cytoskeletal organisation of human mesenchymal stem cells within nanoclay-gel discs

Cytoskeletal organisation of hMSCs within Laponite-based gel discs was investigated using phalloidin staining, with representative images shown in Figure A-8. Phalloidin staining revealed a restricted cytosekelal organisation with rounded morphology of hMSCs encapsulated within nanoclay-based gel discs whereas hMSCs seeded on TCP showed a distribution of stress fibres.

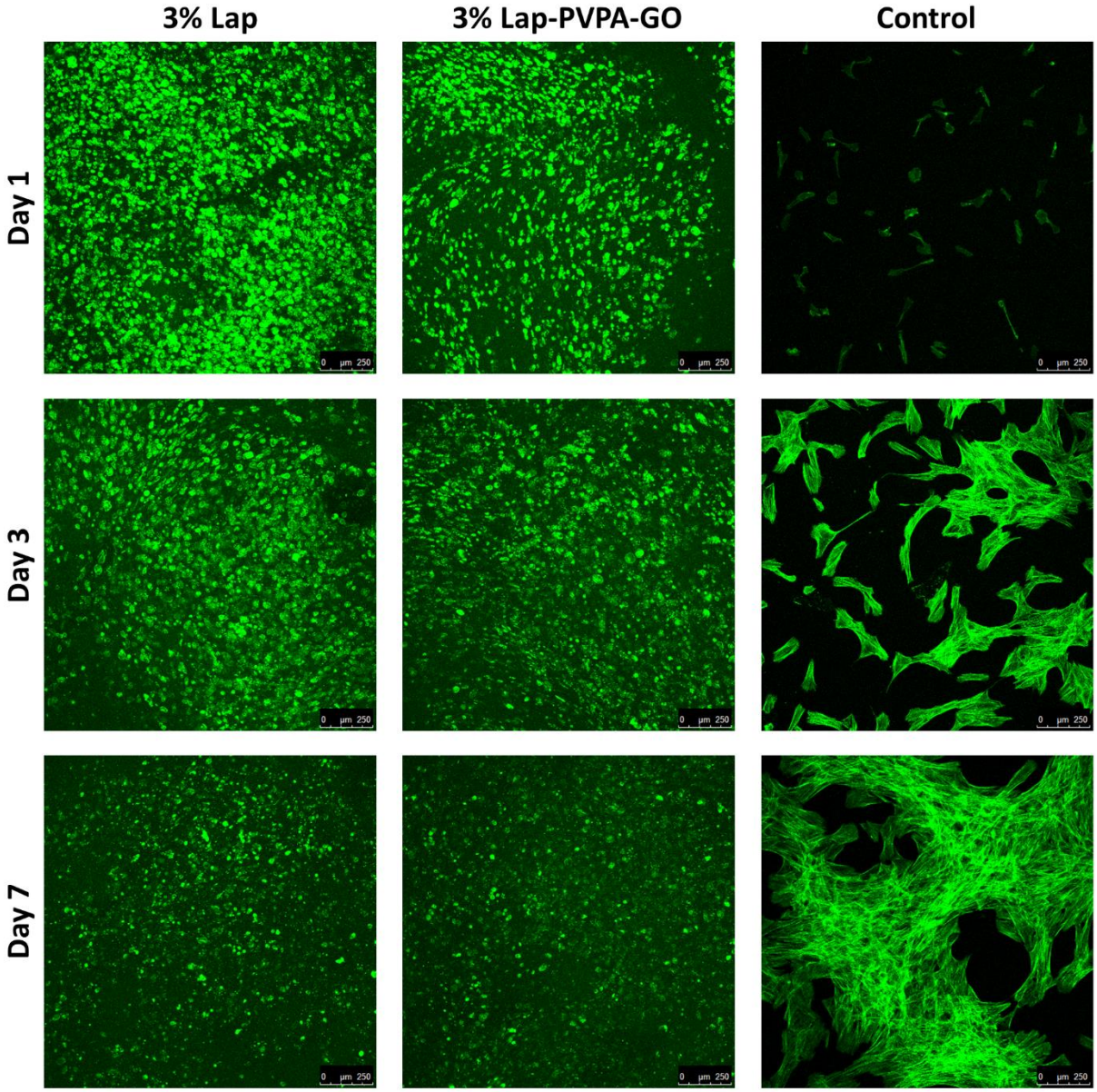

Figure A-8. Phalloidin staining of in vitro hMSCs (passage number 6) encapsulated within nanoclay-gel discs. Scale bar represents 250 µm.